Hybrid Integration of Er-doped Materials and CNTs on Silicon for Light Emission and Amplification

Weiwei Zhang

To cite this version:

Weiwei Zhang. Hybrid Integration of Er-doped Materials and CNTs on Silicon for Light Emission and Amplification. Optics [physics.optics]. Université Paris Saclay (COmUE), 2017. English. NNT : 2017SACLS001 . tel-01587797

HAL Id: tel-01587797

https://theses.hal.science/tel-01587797v1

Submitted on 14 Sep 2017

NNT : 2017SACLS001

THESE DE DOCTORAT
DE
L'UNIVERSITE PARIS-SACLAY
PREPAREE A
L'UNIVERSITE PARIS-SUD

ECOLE DOCTORALE N°575
Physique et ingénierie : Electrons, Photons, Sciences du vivant

Spécialité de doctorat : Physique

Par

Weiwei ZHANG

Hybrid integration of Er-doped materials and CNTs on silicon for light emission and amplification

Thèse présentée et soutenue à Orsay, le 13 janvier 2017 :

Composition du Jury :

Mme Béatrice Dagens	Université Paris-Sud	Présidente du Jury
M. Raphaël Clerc	Institut d'Optique Graduate School	Rapporteur
M. Blas Garrido	University of Barcelona	Rapporteur
M. Loïc Bodiou	FOTON	Examinateur
M. Raphael Salas	Université de technologie de Troyes	Examinateur
M. Stéphane Parola	ENS Lyon	Examinateur
M. Eric Cassan	Université Paris-Sud	Directeur de thèse

Acknowledgement

I express the first gratitude to my supervisor, Eric Cassan, who motivated me entering the silicon photonics research field, guided me from a master student and helped me a lot during my first hard year study in Paris. Not only the research knowledge has been learned from him, but also the dedicated and rigorous attitudes to research. He is very kind and concerned to his students. It’s my honor to have such a scholarly mentor.

I am also very grateful to Prof. Laurent Vivien, who guided my experimental works related to the integration of CNTs with silicon and offered me a lot of opportunities to learn different optical measurements inside and outside the group. In particular, I wish to express my deep gratitude towards Xavier Le Roux, clean room engineer expert, who taught me nano-fabrication techniques and transmitted me part of his experience with respect to the silicon photonics technology. Thanks also to Prof. Delphine Marris-Morini, who also helped me to learn experimental measurements, fundamentals of the optical setup and fiber optics. Thank you to all the collaboration members of the Professor. Daming Zhang’s group and Professor. Zhipei Sun’s one for the two/three years co-working activity.

I also would like to thank my working partners, Dr. Samuel Serna, Mrs. Elena Duran, Dr. Carlos Ramos and Mrs. Thi Hong Cam Hoang, Dr. Jihua Zhang, Dr. Diego Perez-Galacho, Dr. Pedro Damas, Meiling Zhang (Jilin University), John Rönn (Aalto University) with whom I have worked, discussed, and learned a lot from them.

At last, I would like to acknowledge École normale supérieure de Cachan for the international master scholarship, University Paris Saclay for the admission of Nanoscience Master program, and the ANR/NSFC POSISLOT project for funding my three years’ studies.

Sincerely, I express my deep gratitude to all members of my family, who supported me so many years.

Zhang Weiwei

September, 2016

Orsay, France

Introduction

Silicon photonics has been characterized by a huge development in the last years, boosted by academic research efforts and available commercial CMOS facilities for potential mass-production applications. In the past years, versatile passive and active silicon based nanophotonic devices have been demonstrated for the applications of optical interconnects, optical routers/signal processors, long range telecommunications, light-field displays, and bio-sensing.

However, challenging tasks still remain, including the demonstration of reliable on-chip silicon sources fulfilling CMOS fabrication compatibility, low cost, weakly sensitive to temperature variations, and able to emit sufficient optical power for on-chip system applications. Few years ago, integrated stimulated Raman scattering silicon lasers were demonstrated. Although related works opened promises to build 100% silicon optical sources, the demonstrated devices were characterized by intrinsic fundamental drawbacks including an optical pumping scheme and limited microwatt emission ranges. Electrically pumped on chip lasers are indeed usually preferred, and silicon can unfortunately hardly handle this result due to its indirect bandgap. Meanwhile, germanium-on-silicon lasers have been demonstrated by n-doping and the use of either strained layers or germanium-tin alloys and have been proved to reach lasing. However, state of the art germanium based silicon lasers cannot emit sufficient power yet and still need further improvements. To date, the most reliable on chip lasers are hybrid III-V on silicon semiconductor lasing diodes, compatible with electrical pumping, high temperature stability and able to emit sufficient power. However, the use of III-V hybrid on silicon diode requires additional bonding techniques on silicon, making the whole fabrication process more sophisticated.

Alternative solutions have been proposed and reported, which are based on cladding or sandwiched active materials integrated with silicon photonic structures. The potential advantages of such hybrid on silicon approaches include low cost, easy processing and the possible use of various active materials.

In such hybrid on silicon approaches, silicon is mainly used for the qualities of the silicon on insulator (SOI) waveguide platform, eg for the low loss and strong index contrast of SOI optical waveguides. Active materials integrated on silicon through growth, spin-coating or other deposition techniques, bring on their side nonlinearities, modulation or luminescence properties that silicon cannot exhibit alone. With respect to such a scheme, a key point is to ensure that propagating or resonance optical modes are characterized by a sufficient overlap with the incorporated active materials that usually have lower refractive index values than Si. In this thesis, the focus has been made on the design, fabrication, and characterization of hollow core silicon waveguides and resonators for the integration of Erbium doped and carbon nanotubes thin film materials. The investigated hybrid integration of these materials within slotted silicon waveguides has been mainly made in the purpose of on-chip light emission and amplification.

The thesis manuscript is organized as follows:

(1). In chapter-1, a review of hybrid silicon photonics is presented.

(2). In chapter-2, we explore light confinement properties of different kinds of silicon hollow core structures.

(3). In chapter-3, integration of two kinds of Erbium doped active materials is depicted, including the description of material properties, integration methods, hybrid integration challenges and optical gain measurements.

(4). In chapter-4, Carbon nanotube hybrid integration on silicon is presented. Progress related to the integration of high concentrations of semiconductor carbon nanotubes within silicon waveguides, ring resonators, and nanobeam cavities with respect to photoluminescence enhancement and light coupling into SOI waveguides are reported.

(5). Thesis achievements, challenges, and perspectives are finally discussed in conclusion.

Contents

1. Silicon photonics: A versatile hybrid integration platform

1.1 Silicon photonics needs hybridization

1.1.1 Silicon photonics: towards co-integration with electronics

Silicon photonics has been developed for some years as a mature tool for the realization of next generation high speed on-chip data communication systems benefiting from previous fruitful research developments. Nearly, most of the needed optical devices enabling on-chip data links have been developed within the planar metal-oxide-semiconductor (CMOS) technology. Moreover, whole-wafer processing and compatibility with the existing micro-electronic facilities have strongly pushed Si photonics towards a rapid development [1]. To meet the trend of global network capacity rapid growing and get rid of bandwidth and power limitations of on-chip electric interconnects, optical interconnects have been proposed and implemented [1]–[3].This technology mainly consists in implementing optical links at the chip level, i.e. by using a combination of CMOS-compatible light sources, optical modulators, and photon detectors, thus enabling a photonics–electronics convergence [4], [5].

Bandwidth of optical interconnects mainly depends on the performances of optical transceivers, including optical modulators (E/O signal converters) and photodetectors (O/E signal converters). Electro-optic silicon modulators (EOM) are usually realized through electrical free carrier concentration modulation in silicon photonic devices, giving typically rise to high data rates up to 50 Gb/s [6]–[8]. Zero-bias 40Gbit/s germanium waveguide photodetectors on silicon have also been demonstrated [9]. Advanced multiple levels of phase or amplitude modulations, such as quadrature phase-shift keying (QPSK), quadrature amplitude modulations (QAM), have also pushed the total data rate frontier much higher than 40GBits/s. For instance, a 112Gb/s optical link was realized in [10], while on chip wavelength-division-multiplexed (WDM) technology was proved to enable 1.6Tb/s receivers with 40 channels [11] and 250Gb/s for 10-channels modulation [12]. As a whole, the maturity of silicon passive and active devices has led to the design and successful demonstration of on-chip systems [4].

For instance, optical communications enabled by silicon based nano-photonic devices has been successfully demonstrated on chip-scale electronic-photonic systems [4], as shown in Figure.1.1.

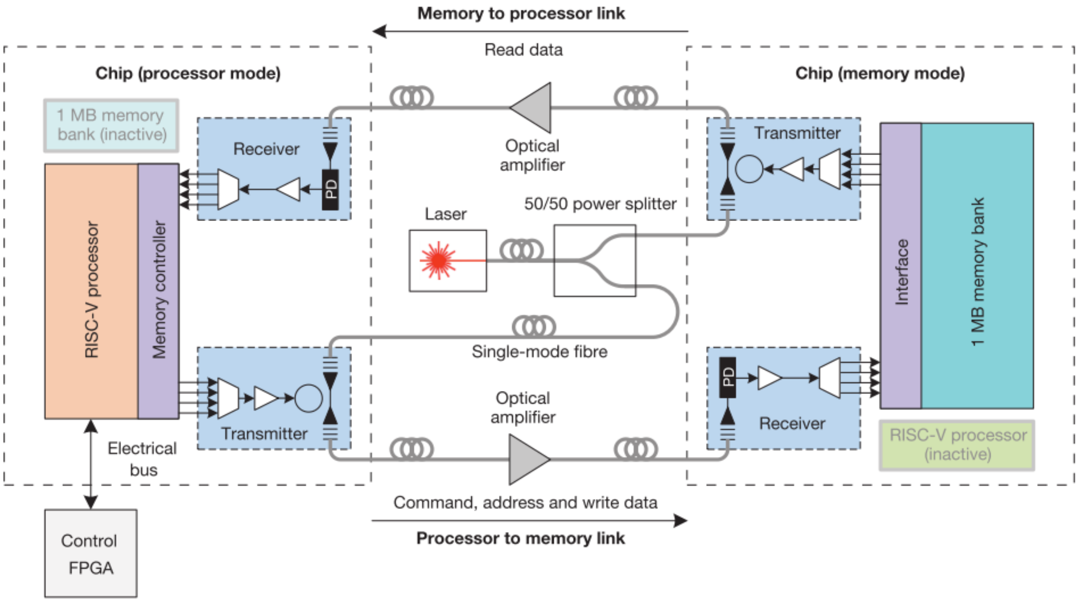

Figure 1.1 The electronic-photonic system uses one chip acting as the processor and the other acting as memory, connected by a full-duplex optical link with a round-trip distance of 20 m by fiber [4].

1.1.2 Limits of Silicon for optical interconnects

To achieve the success of the silicon photonic circuit co-integration with electronics and investigate other prospects such as full nonlinear optical signal processing, some silicon photonic limitations have to be overcome. To sum up, the dominant shortcomings in silicon are inabilities for efficient lasing, and intrinsic detrimental free carrier effects on optical third order nonlinearities. In the next sub-sections, we will draw a rapid overview of these two points.

1.1.2.1 Lasing in Silicon

On-chip laser sources are always the first choice for photonic chips in order to avoid off-chip laser coupling losses, high cost expense of package, and to pursue better performance with less energy consumption. However, such on-chip, broad band and high power emitting lasing sources are presently not possible due to silicon's low emission efficiency that it is intrinsically related to its indirect bandgap. Hence, on chip light sources should be realized through other gain mechanisms, for instance nonlinear processes including Raman effects [13], [14] and phase matched nonlinear four wave mixing [15]. The former Raman effects based lasers can be obtained and strongly enhanced by high *Q* resonators to reduce threshold powers down to microwatts and by reversed biased PIN diodes to removed free carriers [16]. In another direction, with the use of the four wave mixing process was demonstrated for example in [15], not directly light emission, but light amplification. A broad band nonlinear gain up to 80nm wavelength range (1511-1591nm) was demonstrated and an optimal gain of 5.2dB was obtained at λ=1.53µm.

To sum up, these works highlight the main current status of silicon lasing sources: i) light emission is difficult in silicon; ii) nonlinear third order processes can be used for light amplification to circumvent the intrinsic drawback of Si indirect bandgap, but, considering CMOS compatibility constraints, dense integration and small footprint, the demonstrated optically pumped lasing sources and amplifiers are not directly acceptable. Moreover, optical gain of Si-amplifier is limited to few dBs at telecom wavelengths due to the effect of free carriers, as explained hereafter.

1.1.2.2 Free carriers effects in silicon photonics

Free carriers present in semiconductors can either enhance or spoil device performances depending on the situation. Free carriers can be produced in silicon waveguide cores by doping or light absorption. Doping is classically used to realize PN junctions that are used, for instance, in germanium photo-detectors with n/p doped regions to prepare a high electric field (in Figure.1.2.a) and in silicon optical modulators to obtain high speed electrical free carrier concentration modulation (in Figure.1.2.b).

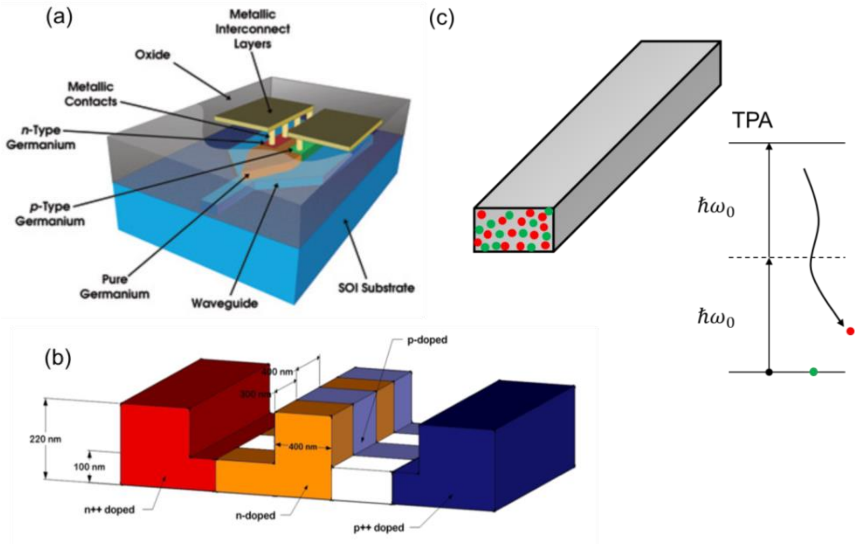

Figure 1.2 (a) Various layers used in Germanium detector [17] (b) Schematic view of the interleaved diodes phase shifter as part of a silicon modulator [18]. (c) TPA generated free carriers in silicon channel waveguides.

Free carriers generated through light absorption can be classified into three kinds of situations [19]: low concentrations due to low light intensities, low concentration but with metal like surface carrier distribution due to moderate light intensity, and high concentrations due to two photon absorption (TPA) in high power pumping regime [20]. Free carriers primarily perturb light propagation through their induced polarization (P_i^f), which is linearly dependent on the free carrier densities (electrons N_e and holes N_h) in silicon waveguides:

$$P_i^f(r,t) = \varepsilon_0 \sum_\mu \chi^f(\omega_\mu, N_e, N_h) E_i(r, \omega_\mu, t) \tag{1-1}$$

$$\chi^f = 2n_0(n_f + i\frac{c\alpha_f}{2\omega}) \tag{1-2}$$

$$n_f(\omega_r, N_e, N_h) = -(8{,}8\times10^{-4}N_e + 8{,}5N_h^{0{,}8})\times10^{-18} \tag{1-3}$$

$$\alpha_f(\omega_r, N_e, N_h) = (8{,}5N_e + 6{,}0N_h)\times10^{-18} \tag{1-4}$$

In equation 1-1 and 1-2, χ^f is the free carrier induced susceptibility and its real and imaginary parts are related to refraction index change (n_f) and light absorption (α_f), respectively.

The nonlinear Two-Photon-Absorption process (TPA; related to the imaginary part of $\chi^{(3)}$) can be responsible for the generation of non-negligible free electron and hole concentrations (Figure.1.2.c). These generated carriers not only absorb light but also affect the nonlinear wave propagation by changing the refractive index, thus countering the nonlinear Kerr effect (related to real part of $\chi^{(3)}$) [21]. Therefore, a high concentration of free carriers can strongly spoil the silicon third-order nonlinearity due to the strength of two-photon-absorption (TPA). The relative importance between the third-order nonlinear optical Kerr and TPA effects is usually quantified by the use of the figure of merit: $FOM_{Bulk} = n_2/\lambda\alpha_2$, with n_2 the nonlinear refractive index and α_2 the material TPA coefficient, which for silicon waveguides is only 0.4, ie extremely small for fast nonlinear silicon photonic devices. Free carrier influence has been widely reported in four wave mixing[22] and Raman lasers [23], and has, on average, a detrimental effects on nonlinear effects in silicon.

1.1.3 Hybrid integration in/on silicon photonics

As discussed above, silicon itself is unable to accomplish the mission of efficient integrated optical interconnects alone. Other processes integrating other alternative materials in/on silicon are necessary to improve the performances of integrated components and/or enable some optoelectronic functions (eg light emission).

1.1.3.1 Integration of III-V and Ge devices

As the silicon platform suffers from the drawback of lack of lasing, as discussed in section-1.1.2.1 due to its indirect bandgap, direct band semiconductor compounds, like GaAs and InP, have been integrated in the silicon platform following different approaches.

III-V materials on silicon hybrid integration process can be realized through: flip-chip integration, wafer bonding and heteroepitaxial growth [24]. Heteroepitaxial growth method faces the problem of lattice mismatch ((GaAs)4%, InP/InGaAsP 8%) with silicon substrates, which is eased by thick buffer layers growth to avoid defects [25]. Flip-chip integration, namely die-to-wafer bonding, consists in locally aligning III-V layer stacks on top of silicon. For large and dense hybrid integration, wafer bonding techniques, adhesive semiconductor wafer bonding and molecular wafer bonding approaches, are the suited solutions to integrate high quality III-V layers and devices on silicon.

III-V materials are typically prepared as Quantum wells (QWs) or QDs and are electrically pumped to reach lasing. Related external lasing sources can be coupled with silicon waveguides. As a matter of illustration, Figure 1.3 shows an example of a hybrid III-V on silicon lasers/amplifier realized through double tapered III-V diode with QWs coupled with tapered SOI waveguides. At the present time, hybrid III-V lasers allow high emitting powers (> tens milliwatts) and can operate at high temperatures >60°C [26]–[29].

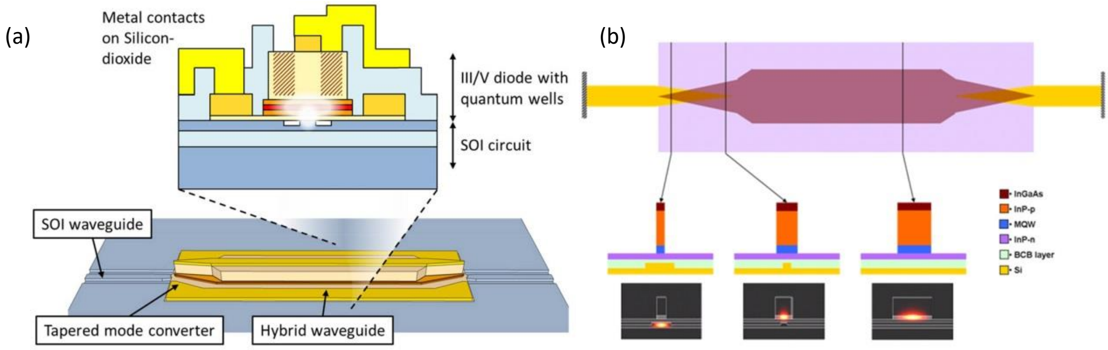

Figure 1.3 (a) Diagram showing a hybrid-silicon III-V optical Laser/amplifier integrated with a silicon waveguide [30]. (b)Top view, cross sections and calculated mode profiles of the III-V/SOI laser [31].

However, such kinds of highly performant lasers require complex fabrication epitaxial processes and tend to be costly for massive applications that require further low costs and large scale integration. Alternatively, germanium (Ge)-on-Si devices are becoming more and more competitive considering recent progress in integrated optical sources , modulators, and detector within the Group IV photonics technology [32].

1.1.3.2 Integration within Si_3N_4/SiN

Integrated silicon nitride photonics has recently progressed a lot and is considered as a performant platform for silicon photonic integration [33]. Compared with pure silicon waveguides, silicon nitride waveguides have a core refractive index ~2 and a cladding silica index ~1.44. The index contrast is thus smaller than those of silicon (ie SOI) waveguides, thus suffering less roughness induced scattering losses and a smaller influence from lithography channel waveguide variations and phase errors. The typical cross-sections and propagation losses (α_l) as a function of bends of these two waveguide families are illustrated in Figure.1.4 and Table.1.1. With bends of few tens of micrometers, optical losses in silicon nitride waveguides are one order of magnitude less than for their silicon single-mode counterparts.

Compared with the SOI platform, which suffers from strong two photon absorption (TPA) around wavelength 1.55µm, **silicon nitrides (**Si_3N_4**)** waveguides have been widely demonstrated for some few years as an alternatively efficient route for integrated on-chip nonlinear optics. The success of the silicon nitride platform is due to a good balance between optical linear/nonlinear losses and third-order nonlinearities (Table.1). Small losses indeed allow a large nonlinear effective length $l_{eff} = (1 - e^{-\alpha_l L})/\alpha_l$, which leads to a large Kerr induced phase shift $\phi_K = \gamma_0 \int_0^l P(z,t)dz = \gamma_0 P_{in} L_{eff}$ [34]. As the third order nonlinearity is one order higher than in silica and only one order less than in silicon, silicon nitride allows even larger ϕ_K than silicon waveguides. Besides, the nonlinear *FOM* of silicon nitride is much larger than the silicon one due to a larger bandgap (as compared in Table.1.1). TPA in SiN is indeed negligible and does not spoil ϕ_K as it happens in silicon waveguides.

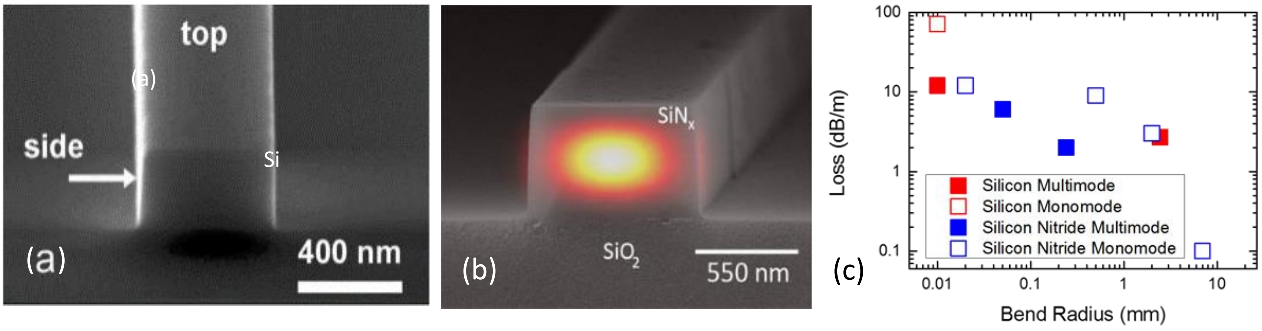

Figure 1.4(a)Silicon waveguides [35],(b)silicon nitride waveguides [36]; Overview of planar waveguide propagation loss as a function of bend radius. (c) Data for Si_3N_4 waveguides taken from [37]–[39] ;Data for Si waveguides taken from [40], [41] [42].

Table 1.1 Nonlinear properties and relative parameters of three important materials in Si photonics

	Si	SiO_2	Si_3N_4
n_0@1550nm	3.45	1.46	1.99
E_g(eV)	1.12	9	5
Transparency window (µm)	1.1-9	~0.13-3.5	0.25-8
β_{TPA} (cm/GW)@1550nm	0.79	<< 0.01	~0
n_2 (m^2/W) @1550nm	~6×10^{-18}	~2.5×10^{-20}	~2×10^{-19}
FOM_{TPA}	~0.4	>>1.0	>>1.0
Liner loss of photonic wave-guides	~50dB/m		1dB/m

Technically, this excellent balance between loss and nonlinear properties has led to a series of demonstrations of nonlinear parametric gain [43], optical frequency comb generation in a ring resonators (see Figure.1.5) [44], advanced Octave-spanning frequency combs [45] and supercontinuum generation [46] in silicon nitrides. Gain bandwidth of 150nm, Octave-spanning frequency combs from 1.1-2.4µm and supercontinuum generation from 665nm-2µm have been achieved. All these successes clearly shown the potentials of all optical signal processing based on Si_3N_4 photonic integrated devices.

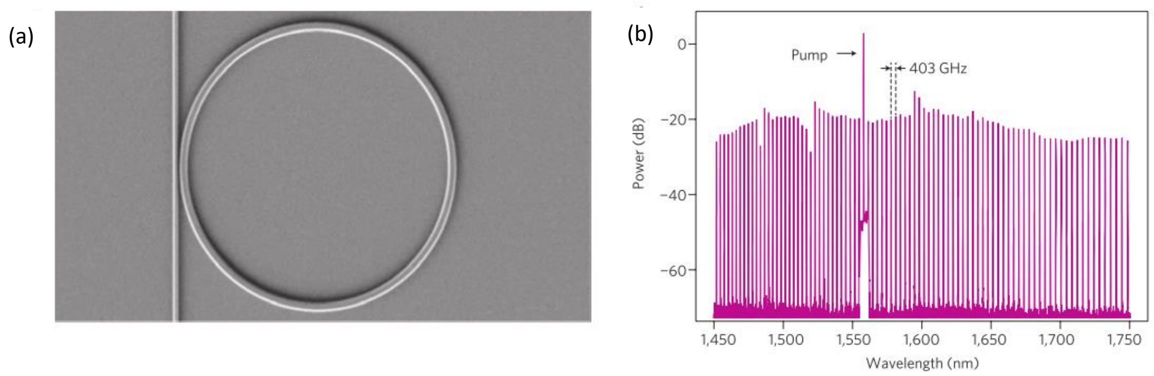

Figure 1.5 (a) SEM image of a SiN microring resonator (58 µm radius, Q = 500,000, FSR = 403 GHz). (b), Output spectrum [43] of a 58-µm-radius SiN ring-resonator optical parametric oscillator.

1.1.3.3 Integration of Carbon-based nano materials

In another direction, huge research efforts have been recently devoted to carbon-based materials with the motivation of integrating them on silicon for light emission/modulation or to exploit their nonlinear properties. Graphene [47], [48] and carbon nanotubes [49], [50] are the two main families leading to this possible integration scheme.

Graphene properties have been broadly investigated for a possible application to photonics, plasmonics or opto-electronics. Graphene indeed presents a high thermal conductivity, a possibly tunable Femi level, an ultra-high threshold optical damage power, and large third order nonlinearities, as summarized and compared with other materials in Table 1.2 [48]. Fruitful prototype devices have been achieved in recent years, such as photodetectors [47], optical modulators [51]–[54], saturable absorbers [55], [56], and nonlinear-optical devices [57]–[59]. All these demonstrations seem to show a trend towards graphene integrated hybrid silicon photonics. As shown in Figure.1.6, the envisioned hybrid graphene photonic circuits consist of a graphene mode-locked laser with a ring cavity (left), graphene optical modulators (middle), and microcavity enhanced graphene photodetectors (right) [60]. However, the challenges to develop such bright graphene based photonic circuits, including preparing and depositing high quality monolayers at right positions with high accuracy and "tightly bound" on waveguide surfaces for large scale integration and fabrications, are still effort-demanding.

Table 1.2 Comparison of different soft material properties for hybrid silicon photonics

	Thermal conductivity (W $m^{-1}K^{-1}$)	Energy Gap (eV)	Refractive index	Optical damage Threshold mW/cm^2	Second order nonlinearity	χ(3) (esu)
Graphene	5300	0	2.6	3×10^6	no	$\sim 10^{-7}$
CNT	3000					$\sim 10^{-6}$
DDMEBT		~1,7	1.8			$\sim 10^{-10}$
Si	149	1.11	3.44	500	no	$\sim 10^{-10}$

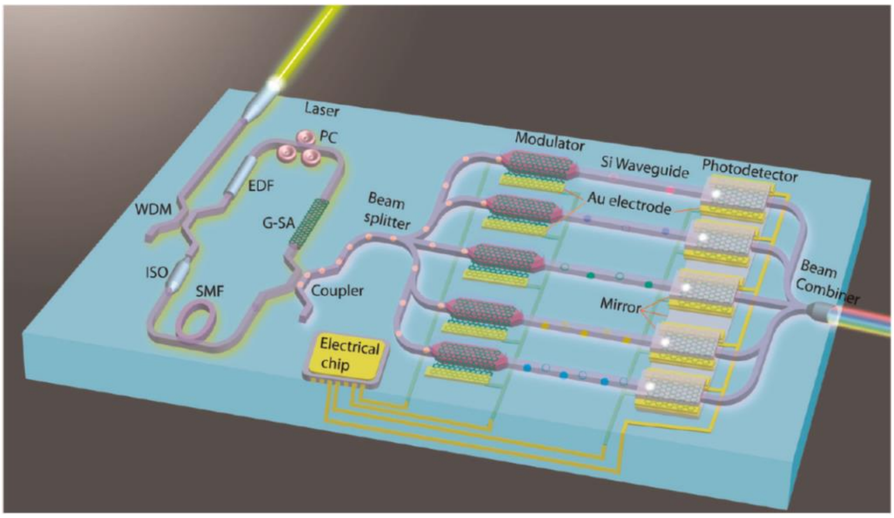

Figure 1.6 Schematic illustration of an integrated graphene silicon hybrid photonic chip consisting of a graphene mode- locked laser with a ring cavity (left), graphene optical modulators (middle), and microcavity enhanced graphene photo detectors (right)[48].

Carbon nanotubes (CNTs), which possess excellent electrical and thermal conductivity, large opto-mechanical strength, have raised a strong interest even earlier than graphene. With different chirality properties, CNTs can behave as metals or semiconductors, thus inducing possible applications from fundamental electronics to photonic devices. As semiconductor carbon nanotubes (sCNTs) are direct gap materials, by integrating them into opto-eletronic devices, a combination of light detection, emission and transistor functions can be implemented into a single chip [49]. The interest of integrating carbon nanotubes into telecommunication photonic chips partly origins from their photoluminescence properties, which cover full the O&C telecommunication band and are potentially useful for laser sources, as shown in Figure.1.7, considering that the quantum yield efficiency of carbon nanotubes has been greatly improved up to 20% for toluene-dispersed, FC12-wrapped nanotubes [61] and dimensionality modified carbon nanotubes [62]. Their integration in Si photonics opens interesting routes for the development of integrated on-chip functions.

At the present time, CNTs LEDs [63], [64],[65] optical gain [66], broadband polarization-sensitive photodetectors [67], and optical biomedical sensors [68] have been already demonstrated. A further demonstration of lasing would be very useful for building next-generation sCNTs based photonic circuits.

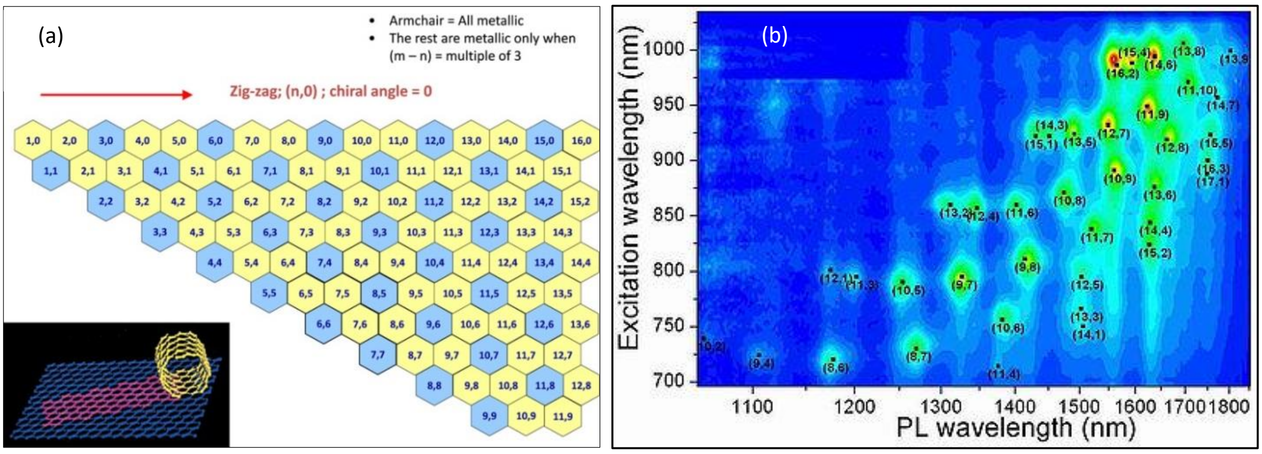

Figure 1.7 (a) CoMoCAT® Single-wall Carbon Nanotubes [69], (b) Photoluminescence of different kinds of carbon nanotubes [70].

1.1.3.4 Integration of polymers

Polymers, as soft materials, have usually small refractive index values (1.4-1.8). They have been developed as organic photonic materials and also integrated within high index photonic platforms as top cladding materials to explore gain and nonlinear responses, excited states to reach light emission, or modulation and detection [71] [72]. As synthesizing soft materials relies on flexible chemistry processes, functional polymers can be artificially designed and fabricated according to targeted requirements. For instance, nonlinear polymers [73] and polymers with gain [74]. In terms of fabrication and integration, polymers can be solution-processed at low cost, easily realizing large scale deposition materials (contact printing, spin coating, for example) on various substrates.

Among the rich literature regarding polymer-based photonics, functional Er-doped polymers such as organo-erbium [74], Er & Yb co-doped PMMA [75] have been proposed to realize hybrid integrated lasers and amplifiers [64,65]. Laser dye doped PMMA in silicon waveguides can emit peak optical powers up to 1.1 watts. High nonlinear $\chi^{(2)}$ polymers can be integrated as hybrid silicon modulators [76]. For instance, polymer wavelength-division-multiplexed photonic optical networks, having 40-channel optical terminals with 100-GHz spacing, integrated with InP- based multi-wavelength lasers and planar photodetectors as transmitter and receivers, have been demonstrated in [77], [78]. Besides, polymer hybrid silicon organic modulator operating at 3dB bandwidth 100 GHz and with data rates up to 140 Gbit/s has been also demonstrated in [76]. Those $\chi^{(3)}$ nonlinear polymers, for instance DDMEBT [79] (Figure1.11), have been successfully applied to all optical signal processing in hybrid silicon waveguides [80].

1.1.4 Conclusion

To conclude this section, two main points have been highlighted in the last discussion: the intrinsic properties of silicon are not enough to provide the flexibility for realization all the needed integrated photonic/optoelectronic functions. Therefore, hybrid integration within silicon platform is welcoming to push the whole photonic platform becoming even lower cost, easier processing, more robust and efficient by exploring the integration methods and novel possible materials.

In this context, a rich and burgeoning set of research works have been recently carried out to push the integration of carbon based and/or soft-matter materials on silicon. We report just hereafter the recent progress of this approach by focusing on key results.

1.2 Recent progress in silicon photonic hybrid structures

Recent progress in hybrid silicon photonics has been obtained by a proper integration of active materials with silicon fast/slow (hollow or plain core) waveguides, micro-resonators and nano cavities. The focus is put just hereafter on the main hybrid strategies and applications recently developed.

1.2.1 Waveguide configurations for material hybridization

1.2.1.1 Standard dielectric waveguides

The main point of hybrid integration of new materials in silicon photonic devices is to find the best method to enhance light matter interactions within photonic waveguides. Silicon on insulator photonic waveguides usually consist in simple strip/rib waveguides with TE-like or TM-like optical modes as shown in Figure.1.8. A general guideline is that active materials (**AM**) (with refractive index n_{AM}) need large mode/AM overlaps ($\boldsymbol{\Gamma_{AM}}$), which is defined in equation 1-5, and should experience as strong electric field ($E(r_\perp)$) density as possible. For instance, a large $\boldsymbol{\Gamma_{AM}}$ can reduce hybrid laser/amplifier threshold [81] and can enhance waveguide nonlinearities [82] [80].

$$\boldsymbol{\Gamma_{cladd}} = \frac{n_{AM}{}^2 \int_{AM} |E(r_\perp)|^2 dxdy}{\int_\infty n^2 |E(r_\perp)|^2 dxdy} \qquad \text{(1-5)}$$

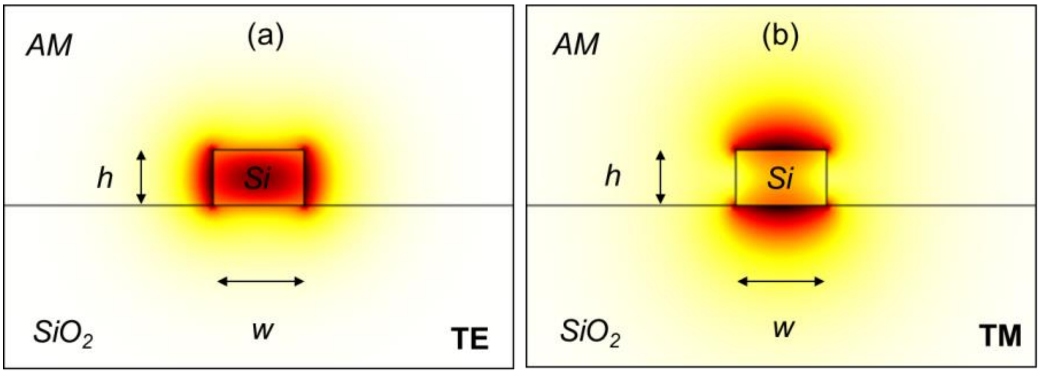

Figure 1.8 Fundamental modes of strip waveguides in (a) TE and (b) TM light polarizations; The waveguide width and height are *w=360nm* and *h=220nm.*

The first strategy in this purpose of light/active-matter overall simply consists in integrating **AM** directly on silicon waveguides **as** a **top cladding layer**, which ensures its interaction with the evanescent tail of the guided propagating mode field (mainly in TM-like polarized modes). Materials with several hundred nanometers thicknesses can be coated as top cladding to obtain a larger interaction. As an example, nonlinear $\chi^{(3)}$ polymers [82], lasing dyes [81], and Erbium doped materials [83] were integrated as thick cladding layers. Besides, nano layer materials are also possible to be integrated with silicon waveguides by interacting with surface stronger evanescent fields. For instance, carbon nanotubes were transferred on top of silicon nitride waveguides after grown and alignment, as shown in Figure.1.9 [84]. Graphene 2D sub-nano-meter sheets were also deposited on top of silicon waveguides, strongly interacting with a TM polarized optical mode, as shown in Figure 1.17 [51].

Similar hybrid waveguide approaches were also widely applied to optical sensing in silicon waveguides/devices, of which surfaces can be coated with thin layers of organic materials such as proteins, spherical molecular chains and antigens to be used for detection of different analysts [85]. Both homogeneous (S_h) and surface sensing (S_s) can be performed by monitoring cladding index(n_c) variations and surface thickness ρ variations through resonances shifts of cavity peaks [86].

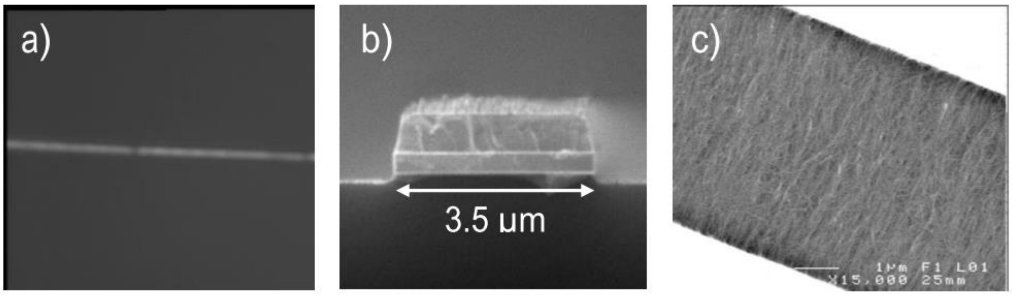

Figure 1.9 (a) Intensity profile of planar SWCNTs incorporated in a waveguide output, (b) SEM picture of ridge SiN waveguide with BCB lower cladding (resin was not removed), (c) SWCNT aligned by dielectrophoresis between gold electrodes. [84]

The second strategy starts from the notice that in standard high index waveguides, the central part of the guided modes cannot interact with the surrounding AMs and the mutual interaction is only limited to the evanescent field regions. **Another strategy** is thus to explore **hollow core waveguide configurations**, in which light is partially guided in low index cladding layers. In this purpose, slot waveguides were proposed in 2004 [87] by using two narrow rails to guide the light, as shown in Figure.1.10. By properly choosing the rail width (W_{rail}) and slot width (W_{slot}), a fundamental TE mode could be formed as in Figure.1.10.a, which shows a strong enhanced electrical field energy in AMs between two rails by about n_{si}^2/n_{AM}^2 times larger than the field intensity in silicon [87]. AMs suitable for slot waveguides have typically low refractive index values (<1.7) and should be well infiltrated in the nano slots (50nm~200nm).

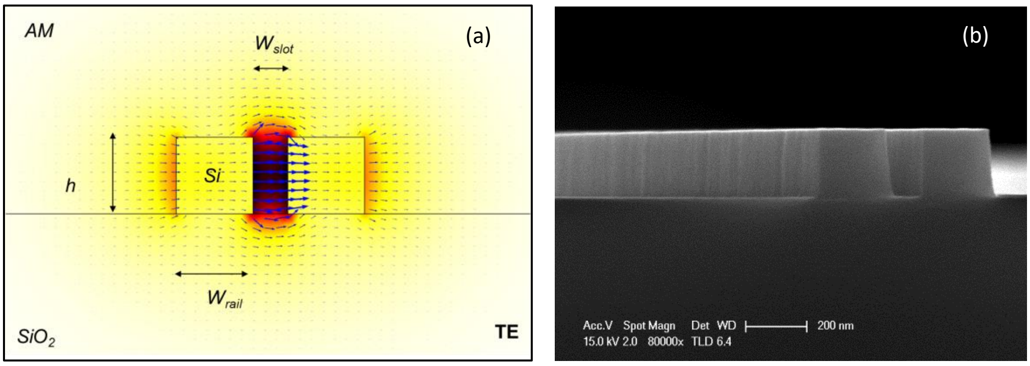

Figure 1.10 (a) Eelectrical field E of the fundamental TE mode of a typical silicon slot waveguide with a waveguide height h=220nm, rail width W_{rail}=220nm and slot width W_{slot}=100nm. The active material was assumed to have the same refractive index as SiO_2. The considered wavelength is 1.55μm. (b) An example of fabricated slot waveguides (in C2N/Orsay, former IEF laboratory, Orsay).

For the widely used SOI waveguides with a silicon height h=220nm, the optical power confinement in single TE mode slot waveguides is around 20% and in the whole low index top cladding around 50%. Such high optical overlap and field energy enhancement (n_{si}^2/n_{AM}^2~5) make slot waveguides very good candidates to study and exploit light matter interactions. For instance, electro-optical slot waveguide modulators embedded with $\chi^{(2)}$ have been proved in [88] by using slot TE modes, as shown in Figure.1.15. Highly nonlinear $\chi^{(3)}$ polymers with material Bulk nonlinear *FOM* up to 5 filled in slot waveguides could result in hybrid slot waveguides with overall waveguide nonlinear $FOM_{wg}=-Re(\gamma)/4\pi Im(\gamma)$ much larger than those of hybrid silicon strip waveguides [82] (γ being the waveguide nonlinearity coefficient).

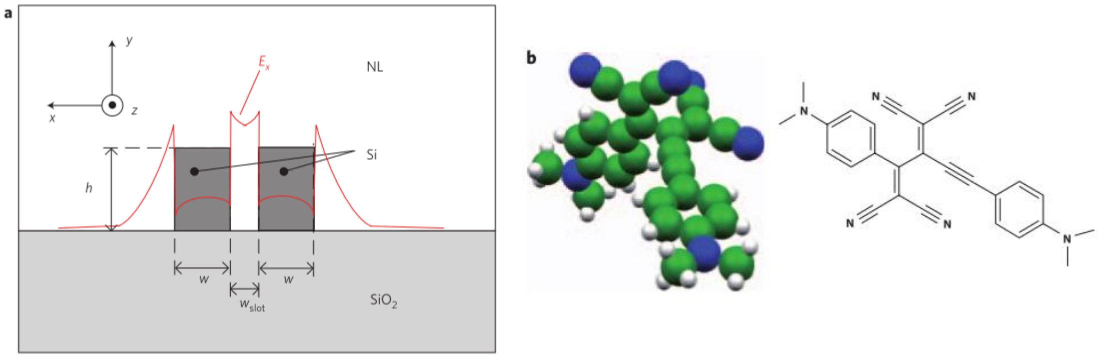

Figure 1.11 (a), Schematic picture of a slot waveguide cross-section comprising two silicon rails on a silicon dioxide buffer layer covered by a nonlinear optical organic material, here DDMEBT [82] [80] [79]shown in (b).

1.2.1.2 Further enhancement of light-matter interaction using slow light waveguides and cavities

Beyond the use of slot waveguides, other physical approaches have also been proposed to enhance hybrid light matter interactions within silicon photonic structures, including slow light photonic crystal waveguides [89] and silicon photonic nano cavities [90].

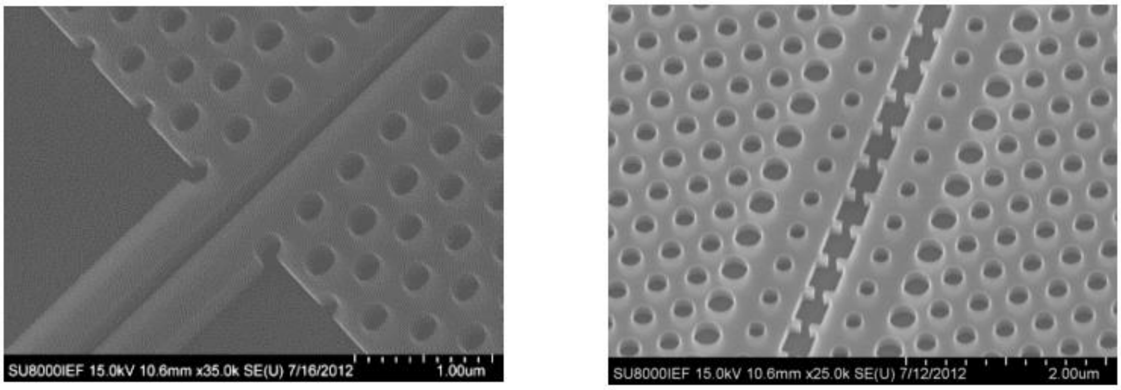

Figure 1.12 Slow light 2D photonics crystal waveguide platform. (left),Slotted photonic crystal waveguides, (right) corrugated and dispersion engineered slot photonic crystal waveguides. [91]

Slow light means light propagating with reduced group velocity v_g with respect to the situation in standard materials. The group velocity v_g is given by the dispersion of the wave propagation constant k **(equation 1-8)**, and usually the group index n_g is used as a slowdown factor referring to light velocity in vacuum (equation 1-9). Slow light effects in photonic crystals (PhCs) have been widely investigated both experimentally and theoretically. For instance, slow waves in photonics could linearly enhance modal gain $g_{mod} = \Gamma_{AM} \frac{n_g}{n_{AM}} g_{AM}$ [92], where g_{AM} is the gain coefficient of the bulk AMs and n_{AM} is the refractive index of the AM.

$$v_g = \frac{d\omega}{dk} \qquad \textbf{(1-8)}$$

$$n_g = \frac{c}{v_g} \qquad \textbf{(1-9)}$$

Silicon slow light photonic crystal waveguides with group index values typically ranging from 10 to 40 are reasonable, i.e. they can strongly enrich interactions in very short structures while maintaining optical losses at a reasonable level [93]. To achieve desired slow down factors, photonic crystal waveguides can be dispersion engineered to tune the bandwidth, group index, group velocity dispersion and higher order dispersion terms for controlling light-matter interactions [91], [94]. By chirping the holes size/position, lattice constant, slot size, dispersion engineered slow light slotted photonic crystal waveguides with constant group index band and anomalous dispersion can be achieved (see Figure.1.14) [95]. Ultra-high Q nano cavities with mode volume ~$(\lambda/n)^3$ have been also achieved in slow light 2D photonic waveguide structures [96]. **Photonic crystal cavities** with enhancement given by the Purcell factor, were also demonstrated in low index void configurations [97]–[101] The cavity mode confined in the low index region then enables much smaller mode volumes ($<(\lambda_{vac}/n)^3$) than in standard dielectric cavities. For instance, in [98] as shown in Figure.1.13, an optical mode volume down to 0.0096 $(\lambda_{vac}/n)^3$ and a Q factor up to 150,000 were reported.

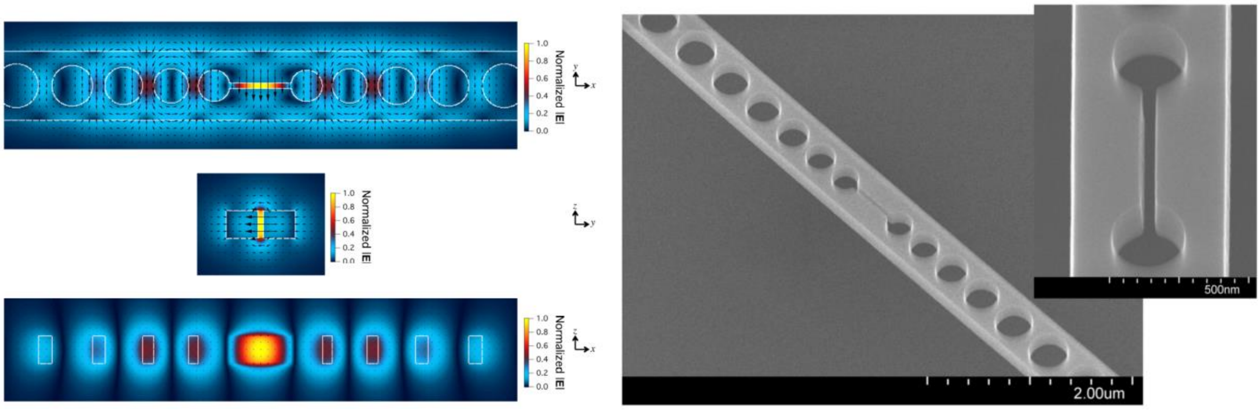

Figure 1.13 (Left) Simulated TE mode field distribution of the slotted nanobeam cavities, (Right) fabricated membrane slotted nanobeam cavities.

Sandwiched silicon devices as shown in figure 1.14 have also been demonstrated as robust hybrid approaches, in which the functional materials are deposited between two semiconductor layers as an active core layer, requiring at least that the core layers are robust enough and compatible with CMOS fabrication conditions such as temperature, stress, uniformity of the surface, and etching processes. Typically, simple rib waveguides, one dimensional nanobeam cavities, 2D photonic crystals have been proposed, fabricated and investigated, as shown in Figure.1.14. Lasing was also reported within sandwiched silicon nitride QDs hybrid disks [102].

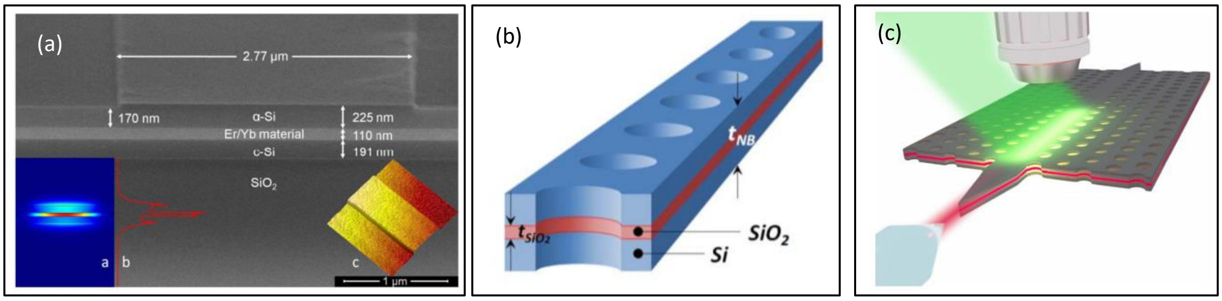

Figure 1.14 (a) SEM image of an as-fabricated slot wave- guide. a The calculated fundamental TM-like mode profile, b. the plot of normalized electric field along vertical direction at waveguide center and c. AFM image of the fabricated slot waveguide. [103]. (b) Scheme of 1D PhC nanocavity on a horizontally SiO_2-slotted Si NB [104] (c) Schematics of an active membrane exposed to a focused pump beam (green) and the fibre collecting light from the taper. [92]

1.2.2 Hybrid silicon photonic applications

Due to the broad and rich set of reported works, an exhaustive overview of hybrid silicon photonic applications is difficult. We will mainly focus hereafter on three topics related to applications in optoelectronic devices, optical amplification/lasing, and on-chip index sensing.

1.2.2.1 Hybrid silicon optoelectronic devices

The typical and widely demonstrated hybrid silicon optoelectronic devices are electro-optical modulators relying on the integration of materials such as nonlinear $\chi^{(2)}$ polymers , graphene [51] or carbon nanotubes in silicon waveguides [67] [47], [48].

Hybrid silicon organic hybrid (SOH) modulators operating at 100GHz with 3dB bandwidth have been demonstrated in [76]. The EO polymer cladding was coated on top of the silicon slot waveguides and two shallow etched silicon rails were connected with electrodes with reduced resistance by an additional direct voltage, as shown in Figure.1.17.c. This kind of devices was expected to work with on-off-keying data rates up to 140Gbit/s and with voltage-length product as low as $V_{\pi}L$=11Vmm.

To reach more compact, lower voltage-length product efficient hybrid modulators, slotted slow light photonic crystal waveguide active devices have been demonstrated. The hybrid integration scheme of such silicon organic modulator based slow light waveguides is shown in Figure 1.16 [105]. This ref reported a voltage–length product modulating device with a $V_\pi L$ factor of only 0.29 V.mm..

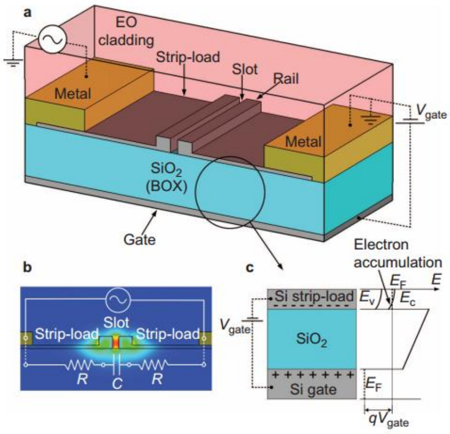

Figure 1.15 **Schematic of a Silicon-organic hybrid modulator**. (a) The silicon slot waveguide is connected to the metal electrodes by thin silicon strip-loads. The EO polymer cladding covers the waveguide and fills the slot. The shallowly doped silicon substrate is used as a gate. (b) The cross-section of the waveguide and the electric field distribution of the optical quasi-TE mode, where the light is concentrated in the slot. (c) When a positive gate voltage is applied across the 2-mm thick SiO_2substrate, a highly conductive electron accumulation layer is formed in the strip-loads.

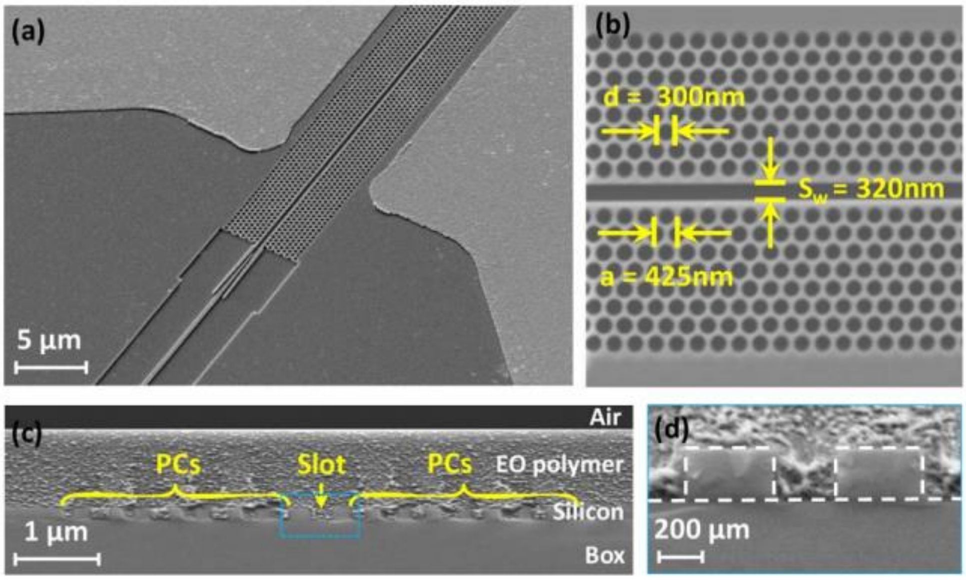

Figure 1.16 Scanning electron microscopy (SEM) images of a fabricated device. (a) Tiled view of a local area of the silicon slot PCW modulator. (b) Top view of the slot PCW area. (c) Cross sectional view of the EO polymer refilled silicon slot PCW. PCs, photonic crystals. (d) Zoom-in image of the dashed square area in (c) [105].

Graphene hybrid silicon modulators based on electrically tuned Fermi level of the graphene sheet enabled modulation of the guided light in silicon with frequency over 1GHz [51]. Figure.1.17 shows a schematic view of the graphene layer deposition on top of a silicon waveguide and the presence of Au electrodes. By using ring resonators and detuning the critical coupling extinction ratio, hybrid graphene modulators could operate with modulation efficiency of 15dB per 10V and at 30 GHz bandwidth [106].

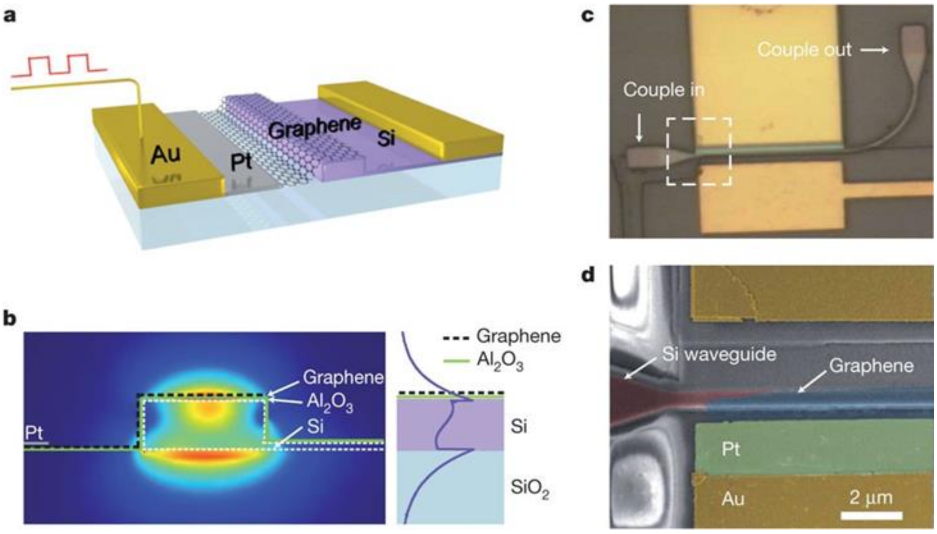

Figure 1.17 (a) Three-dimensional schematic illustration of a device based on a graphene sheet placed on top of a silicon bus waveguide, separated from it by a 7-nm-thick Al_2O_3 layer (not shown). (b) Left, cross-section of the device, with an overlay of the optical mode plot, calculated by finite element simulation. (c,d) Top view of the whole device [51].

To quote few results from the rich literature, graphene and carbon nanotube based photodetectors have also been broadly demonstrated. Typically, graphene photodetectors, as shown in Figure.1.20, could operate from O band to U band at a multigigahertz frequency, with extremely high carrier mobility 200,000cm^{2}V^{-1}s^{-1} at room temperature and low power consumption 0.5 fJ/bit [47].

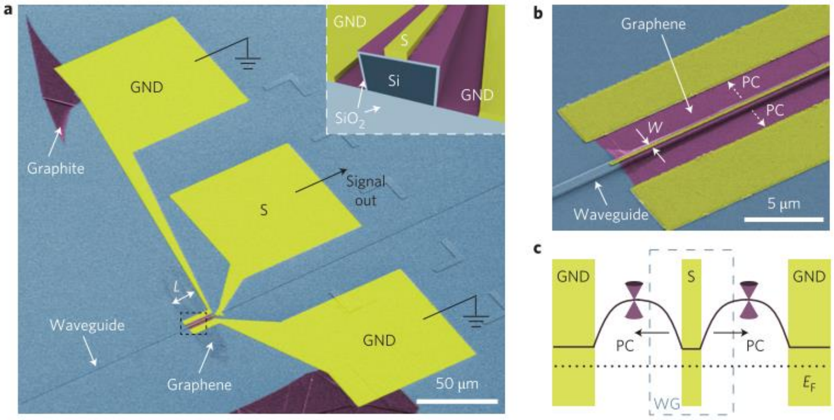

Figure 1.18 Waveguide-integrated graphene photodetector. a, Colored scanning electron micrograph of a waveguide-integrated graphene photodetector. The ‘active region’ of the graphene sheet is shown in purple. The inset shows a cross-section of the device. The graphene sheet coats both the top surface and sidewalls of the waveguide. b, Enlarged view of the section highlighted by the black dashed rectangle in a. The PC flows from the central electrode S towards the GND electrodes. c, Schematic illustration of the band diagram. The dotted line represents the Fermi level, EF. PC is generated in the vicinity of S.WG, waveguide [47].

1.2.2.2 Hybrid silicon optical amplifiers and lasers

As previously mentioned, silicon is an indirect bandgap material and hardly suitable for on-chip lasing. Table.1.3 reports some of the possible approaches that have been investigated in recent years.

Table 1.3 Silicon light sources: strengths and challenges of the reported solutions; data partly based on [107].

Candidates	Er-related light source	Ge-on-Si laser	III-V based laser	Carbon nanotubes
Mechanism	Er^{3+} as emitting source	Via bandgap engineering	III-V direct bandgap material as gain medium	Semiconductor nanotubes
Materials	SiOx:Er, SiNx:Er, Er silicates, Al2O3 : Er	Ge, GeSn alloy	InAlGaAs QW ; InGaAsP QW ; InAs/GaAs QD	Semiconductor nanotubes with Emission at 1.2-1.6µm
Advantage	CMOS compatible, wavelength stability	CMOS compatible, large gain spectrum	High gain and output power, commercial product existed	Both for electronics and photonics
Challenge	Low electroluminescence, lager net gain per length	Ge materials, ultrahigh threshold current	Reduction of the cost and integration complexity	Nanotube alignment, high concentration integration, obtain gain and lasing.

The first promising approach to reach hybrid silicon lasers is to integrate Erbium-doped active materials (AM) on silicon [108]. Erbium, which was demonstrated as an efficient amplifier/laser source in fiber optics, has attracted huge efforts for the realization of on-chip light/amplifiers sources for telecommunications. However, only few devices have been demonstrated with net gain within this approach. Indeed, low loss waveguides and high quality Erbium doped host materials are required for an efficient integration in Silicon. For instance, erbium doped Al_2O_3 waveguides [109]–[111], Erbium-doped phosphate glass waveguide [112], erbium silicate [113], organo-erbium [74] have been demonstrated with net gain values of around ~1dB/cm to 100dB/cm. However, none of them directly demonstrated such results on silicon photonic waveguides with a net gain of at least on the level ~1dB/mm. The most promising Si-hybrid approach demonstrated in recent years was a silicon (core)/Erbium silicate (shell) nanowire, as shown in Figure.1.20. The crystalline Er silicate corresponds to the cladding of the silicon waveguides and provides gain when light propagates along the nanowire, which typically sustains optical modes that are partially confined in Er silicates, as illustrated in Figure.1.19. This submicrometer optical core (Si) shell (erbium-ytterbium silicate) nanowire, which behaved as an amplifier (see figure.1.19 and 1.20), was demonstrated with a relative gain up to 120dB/mm, but if suffering total loss 210dB/mm, which is possible reduced when nanowire is suspended. However, nanowires are not directly suitable for integrated silicon photonics. Further demonstrations in lithographically fabricated silicon waveguides with a coated erbium silicate cladding would be required in order to confirm that transforming core-shell nanowires to a cladded-Si-waveguides could conserve such high gain stability properties within the silicon platform.

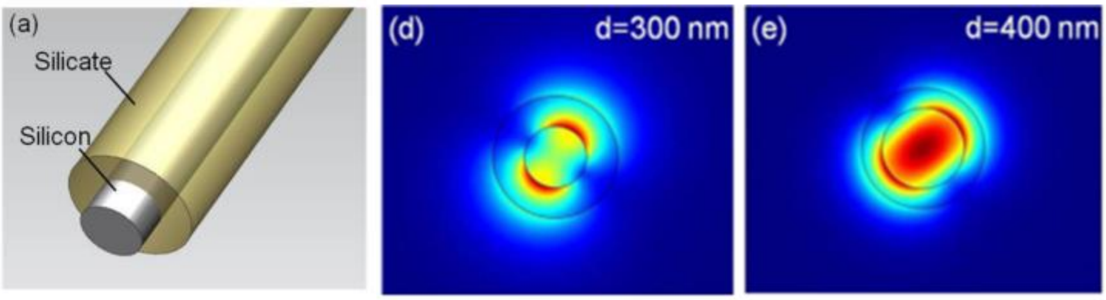

Figure 1.19 (a) Schematic of the core-shell nano- structure. (d) (e), optical electrical-field distribution images for HE11 mode with core diameters of 300 nm, 400 nm [114].

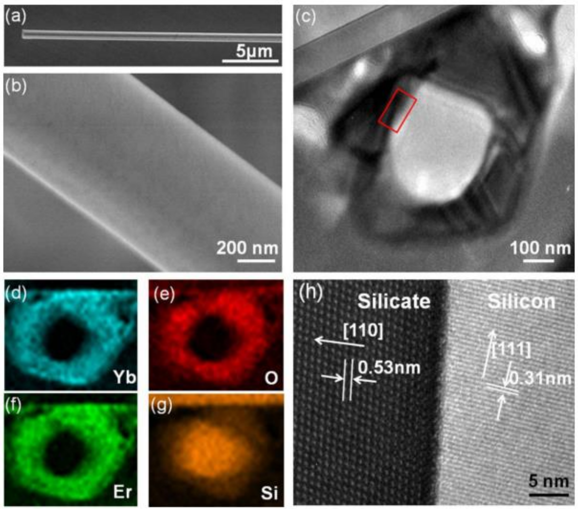

Figure 1.20 Microstructure characterization of the Si-EYS core-shell nanowires. (a) Typical SEM images of part of a single nanowire, and (b) its locally amplified image. (c) Cross- sectional TEM image of the wire, and its corresponding two- dimensional element mapping (d)–(g). (h) Typical HRTEM image collected at the core-shell interface of the wire [red rectangle area in (c)] [114].

Another step showing possible progress towards lasing in hybrid silicon waveguides was provided by the following example. In this hybrid work, a commercial dye-doped organic cladding material, about 500nm thick, was coated on top of 4.8mm-long silicon strip and slot waveguides [115]. As shown in Figure.1.21, Bragg reflectors assisted silicon waveguides coated with an organic cladding were considered.

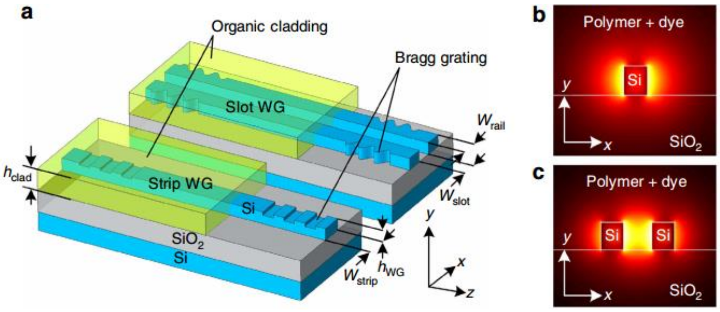

Figure 1.21 Silicon organic hybrid laser concept. (a) Light is guided by SOI strip or slot waveguides consisting of thin silicon nanowires (width w_{strip}≈150–500nm, height h_{WG}≈200–350nm). Optical gain is provided by a fluorescent organic cladding material (thickness h_{clad}≈500±50nm). (b) Dominant electric field component (Ex) of the fundamental quasi-TE mode for a narrow strip. (c) Dominant electric field component (Ex) of the fundamental quasi-TE mode for a slot waveguide [81].

To reach lasing with nanomaterials, hybrid silicon laser sources with carbon nanotubes have also been proposed. So far, optical gain properties of carbon nanotubes have been demonstrated with CNTs operating at room temperature [66] in pulsed pump regimes within a strip waveguide coated with a-CNT-doped organic layer [116]. In order to reach lasing, CNT interaction in ring resonators[117] and nanocavities [65], [118] have been investigated for possible silicon integrated light sources, as shown in Figure.1.23 and Figure.1.24, respectively. Fully integrated carbon-nanotube silicon ring resonators are capable of reaching light emission, as shown in Figure.1.24, but still not in the lasing mode. The optical net gain inside the ring resonator was indeed still not sufficient to compensate for optical losses in this work. Several recent works have yet shown that integrating carbon nanotubes into silicon photonic nanocavities could potentially enable on-chip lasing [118] [65] by benefiting from high *Q* and small mode volume effects. At the present time, hybrid carbon nanotube lasing in silicon cavity/resonator is still required to be demonstrated.

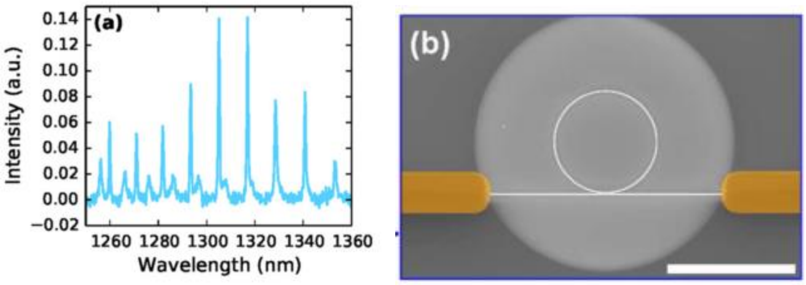

Figure 1.22 Integrated carbon nanotube (8,7) silicon ring resonator. (a) Photoluminescence coupled to silicon bus waveguides from the ring resonators, was collected from the end of the silicon bus facet by single mode fiber. (b) silicon ring mode ring resonator with diameter of 10μm and coupled with bus waveguides; HSQ was used to protect the access waveguides (yellow part); single wall nanotube bundles in PFO were spin coated on top of ring resonators in order to have a homogeneous layer as top cladding. The ring resonator was pumped with continuous a laser perpendicularly to the device plane on top [117].

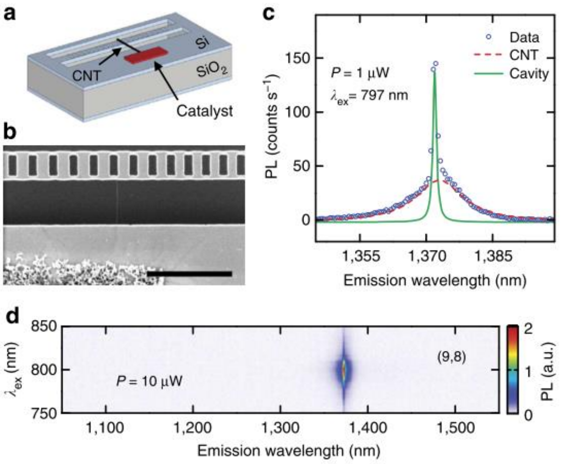

Figure 1.23| An individual carbon nanotube coupled to a nanobeam cavity. (a) A schematic of a device. (b) Scanning electron microscope image of a device with a suspended nanotube. Scale bar is 2 mm. (c) Typical PL spectrum of an air-mode device coupled to a nanotube. The dots are data and the lines are Lorentzian fits. (d) PL excitation map of the device shown in c taken with P¼10mWand the laser polarization perpendicular to the nanobeam [118].

1.2.2.3 Hybrid bio-photonic sensing

Hybrid silicon photonic waveguides and resonators described in previous sections also represent an opportunity for other kinds of applications than optical interconnects, among those on-chip sensing is the main one. Bio-detection implemented with microfluidic channels assembled by Lab-On-Chip technologies is required for future healthcare diagnostics[119], [120]. In this perspective, silicon photonics enabling large-scale fabrication of compact planar sensors by integrated CMOS processes is seen as a viable route for massive on chip bio-detection.

Hybrid bio-photonic sensing relies on the functionalizing of the surface of hollow core waveguide resonators/nanocavities with antibodies or other probes, and on the detection of special antibodies binding with antigens by monitoring the resonance shift induced by the bio-chemical reaction, as shown in Figure.1.25 and Figure.1.26. Besides, homogeneous sensing (S_h) is also used to detect gases [121].

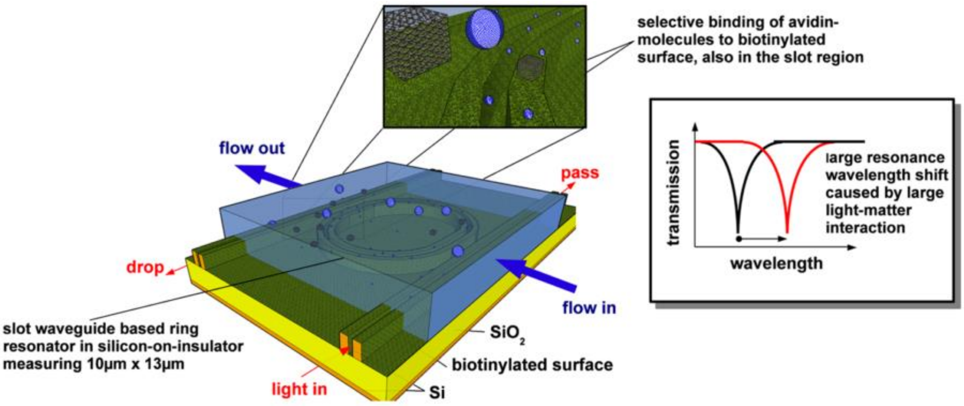

Figure 1.24 Slot waveguides ring resonators with surface treatment of a biotinylated layer in order to bind with avidin-molecules. As slot waveguides have very strong light-matter interaction ability due to enhanced electric field in slot, they have been demonstrated with large waveguide sensitivities according to cladding index changes [122].

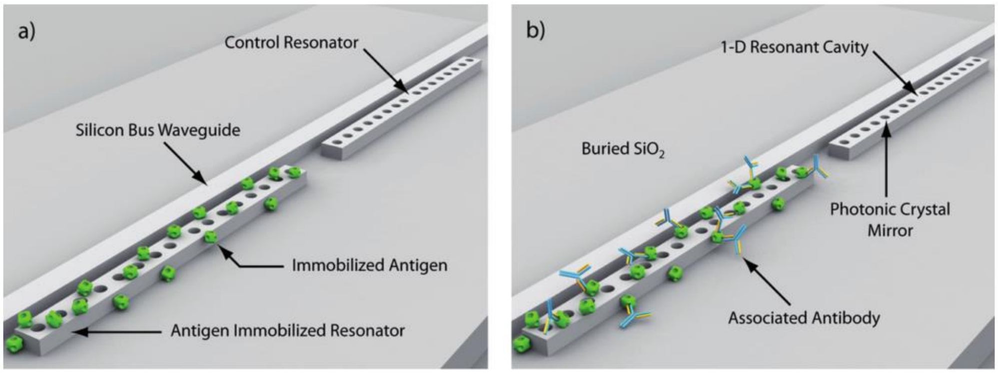

Figure 1.25 (a) 3D rendering of the nanoscale optofluidic sensor array device showing two 1-D photonic crystal resonators evanescently coupled to a silicon bus waveguide. The first resonator is immobilized with an antigen whereas the second resonator acts as a control. (b) 3D rendering illustrating the association of the corresponding antibody to the antigen immobilized resonator (not drawn to scale) [123].

Ring resonators and nanocavities have been thoroughly investigated to minimize the so-called sensing limit of detection, i.e. the minimum detectable information. Generally, the monitoring accuracy is qualified in terms of sensitivity and limit of the detections (*LOD*) of the detection system. In this context, recently developed silicon on insulator (SOI) optical devices have displayed detection ability with *LOD* down to 10^{-8}RIU and sensitivities exceeding 103µm/RIU by using Vernier effects [124]–[127]. Versatile structures, like single ring resonators (RR) [122], [128], [129], Vernier ring resonators [127], photonic crystals (PhC) [99], [130], [131], Mach-Zehnder interferometers (MZI) [126], [132] and Bragg gratings [133] have been demonstrated as highly efficient sensors by the detection of refraction index (RI) changes from the surrounding fluidic channels [120].

1.3 Conclusion

Hybrid silicon photonics has been discussed in this chapter, from the material level to the material-waveguide integration and device function ones. Though on-chip lasing through III-V on Si hetero-integration approach has been demonstrated for years as the most successful solution to overcome silicon incapability of light emission, new solutions for silicon light sources still deserve special investigation within silicon hybrid photonic waveguides for further progress, better integration capability, and cost reduction. New demonstrations of silicon hybrid integration with erbium doped oxides, graphene, carbon nanotubes, highly nonlinear polymers, lasing dyes, quantum dots are thus welcome for the realization of on-chip lasers sources and amplifiers. At the present stage of progress, no hybrid integration approach has definitely emerged, so that further investigations are necessary.

1.4 Motivations and contexts of the thesis

In this context, the motivations of this thesis are: (1) Exploring how properly integrating Er-doped materials, semiconductor single wall carbon nanotubes into silicon photonic waveguides; (2) Demonstrating possible hybrid waveguide approaches that could constitute milestones towards integrated optical amplifiers and lasers; (3) Investing the performances of silicon hollow core waveguides for optical index sensing.

The remaining of the manuscript is organized as follows.

Chapter 2 focuses on the design, fabrication and characterization of silicon photonic passive devices including slot waveguides, micro resonators and nanobeam cavities. Optimization of slot waveguides for low losses and high *Q* factors will be discussed. New types of air mode cavities with high *Q* and low mode volumes will be introduced in order to maximize light-matter interaction and improve the stability of the hybrid modes and resonances.

Chapter 3 is dedicated to the integration of Erbium doped PMMA and Er_2O_3-Al_2O_3 layers into hollow core Si waveguides for light amplification at λ=1.55µm. Both numerical and experimental studies will be reported.

In chapter 4, we study the integration of carbon nanotubes with Si waveguide ring resonators and nanobeam cavities in the purpose of optical gain and lasing (yet not fully achieved).

Then, chapter 5 summarizes the main results of this thesis regarding the state of the art. Some limitations of the carried out experiments will be mentioned in comparison with new strategies for next steps improvements. The perspectives for silicon amplifiers and hybrid Er-doped polymers and CNTs lasers will then be discussed.

2. Design and fabrication of passive silicon photonic structures

2.1 Silicon photonic rib and strip waveguides

The basic components of photonic integrated circuits (PIC) are photonic waveguides that are used to draw communications between different blocks by light propagation. When the technologies used to develop PICs are constrained under CMOS fabrication processes, waveguides are formed by lithography & etching that usually keep rectangular shape cross-sections, as shown in Figure 2.1. The etched sidewalls contribute as the main source of waveguide scattering losses [40][38]. These losses can be reduced by engineering the waveguides cross-section profiles either by considering large width strip waveguides[40] or Rib waveguides [42] (as shown in Figure 2.1.b) to make the electric field intensity interaction with sidewalls decrease. Another option is to increase/decrease (with respect to the mode polarization) the waveguide aspect ratio to push the mode in the low index BOX or cladding layers [38]. Benefiting from advanced 300-mm wafer scale processing techniques [42] for silicon photonic device fabrication, record low loss waveguides (Table.2.1) have been demonstrated in standard waveguides, slot waveguides [134], and grating couplers.

Table 2.1 Present optical loss levels of strip and rib SOI waveguides

Waveguides Type	Rib (dB/cm)	Strip(dB/cm)
300mm CMOS-platform	0.12±0.01[42]	0.45±0.12dB/cm [134]
Multimode waveguides		0.026 [40]

For silicon platform with 220nm thick silicon film and a 2µm BOX, fully etched silicon strip waveguides in TM polarization are usually preferred to study the hybridization with cladding active materials (AM), as shown in Figure.2.2. Figure.2.3 quantitatively shows that TM modes in strip waveguides have indeed typically ~35% of light power confined in the top cladding material while for TE modes this confinement is only about 15% for single mode situations.

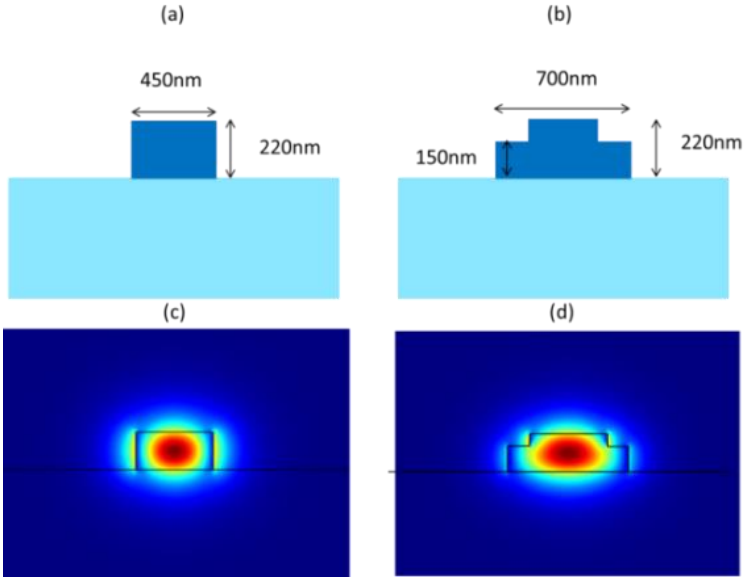

Figure 2.1 Schematic pictures of: (a) Rib waveguides, (b) Strip waveguides. Waveguide modes are shown at λ=1.55µm for a TE-like polarization in (c) and (d).

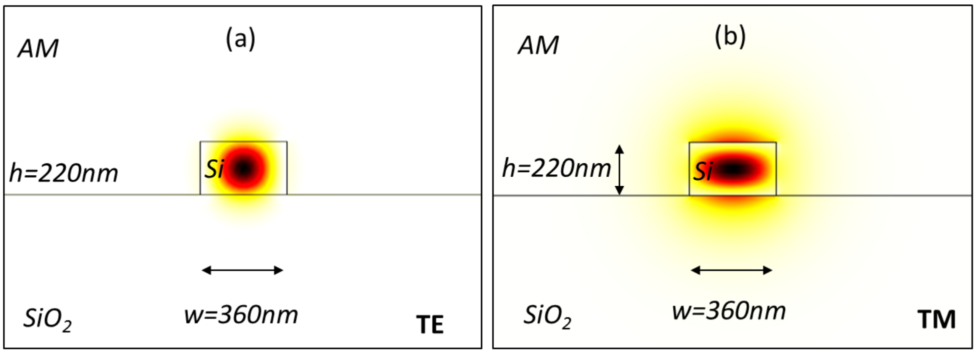

Figure 2.2 Cross-sectional view of power confinement of typical SOI strip waveguides at λ=1.55µm: (a) TE polarization; (b) TM polarization.

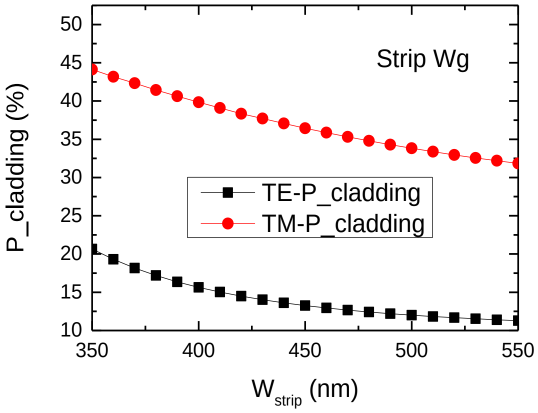

Figure 2.3 Total Power confinement in top cladding for strip SOI waveguides (h_{Si}=220nm) in TE and TM polarizations as a function of the waveguide width (λ=1.55µm).

2.2 Slot waveguides

In view of the limited amount of optical power interacting with surrounding materials in Si strip waveguides, hollow waveguides entitled slot waveguides have been proposed for years [135]. We report in this part our contribution to the design, fabrication, and characterization of such silicon and silicon nitride slot waveguides for the hybrid integration of soft materials and liquids on silicon.

2.2.1 Silicon slot waveguides

2.2.1.1 Silicon slot waveguides modes and energy confinement

As stated in chapter 1, slot waveguides with TE modes (Figure2.4.a) not only partially confine light in the void low refractive index (**RI**) regions but are also responsible for a field reinforcement in the slot by a ratio of n_{Si}^2/n_{cladd}^2. An interesting metrics of these waveguides in Si photonics is the optical power confinement in the tiny slot, which is about 22% for different slot widths for TE modes (Figure2.5), while for TM modes (Figure2.4.b) light confinement maximum value is about 10%. However, the whole power confinement in the top low **RI** cladding material for both polarizations is above 40% with a 5-8% higher level for TE than for TM modes (Figure2.5). To conclude, both of the two polarized modes have a large power overlap with the top cladding material in slotted waveguides. TE modes are yet much better suited than TM ones for light-matter interaction considering much strong electric field enhancement in the slot region and a bit higher power confinement in the total cladding region.

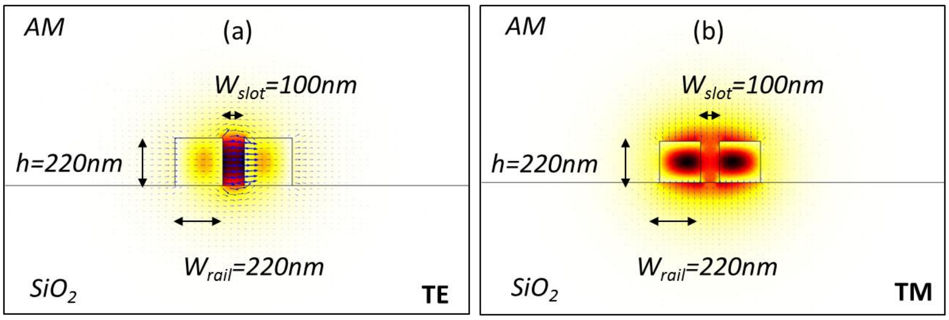

Figure 2.4 Cross-sectional view of total power confinement of typical SOI slot waveguides for TM and TE light polarizations. (a) TE and (b) TM at λ=1.55μm.

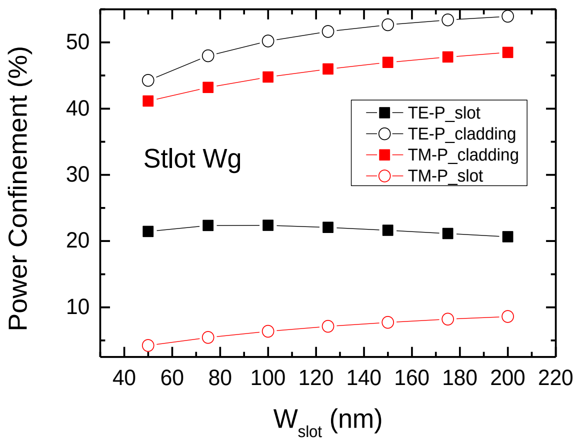

Figure 2.5 Total power confinement in slot region only and whole cladding (including slot) of slot SOI waveguides as a function of the slot width and for TM and TE polarization of light (λ=1.55µm).

Optimization of light confinement in the top cladding region for TE modes can be investigated by considering wide ranges of slot and rail widths, as shown in inset of Figure.2.6.b, which gives an example [136] considering a highly nonlinear $\chi^{(3)}$ top cladding polymer with refractive index 1.8. It can be seen, as a general trend, that when the rail width becomes smaller and the slot width increases, light confinement in the slot region increases. Typically, maximum confinement power levels around 75% are possible for silicon slot waveguides. For real device design, the whole set of parameters, including the slot and rail widths should be globally considered. For instance, optimization of non-linear *FOM* should be considered [136] for nonlinear hybridization, waveguide sensitivity needs to be maximized for optical sensing [137], and propagation losses should be reduced for optical amplification or lasing. With the development of the etching processes, silicon slot waveguide losses have been now reduced down to 2dB/cm in present state of the art works [134].

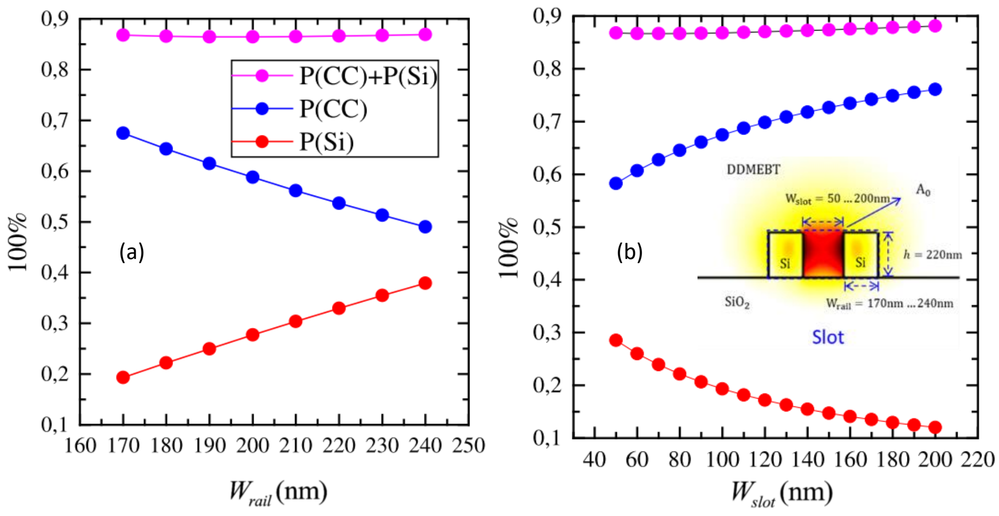

Figure 2.6 Optical power confinement in silicon rails (Si), top cladding (CC) and above BOX (CC+Si); (a) when considering slot width =100nm; (b) when considering rail widths of 170nm width (λ=1.55µm). The top cladding is envisioned as nonlinear polymer DDMEBT with refractive index 1.8.

2.2.1.2 Silicon slot waveguides fabrication

2.2.1.2.1 Fabrication challenges

Fabrication challenges of slot waveguides mainly include two parts: mode converters and low loss long slot waveguides. Mode converters are usually used to properly connect strip and slot waveguides with the purpose of reducing back reflections while reaching high transmission efficiencies. Long (>>100µm) slot waveguides fabrication under e-beam lithography face e-beam current instabilities during long and large scale path writings, which also inevitably induce stitching errors, slot width variations along the whole waveguide and thus larger propagation losses.

2.2.1.2.1.1 Slot mode convertors

A slot waveguide mode converter, which transforms a strip mode to a slot mode, can be realized through symmetric multimode interferences [138], Y-branch couplers [139], “tip insertion” [140] and logarithmic side tapers [141]. All these kinds of couplers can reach coupling efficiencies more than 90% and logarithmic side tapers could reach the best efficiency of 99.5% with logarithmically tapered width [141]. However, all the mode converters face the problems of the conversion efficiency when slot size goes down to 100nm considering the larger scattering losses in tiny slots and minimum lithography exposure/etching feature sizes. Besides, the designed mode converters are not universal for all different slot and rail width configurations.

The minimum slot feature size in our clean room fabrication is around 40nm. The slot feature size in our *.gds-II* file is 20nm in order to well isolate silicon to form a minimum slot ~40nm, as shown in Figure.2.7 and Figure.2.8. Figure.2.7 shows an example of “tip insertion” mode convertor fabrication, where slot size at beginning was set with 20nm and ends with 10nm in the *.gds-II* file (shown in Figure.2.7.a). Figure.2.7.c shows that the slot nearly vanishes when the *.gds-II* slot dimension is reduced to 10nm and indeed, Figure.2.7.b proves that the slot was not successfully formed for the 10nm *.gds-II* value.

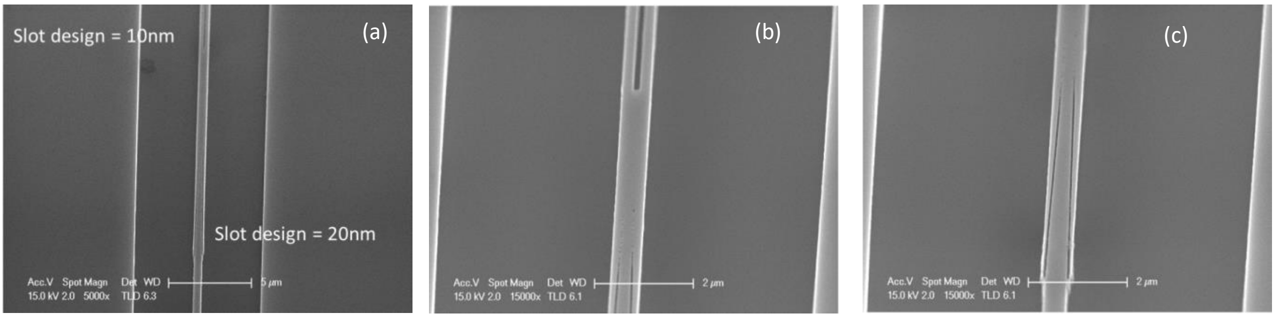

Figure 2.7 “Tip insertion” slot mode converters. (a) Insertion slot size from bottom to top was modulated from 20nm to 10nm in *.gds*-II files; (b) The top tip slots was not isolated due to a too small exposure; (c) The bottom slot was, on the contrary, well isolated.

A good control of the this “tip insertion” mode convertor is obtained by reducing the *.gds-II* slot dimension from 20nm to 15nm, which finally contributes to a proper isolation of the silicon rails, as illustrated in Figure.2.8. The present whole mode convertor length is 20µm and the two side slot widths are around 50±10nm from beginning to end, as measured in Figure.2.8.

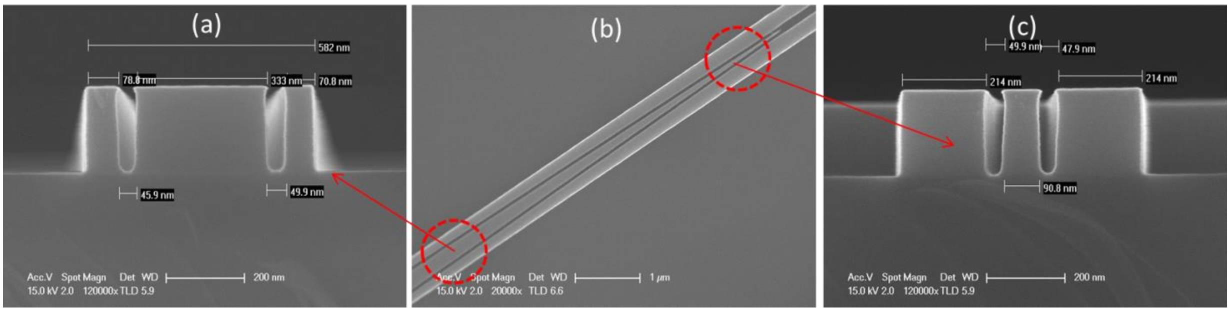

Figure 2.8 Tip insertion slot mode converters. (a) Cross-section of the beginning part of the taper; (b) SEM global view of the well fabricated taper; (c) Cross-section of the end of the taper.

A second type of “side” mode convertor [142] was also fabricated by following ref [142], which rigorously explains that logarithmically tapering the waveguides width would optimize the transmission efficiency as displayed in Figure.2.9. The strip waveguide initially that sustains a single mode (Figure.2.9.a) begins to evanescently excite the slot waveguide field due to its narrowing width and ultimately a true slot mode as plotted in Figure.2.9.c. Let notice that this design is made of only one slot width, which is of a larger width than the ones used in the “tip insertion” mode convertor configuration, which eases the slot fabrication. In this second convertor type, a side rail follows the strip waveguide with a constant slot width until the strip width (linearly or logarithmically) reducing down to the same width as the side rail. Figure.2.10.b shows one fabricated “side” mode convertor with a slot width of 95nm and a rail width of 220nm by linearly tapering the strip waveguide width down to 220nm. Logarithmically tapering methods were not adopted by us considering that a linear tapering was enough with respect to fabrication uncertainties in the design of a logarithmic profile. Experimentally, we characterized the losses per “side” mode converter to around 0.07dB for different slot widths, as summarized in Table.2.2, which is a bit larger than the state of the art of 0.02dB for the logarithmically tapered ones but yet fairly acceptable. “Tip insertion” slot mode converters proved to have transmission losses around 0.25dB, ie 3 times larger than “side” converters. Sometimes, fabrication instabilities could also enlarge conversion losses several times higher, for instance, 1.2dB for “tip insertion” converter with slot width 110nm and 0.21dB for “side” converter with 130nm slot width.

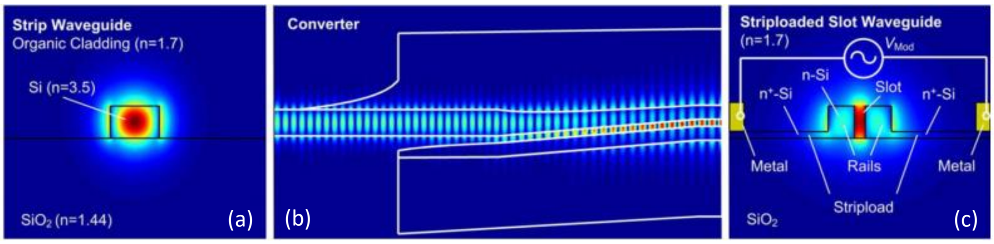

Figure 2.9 Mode transitions along the "side" mode converter from (a) strip waveguide mode to (c) slot waveguide mode. The whole transitions process are depicted in (c) [142].

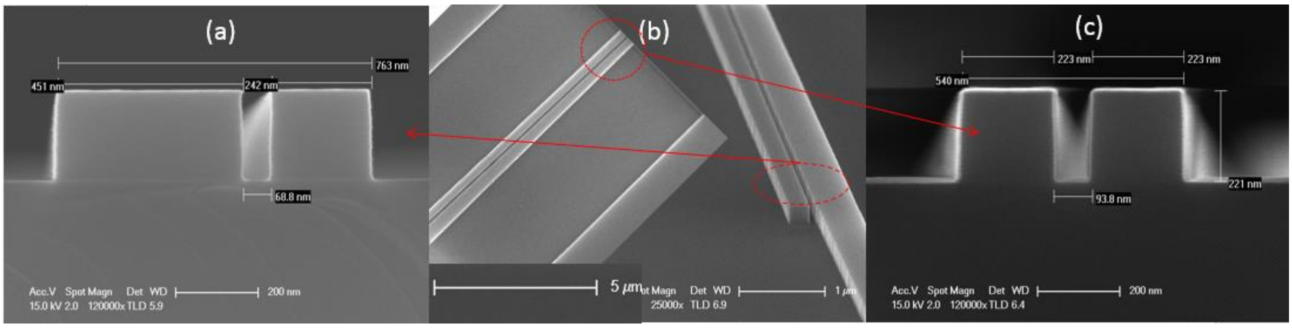

Figure 2.10 "Side"-type slot mode converters. (a) Cross-section of the beginning part of the taper; (b) SEM overview of the well fabricated taper; (c) Cross-section of the end of the taper.

Table 2.2 Summarized losses per mode converters with different slot widths at the wavelength of 1.55μm.

Slot width	90nm	110nm	130nm	150nm
"Tip"	0.26dB	1.2dB	0.67dB	0.25dB
"Side"	0.088dB	0.074dB	0.21dB	0.059dB

To conclude this part, the design method of "side" mode convectors is simple and their fabrication was verified as very robust compared with "tip insertion" convertors. The reasons for this stem in several points: i) Lateral tapers do not require tiny slots as "tip convertors" do , thus inducing less fabrication errors; ii) They suffer lower light back reflection levels. This is the reason why lateral strip to slot convertors have been preferred and considered for most of the realizations presented in this manuscript.

2.2.1.2.1.2 Stitching errors in slot waveguides

Stitching errors, the deviation from perfect alignment between consecutive writing subfields or main fields, have been found more frequently in fabricated slot waveguides than in strip ones, especially inside bended slot waveguides between two consecutive writing subfields, as shown in Figure.2.11.a. The realization of slot ring resonators with a diameter of 100μm, for example, requires an e-beam exposure in 58 subfields (10μm×10μm) during the e-beam lithography writing process. This long curved slot waveguide path needs to be cut into different small polygons in each subfield. In some subfields, the polygons are so small that stitching errors occur when the *gds-II* files are interpreted into our e-beam writer (*NanoBeam nB 4* from *NanoBeam Limited in UK*) readable file format (*.npf*). The nanobeam machine/system can somehow be limited when interpreting *.gds* files into *.npf* ones. The captured scattering losses from near infrared camera (Figure.2.11.b) shows that there are more scattering losses in the borders of the subfield, which has been proved to be related to stitching errors, as shown in Figure.2.12 and Figure2.13, respectively.

A possible solution to reduce stitching errors consists in to regenerating *.npf* files two times with a shift of half subfield, which has been verified several times. Regeneration of *.npf* files indeed forces interpreting .gds files with more details in .npf outputs. Figure.2.13 shows one case of application of this processing technique to remove stitching errors in a slot waveguide design configuration. This solution, which was empirically found as stable and reproducible, was systematically adopted for the fabrication of complex structures in one main writing field.

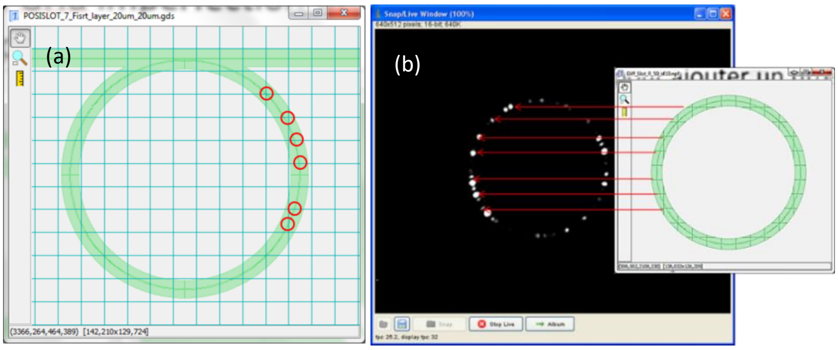

Figure 2.11 (a) Subfields of the slot ring resonator *gds*, where the red circles or equivalent places are the risky regions giving rise to stitching errors; (b) captured scattering losses of slot waveguides from near infrared camera (from the top, at λ=1.55μm, when injecting light in-plane from an input SOI strip).

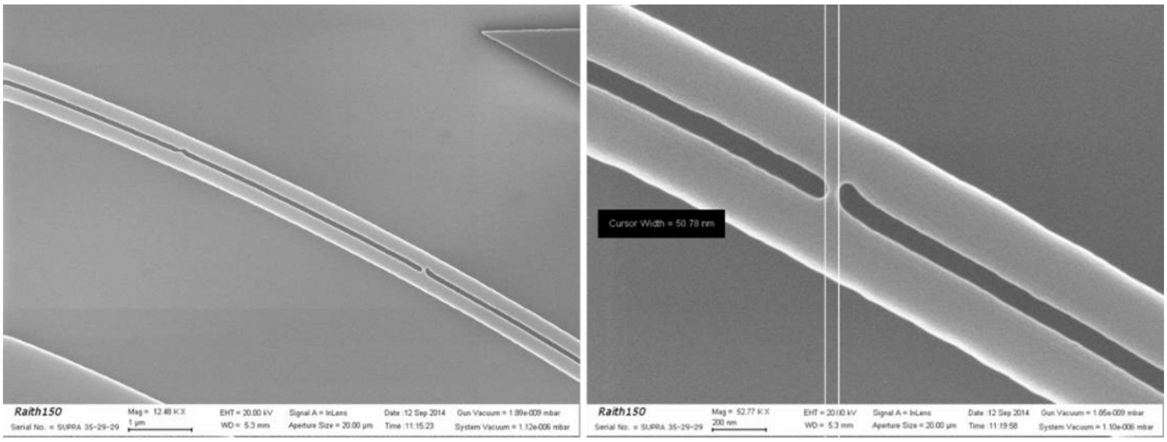

Figure 2.12 Stitching errors in bended slot waveguides.

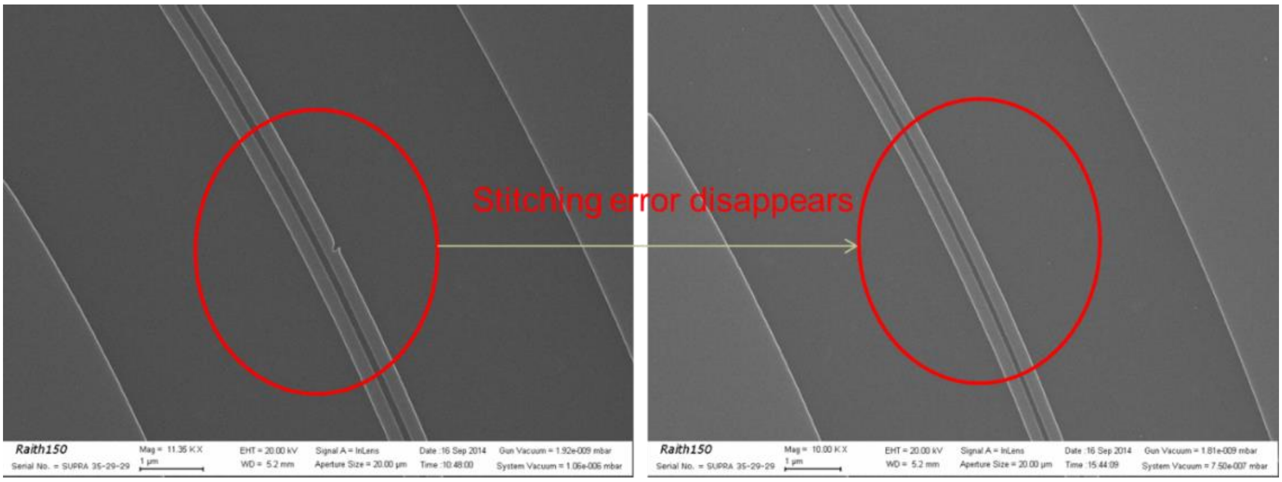

Figure 2.13 Improved fabrication process of slot waveguides (on the right), which successfully removed stitching errors visible on the left.

2.2.1.3 Losses of silicon slot waveguides

To measure optical losses of slot waveguides, different lengths of slot waveguides were fabricated with slot sizes, 80±10nm, 130±10nm, and 180±10nm, respectively. Both the rail width and height were of 220nm. Cargille liquids with refraction index around 1.46 (Cargille commercial liquid) were drop-casted on top of the slot waveguides as top cladding materials, thus mimicking the integration of hybrid soft materials. Slot waveguide lengths ranging from 200μm to 18mm were fabricated and optically characterized in the near infra-red around λ=1.55μm. Measured transmission spectra of 80nm wide slot waveguides are depicted in Figure.2.14. It shows a loss level around 7±2dB/cm by linear fitting the slope (Figure.2.14.b).

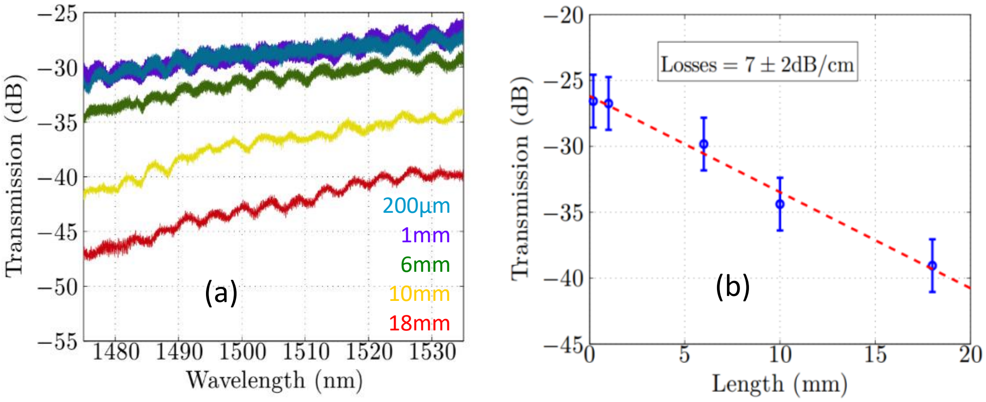

Figure 2.14 Propagation losses of filled silicon-slot waveguides: (a) Transmission of the 80±10 nm slot waveguide for different lengths. (b) Linear regression of optical transmission at the signal wavelength (1530 nm) versus slot waveguide lengths for an 80±10 nm slot width silicon waveguide.

Losses of different slot width waveguides are summarized in Table.2.2. Generally speaking, larger slot width waveguides have larger losses than narrow slot ones. Slot waveguides with a moderate slot width of 80-130nm have optical losses smaller than 10dB/cm; while losses nearly double when slot size goes up to 180nm. Slot waveguide losses are quite (dispersive) wavelength dependent, and exhibit large losses for short wavelengths (1.48µm) than larger ones (1.53µm), which increases the difficulties to optimize slot ring resonator *Q*-factors for an extended wavelength range.

Table 2.3 Summary of waveguide loss for two wavelengths in different slot widths.

Slot width (nm)	Loss @ λ=1.53µm (dB/cm)	Loss @ λ=1.48µm(dB/cm)
80±10	7±2	9±2
130±10	8±2	10±2
180±10	15±1	19±1

2.2.2 Silicon nitride slot waveguides

2.2.2.1 Silicon nitride platform

With recently fabrication technology development of low pressure chemical vapor deposition techniques (LPCVD), thin stoichiometric Si_3N_4 film with roughness down to 0.5nm on 200mm substrates can be fabricated in CMOS compatible cleanrooms. The Si_3N_4 film encapsulated with oxide has to be annealed at 1150-1050 °C about 3-7 hours to remove the hydrogen in order to suppress the N−H bond and O−H bond absorption peaks. With mature and reliable fabrication processes of Si_3N_4/SiN_x (depending on the material stoichiometry), ultra-low loss photonic platform has been reported with large scale, dense integrated devices in multilevel photonic chips [143].

Typically, compared with traditional SOI photonic waveguides, optical loss levels down to 1dB/m have been demonstrated in industrial platform like the Hydex one [144], enabling not only excellent passive photonics structures, such as ultra-high *Q* ring resonators, tunable delay lines, grating couplers and AWG, but also nonlinear optical processing, for instance frequency comb generation based on ultra-high *Q* ring resonators [45] and supercontinuum generation in long spiral waveguides [46]. Besides, benefiting from a wider transmission window from 0.13µm to 3.5 µm and low index contrast, silicon nitride is also a good candidate for developing bio-photonic chips, especially considering that water absorption limited *Q*-factor of the resonator is around 10^8 @ 0.6 µm whereas it is only 10^4 @1.55µm [145].

2.2.2.2 Fabrication of the Si_3N_4 waveguides

In the fabrication of silicon nitride waveguides, we firstly studied the etching rate competition between the ZEP520 resist and silicon nitride itself. As shown in Figure 2.15, a thin layer of ZEP520 was spin coated on top of the silicon nitride wafer and then followed by e-beam lithography exposure and development of the resist itself to form the slot waveguide pattern mask. Finally, the samples were etched under ICP (SPTS) equipment.

Figure 2.16 shows that about 500 nm thick ZEP520 resist was coated on top of the silicon nitride layer. The developed mask pattern of ZEP520 resist is displayed in Figure 2.17, which shows nearly 90 degrees etching of the slot walls and rail sidewalls. The critical controlled parameters of the resist are height and development temperature [62]. With enough thick ZEP520, the mask could successfully protect silicon nitride and still did not vanish. A good temperature control of the ZEP520 development could enhance the MASK contrast and roughness, which were supposed to result in reduced roughness, quite perpendicular sidewalls and rectangular corners for waveguides [62].

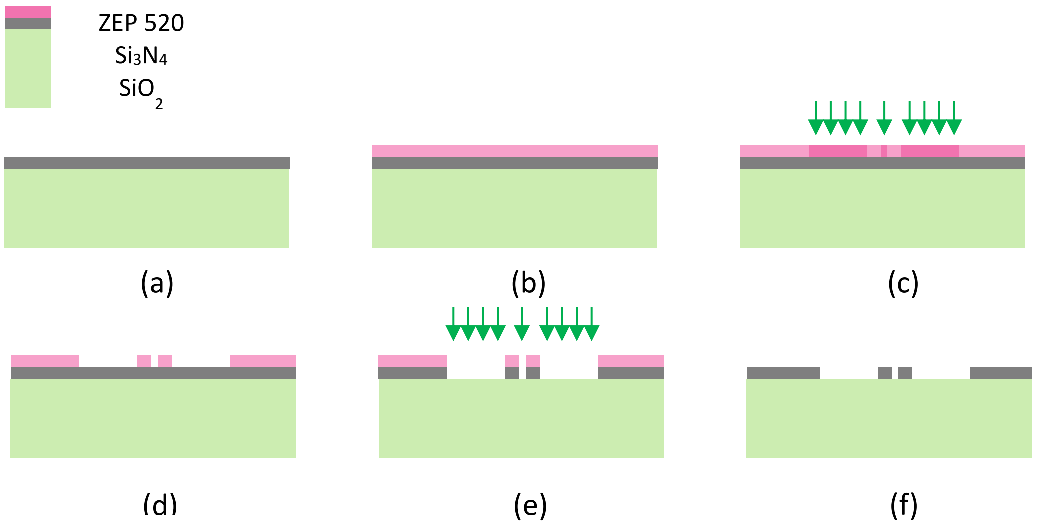

Figure 2.15 Overview of fabrication processes of Si3N4 slot waveguides. (a) Wafer after O2 plasma cleaning; (b) ZEP520 spin coating on top of Si3N4; (c) e-beam lithography of our slot waveguide GDS-II mask; (d) ZEP520 resist mask after development and removal of the exposed parts; (e) ICP etching of the Si3N4; (f) Slot Si3N4 waveguides finally obtained after resist cleaning.

To etch 400nm thick silicon nitride waveguides, we found that at least 400nm thick ZEP520 was needed. Different ICP etching times, 135s & 155s were tested to ensure full etching. Figure.2.18 shows the final etched cross-section profiles of the silicon nitride waveguides with a 20 seconds difference, which finally evidences that extra 60nm ZEP520 and 30nm SiO_2 are etched in Figure.2.18b. The profile of the ZEP520 MASK is heavily destroyed and around 400nm layer were etched away. A good compromise of the etching time to 140s was finally adopted to ensure a satisfying etching quality. Figure.2.19 shows the final obtained slot waveguide with different slot sizes, ~120nm, 170nm and 220nm. Sidewalls are finally obtained with about 10 degree slope, which originates from the different ICP etching rates when ZEP520 MASK thickness is reduced along the whole etching process. A further step to improve the sidewall perpendicularity would be to use thinner and harder

ZEP520 layers, which could ensure nearly same ICP etching rates to open 90° slope 400nm height Si_3N_4 slots.

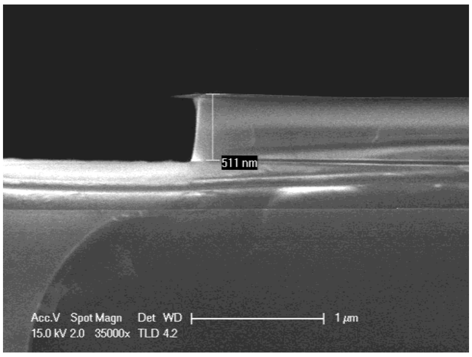

Figure 2.16 500nm thick ZEP520 has been spin coated on silicon nitride wafer

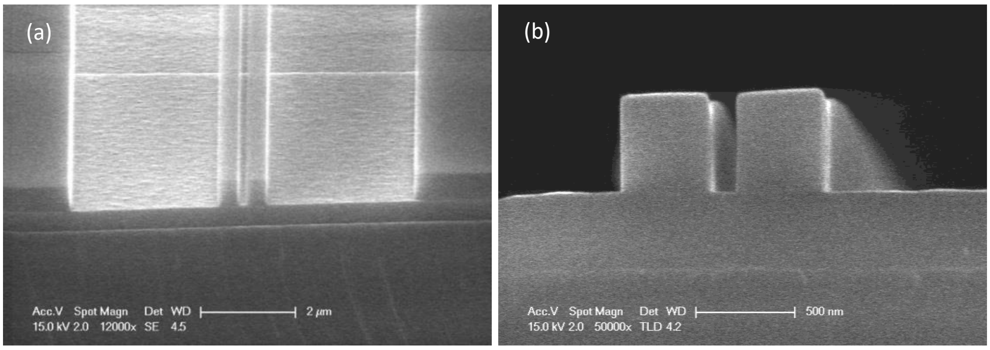

Figure 2.17 ZEP520 slot waveguide MASK (a) Top view and (b) Cross section view.

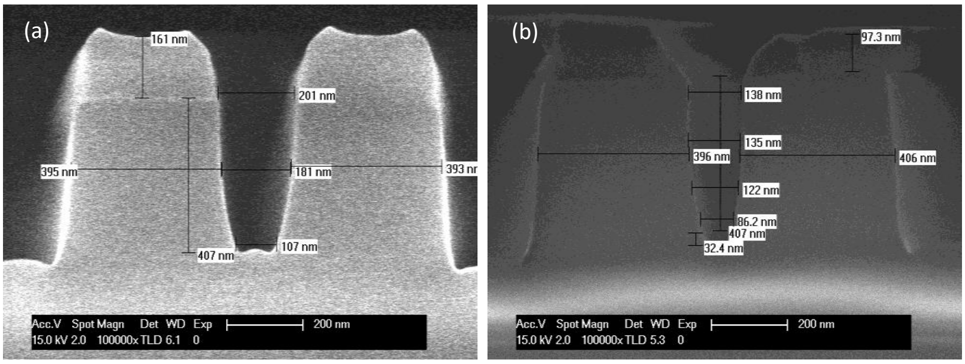

Figure 2.18 Results after different ICP etching times, (a) 135s and (b) 155s; Original cross sections with resist are shown in Figure.2.17.

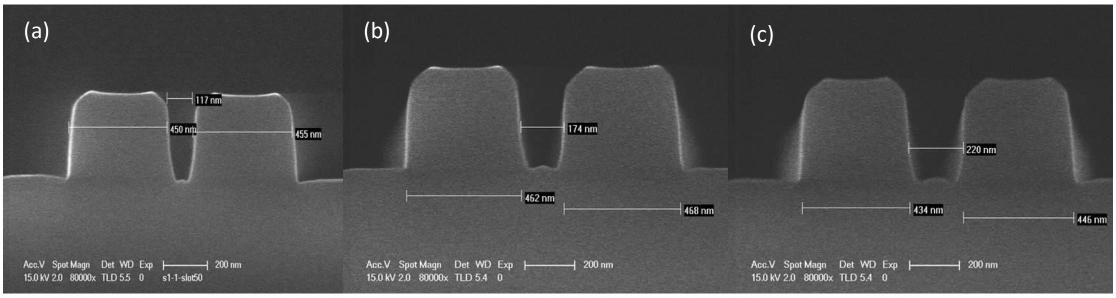

Figure 2.19 Three different slot waveguides with slot sizes (a) 120nm, (b) 170nm, and (c) 220nm.

2.2.2.3 Losses of Si_3N_4 slot waveguides

In the first step, simple slot waveguides with different lengths were fabricated to measure the waveguide linear losses. The length of spirals (Figure.2.20.a) was swept from 250µm to 2cm and the corresponding linear transmission spectra at C&L bands are shown in Figure.2.21. A rough estimated total propagation loss (TE modes) of the fabricated slot spiral waveguides is around 4dB/cm for both cases with slot size of 170nm and 220nm, respectively, as shown in Figure.2.21, i.e. around half the level obtained for silicon slot waveguides. A top captured light scattering view of a 2cm long spiral waveguide is also shown in Figure.2.20.b.

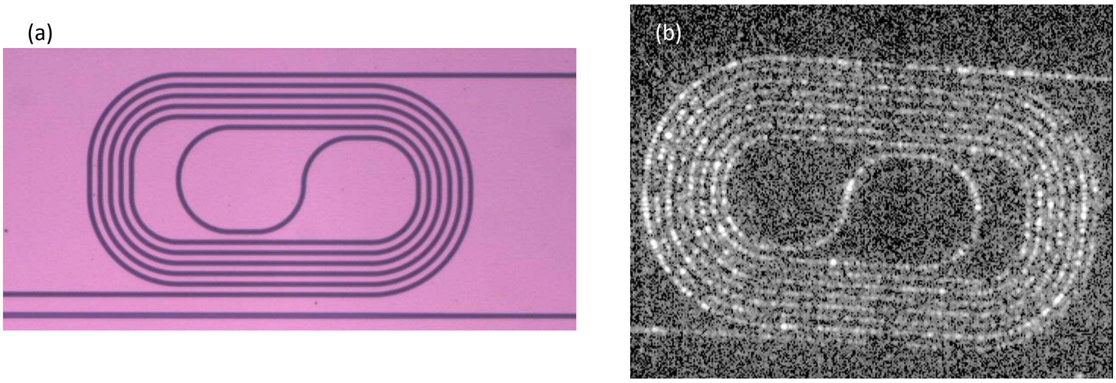

Figure 2.20 (a). Optical view of the fabricated slot spiral waveguides (b). Scattering light of propagation in spiral slot waveguide capture from the near infrared camera.

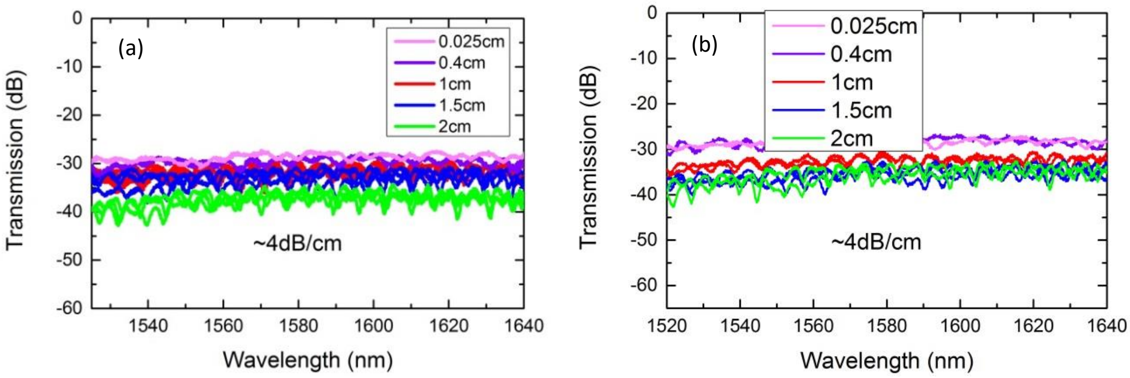

Figure 2.21 Linear Transmission spectrum of the fabricated silicon nitride slot waveguides with slot size (a) 170nm and (b) 220nm.

2.2.3 Conclusion about slot waveguides

Reasonably low loss (few dB/cm) slot waveguides have been achieved both in silicon and silicon nitride waveguides with TE polarized optical modes. Silicon slot waveguides with tighter mode confinement suffered fabrication stitching errors and exhibited around 2-4 times larger propagation losses than silicon nitride slot waveguides. A further step of propagation loss reduction in silicon slot waveguides was realized in one lithography main field, which could avoid stitching errors at the borders of the main fields.

2.3 Micro ring resonators

Silicon micro ring resonators enable light looping in an enclosed optical path with miniaturized sizes down to 1 micro radius due to high index contrast, supporting several resonances separated by the free spectrum range (FSR). As light loops many times in the resonator, light matter interactions are significantly enhanced when the number of looping round trips is large (this point is related to the micro-ring *Q*-factor parameter).

Typically, silicon micro resonators can be classified into different types, mainly including disks and ring resonators, slot ring resonators and photonic crystal ring resonators [146]. A silicon micro-disk can reach much higher *Q*-factors (several millions [147] [148]) than the other types (~ hundred thousands [149]) benefiting from less roughness induced losses. Slot ring resonators can be infiltrated with polymers in a hybrid integration approach and have been demonstrated with low loss (~2dB/cm) and high *Q* factors (several tens of thousands [150]). Photonic crystal ring resonators introduce slow light effects into the ring resonators [146], [151] with group index values more than 20 to enhance the light matter interactions, such as for lasing purpose [152].

Light coupling between bus waveguide and ring resonator part can be described by Figure.2.22 and equations 2-1 &2-2. Incident light from the bus waveguide has electric field amplitude a_1 and output amplitude b_1. On the left of the coupling region, the ring resonator keeps amplitude a_2 and on the right side of the coupling region, the electric field is b_2. The energy exchange in the coupling region can be described by the matrix equation 2-1, in which t represents the bus light self-coupling coefficient and k represents light crosstalk coefficient. Ideally, the coupler is lossless and the relation $k^2+t^2=1$ then holds, meaning power conservation. α' is the one round trip electric field attenuation coefficient per unit length and L is the ring resonator circumference. The derivate transmission spectrum is casted as equation 2-2, where $a'=exp(-\alpha' L)$ and n_{eff} is the effective refractive index of the propagation mode.

For one resonance mode, there are three types of coupling regimes: critical coupling ($t=a'$), over-coupling ($t<a'$) and under-coupling coupling ($t>a'$). For critical coupling condition, the transmission T drops down to zero due to coupled light power equaling the internal resonator losses [153].

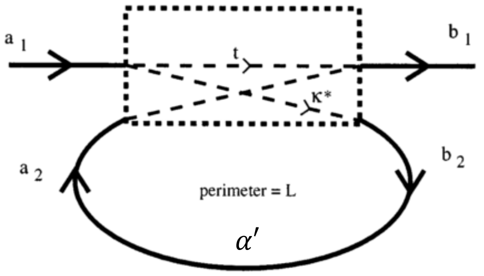

Figure 2.22 Schematic view of the ring resonator. α' represents one round trip electric field attenuation per unit length; t represents the bus light self-coupling coefficient and k represent the cross talking coefficient. [154]

$$\begin{vmatrix} b1 \\ b2 \end{vmatrix} = \begin{vmatrix} t & k \\ k^* & -t^* \end{vmatrix} \begin{vmatrix} a1 \\ a2 \end{vmatrix} \qquad (2\text{-}1)$$

$$T(\lambda) = \left|\frac{b1}{a1}\right|^2 = \frac{a'^2 + t^2 - 2a't\cos\left(\frac{2\pi L n_{eff}}{\lambda}\right)}{1 + a'^2 t^2 - 2a't\cos\left(\frac{2\pi L n_{eff}}{\lambda}\right)} \qquad (2\text{-}2)$$

In the following sections, the fabrication of silicon micro-disks and strip/slot ring resonators is shown and measured Q-factors for different radii are compared. A special focus is put on slot waveguide ring resonators, which are less broadly reported in the literature than their strip waveguide counterparts, in the purpose of minimizing their losses and increasing their Q factors.

2.3.1 Micro Disks

Silicon strip micro-disks with radii of 2.5μm, 4.5μm, 9.5 and 14.5μm, respectively, were fabricated, as illustrated in Figure.2.23. Bus waveguides with a width of 290nm were chosen for single mode operation at λ=1.3μm. TM polarized modes have much higher cladding confinement factors than TE modes, which is supposed to strongly enhance light matter interactions in hybrid integration schemes. TM polarization modes in disks were thus characterized and results are shown in Figure.2.24 & Table.2.4.

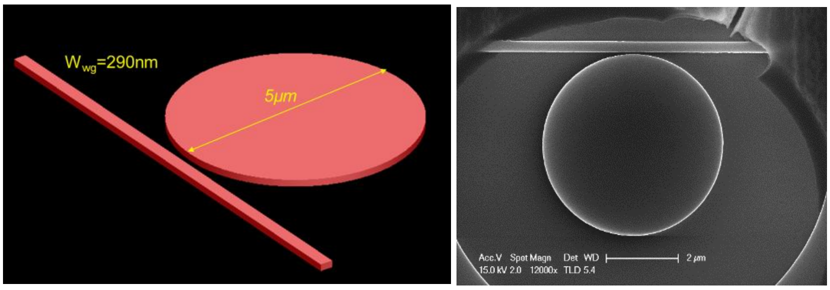

Figure 2.23 Schematic & SEM view of integrated silicon micro disk with 5μm diameter.

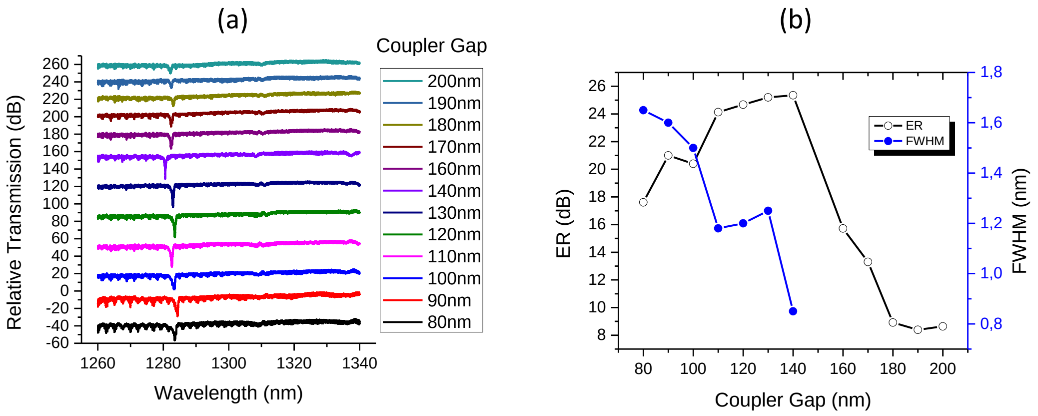

Figure 2.24 Linear TM light transmission spectrum of 5μm diameter disk with different coupler gaps; (b) Full width of half maximum (FWHM) and extinction ratio (ER) of the resonance peak monitored at λ=1.28μm.

The smallest disks with diameter of 5μm were found to have only one resonance mode at λ=1.283μm (Figure.2.24) by wavelength sweeping in the 1.26-1.34μm range. This result was due to the fact that other intrinsic resonance modes were far from critical coupling. As shown in Figure.2.24.b, ER increases up to 25dB when coupler gap approaches 140nm, and then decreases to 8dB when the coupler gap is far above 200nm. This global trend is due to the self-coupling coefficient t increase when the coupler gap is enlarged. Therefore, ER goes through over-coupling regime, then critical coupling regime to final weak coupling regime. As compared in Figure.2.24.b, the full width half maximum decreases to minimum when ER reaches its maximum.

Table 2.4 Maximum Q-factor of the TM modes of the silicon micro disk with different radius.

Disk Radius	2.5μm (TM)	4.5μm(TM)	9.5μm(TM)	14.5μm(TM)
Q-factor	1,800	22,000	44,000	58,000

The measured Q-factors of different radius micro-disks are summarized in Table.2.3. A silicon disk with diameter of 9μm shows a 10 times larger Q-factor than a disk with a diameter of 5μm. Almost twice-value Q-factors are measured for 19μm diameter micro-disk when compared disk with diameter 9μm. The maximum Q-factors around 58,000 are measured in the disks with diameter of 29μm. Compared with the other published high Q silicon micro disks with TE modes [147] [148], here our results are one order lower, for instance, Q-factor of 88,000 were measured for 2.5μm radius disk in [155], but yet acceptable in the purpose of top cladding material integration.

2.3.2 Strip Ring resonators

Strip ring resonators were also fabricated, as shown in Figure.2.25 and measured by coupling light with the help of sub-wavelength grating couplers. Strip ring resonators with a radius of 70μm and waveguide width 650nm, have a maximum *Q*-factor (TE mode) of 81,000 and ER of 15dB (Figure.2.26), which is comparable to previous results obtained for etch-less ultralow loss ring resonators [149], indicating that the ring resonator waveguide losses are around 1.2 dB/cm in the studied case. The smallest ring resonators with radius of 5μm were measured with *Q* factor around 4,000 and 5,000 for TM and TE polarizations, respectively.

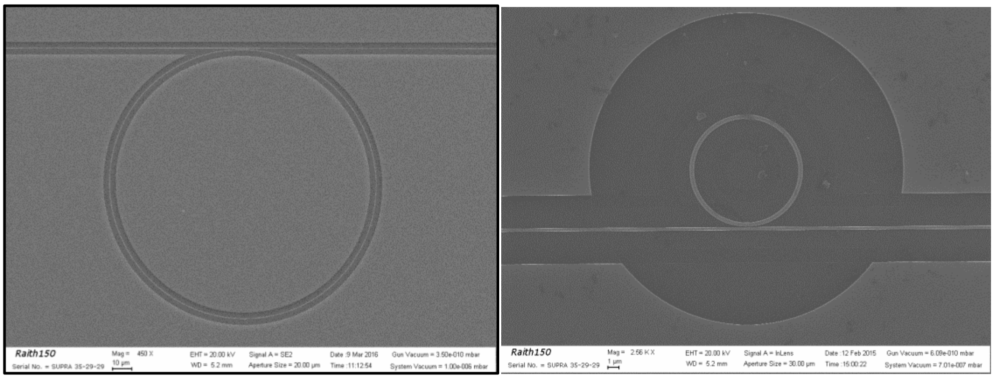

Figure 2.25 SEM image of a fabricated silicon strip ring resonator with radius of 70μm (left) and 5μm (right).

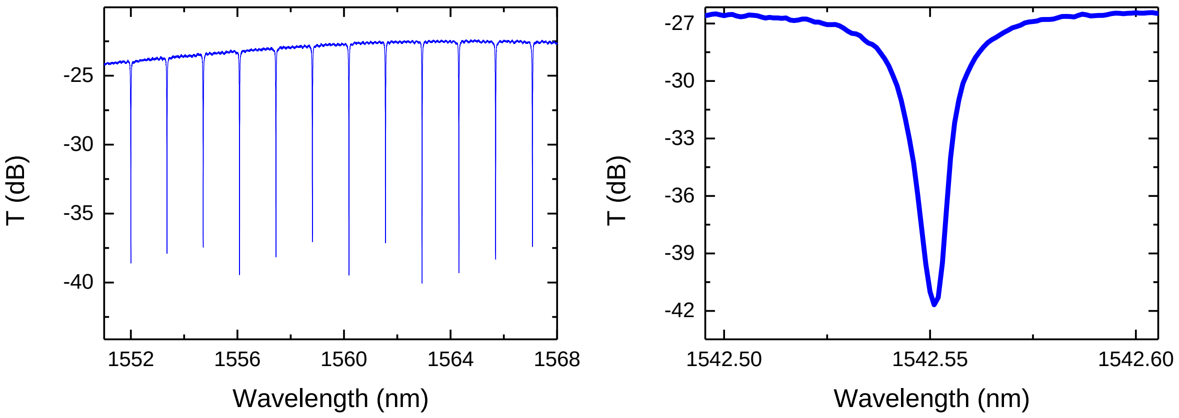

(a) (b)

Figure 2.26 Linear Transmission spectrum of 70μm diameter silicon ring resonator with width of 600nm; (b) *Q*-factor and extinction ratio (ER) of the resonance peak @ 1.542μm extracted are *Q*=81,000 and 15dB for TE polarization.

Table 2.5 Summary of *Q*-factors of rings resonators with different radius

Ring Radius	70μm (TE)	5μm(TE)	5μm(TM)
Q-factor	81,000	5000	4000

2.3.3 Slot Ring resonators

2.3.3.1 Analysis of silicon-on-insulator slot waveguide ring resonators targeting high *Q*-factors

As discussed before, slotted waveguides can be infiltrated with low index active materials that then experience enhanced light matter interaction from electric field n_{si}^2/n_{slot}^2 reinforcement, and have been successfully applied to all optical high speed processing [80], electro-optic modulation [156] and bio detection/sensing [157]. One step farther to reinforce light-matter interactions can then consist in using a ring resonator configuration, which now plays an important role in silicon photonic devices for a broad set of applications including optical modulation [158], frequency comb generation[159] and sensing [160], [161]. Transposing wire waveguide ring resonators into their slot waveguide counterparts is straightforward and has been done for years [162]–[164]. Yet this approach faces the obstacle that the slot scheme leads to higher propagation losses in straight-and-bended waveguides, leading to ring resonators with a moderate *Q*-factor of typically a few thousands in standard situations.

In this context, a better understanding of the loss-limitations of slot waveguide ring resonators and the way to circumvent them to push *Q* factors to higher values is welcome. The aim of this section is precisely to contribute to this goal. Intrinsically, slot waveguides are known to suffer from larger roughness-induced scattering extrinsic losses than Si wires due to a strong electric field interaction with the inner rails' walls defined by lithographic and etching technological processes. Hence, different ratios of slot width to total slotted waveguide width and waveguide aspect ratio lead to different linear losses and *Q*-factors. Typically, the loss levels of straight symmetric slot waveguides are broadly reported around 7dB/cm [165] and after sidewall roughness smoothing of around 4dB/cm [166], which is still larger than for nanowire waveguides (<1dB/cm [149]) and asymmetric slot waveguides (~2dB/cm [167]). The situation becomes even more unfavorable to slot waveguides when considering their higher optical leakage losses in bended waveguides for identical bending conditions [164].

The following study relies on two directions: optimizing the slot waveguide fabrication process, and carefully analyzing the coupler contribution to the overall ring losses consistently with recent works that pointed out its importance in the design of high-*Q* Si_3N_4 low index ring resonators [168]. To briefly summarize our methodology and results, we designed various testing structures typically depicted in Figure.2.27.d and Figure.2.29.a to properly extract the different waveguide-ring coupling coefficients directly from experiments. Following the deduced guidelines, we then fabricated a 50µm radius slot add-drop slot waveguide ring resonator filled by a top cladding index liquid with Q=30,600 in a silicon wafer with silicon thickness of 220nm and a 2µm thick box.

The analysis started with the loaded Q-factor expression of all pass ring resonators that can be casted as [168], [169]:

$$\boldsymbol{Q_{load}} = \frac{\boldsymbol{2\pi n_g L}}{\boldsymbol{\lambda}} / \left[\boldsymbol{\kappa_p} + \boldsymbol{\kappa_c} + \boldsymbol{\kappa_b}\right] \qquad (2\text{-}3)$$

κ_p, κ_c denote here the fraction of power losses due to light propagation in the ring bended waveguides and to the bus-ring coupling, respectively, while κ_b represents the portion of power that is coupled into the bus waveguide and measured from a photodetector. κ_p can be approximated to $\alpha' L$ [170], where α' represents the bended waveguide loss per unit length and L is the unfolded length of the ring. While round trip attenuation also suffers from the ring-bus imperfect coupling, the total round trip attenuation coefficient a=$exp(-\alpha L)$ should account from both κ_p and κ_c, thus the corresponding full propagation/intrinsic loss parameter is α= α'+ κ_c/L.

The intrinsic loss κ_p is highly dependent on the sidewall roughness of the waveguides induced by the fabrication, the thickness of the oxide box and the cladding refractive index. The couplers can result in very different achievable Q-factors due to the coupler loss κ_c that can vary from negligible to severe levels in different types of designs [168], [171], [172]. The detected power ratio κ_p is also linked to the coupler design and dependent on whether it achieves critical coupling or not.

To probe the coupling loss level κ_c/L and investigate how a conventional (straight) directional coupler (depicted in Figure.2.27.c) can affect the slot waveguide ring performances, slotted pass ring resonators loaded by this type of directional couplers but with different coupler gaps (edge to edge) from 0nm to 600nm were fabricated with 10nm step size. After a fabrication process equivalent to the one reported in [173], a Cargille optical liquid with an index of 1.55 (at λ=1.55µm) was used as the top cladding [130], [174]. For the device characterization, subwavelength grating couplers were used to avoid Fabry-Perot fringes and to obtain flat base transmission levels. The silicon rail thickness and width were 220±5nm, 235±5nm, while the slot width was 90±5nm. The analysis method based on equation 2-4 to 2-6 was adopted to extract the intrinsic Q factor (Q_{int}) and loss level α (in /m units), respectively [149].

Equations 2-4 & 2-5 indicate that when the resonance peak extinction ratio T_b is large, the intrinsic loss level α is only dependent on the measured load Q-factor (Q_{load}) for one specific resonance (λ_{res}, with FSR_{res}). It is then possible to compare the coupler losses κ_c among the slotted APR with different coupler gaps by comparing the obtained Q_{load}, since α' and L are kept identical. In our experiments, the first stable resonating conditions at 1.5µm were observed for a coupler gap of 325±25nm, as shown in Figure.2.28. The resonance spectrum shifts to longer wavelengths when the coupler gap increases. The average measured Q_{load} is then limited to around 5,000. However, it is shown that the micro-ring Q_{load} greatly increases up to 21,400 when the coupler gap approaches 500nm, meaning that the coupler losses have been reduced significantly by increasing the gap value, probably due to the minimization of the waveguide side-wall scattering loss effects for wider coupler gaps. Overall, the coupling regime of the ring resonator varies from over-coupling to critical coupling where a very large (25 dB) extinction level is observed.

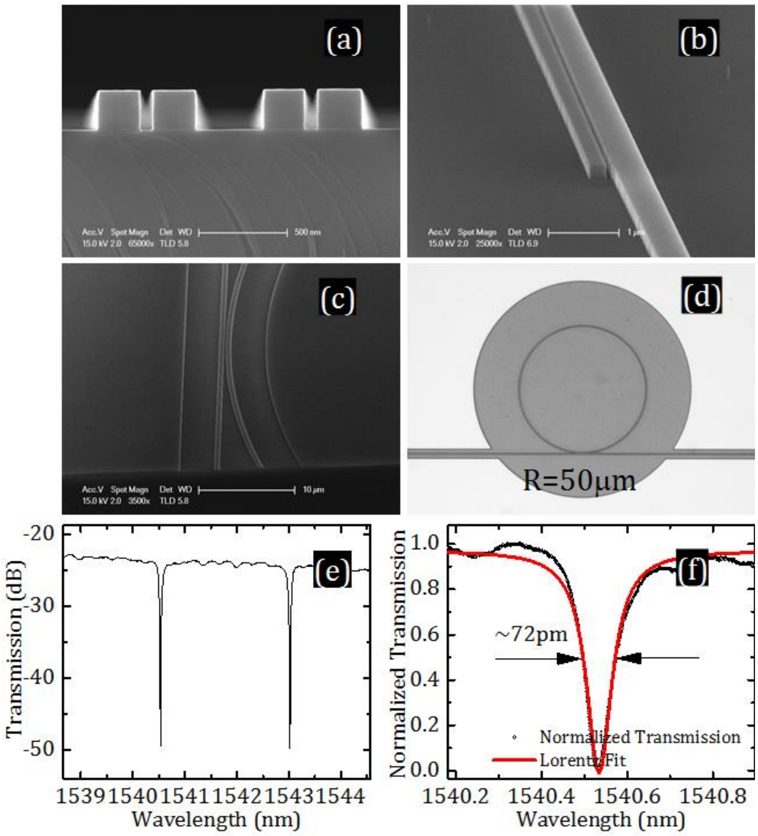

Figure 2.27 Cross-section of ring coupler with a coupling gap here of 310±10nm; (b). Mode converter used to couple light from strip waveguide to slot waveguide; (c). View of the straight bus-ring coupler region; (d). Optical overview of a fabricated slotted all pass ring resonator (APR); (e-f). Normalized transmission spectrum of slotted APR with coupler gap of 500nm with a Lorentzian fitting curve.

$$\boldsymbol{Q_{int} = \frac{2Q_{load}}{1+\sqrt{\kappa_b}}} \qquad (2\text{-}4)$$

$$\boldsymbol{\kappa_b = 10^{-\left(\frac{T_b(dB)}{10}\right)}} \qquad (2\text{-}5)$$

$$\boldsymbol{\alpha = \alpha' + \kappa_c/L = \frac{(1+\sqrt{\kappa_b})\cdot\lambda}{2R\times FSR\times Q_{load}}} \qquad (2\text{-}6)$$

To quantitatively extract κ_p and κ_c, we then implemented a more accurate method [171], which is based on a pair of add-drop resonators (ADR) and ring enhanced Mach–Zehnder interferometers (REMZI) simultaneously fabricated with identical rings and couplers, as shown in Figure 2.29.a.

Since this method is only dependent on measuring the ER, we employed the facet butt method in order to obtain wider and flat transmission spectra.

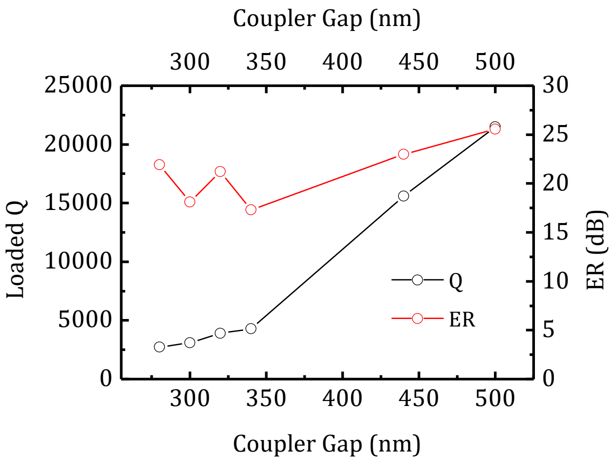

Figure 2.28 Measured maximum loaded Q-factor and the corresponding extinction ration (ER) from the transmission spectra of the slotted ring resonators working at λ=1.5µm.

Three spectra of the ADR pass/drop ports and REMZI structures were measured, the related gathered experimental results feeding a set of three equations (equations 2-7 to 2-9). This experimentally-driven approach allowed us to extract the three characteristic ring resonator parameters t, k, and a', namely the self, cross coupling coefficient and round trip attenuation $a' = exp(-\alpha' L)$. This method completely gets rid of the simple assumption that $k^2 + t^2 = 1$, which is only verified in strip ring resonator configurations when the coupler gap is large enough [171]. The Fabry-Perot fringes of three ports' spectra were removed by filtering high frequency components in order to reduce the uncertainty range. From Figure.2.29, we see that the measured ER of through port is 21.5±0.2dB (T_T), the drop port ER is 5.0±0.2dB (T_D), while the REMZI one is 19.8±0.2 dB (T_{RE}).

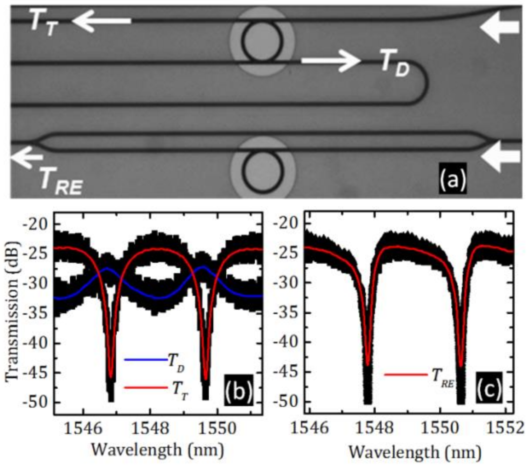

Figure 2.29 Optical overview of ADR and REMZI devices (where the power flow and measured ports are depicted); (b) transmission spectra of ADR; blue line corresponds to the drop port and red one to the through one; (c) transmission spectrum of the related REMZI.

By solving equation 2-7 to 2-9, and considering an uncertainty level of 0.2dB after filtering the spectral high frequencies, the round trip attenuation coefficient a' was found to be 0.9902±0.0058, with $t^2 + k^2$=0.9184±0.0058, corresponding to intrinsic losses of 0.043±0.025dB (1.32±0.87 dB/cm) and coupler losses of 0.370±0.027dB, i.e. 10 times larger than the bended waveguide propagation ones. The max Q_{load} obtained by fitting the experimental spectrum was then 2,560 (see Figure.2.30c)).

$$(\boldsymbol{t^2} + \boldsymbol{k^2}) * \boldsymbol{a'} = \frac{\mathbf{10}^{(T_T+T_D)/20}-\mathbf{1}}{\mathbf{10}^{(T_T+T_D)/20}+\mathbf{1}} \tag{2-7}$$

$$\boldsymbol{t^2 a'} = \frac{\mathbf{10}^{T_D/20}-\mathbf{1}}{\mathbf{10}^{T_D/20}+\mathbf{1}} \tag{2-8}$$

$$\left|\frac{1+\frac{t+t^2a'+k^2a'}{1+ta}}{1+\frac{t-t^2a'-k^2a'}{1-ta'}}\right|^2 = \mathbf{10}^{T_{RE}/10} \tag{2-9}$$

If compared with the coupler loss (κ_c) and single round ring propagation loss (κ_p) levels, the coupler loss thus turned out to be the main parasitic source of loss in the slot waveguide directional couplers of ring resonators (see Table 2.6), while the propagation losses in the bended waveguides are as small as 1.32±0.87 dB/cm.

Table 2.6 Loss contributions

	Propagation losses κ_p	**Coupler loss κ_c**
Loss (dB)	0.043±0.025	0.370±0.027

Overall, the gathered results clearly highlighted that large coupler loss level is the key obstacle to achieve higher *Q*-factors and that forthcoming optimization of slot waveguide ring resonators should primarily focus on coupler loss minimization. Therefore, a new racetrack type add-drop resonators (TR-ADR) based on symmetric coupler was investigated by increasing the bus ring gap to 600nm in order to reduce the mode conversion losses in the coupling region. In comparison with the straight coupler slot ring approach, the symmetric coupler shape (see Figure.2.30.b) eases the two even and odd supermodes transition excitation in the purpose of achieving a reduced-loss coupler mode transformation [171]. With this racetrack design and by properly choosing the coupling region length to $L_{Straight}$=8.8µm, the resonance wavelength range was adjusted to λ~1.5µm. In comparison with the previous normal ADR (N-ADR) (in Figure.2.29.a), more than a 10 times larger loaded *Q*-factor was measured in the new RT-ADR configuration (Q_{load}=30,600, Fig.2.30.d) from a split resonance peak due to light back scattering [175]. The fabrication process ensured that the propagation losses κ_p of the RT-ADR remained almost of the same level as for the N-ADR, meaning that the difference between both designs came from the coupler loss κ_c itself. Referring to equation-2-3 for APR, the total losses were now reduced down to 10% of that obtained from the N-ADR (in Fig.2.29.a). In other words, κ_c was significantly decreased in this symmetric coupler.

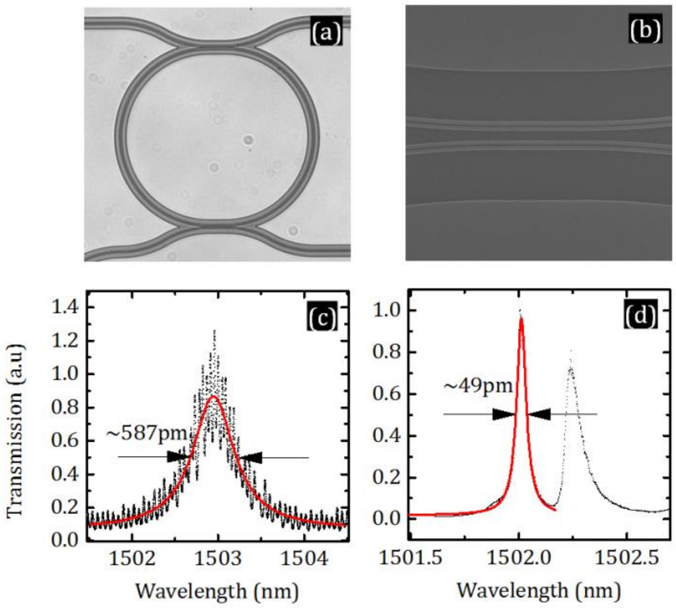

Figure 2.30 Optical view of new designed RT-ADR loaded by a symmetric coupler (b) with coupler gap 600nm; (c, d). Normalized transmission spectrum of N-ADR & RT-ADR together with a Lorentzian shape fitting.

To conclude this part, the loss mechanisms in silicon slot waveguide ring resonators have been experimentally investigated by properly decorrelating the different loss mechanisms from a set of testing structures. The performed studies have revealed the strong influence of the coupler losses on the overall slot ring performances, i.e. with a stronger sensitivity than for strip waveguide-based ring Si resonators. Symmetric couplers with larger gaps have been proposed to efficiently minimize coupler losses and resulted in a 10 times *Q*-factor improvement compared with normal non optimized straight bus-ring coupler. We have demonstrated 50µm radius slot ring resonators with propagation loss in bended waveguides 1.32±0.87 dB/cm and with a *Q* factor of 30,600 when filled by a top cladding liquids. These results show that slot ring resonators can potentially reach high performances for linear/nonlinear hybrid optical processing applications or on-chip sensing.

2.3.3.2 Optical sensing based on slot ring resonator by detuning the critical resonance

After investigating low loss and control of slot ring resonator fabrication, our first application study was performed by focusing on optical sensing. Slot waveguide resonators were fabricated again in the purpose of index sensing.

To evaluate the performances of resonator-based integrated refractive index sensors, the sensitivity (*S*) and the limit of detection (*LOD*) are usually considered as two of the most important device parameters. The sensitivity relates to how much the resonance shifts following a variation of the surrounding material refractive index (RI), while the limit of detection (*LOD*) assesses the minimum RI change that can be detected. Generally speaking, index sensing optical integrated sensor structures can be mainly classified into two types. Dielectric mode sensing and air modes sensing structures, respectively, which are both related to the optical mode interaction with the cladding material.

For dielectric mode sensing, devices intrinsically perform low sensitivities (typically ~200nm per Refractive Index Unit (RIU)) because the optical mode is mainly confined in the dielectric core and has a weak interaction with the surrounding material [129]. However, due to very low optical losses, these devices can exhibit high quality factors (Q>>10^4).

For air mode sensing, the optical mode is largely confined in the low index material, and intrinsically presents much higher *S* values, with yet lower *Qs* due to larger mode confinement losses. This second kind of sensors, mainly including air-mode photonic crystal cavities and slotted waveguide micro-ring resonators [99], [122], [130], [131], [133], [176], is yet of greater practical interest due to better filling properties by water and other liquids. Typically, for slotted nano-cavities, the reported lowest intrinsic *LODs* are around 3×10^{-4}, with *Q* factors about 10,000 and sensitivities around 400nm/RIU [99], [133].

The intrinsic *LOD* is then defined by $\lambda/Q\times S$. Slotted ring resonators have been demonstrated with *LOD*~5×10^{-3}. These devices usually suffer from large losses with associated *Q*-factors of only a few hundreds [122], [128]. Their sensitivities have been experimentally demonstrated around 300nm/RIU[122]. Therefore, efforts to achieve high *Q* and *S* simultaneously in air mode sensing configurations are needed, especially for slot mode microring sensor configurations.

The usual strategy for refractive index sensing is to monitor one resonance peak shift. The detected *LOD* is highly dependent on the tunable laser resolution, the noise from the sample edge Fabry-Perot fringes, and the designed cavity itself. Tracking complex resonance spectrum profiles can also be used by arranging ring resonators in Vernier configurations [121], yet adding complexity in device design and results analysis.

Here, we propose a simple one-ring detection scheme based on the exploitation of the V-shape properties of a micro-ring resonator spectrum envelope enabled by specific design conditions. The underlying idea is to promote a situation in which the bus-waveguide/micro-ring critical coupling condition becomes strongly sensitive to light wavelength, i.e. strongly dispersive. We show hereafter that the obtained V-shape spectrum envelope shift is extremely sensitive (1,300nm/RIU) to the top cladding index when considering filling liquids with an index around 1.33. The critical coupling resonance is quantified by an extinction ratio over than 20dB.

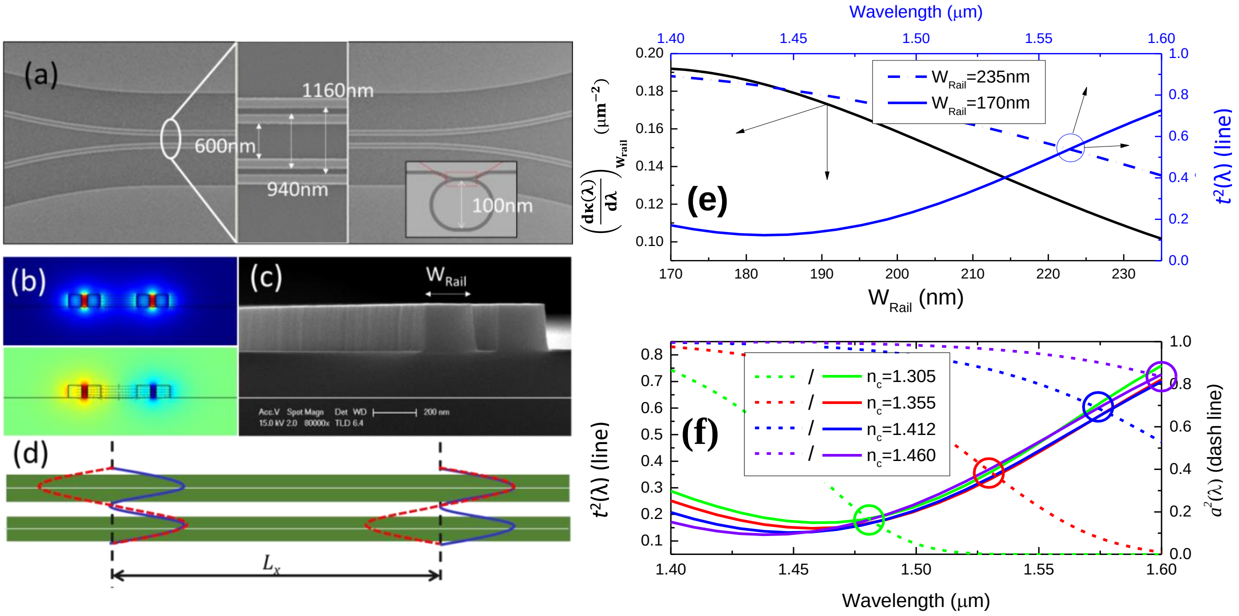

Figure 2.31 (a) SEM view of the considered racetrack coupler, which consists in a bended waveguide ring resonator/bus scheme and a 20µm long straight directional coupler. The straight coupler gap, edge to edge, is 600nm and the slot size is 110nm±5nm, while the rail width is 170±5nm; (b) The symmetric and anti-symmetric supermodes and their effective indices used to calculate the coupling L_x, (c) Cross-section of the slot waveguide. (d) Schematic view of the directional slot coupler and phase shifts of the two supermodes and coupling beating length L_x. (e) Calculated coupling dispersion $d\kappa(\lambda)/d\lambda$ as a function of the rail width at λ=1.55µm, and self-power coupling $t^2(\lambda)$ of the coupler shown in (a) with W_{rail} 170nm and 235nm. (f) Simulated results of self-power coupling coefficient $t^2(\lambda)$ of the racetrack coupler estimated by 3D-FDTD, and round trip intensity attenuation coefficient $a^2(\lambda)$estimated by assuming that propagation losses are 10 times larger than the simulated ones obtained from a mode solver. The simulated results are based on the coupler design in (a) with W_{rail}=170nm and the crossing points of the $t^2(\lambda)$ and $a^2(\lambda)$ correspond to the critical coupling condition of the ring resonator.

The chosen option to make the bus-waveguide/microring critical coupling condition strongly sensitive to wavelength starts from analyzing a simple straight directional coupler as the main part of the racetrack coupler shown in Figure.2.31.a. As it is well known from textbooks, $L_x=\pi/2\kappa$, with L_x the light coupler beating length, κ the coupling coefficient between the two unperturbed waveguide modes (Figs.2.31.b-c) at a given wavelength λ. Simultaneously, $L_x=\lambda/2\Delta n_{eff}$, with Δn_{eff} the effective index mismatch between the two supermodes of the set of coupled waveguides considered in a single approach. Recasting these two equations into one gives $\kappa=\pi\Delta n_{eff}/\lambda$ and thus:

$$\frac{d\kappa(\lambda)}{d\lambda}=\frac{\pi}{\lambda}\frac{d\Delta n_{eff}(\lambda)}{d\lambda}-\frac{\pi}{\lambda^2}\Delta n_{eff}(\lambda) \qquad (2\text{-}10)$$

This equation is a formulation of the wavelength dispersion properties of the coupler design, $d\kappa(\lambda)/d\lambda$ being simply estimated from the calculation of the two coupler supermode effective indices. This approach thus opens the possibility of designing dispersive couplers. As shown hereafter, we have used this strategy to prepare couplers operating at critical coupling in a narrow bandwidth, i.e. in which the critical coupling condition adjusted at a wavelength of interest (λ_0) is efficiently suppressed by wavelength detuning by a few nanometers from λ_0.

The investigated racetrack coupler (as shown in Figure.2.31.a) consists in slot waveguides which have been fabricated on a standard silicon platform with 220nm silicon thickness, 2µm BOX and 110nm wide slot width and filled by a low loss commercial Cargille liquids[130], [174], [177]. As the light coupling process is mainly related to the straight directional coupler region, at least when the directional coupler length (L) is long enough, the coupler dispersion is estimated by neglecting the bended parts of the racetrack coupler. To efficiently engineer the dispersion properties of $\kappa(\lambda)$, the rail width (W_{rail}) of the slot waveguides was swept (Figure.2.31.e) from 235nm to 170nm by using a commercial finite element method mode solver [178]. Figure.2.31.e shows for example that a slot waveguide coupler with 170nm narrow rails has two times larger dispersion ability than a slot waveguide coupler with a rail width of 235nm at λ=1.55µm (with cladding RI equals to 1.55). 3D FDTD simulation [179] of the racetrack coupler was also performed to estimate the power cross-coupling coefficient $k^2 \approx sin^2(\kappa L_x)$, or alternatively the self-power coupling coefficient t related to k by $t^{2=}1-k^2$. As illustrated in Figure.2.31.e, one can see that the dispersion of $t^2(\lambda)$ is much stronger for the $W_{rail}=170nm$ case than for $W_{rail}=235nm$. In other words, the coupling dispersion strength is enhanced in the design of Fig. 2.31.a with narrow rails.

We then envisioned that such a dispersive coupler could modulate the extinction ratio (ER) along a series of resonance peaks of a micro-ring resonator spectrum. The ring resonator indeed reaches the critical coupling for a given resonance λ_c when $a(\lambda_c)=t(\lambda_c)$, where a is the roundtrip electric field attenuation coefficient. The ring resonator has then theoretically a zero transmission power and an infinite ER. If $a(\lambda)$and $t(\lambda)$ can have opposite slopes, then $|a(\lambda)-t(\lambda)|$ can rapidly depart from 0 by resonance wavelength (λ_{res}) detuning from the critical coupling resonance λ_c. To achieve opposite monotonicity for $a(\lambda)$ and $t(\lambda)$, respectively, the directional coupler length L was set in the domain [L_x, 2L_x], a narrow rail slot waveguide configuration was chosen (W_{rail}=170nm) and $a(\lambda)$ and $t(\lambda)$ were estimated by using 3D FDTD calculation. Figure.2.31.f presents the simulation of the loaded racetrack ring resonator of Figure.2.31a with a radius of 50µm. We also simulated different $a(\lambda)$ and $t(\lambda)$ for different cladding materials with refractive index values (n_c) of 1.305, 1.355, 1.412 and 1.460, respectively. Meanwhile, we assumed that experimental propagation losses were around 10 times larger than the simulated ones obtained from the a full-vectorial optical mode solver calculation. The final related results obtained for the loaded racetrack ring resonator of Figure.2.31.a with a radius of 50µm are shown in Figure.2.31.f. As visible, Figure.2.31.f illustrates the predicted λ_c, giant shift ($\Delta\lambda_c$ cross point shift) as a function of n_c.

Figure.2.32. depicts the proposed sensing regime and highlights its differences with the standard cavity sensing method based on a single resonance peak tracking. In the proposed dispersive-coupler scheme, sensing is based on probing the resonance having the largest extinction ratio as a function of the top cladding material index as shown in Figure.2.32.b.

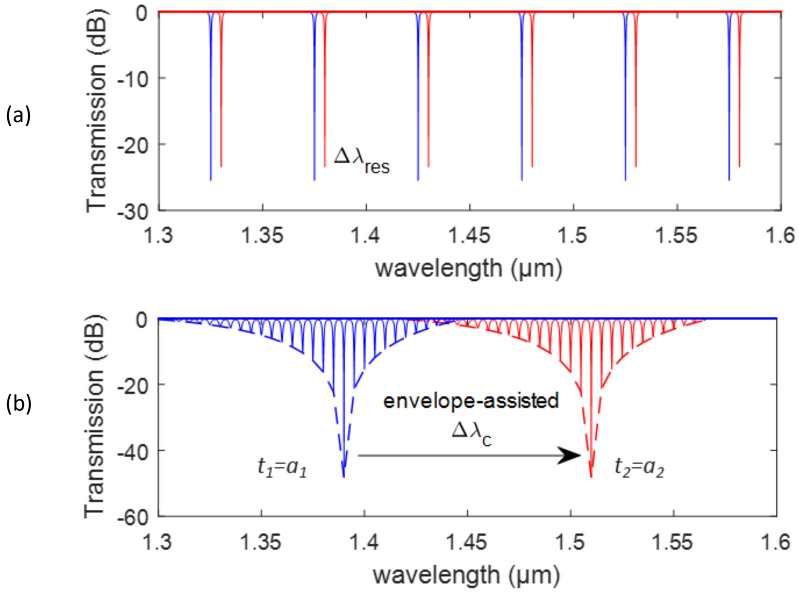

Figure 2.32 Schematic explanation of the sensing mechanism normally used by tracking one specific resonance λ_{res} (a) and the one that we propose by tracking the critical coupling resonance through the spectrum envelope monitoring (b).

Experimentally, racetrack all pass ring resonators (RT-APRR) with a ring radius of 50µm were fabricated. In the chosen design, the coupler bus waveguide enters and leaves the coupling region with the same curvature as the ring resonator one, as depicted in Figure.2.31.a. The detailed fabrication processes and characterization methods of the RT-APRR resonators have been reported in [177]. The cut-butt coupling method was used to measure the resonance for wavelengths ranging from 1.375µm to 1.64µm.

First, we compared the two transmission spectra of the RT-APRR having rail widths of 235nm and 170nm, respectively. The related results are shown in Figure.2.33.a. The measured spectrum of the RT-APRR with W_{rail} 235nm has a very wide spectrum envelope of about 170nm. In this configuration, the spectrum envelope is so wide that many resonance peaks are close to the critical coupling condition. On the contrary, the RT-APRR with slot waveguide rail width of 170nm clearly displays a narrow V-shape comb resonance profile with only 60nm width. In this case, a nearly-unique critical resonance peak with the highest ER from surrounding peaks can be distinguished. Let us emphasize that this critically coupled peak does not perfectly correspond to the $t=a$ condition, yet $a(\lambda_c)\approx t(\lambda_c)$. As a whole, the comparison between the two experimental micro-ring spectra clearly sustain the strong influence of the slot waveguide rail width (remind that except this parameter, the two micro-ring resonators are identical), as anticipated before.

To investigate the critical coupling envelope sensitivity, we changed the top cladding liquid refraction index. n_c to match the 1.305, 1.355, 1.412, 1.458, and 1.460 values, respectively. The successive transmission spectra were measured by cleaning the sample and redoing new experiments after a new drop casting step, are depicted in Figure.2.33.b. As visible, all the resonance combs sustain similar widths when the cladding RI varies from 1.3 to 1.5. Deepest probed resonance peaks can be figured out through few dB ER differences, demonstrating the viability of the proposed sensing approach.

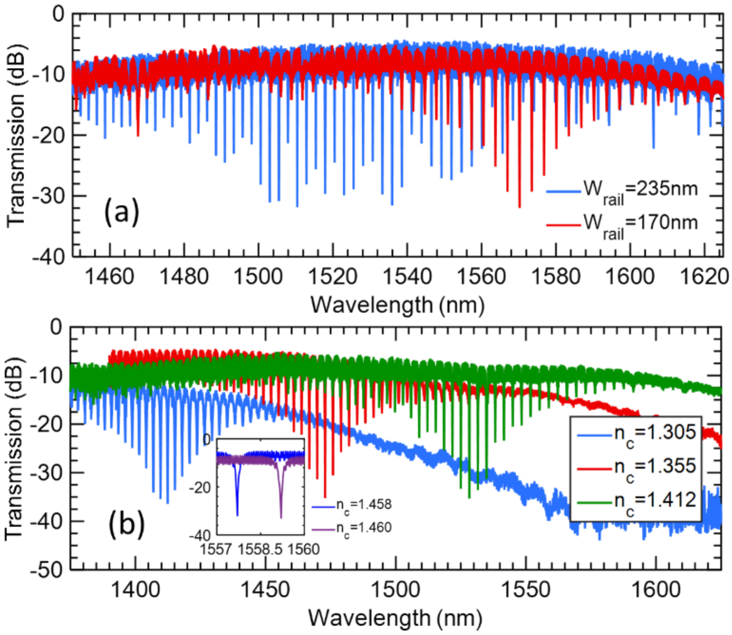

Figure 2.33 (a) Transmission spectrum comparison between slotted RT-APRR with rail width 235nm and 170nm, respectively; the slot size of the two resonators is 110nm and the top cladding liquid RI is equal to 1.55 at λ=1.55µm; (b), Transmission spectra of slotted RT-APRR with slot waveguide rail width of 170nm for different top cladding liquids with RI values of 1.305, 1.355, 1.412. The inset shows the critical resonance (λ_c) shifts when n_c is 1.458 and 1.460, respectively.

The transmission spectrum envelope has been fitted for each cladding index value (n_C) by a Gaussian distribution law. The obtained envelope peak wavelength law (λ_{env}) is shown in Figure.2.34a. The sensitivity of the envelope has then been obtained through λ_{env} differentiation.

The minimum index change Δn_c=0.002 induced $\Delta\lambda_c$=1.497nm, as shown in the insect of Figure.2.33.b, which corresponds to S_{env}=*748.5*nm/RIU. The total shifts of the spectrum envelope peak wavelength are summarized in Fig.2.34. The observed shift dependence on the cladding RI is not linear for the whole RI range 1.3 to 1.5, due to the decrease of the sensitivity S_{env} as shown in Figure.2.34.b. S_{env} decreases from 1300nm/RIU down to 400nm/RIU when n_{c} increases from 1.3 to 1.5, while the individual single-peak Q factor grows up to 6000 for n_c=1.46 (symmetrical slab membranes tend to lead to larger Q-resonators).

In term of achievable optical sensor *LOD*, the proposed envelope-assisted wavelength peak approach is essentially efficient provided that two conditions can be fulfilled: i) A single resonance should be close to the critical coupling condition, ii) The top cladding index perturbation (δn_{clad}) is capable of inducing a shift of several microring resonator FSRs. It thus turns out that the device *LOD* is finally given by $LOD=2FSR/S_{env}$. Microring resonators based on cm-long spiral-shape slot waveguides can thus provide *LOD* values typically around 10^{-4}.

Another advantage of the proposed sensing configuration is to enable index sensing in a very wide index range from $n_{clad}\approx1.3$ to $n_{clad}\approx1.5$.

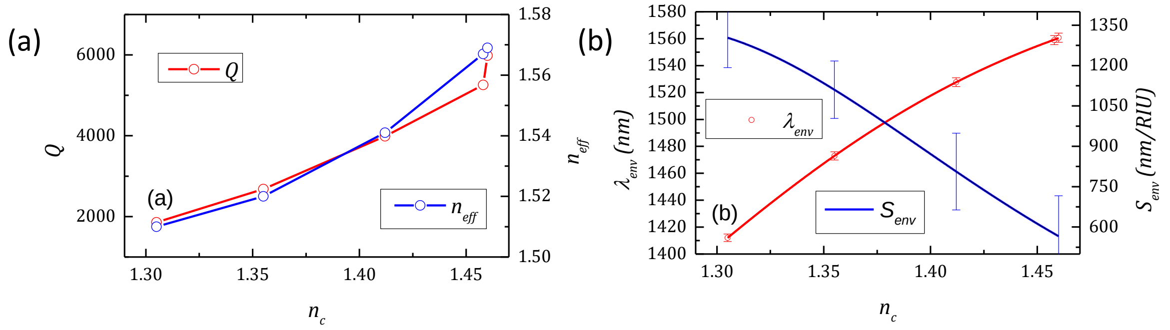

Figure 2.34 (a), Effective mode index (n_{eff}) of the involved slot waveguide mode and *Q*-factor of the critical coupling resonance as a function of the top cladding refraction index liquid (n_C); (b) Fitted slotted RT-APRR envelope bottom wavelength (λ_{env}) and calculated sensitivity S_{env}. The different values have been estimated as a function of the top cladding liquid refraction index in the range from 1.3 to 1.5.

To conclude this part, a new approach to on-chip index sensing using silicon-based micro-ring resonators has been presented. The proposed mechanism relies on the fast detuning of the bus-waveguide/ring critical coupling condition and mainly stems on a highly dispersive slot waveguide coupler design. This specific feature provides narrow resonance spectrum combs with few distinguished critical resonance peaks if compared with a standard design. The spectrum envelope peak wavelength can be easily figured out and treated as a sensing probe to monitor the cladding index changes. The proposed concept is experimentally evidenced by characterizing a series of fabricated structures at around λ=1.50µm. Around the refractive index of water, we observed sensitivities S_{env} up to 1300nm/RIU. Additionally, the sensor Limit of Detection scales down as $LOD=2\,FSR/S_{\text{env}}$, meaning that *LOD* typically lower than 10^{-4} can be obtained for spiral-engineered micro-ring resonators in SOI photonics. This result brings improvement of Si slot-waveguide resonator sensors and opens interesting perspectives for on-chip optical sensing.

2.4 Nanobeam Cavities

In spite of the excellent properties of slotted waveguides and microscale micro-ring resonators, integrated optical nano-cavities have also been investigated in a complementary fashion due to the possible higher quality factors (*Q*) and smaller mode volumes (*V*) they allow [90], meaning larger *Q/V* Purcell-like factor of merit for light matter interaction enhancement. Dielectric nano-cavities, in which optical modes are confined in high index cores (III-V materials, silicon, germanium, etc.), have been successfully demonstrated with numerous applications, such as, on-chip light sources [96], optical switching [180], frequency converters [181], optical tweezers/sensing [182], optomechanical resonators [183], or even quantum electrodynamics [184][185]. However, for hybrid interaction, these kinds of cavities are not desirable regarding to the cavity mode mainly confined in silicon rather than in cladding layers, also meaning issues to two-photon absorption and other derived free carrier effects.

The alternative solution relies on choosing air mode cavities, with enhanced electric field in low index regions, well suited for hybrid-photonics and on-chip bio-sensing. With respect to previous results [53-57], one dimensional nanobeam cavities, which are formed in simple silicon strip waveguides(eg Si nanowires), turn out to have small footprints, small mode volumes, high *Q* compared with slotted ring resonators or 2D photonic crystal cavities [98], [186]–[190].

The general design guidelines of these resonators is based on tapering either the dielectric band or the air band of the 1D distributed mirrors [191], [192] to form deterministic resonances through photonic-band-diagram engineering. Figure.2.35.a&b show the case of a dielectric cavity designed and fabricated by linearly reducing the air hole filling factor proposed in Ref. [193]. High transmission efficiency (only 5dB of excess loss with respect to the bandpass level), a nearly-Gaussian optical mode distribution along *x*, and a high *Q*-factors 84,000, are then obtained. Figure.2.35.c shows that linearly increasing the filling factor of ladder kind lattices from center to two sides could also form cavities mirrors on two sides and finally result in an air mode cavity (verified here through 3D-FDTD simulations) [192]. In this example, the nanobeam width is 800nm and the lattice constant is 300nm. The void low index (considered as SiO_2) slits have a height of 400nm and the width of the central slit is 100nm, followed with lateral slit widths increasing up to 160nm with 5nm step.

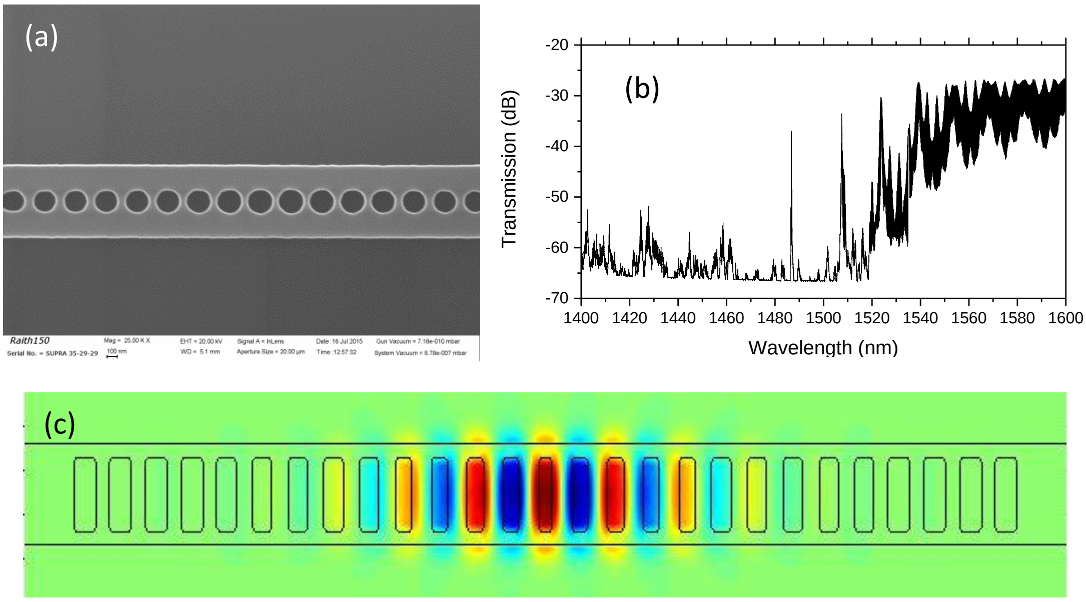

Figure 2.35 Cavities created by a linear decrease of the air-slit filling factor (a) and increasing factors (b). (a) is dielectric nanobeam cavities with mode confinement mainly in the high index silicon region. (b) shows the fabricated cavity (a) with Q factor of 84,000 which 5dB transmission loss. (c) Air mode nanobeam cavities formed by increasing the filling factor, with mode confinement mainly in the low index slits. The slit width at middle is 100nm.

2.4.1 Hybrid air-dielectric nanobeam cavities

In order to simultaneously promote high *Q* factors cavities and a large overlap of engineered cavity modes with low index active materials, we propose here a deterministic approach to design air-mode cavities with yet dielectric-mirrors and targeting a desired resonance frequency λ_{res}. The proposed method only requires band diagram calculation of the dielectric mirrors. As shown hereafter, the designed air mode cavities are flexible with respect to different numbers of air mode cells (N_{Air}) at λ_{res} and exhibit first order mode with cladding refractive index sensitivity *S* around 50nm/RIU with *Q* factor around 60,000±15,000 under cladding index values (n_c) ranging from 1.3 to 1.5.

Our design principle is to sandwich an air-kind localized mode between two dielectric mirror modes. This approach relies on coupling dielectric modes of the mirror regions into air mode cells of the cavity central part, while ensuring a correct phase matching at the interface between both regions, as shown in Figure.2.36.

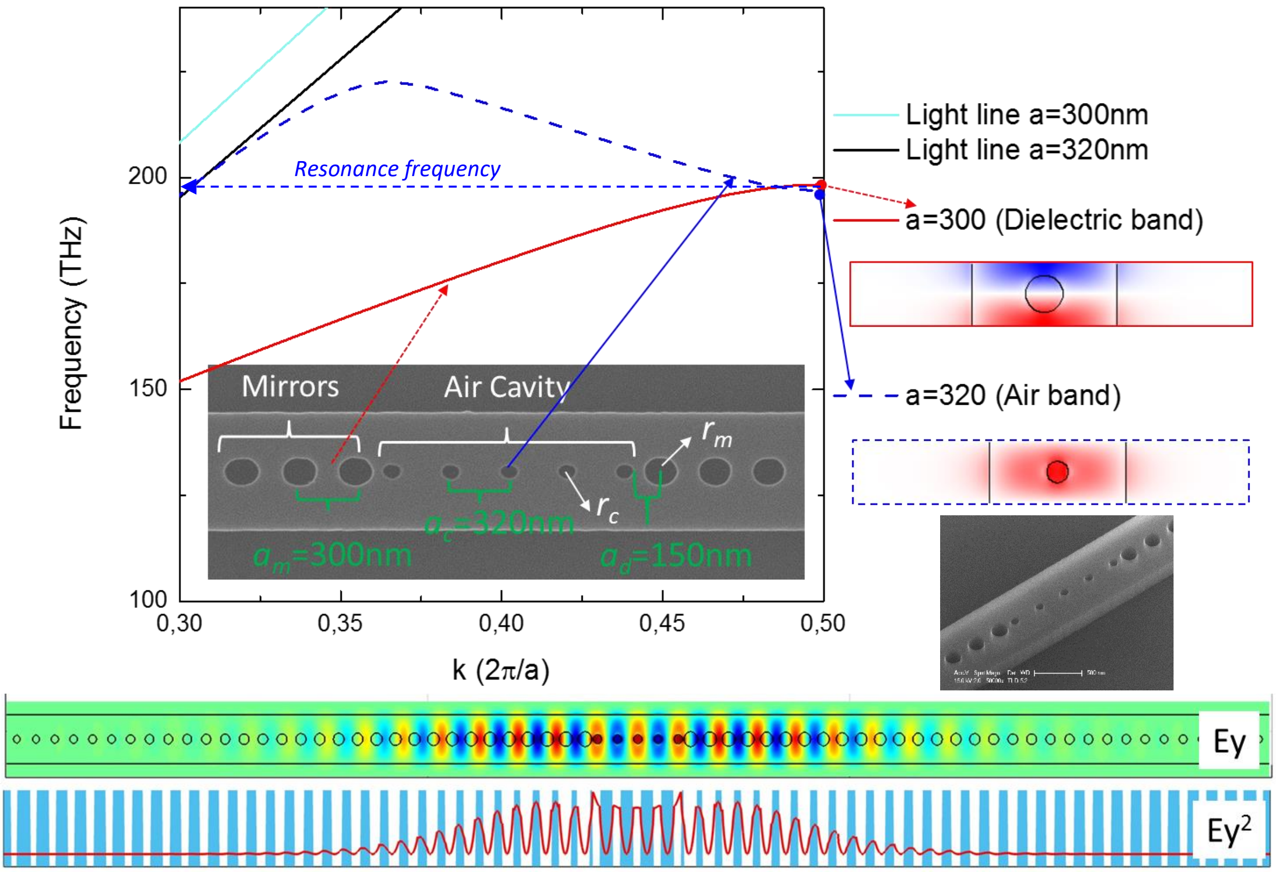

Figure 2.36 TE band diagram for dielectric mirrors with lattice constant am=300nm, hole radius of rm=100nm, and air mode cavity resonance prepared with another couple of a and r parameters: ac=320nm, rc=60nm. The Ey field profile of the dielectric mirror and air modes are depicted on the right. The inset is the SEM image of the fabricated structure, where hole radii are modulated with Electron beam lithography dose to achieve sizes ranging from 40nm to 60nm. The FDTD simulated cavity mode Ey field and |Ey|2 distributions along the central x-line are shown in the bottom.

As proposed in [193], dielectric mirrors are formed by linearly decreasing the hole radius (r_m) from the center (as shown in Figure.2.36) while keeping a constant lattice a_m. As shown in Fig. 2.36, this approach well leads to the appearance of a dielectric cavity resonance (at λ_{mirror}) with a Gaussian field profile [193]. The novelty, here, is that engineering the resonance mode confinement within lower index holes with reduced diameter ~100nm, allows an air mode resonance to be confined between the two dielectric mirrors. (Fig.2.36).

Technically speaking, we have performed 3D-PWE calculation to match the desired hole size (r_{res}) for which the air mode band edge (λ_{res}) crosses the mirror one (λ_{mirror}), as depicted in Fig.2.36. Another design guideline was also taken into account: the electrical field phase between the mirror and cavity air modes must be matched, too, which is realized through engineering hole position of the air mode (see Figure.2.36).

The number of the air mode cells is flexible and typically can reach up to $N_m/10$, N_m being the total number of the mirror holes on each side of the nanobeam cavity. According to 3D-FDTD resonance mode simulation, as illustrated in Fig.2.36, the obtained overall cavity optical modes is partially confined in the 5 air mode holes with enhanced electric field in the two lateral air cells. The field distribution of $|E_y|^2$ keeps a quasi-Gaussian profile (which is a good point to minimize out-off plane losses) and transits from the two lateral dielectric mirrors into the middle low index holes. The performed cavity mode simulations agree with our discussed design strategy and reveal light resonating at air mode wavelength with good phase transmission from dielectric mirrors to air mode cells.

The related Q-factor and mode volume (V) simulation have been performed through 3D-FDTD simulations by considering different groups of real fabricated parameters (N_{Air}, r_{mirror}, r_c), as summarized in Table.2.7. The target wavelength (λ_{res}) was found to be nearly-insensitive to N_m, and the obtained Q-factors remained of the order of 10^4, i.e. typically only one order of magnitude lower than for purely dielectric cavities (without air mode cells). According to 3D-FDTD simulation, the maximum electric field is localized in low index holes, as depicted in Figure.2.36. Such cavity modes have also reduced mode volumes if compared with dielectric cavity ones.

Table 2.7 3D-FDTD simulated results of the nanobeam cavities

(N_{Air},r_{mirror}, r_c)	λ_{res}(μm)	Q(I-Mode)	$V(\lambda/n)^3$
(0,100,0)	1.5	10^7	1.2
(1,90,55)	1.547	77,226	0.022
(5,90,55)	1.547	77221	0.031
(1,100,60)	1.528	135,948	0.039
(5,100,60)	1.528	33,000	0.046

Experimentally, we fabricated a series of defect air mode cavities with numbers of air mode cells ranging from 1 to 9, in a 220nm thick silicon wafer with a 2μm silica BOX layer, and measured all samples after drop-casing a 1.46 refraction index Cargille liquids on top. Dielectric mirrors with a linearly reduced filling factor were realized through modulated electron beam exposure/dose sizes, with a 2nm decreasing step down to 15nm. The same method was used for modulating the hole sizes of the air mode cells.

In Figure.2.37, the transmission efficiencies of the designed are shown, which firstly illustrates the sensitivity of λ_{res} with r_c (shift from 1.532μm to 1.547μm). The transmission efficiency (T) is in the 10%-25% range.

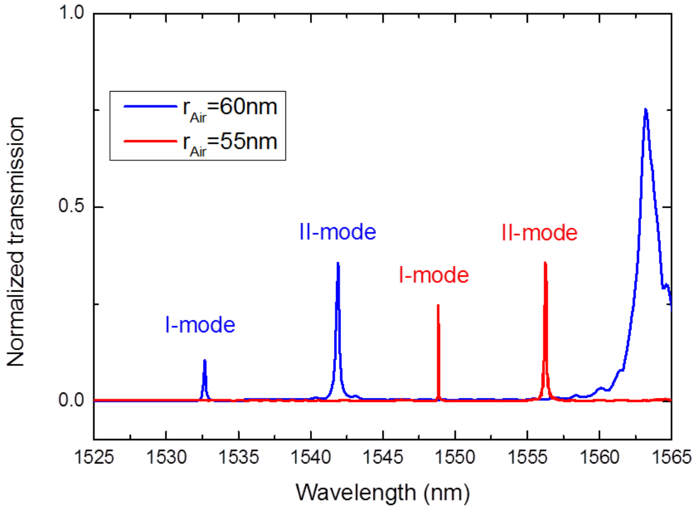

Figure 2.37 Transmission spectrum of fabricated nanobeam cavities with [r_m=100nm, r_c=60nm] and [r_m=90nm, r_c=55nm], which have been normalized by referring to the stable transmission level at the wavelength of 1.6μm, as shown in Figure.2.38.a.

The whole transmission spectra of different air cell numbers (N_{Air}) from 1-9 are shown in Figure.2.38.a, which displays a stable λ_{res} 1548.95±0.25nm and Q-factor 61,500±9,500. The resonances have extinction ratio (ER) about 20dB and FWHM down to 20pm.

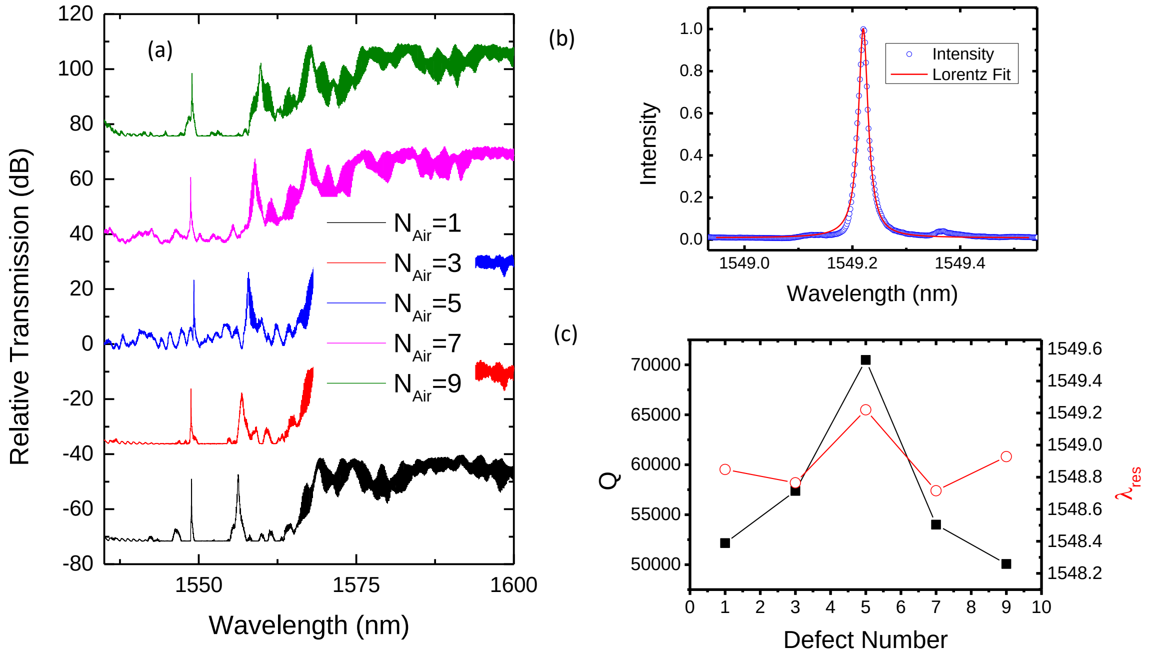

Figure 2.38 Transmission spectra of nanobeam cavities with r_m=90nm, r_c=55nm, consisting of different numbers of air mode cells ranging from 1 to 9. (b), Lorentzian fit of one cavity resonance. (c), Fitted Q-factor and resonance λ_{res} as a function of the number of N_{Air}.

In order to verify the robustness of these air mode cavities for hybrid integration of different materials, we performed liquid index sensing experiments by making the top cladding refractive index (Cargille liquids) RI vary from n_C=1.3 to n_C=1.5. In Figure.2.39, the shifts of resonance spectrum with different

Cladding RI values, respectively, were measured and are depicted from the nanobeam cavity with N_{Air}=7. The corresponding λ_{res} displays a quite linear dependence on the cladding RI, which shows a bulk *RI* sensitivity $S=\Delta\lambda_{res}/\Delta n_c$ with 51nm/RIU, very close to the simulated one (42nm/RIU). The maximum *Q*-factors measured from different N_{Air} are also summarized in Figure.2.39.c, which more or less indicates that the maximum of *Q* usually happens for large N_{Air} or large mode volume cavities.

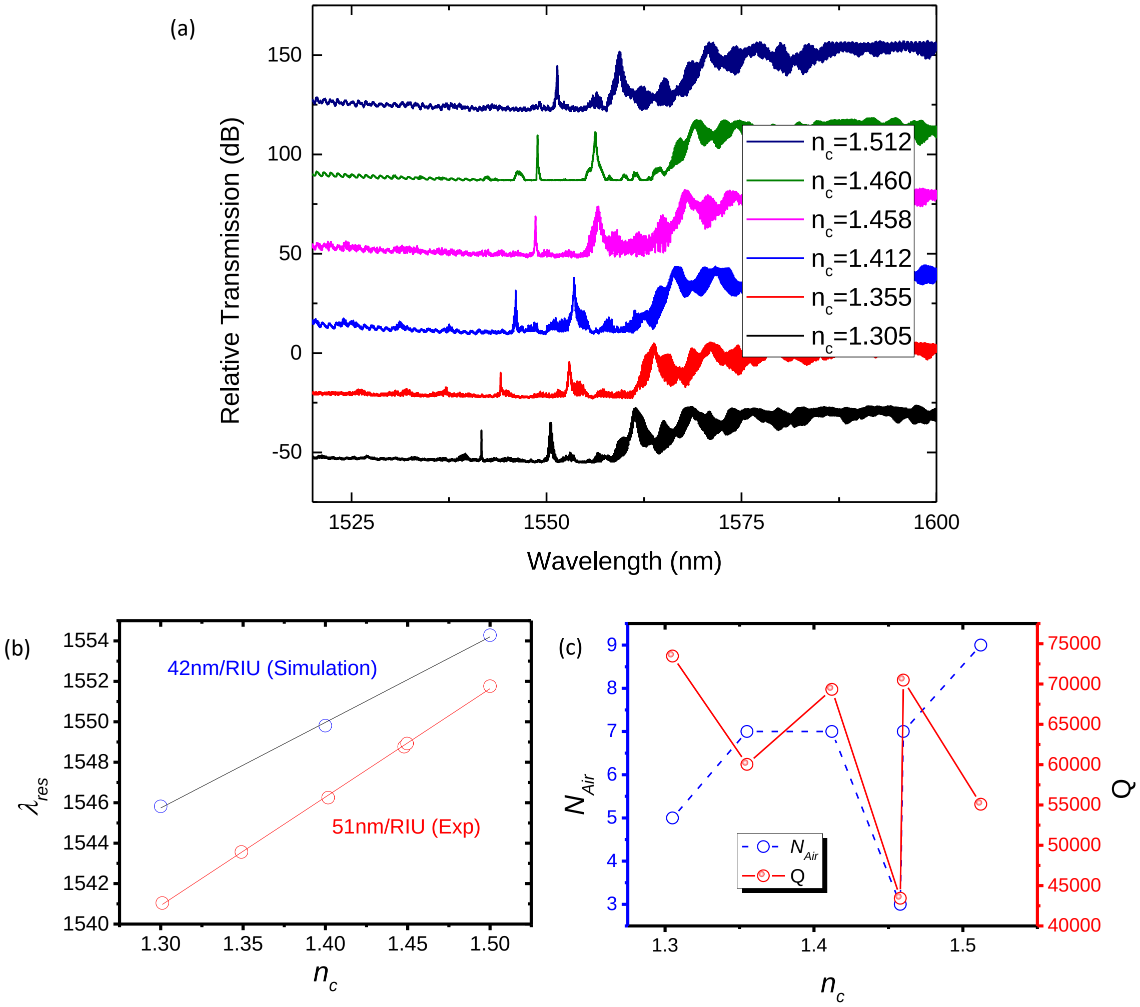

Figure 2.39 (a), Resonance wavelength shift as a function of the cladding RI. (b), simulated and experimental sensitivity of the first cavity I-mode. (c) Measured max Q-factor of the I-mode resonance as a function of the cladding RI.

To conclude this part, we demonstrated a hybrid design method to achieve air-mode nanobeam cavities assisted with dielectric mirrors by 3D-band diagram calculation, 3D-FDTD simulation, fabrication, and characterization. The experimental results show its robustness for different cladding index values ranging from 1.3 to 1.51, with *Q*-factor ~60,000 and cladding sensitivity 50nm/RIU, which corresponds to a sensing $FOM = S*Q/\lambda$~1940. This type of robust nanobeam cavity could be applied to future hybrid silicon photonics integration with active materials for luminescence enhancement, lasing, bio-sensing and optical trapping.

2.4.2 Slot waveguide-nanobeam cavities

Another most straight forward method to create slot mode cavities is arranging two nanobeam cavities close enough to partly confine light between two rails, like silicon slot waveguides and as displayed at Figure.2.40.a. Similarly as for single nanobeam cavity design, only band diagram calculations is needed to the first order to design such resonators (see Figure.2.35 or [193]). To create such a cavity, the parameters to be considered in 3D-PWE (MPB) calculations are the slot width 100nm, the lattice constant 280nm, the hole radius of the resonance cell (adjusted to 105nm), and the hole radius of the last mirror (finally chosen to 75nm).

The 3D-FDTD calculated transmission spectrum of such a cavity is shown in Figure.2.40.b with 10 mirror cells on each side. Such a starting configuration has intrinsically a low *Q*-factor, around 2000. By increasing number of mirrors and number of the taper mirrors, a maximum *Q* factor of 1.2 million can yet be predicted, as shown in Figure.2.41. Further fabrication and measurement steps are required to demonstrate slot waveguide nanobeam cavities and are among the perspectives of this thesis.

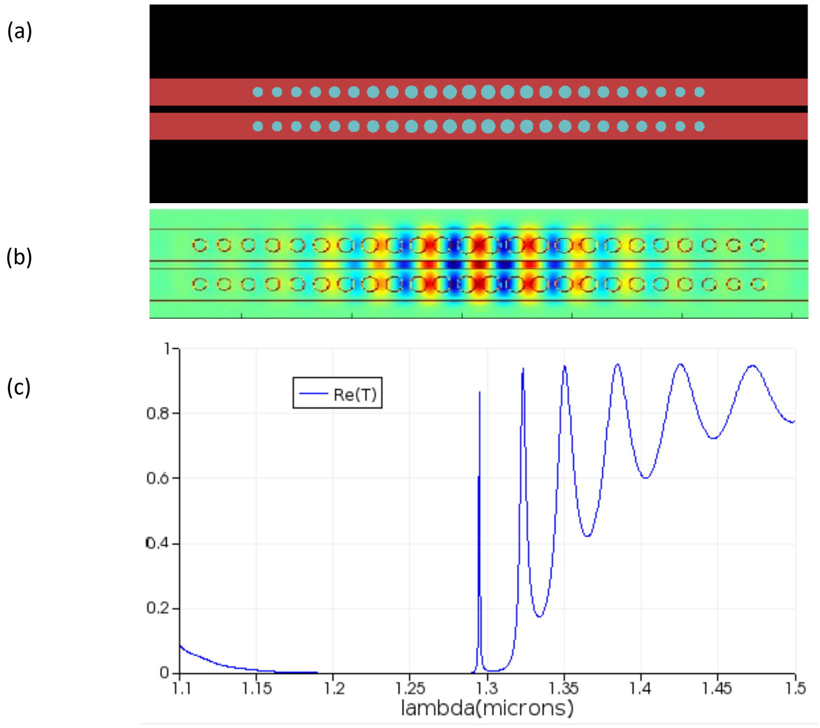

Figure 2.40 Schematic view of a slot double nanobeam cavities (a) and simulated resonance mode (b). (c) Transmission spectrum of the nanobeam cavity in (a).

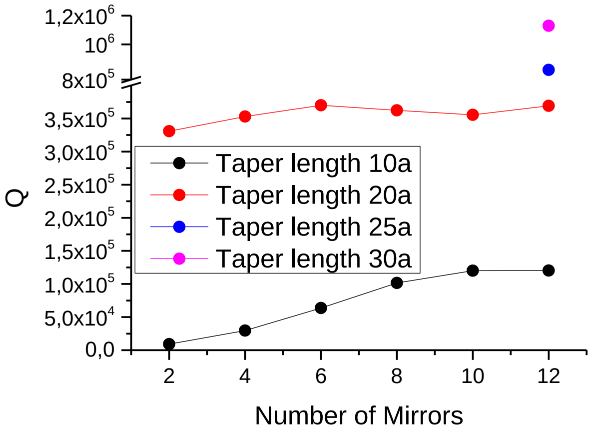

Figure 2.41 Q factor obtained improvement by increasing the number of the mirror cells. The total number of lattice cells is set to10, 20, and 40, respectively.

2.5 Conclusion

To summarize the works presented in this chapter, we have designed, fabricated, and characterized silicon dielectric strip and slot waveguides, strip/slot SOI waveguide resonators, and SOI slotted nanobeam cavities. If compared with state of the art results, the losses and *Q*-factors are comparable. Instead of focusing only on TE modes, we have also explored TM mode behaviors in micro resonators, which have been demonstrated as not very lossy and being able to sustain comparable *Q*-factors as TE-modes in some situations.

Slot waveguides, air mode nanobeam cavities have been optimized. We successfully demonstrated that silicon slot waveguide losses can be decreased down or less than 2dB/cm. Directional slot ring coupler has been demonstrated as the key loss sources to reach high *Q*-factors for silicon slot ring resonators. Symmetrical couplers with large gaps (600nm) are then able to reduce coupler losses and to bring *Q*-factor up to 30,000 for add-drop slot ring resonators. A new proposed air mode nanobeam cavity with ultra-high *Q/V*, transmission efficiency ~20% and low cladding refractive index sensitivity has also been experimentally demonstrated for light matter interaction enhancement purpose.

All these results demonstrate that passive slotted SOI waveguides and resonators have the desired properties for hybrid integration with active/nonlinear optical materials. In the next two chapters, we will put the focus on the integration of Erbium-based materials (chapter 3) and carbon nanotube materials (chapter 4) in such slotted waveguides and resonators, respectively.

3. Er^{3+} integration in slot silicon photonic waveguides

3.1 Introduction

The main purpose of integrating Er^{3+} doped materials in silicon photonics is to achieve light amplifiers and laser sources with a close proximity of Erbium doped optical fiber components: Er-doped fiber amplifiers (EDFA) and optically pumped Er-doped fiber lasers (EDFL), which are standard and necessary components in telecom networks. Successes related to these components are due to the fact that erbium intrinsically presents a broad gain in the telecom C (1525-1565nm) and L (1565-1610) bands, and is compatible with fiber telecom systems benefiting from low loss, low noise, low dispersion, negligible nonlinearities, and high net gain up to 30-50dB within several tens meters long fibers. The optical amplification ability of erbium ions come from the unique nature of their energy levels that allow C&L band signals to be amplified by stimulated emission. A pump laser with λ_P=1480nm or λ_P=980nm excites erbium ions into higher energy levels (2 or 3) where they can decay via stimulated emission, as shown in Figure.3.1.

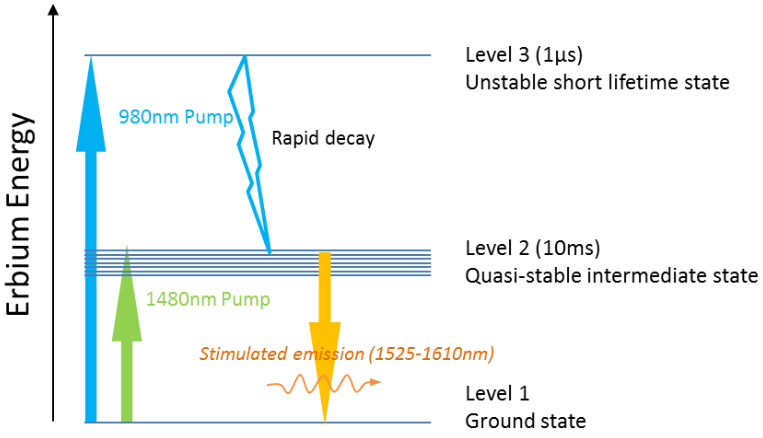

Figure 3.1 Schematic diagram of Erbium energy levels; two pumping methods (980nm and 1480nm) and stimulated emission of C & L bands light, which is the key physical process to amplify light for optical telecommunications.

Similarly, the integration of Erbium ions within on-chip micro scale optical waveguides is envisioned to bring rich potentials for light amplification and lasing in the C&L wavebands for on-chip applications. On chip waveguide technologies can rely on various materials including semiconductors, silica, chalcogenide glasses, polymers, Al_2O_3 and so on. Among them, high refraction index contrast platforms have been demonstrated in the last years, leading to the realization of compact optical waveguides and circuits and relying in silicon compatible processes: the silicon on insulator and silicon nitride platform, respectively. Relying on low loss waveguide technologies, the first crucial task is to properly integrate erbium ions and related materials within these on chip micro-/nano-waveguides, then allow high efficient interactions of the pump and signal with erbium ions inside of the hybrid waveguides, which have much more compact modes than optical fibers. Another task is to develop robust erbium materials with extremely high erbium ions concentrations or large enough quantity of Erbium ions for high optical amplification gain in much shorter waveguide distances than optical fibers. As these high Erbium concentrations are easily responsible for new detrimental effects (ion/ion quenching effects, etc), additional challenges are raised to prevent spoiling spectroscopic transitions due to short distance ion-ion interactions.

Up to now, several high efficient erbium materials or erbium hybrid on chip planar waveguides have been reported with high gain since year 2013, such as Er^{3+} doped Al_2O_3 [109], Erbium silicate [194], or Erbium organic materials [74]. 20dB high net gain [109] and lasing were demonstrated in Er^{3+} doped Al_2O_3 waveguides with silicon substrate. Erbium-ytterbium silicate (EYS), demonstrated with 300dB/cm net gain or ~5dB relative gain in few tens micrometer length core-shell nanowires [194], is a very good candidate to be integrated with silicon photonic waveguides. Erbium yttrium chloride silicate (EYCS) and Erbium chloride silicate (ECS) single crystal nanowires have been also been predicted with net gain higher than 100dB/cm[195] and experimentally displayed ~70dB/cm[196], [197], respectively.

In another material strategy, Er^{3+} can also serve to dope different organic host matrices and co-doped with sensitizers, which can be easily fabricated and optimized, with more freedom to improve ion dispersity, concentration, and pumping efficiency. Especially, when the organic host containing light harvesting chemical groups, chromophores coupled to erbium, the needed pumping intensity can be decreased [74].

However, all above discussed high gain amplification materials were limited on low refractive index contrast waveguides such as Al_2O_3 [109], phosphate glass [198] and not CMOS compatible nanowires [194]–[197]. Therefore, so far, very few demonstrations of Erbium integration in silicon optical waveguides have been directly demonstrated. As directly doping silicon and silicon nitride waveguide cores with erbium ions is difficult, alternative ways to develop erbium hybrid silicon photonic amplifiers are relying on integrating erbium as the waveguide cladding material. As discussed in chapter-2, the evanescent field in the cladding layers is much weaker than the in–core field. Moreover, the optical amplification ability of hybrid erbium silicon waveguides is highly dependent on the cladding material properties and the overall detrimental waveguide propagation losses due to roughness scattering. Therefore, the main challenges to develop silicon-erbium core-cladding waveguide amplifiers are: (1) Properly integrating highly efficient active erbium doped materials on top of the silicon or silicon nitride waveguides cores with negligible integration defects and additional waveguide scattering losses; (2) Successfully transferring the material amplification ability to the hybrid waveguide to enable an as large as possible internal net waveguide gain.

For the development of highly efficient materials, the priority of Erbium doped materials is exploring high optical gain, which is often limited by counteractive effects when increasing Erbium ion concentration, as shown in Figure.3.2. As illustrated here, different host materials have been reported in the state of art. Erbium concentration has been improved from 0.01 $\times 10^{20}/cm^3$ in sol-gel silicate to 100 $\times 10^{20}/cm^3$ in ECS, while lifetime decreases from 10ms down to 0.5ms. Counteractive effect can be explained by the ion-ion cooperative upconversion mechanism, which is significantly enhanced when Er^{3+} density grows. To compare these different Er^{3+} doped materials, a figure of merit defined as lifetime-density-product ($LDP = \tau_{PL} N_{Er}$) was used to evaluate the light emission strength [199], where τ_{PL} is the lifetime of collected photoluminescence (PL) and N_{Er} is the Erbium density (concentration). As shown in Figure.3.2.b&c, the defined LDP reaches an optimum when N_{Er} is close to the order of $10^{22}/cm^3$, which potentially leads to optical gains increasing to the order of $100 cm^{-1}$[199]. To conclude, Er^{3+} doped layers with such high optical gain have become a promising material for light amplification and lasing in integrated photonic platforms.

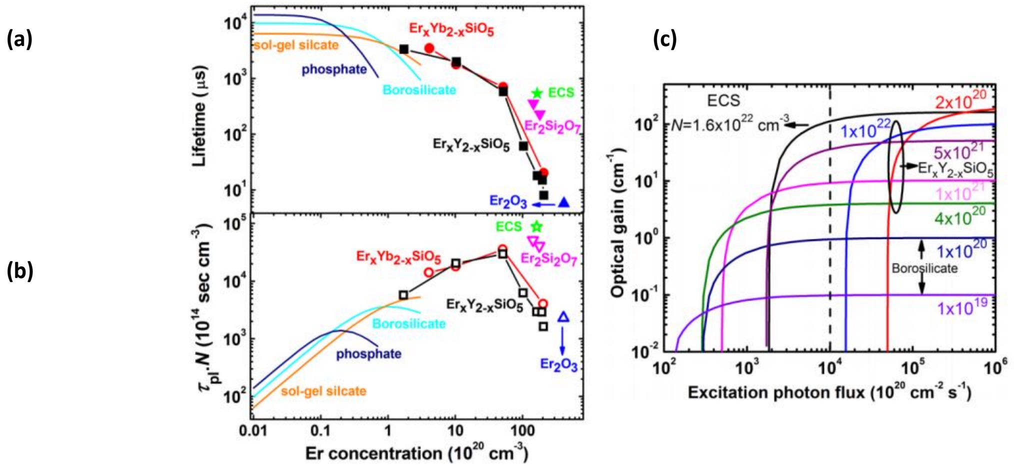

Figure 3.2 Lifetime **(a)** and lifetime-density product (LDP) **(b)** comparison of different ***Er***–doped materials. (c) Pump dependent optical gain of different erbium materials, where lifetime and density information are the same as in (a,b). [199]

In the viewpoint of applications, Erbium-based amplifiers could be integrated in/on silicon through CMOS-compatible processes, enabling several key applications in silicon photonics. Er-amplifiers could be fully integrated with passive structures to compensate their losses (a displayed in Figure.3.3).

By optical pumping, Erbium lasers could realize on-chip light sources in hybrid chips, sending light into Si_3N_4 or Si waveguides and circuits, feeding complex photonic circuits made of optical modulators and Ge detectors, as envisioned in Figure 3.3.b [200]. In this context, silicon photonic circuits working in C&L bands could get rid of III-V integration and also could be realized through monolithic CMOS steps.

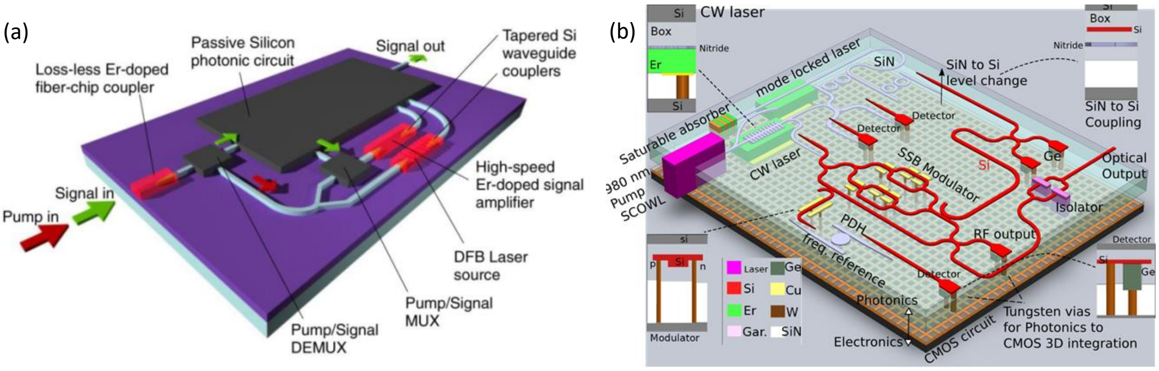

Figure 3.3 (a), Schematics of a SOI on-chip optical circuit including monolithically integrated Al_2O_3 layer [33]: Er^{3+} waveguide amplifiers and lasers (red sections); (b) Electronic-Photonic Hybrid Integration (*Erbium Silicon Photonic Integrated Oscillator EPHI*) [200].

In this context, this chapter reports our contribution towards light amplification by using Erbium materials and their integration in silicon photonics. It is composed of several parts: in section 3.2 and section 3.3, the fundamental spectroscopy of Er^{3+} and state of the art of Erbium doped materials are presented and analyzed. In section 3.4, we perform net gain simulations considering silicon/silicon nitride slot waveguides infiltrated with Erbium doped materials. In the later sections (3.5 &3.6), two different Erbium doped materials are investigated, followed by the investigation of hybrid integration of *Er* in slot waveguide devices.

3.2 Erbium ion (Er^{3+}) spectroscopy

3.2.1 1480 pumping regime

Trivalent rare-earth ions Er^{3+}, existing with oxidation states, are usually incorporated with host matrices. Compared with the neutral state $(Xe)4f^{12}6s^2$, oxidation state $(Xe)4f^{11}$ experiences localized electronic environment due to weakly bond $6s^2$ electrons and a $4f$ one are removed. After doping into a host matrix, different electronic transitions within 4f shells are allowed. The 7 lowest energies [201] of the Er^{3+} ion exist in 4f shell and start from $^4I_{15/2}$, $^4I_{13/2}$, $^4I_{11/2}$, $^4I_{9/2}$, $^4F_{9/2}$, $^4S_{3/2}$, $^2H_{11/2}$ to $^4F_{7/2}$ as partially depicted in Figure.3.4 & Table 3.1. The fundamental transition process of **(1),** $\boldsymbol{R_{12}}$**,** means ground state absorption of pump at λ=1480nm. The **(2)** process**,** $\boldsymbol{R_{21}}$**,** is the stimulated emission of the pump. For probe or signal, transitions **(3)** and **(4)** represent ground state absorption (W_{12}) and stimulated emission (W_{21}), respectively. These four transitions are the dominant ones to reach the population inversion for obtaining net gain of the signal due to energy transferred from the pump. **(5)** and **(6)** processes represent the non-radiative decays, $\boldsymbol{A_{43}}$ and $\boldsymbol{A_{32}}$**,** respectively. The spontaneous emission of signal is noted as transition **(7)**. The transition of **(8)** represents the excited state absorption of pump (ESA), which is a detrimental process in terms of amplification or lasing leading to higher pump absorption by the material but lower signal emission. Transition **(9)** corresponds to an energy-transfer-upconversion (**ETU**) process between two ions, square population dependent ($\boldsymbol{N_2^2}$), which reduces the number of ions with state of $^4I_{13/2}$ denoted as N_2 that is available for stimulated emission of the signal. Therefore, **ETU** transition significantly influences the gain properties of the Er^{3+} doped materials and should be reduced especially for high Er^{3+} ion concentrations [202]. The last transition is the cross-relaxation process, C_{14} **(10)**. All the transitions are also summarized in Table.3.1.

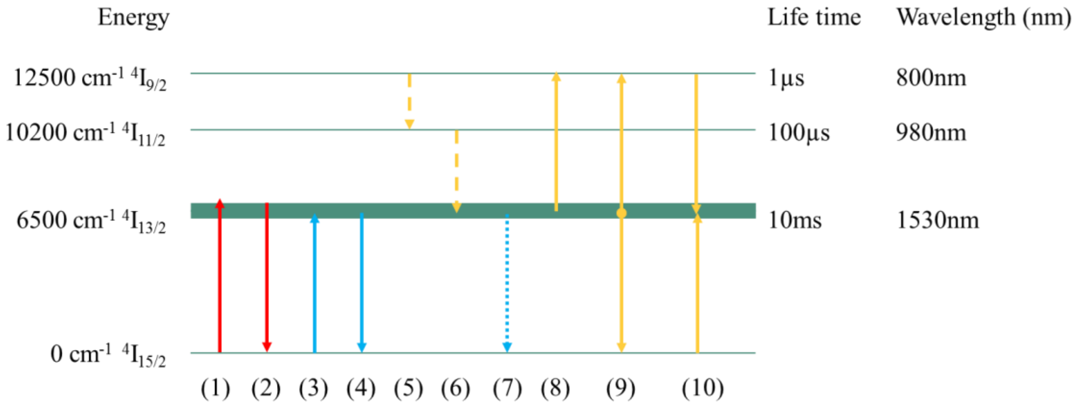

Figure 3.4 Schematic energy levels of Er3+ ions and transitions that happen for a 1480nm wavelength optical pumping scheme.

Table 3.1 Energy transitions during 1480nm optical pumping

Process	Symbol	Physics
(1)	R_{12}	Ground state absorption of Pump
(2)	R_{21}	Stimulated emission of Pump
(3)	W_{12}	Ground state absorption of Signal
(4)	W_{21}	Stimulated emission of Signal
(5)	A_{43}	Nonradiative decays
(6)	A_{32}	Nonradiative decays
(7)	A_{21}	Spontaneous emission of signal
(8)	R_{ESA}	Excited state absorption of Pump
(9)	C_{up}	Energy transfer upconversion between two ions
(10)	C_{14}	cross-relaxation process

3.2.2 980 pumping regime

The transitions between energy levels under a 980nm laser pumping are illustrated in Figure.3.5. To enhance the Er^{3+} pumping rate and provide higher gain, co-doping with Yb^{3+} ions is frequently chosen. The excitation of the Er^{3+} ions can be achieved both through transition processes **(6)** or **(4)→(5)**, which represent Er^{3+} ground state absorption of 980nm and energy transfer from an excited state ion Yb^{3+} at energy level of $^2F_{5/2}$ to a ground state Er^{3+} ion, respectively. **(4)→(5)** process significantly improves the pumping efficiency and improves the gain properties. **(1)** and **(2)** processes are the absorption and emission of the pump. Spontaneous emission in Yb^{3+} has been denoted as **(3)**. Transitions from **(7)** to **(12)** have been already explained in the 1480 pumping regime. All the processes are also listed in Table.3.2.

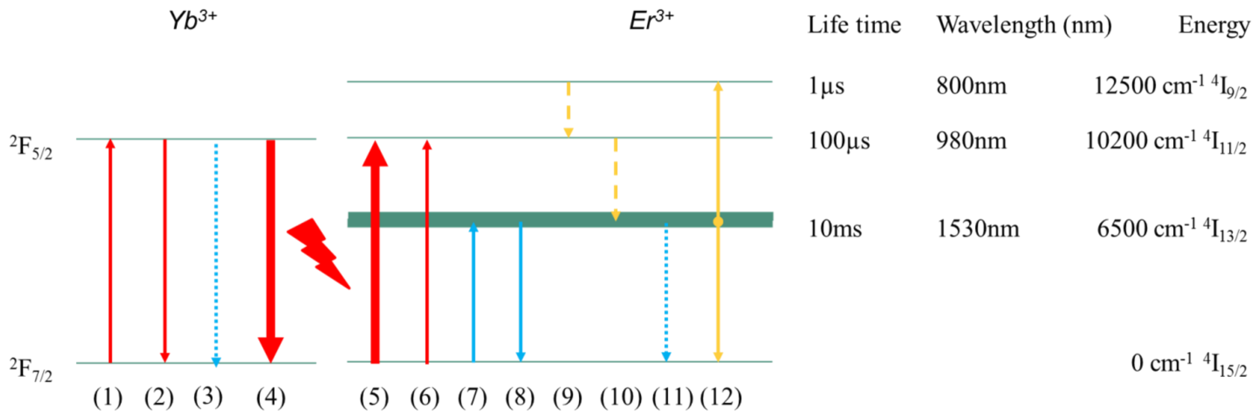

Figure 3.5 Schematic energy levels of Er3+ ions and transitions that happen during 980nm wavelength optical pumping.

Table 3.2 Energy transitions during 980nm optical pumping

Process	Symbol	Physics
(1)	W_{65}	Ground state absorption of Pump, Yb^{3+}
(2)	W_{56}	Stimulated emission of Pump, Yb^{3+}
(3)	A_{65}	Spontaneous emission of signal, Yb^{3+}
(4)→**(5)**	C_{16}	Yb3+ and Er3+ co-operative energy transfer
(6)	W_{13}	Ground state absorption of Pump, Er^{3+}
(7)	W_{12}	Ground state absorption of Signal, Er^{3+}
(8)	W_{21}	Stimulated emission of Signal, Er^{3+}
(9)	A_{43}	Nonradiative decays
(10)	A_{32}	Nonradiative decays
(11)	A_{21}	Spontaneous emission of signal
(12)	C_{up}	Energy transfer upconversion between two ions

3.3 State of the art of integrated Erbium hybrid waveguide amplifier

To demonstrate the gain properties of Erbium hybrid waveguides, Er^{3+} materials have been usually processed as the core or cladding materials of optical waveguides. Generally, the larger the optical mode overlap with Erbium layers was, the larger the achievable gain could be observed [83], [203], as the related modal gain (g_{mod}) of the waveguide can be written as $g_{mod}=\Gamma g_{Bulk}$,, where Γ is the guided mode fractional overlap with gain material region and g_{Bulk} is material gain coefficient.

Up to now, Er^{3+} doped different types of glasses or oxides have been demonstrated as an insufficient approach to obtain large gain in compact/short waveguides due to the restriction of low doping concentrations (Table.3 in ref [201]) in the past decades. For instance, with an Er^{3+} density around 10^{20}cm^{-3}, a maximum gain of 20dB was reported for Erbium doped Al_2O_3 waveguides with 13cm length [109], which is too long for integrated photonic circuits. Therefore, pursuing high net gain in short integrated waveguides is welcome and demanded for hybrid Er-silicon photonics. The solutions and fundamental understanding of net gain achieved from Erbium can be analyzed through the following points.

The stimulated emission contribution of the Erbium ions can be simplified and described by a Lamber-Beer Law to analyze the absorption and emission of the light as a two level system [201]:

$$I(z+\Delta z)=I(z)exp[\sigma_{em}(\lambda)N_2(z)\Delta z-\sigma_{abs}(\lambda)N_1(z)\Delta z] \quad (3\text{-}1)$$

Equation 3-1 describes the light intensity change over propagation distance Δz, $\sigma_{em}(\lambda)$ and $\sigma_{abs}(\lambda)$ represent the emission cross section and absorption cross section, N_2 and N_1 stand for the population density of high ($^4I_{13/2}$) and low ($^4I_{15/2}$) energy levels of Erbium ion states. The population inversion related optical gain $G(\lambda)$ can be directly linked to emission and absorption cross sections as [204]:

$$G(\lambda)=P\sigma_{em}(\lambda)-(1-P)\sigma_{abs}(\lambda) \quad (3\text{-}2)$$

where P means the population fraction of the upper energy levels. Assuming that the total Erbium ions density is N_{Er}, then $N_2=N_{Er}*P$ and $N_2=N_{Er}*(1-P)$. Equation 3-3 combines equation 3-2 and equation 3-1 as follows:

$$I(z+\Delta z)=I(z)exp[N_{Er}G(\lambda)\Delta z] \quad (3\text{-}3)$$

By equation 3-3, it can be seen that to pursue high net gain in hybrid silicon photonic devices, high bulk optical gain coefficient $g_{Bulk}= N_{Er}*G(\lambda)$ is needed to compensate losses of photonic devices, which indicates that: (1), high Erbium concentration N_{Er} is required; (2), a minimum P is required to reach population inversion [204]. Large optical gain $G(\lambda)$ is determined by Er^{3+}spectroscopic parameters considering that, in fact, Erbium spectroscopy cannot be described as a pure two level system as shown in section 3.2.1 & 3.2.2. PL lifetimes, energy transfer upconversion between two excited ions, fast quenching process [202], etc, are all among microscopic parameters influencing the final achievable gain, as discussed in the following sections.

3.3.1 Effects of Erbium concentration & lifetime of $^4I_{13/2}$

To easily reach population inversion, a relatively long lifetime of the Er^{3+}excited state ($^4I_{13/2}$) is required. Fortunately, the lifetime of energy level $^4I_{13/2}$ is usually of the order of *ms, w*hile N_{Er} density is around $10^{20}cm^{-3}$. The related optical net gain has been restricted down to several dB/cm as shown in Table 3.3, according to the state of art of erbium hybrid photonic waveguides/nanowires, for the cases of glass and oxide host materials.

When trying to increase the doping level of $N_{Er},$ the distances between the every nearby Er^{3+} are shortened, which enhances the energy transfer upconversion mechanism (ETU or cooperative upconversion) and Erbium ion quenching [109] [202]. Host matrix supporting high erbium concentration was firstly demonstrated in erbium silicate with stoichiometric nature and crystalline structure, leading to huge PL emission and sustaining lifetime above 500μs [205]. Later, ECS with same order of N_{Er} ($10^{22}cm^{-2}$) and lifetime above 540μs was also demonstrated, with optical net gain above 30dB/cm [194]. A further step of improving optical gain was achieved by co-doping techniques with yttrium (Y) ions and ytterbium (Yb) ions into the erbium silicates to balance the N_{Er} and ETU quenching processes. For instance, EYCS (erbium yttrium chloride silicate), $((Er_xY_{1-x})_3(SiO_4)_2Cl))$, single crystal nanowires were optimized with $x = 0.3$ to emit the strongest PL and achieve optical gain close to 100dB/cm [195].

3.3.2 Effects of energy transfer upconversion (ETU) between two ions

Photoluminescence (PL) intensity of erbium can be expressed as $I_{PL} \propto N_{Er}\tau_{PL}/\tau_r$ [199], which explains why increasing N_{Er} can lead to large optical gain for a constant τ_{PL}-(PL life time)/τ_r -(radiative lifetime) ratio. As pointed out above, the main important detrimental transitions inhibiting even larger optical gain are related to energy transfer processes between Er ions. The first energy interaction between two ions is that an excited ion ($^4I_{13/2}$) transfers its energy to a nearby ground state ion ($^4I_{15/2}$), which increases the losses of excitation energy during diffusion and results in a number of ions at quenching states with impurities, such as OH^-. A proper annealing process could remove these impurities to improve Er lifetime [205]. The second dominant detrimental transition is the upconversion between two ions, in which an excited ion ($^4I_{13/2}$) gives its energy to another excited ion ($^4I_{13/2}$) and excites it to higher energy level ($^4I_{19/2}$). Therefore, a significant depopulation of the ions state ($^4I_{13/2}$) happens and reduces gain or breaks the population inversion. Thus, in order to ease the energy transfer among ions, a homogeneous distribution of the Er^{3+} is needed. The upconversion rate (R_{ETU}) is determined by the population density of $^4I_{13/2}$ and ETU rate per unit volume (W_{ETU}) ($cm^{-3}s^{-1}$), as shown in equation 3-4. Higher order (second order) ETU processes have been also measured and proved to be dependent on square power P^2 (λ~1.53µm) [197] (see equation 3-5). This effect is very strong when choosing a pump wavelength of 1.48µm, which further enhances 2nd order ETU and excited state absorption. All these detrimental processes result in pumping power with an upper limit P_{pump}^{Max}. Considering the effective pumping length that was described in Chapter-1 as $l_{eff} = (1 - e^{-\alpha_l L})/\alpha_l$ [206], the typical effective length L_{eff} for high N_{Er} is limited down to 440µm-9mm, when assuming that the total pump wavelength propagation losses α_l (including absorption α_{abs}) are in the 1-100dB/cm range and with a waveguide length L *of* 10mm. This simple estimation shows that high N_{Er} hybrid integrated waveguides should have moderately short effective pumping lengths (typically ~2mm if the absorption losses are 20dB/cm).

$$R_{ETU} = W_{ETU} N_2^2 \qquad (3\text{-}4)$$

$$I \propto P^2 e^{-2\Gamma \alpha_l L} \qquad (3\text{-}5)$$

3.3.3 State of the art of erbium nano amplifiers

Table.3.3 shows the current state of the art of integrated amplifiers based non-crystalline (#) and crystalline (*) waveguide materials, respectively. As visible, net gain of photonic non-crystalline waveguides is limited to the range of 0.5-4 dB/cm, which is quite lower than the net gain values obtained for crystalline nanowires (typically above 50dB/cm). The reason for that is mainly due to the fact that Erbium is a major constituent of crystalline nanowires. Er concentration (~$10^{22}/cm^3$) is then around two orders higher than in doped non-crystalline materials and most of Er ions are moreover optically active due to well controlled growth fabrication processes [205]. To conclude, to obtain high net gain in integrated hybrid photonic Erbium waveguide based on non-crystalline materials, higher N_{Er} concentration materials presenting high net gain performances are highly welcome.

Table 3.3 State of the art of Erbium nano waveguides.
Refs denoted with #(*) are related to non-crystalline (crystalline) waveguides amplifiers

Concentration-Er $\times 10^{20}/cm^3$	Net Gain dB/cm	Max Gain dB	Efficiency mW/dB	Loss (dB/cm)	Pump @ nm	Pump Power(mW)	Host material	*L* *mm*	Ref
				non-crystalline/ low concentration Er^{3+}					
0.95	0.8	20	1.5	~0.19	980	30	Al_2O_3	244	[109]#
1.1	0.72	0.72	694	0.3	980	550	oxyfluoride silicate glass	10	[207]#
1.7	0.5	0.4	150	3.4	1480	60	Polycrystalline $Er_xY_{2-x}SiO_5$	10	[208]#
1.92	1.9	20	1.5	~0.19	980	30	Al_2O_3	129	[109]#
5.3	4.1	4.1	5.12	0.9	980	21	Phosphate glass	10	[112]#
				Crystalline/high concentration Er^{3+}					
36	30	1.5		130	980		*Silicate*	0.5	[113]*
50	100				980		*Chloride silicate*		[195]*
162	71	0.71	42	660	980	30	*Chloride silicate*	0.11	[197]*

3.4 Amplification simulation based on slot amplifier model

In a complementary fashion with the previous section which was focused on the properties and limitations of Er-active materials, we perform here device simulations aiming at evaluating the gain properties of slotted waveguides filled with state-of-the art Er-active materials. More precisely, this section introduces numerical simulations of the optical gain in hybrid slot waveguides, which are embedded with Erbium doped materials. Two pumping regimes are considered by using 1480nm laser or 980nm laser (considering Yb^{3+} co-doping) pumping schemes. The detailed analytical models of the two kinds of simulations are reported in *appendix*.

3.4.1 1480 pumping regime

The potential net gain of Hybrid Erbium-Silicon Waveguide Amplifier (HESWA) considering Erbium-doped low refractive index materials integrated into silicon/silicon nitride slot waveguides has been investigated. The gain performance of HESWA has been investigated by using a four level spectroscopic model (see Appendix A), which is able to predict the required optimal waveguide length and pumping power to obtain the maximum net gain of filled slot waveguides. In this purpose, cross-section properties of slot waveguides filled by Erbium-doped materials have been considered (see Figure.3.6). The study was based on the calculation of the HESWA optical gain properties as a function of W_{slot} (slot waveguide width) by following the evolution along the propagation direction (z) of the pump and signal powers (see Figure.3.10). Linear propagation losses from 3dB/cm to 10dB/cm have been considered in order to investigate loss limitation to the net gain.

The considered cross-sections of typical single-mode Si and SiN slot waveguides for λ~1.55μm are depicted in Figure.3.6. Only TE modes have been considered. For silicon slot waveguides, thickness of 220nm and rail width of 220nm are considered and fixed. For silicon nitride (SiN), 400nm rail width and a 400nm SiN layer thickness waveguides were considered. By sweeping the slot size from 50nm to 250nm, the effective mode indices of slot waveguides decrease in the two waveguide family cases due to the increase of light confinement outside the core material (see Figure.3.7). The optimal energy confinements in the low refractive index (RI) Er^{3+} cladding are similar for the silicon and silicon nitride waveguides. The maximum cladding dielectric energies for both of them reach 50% for signal and 47% for pump, respectively (see Figure.3.8). The main difference between the two cases in term of energy confinement is related to the portion of light that is confined in the slot region only. The dielectric energy confined in silicon slot waveguides is generally above 20%, which is much higher than for silicon nitride slot waveguides that present a maximum of around 14% (see Figure.3.9).

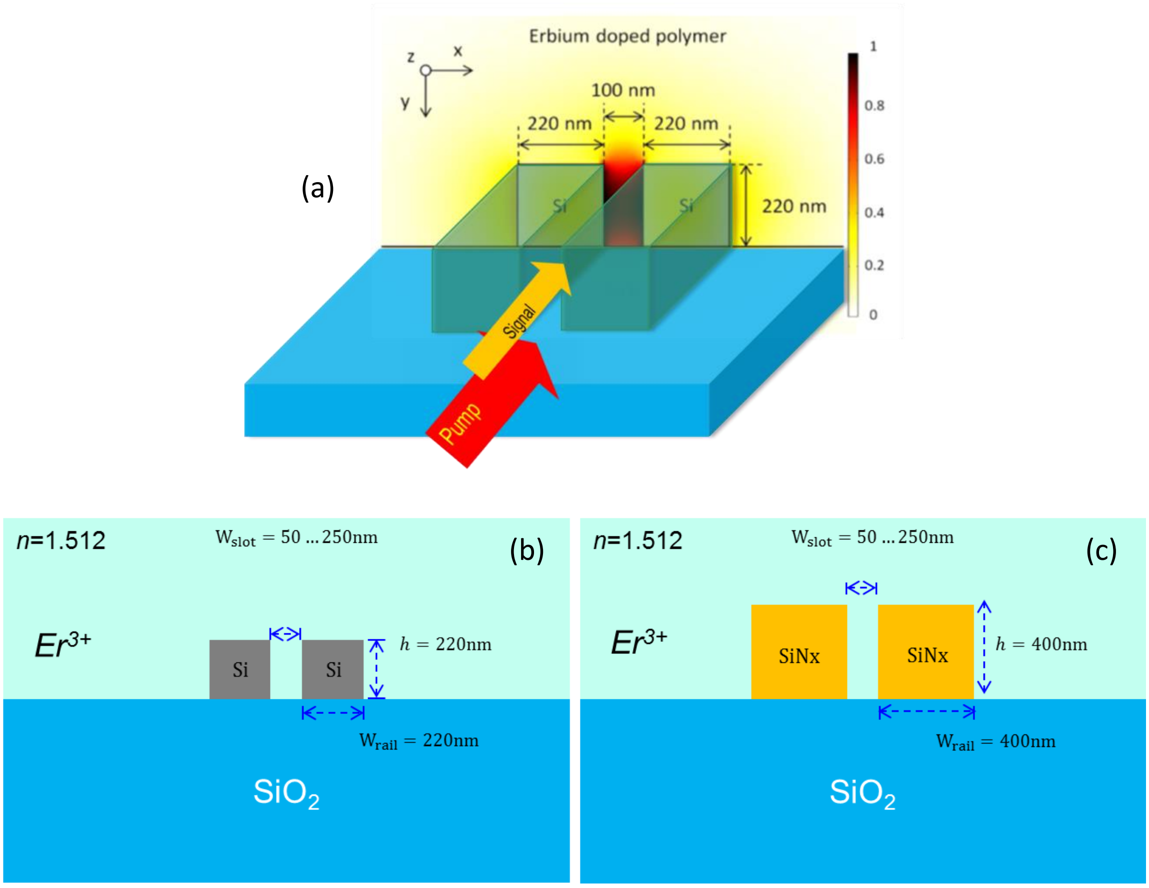

Figure 3.6: (a) Normalized electric field energy of the cross section of silicon slot waveguides filled by Er^{3+}-doped materials for 1530 nm wavelength signal amplification. The slot waveguide cross-sections are considered with different slot sizes both for the silicon (b) and silicon nitride (c) waveguide cases.

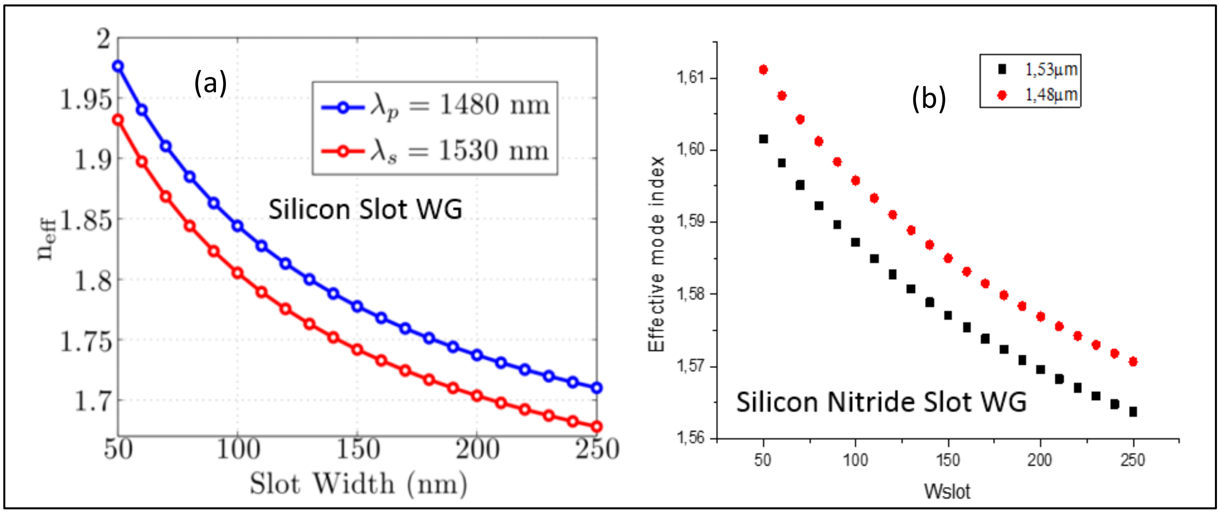

Figure 3.7 Mode effective index as a function of the slot width where the waveguides remain TE monomode.

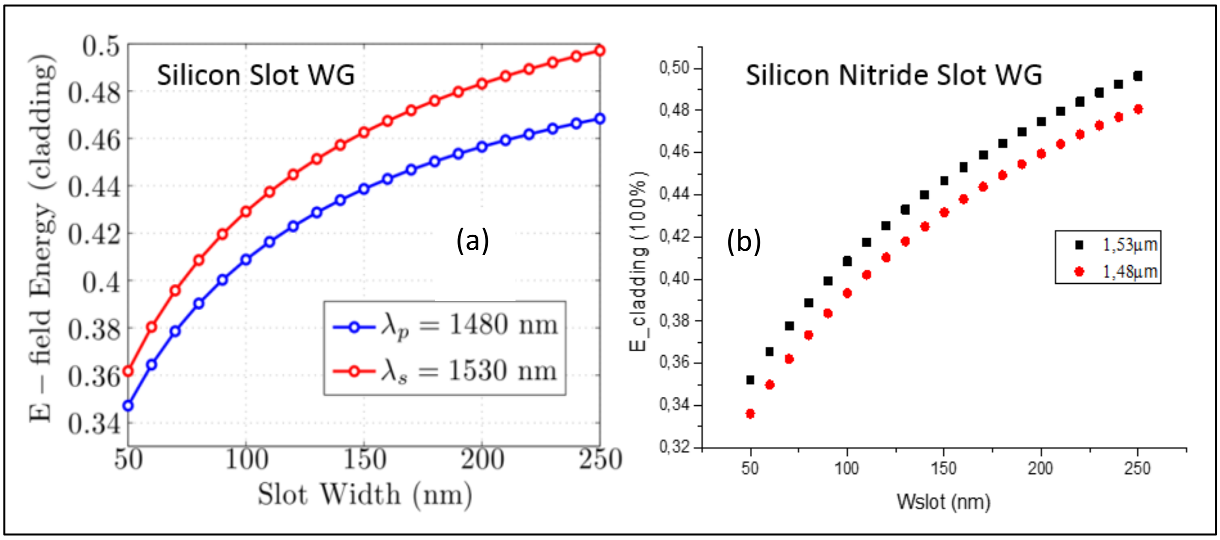

Figure 3.8 Fraction of electric field energy $\int n^2|E|^2dA$ in the whole erbium polymer cladding region

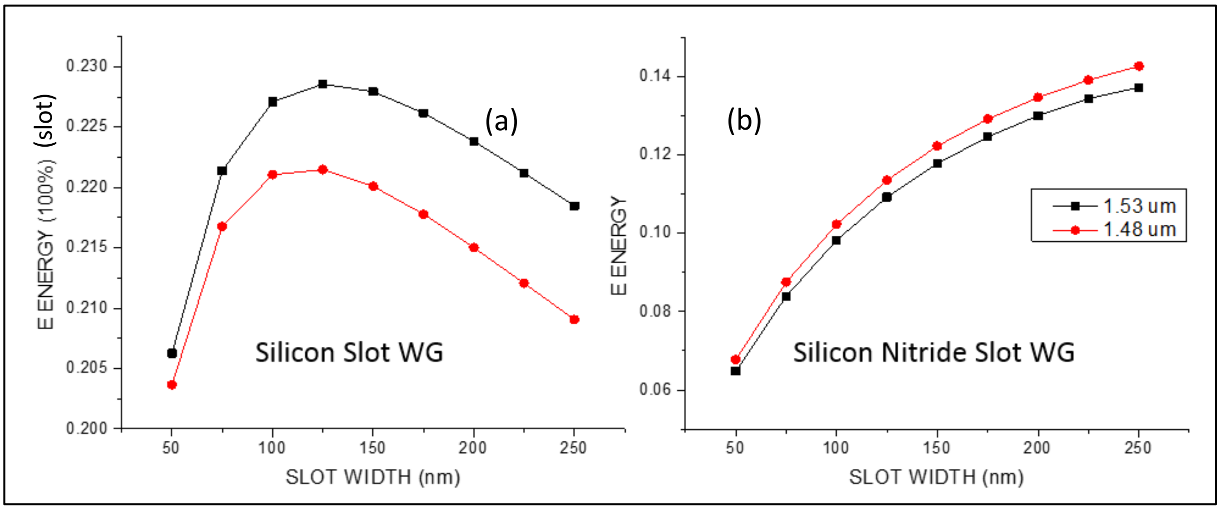

Figure 3.9 Fraction of electric field energy $\int n^2|E|^2dA$ in the Erbium polymer cladding region (slot only).

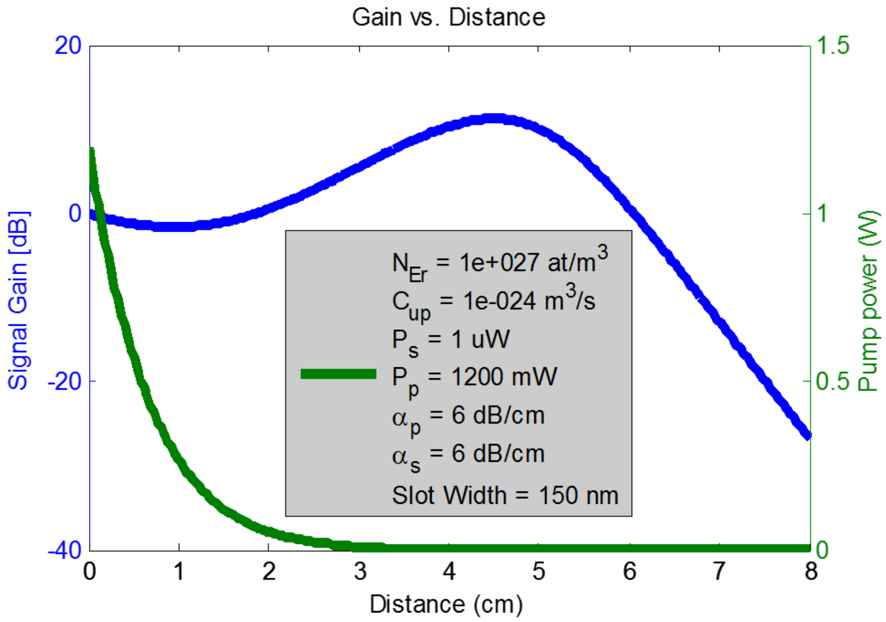

Figure 3.10 As a matter of illustration, we show here the signal and pump power evolutions along the propagation distance (z) in the case of a silicon slot waveguide filled with an Erbium oxide (see Fig. 3.6 (b)).

For the simulation of the light amplification process in the hybrid slot waveguides, we considered a moderate Er^{3+} concentration of 1×10^{21}/cm^3. The other spectroscopic parameters were chosen among the typical values according to reported state of the art (Appendix-A). An input signal power P_S=1µW was considered throughout our simulations. As a matter of illustration, the signal and pump power evolution along the propagation distance are shown in Figure.3.10 for one specific case. The maximum pumping power can be extracted through the propagation distance position where a positive gain is obtained, as shown in Figure3.10. When the pumping power is higher than the optimal value, the gain is inhibited by the excited state absorption & ETU processes. The optimal length of the waveguides can be also obtained at the position where the net gain begins to drop down. Generalizing this approach for the two waveguide families, maximum gain, optimal pumping power and waveguide length have been obtained and are summarized in Figure 3.11, Figure.3.12 and Figure.3.13 according to different scenario in term of propagation losses.

By comparing the summarized results, the first conclusion that can be made is that a moderate slot size (150nm-200nm) is welcome and enough to achieve a maximum net gain. The maximum net gain saturates when slot size goes up to 200nm or does not increase beyond (see Figure.3.11). Typically, a maximum gain around 30dB can be obtained both for silicon and silicon nitride slot waveguides when the propagation losses are set at 3dB/cm both for signal and pump. Optimal net gain shows a linearly decrease when the propagation losses (with dB/cm units) increase up to 10dB/cm, with which the net gain is then only around 2dB. **Therefore, the linear propagation losses strongly influence the achievable net gain and should be minimized as possible experimentally**.

The difference between the two waveguide core/cladding contrasts for the silicon (n_0~3.46) and silicon nitride (n_0~1.99) waveguides finally results in different needed optical pumping powers. As silicon nitride waveguides have a lower index contrast than Si ones, optical modes are distributed over larger waveguide cross-sections in SiN waveguides. To efficiently pump Erbium ions, silicon nitride slot waveguides thus require larger powers than silicon ones, as shown in Figure 3.12. Generally, silicon nitride slot waveguides require about 4-time larger power than silicon slot waveguides to reach the maximum net gain. Meanwhile, the optimal waveguide length for reaching maximum net gain are similar in the two cases (see Figure.3.13), around few centimeters.

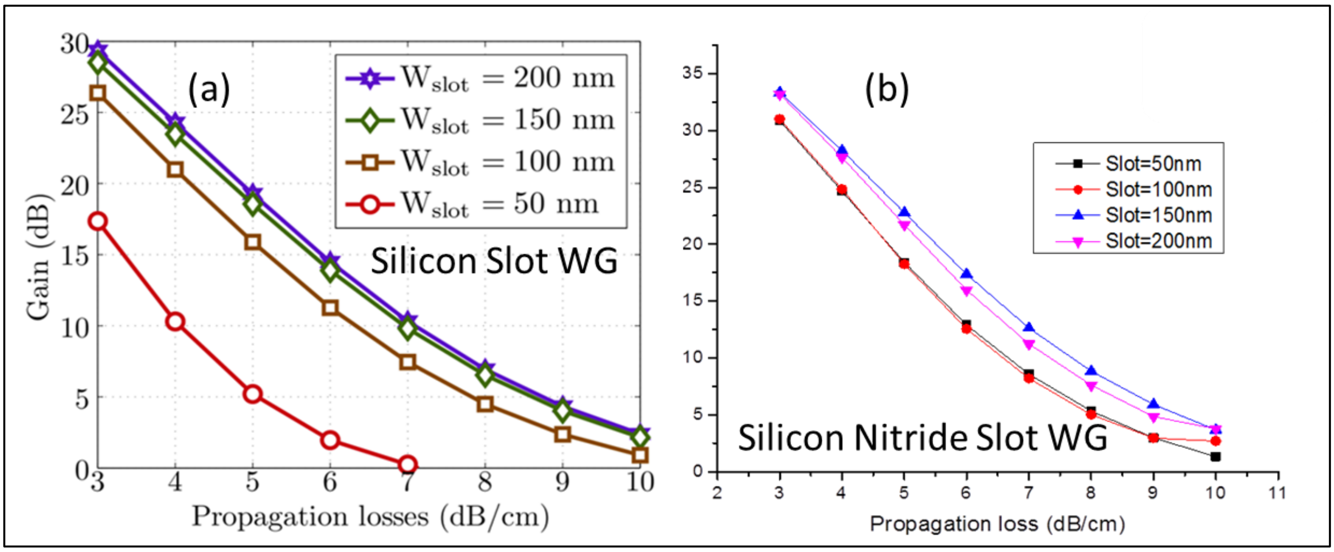

Figure 3.11 Achievable *optimum gain* vs. propagation losses from 3dB/cm to 10 dB/cm for different slot widths of (a) silicon slot waveguide and (b) silicon nitride slot waveguides.

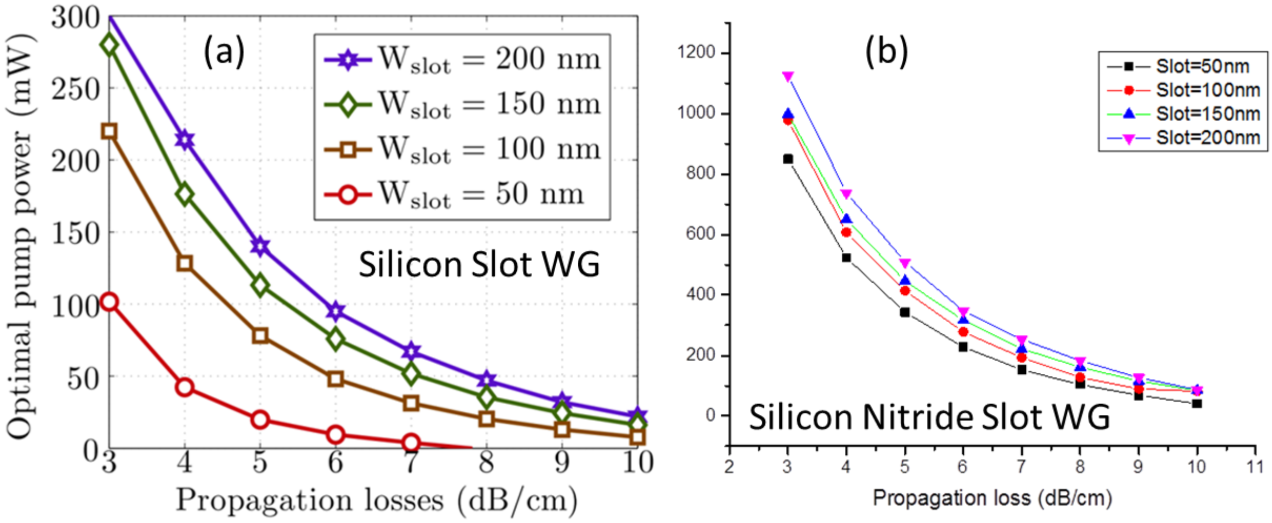

Figure 3.12 The *optimal pump power* coupled into the slot waveguides to achieve the maximum gain at different propagation loss levels from 3dB/cm to 10 dB/cm for different slot widths of (a) silicon slot waveguides and (b) silicon nitride slot waveguides.

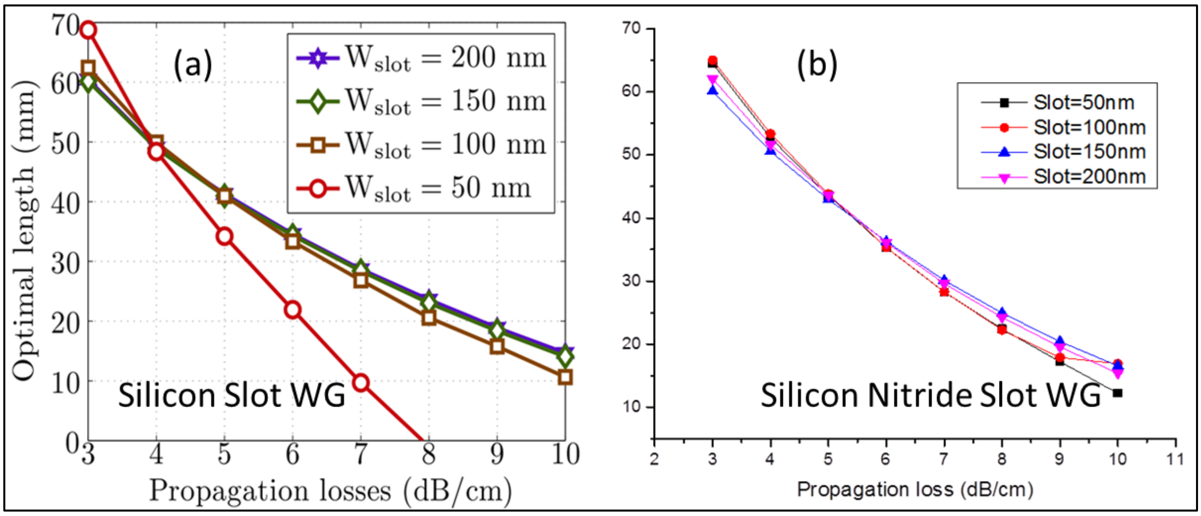

Figure 3.13 The *optimal waveguide length* to achieve the maximum gain at different propagation loss levels from 3dB/cm to 10 dB/cm for different slot widths of (a) silicon slot waveguides and (b) silicon nitride slot waveguides.

3.4.2 980 pumped regime

To study Yb^{3+} co-doped Erbium material integration in slot photonic waveguides, we propose here to use double slot silicon nitride waveguides, for which both the signal and pump wavelengths are single mode and experience a local electric field enhancement in the low index erbium region as shown in Figure 3.14. Besides, silicon nitride platform is preferred due to negligible absorption of 980nm light pump while silicon absorbs 980nm light beams. In order to achieve slot mode for the pump, slot width cannot be set too large and a possible option is considering two single slots with 100nm width each. The middle rail can be fixed at 100nm and two lateral rail widths in the 150nm-250nm range. A thickness of silicon nitride 400nm is considered again here and cladding is supposed to be a Er^{3+}/Yb^{3+} doped polymer with refractive index of 1.512.

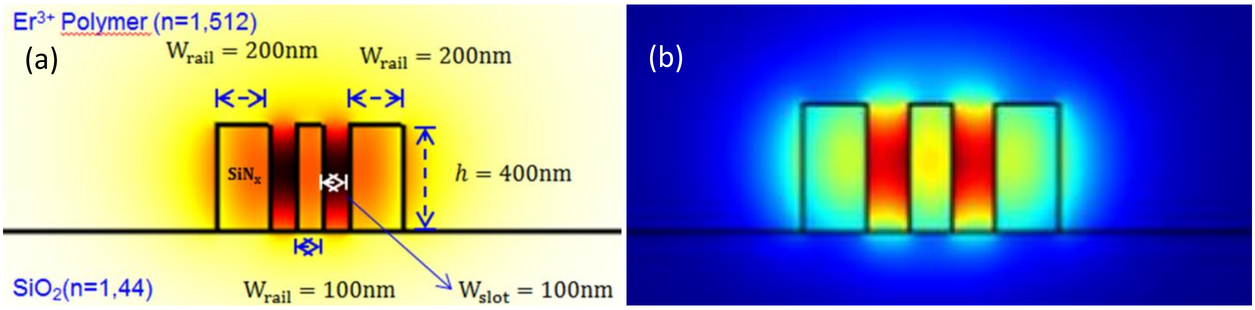

Figure 3.14 Double slot silicon nitride waveguides, for which both pump (980nm) and signal (1530nm) are single mode. Figure (a) shows the TE signal mode (980nm) and (b) shows the TE pump one (980nm).

To simulate the propagation gain inside double slot waveguides, we consider here a moderate Er^{3+} concentration of 1~11×10^{20}/cm^3 and Yb^{3+}/Er^{3+} ion doping ratio of 1:1 to 12.5:1. The total length of the waveguide is 2cm and propagation losses are considered from 2 to 10dB/cm to describe different possible quality realizations. The simulation model is based on solving the population rate equations of the spectroscopic model illustrated in Figure.3.5 and the detailed information that can be found in Appendix B. The simulation methods and approaches are similar to those of previous section. Here, we summarize two kinds of simulation results related to Yb^{3+}/Er^{3+} ion doping ratio effects and net gain limitations due to propagation loss and Erbium concentration.

The effect of Yb^{3+}/Er^{3+} ion doping ratio is shown in Figure.3.15. The propagation loss is assumed here to be 5dB/cm and Erbium concentration is fixed to $7\times10^{20}/cm^3$. It is visible that by increasing the Yb^{3+} concentration, the pumping efficiency is growing very fast and that a small pumping power of 10mW is enough to reach maximum net gain for the case of Yb^{3+}/Er^{3+}=12.5:1, which requires around 10 times less pumping power than for the case of Yb^{3+}/Er^{3+}=1:1. The reachable maximum net gain is almost the same for the different ion ratios. To sum up, this simulation result supports that Yb^{3+} co-doping method could improve the pumping efficiency significantly, thus leading to dramatically reduced pumping power.

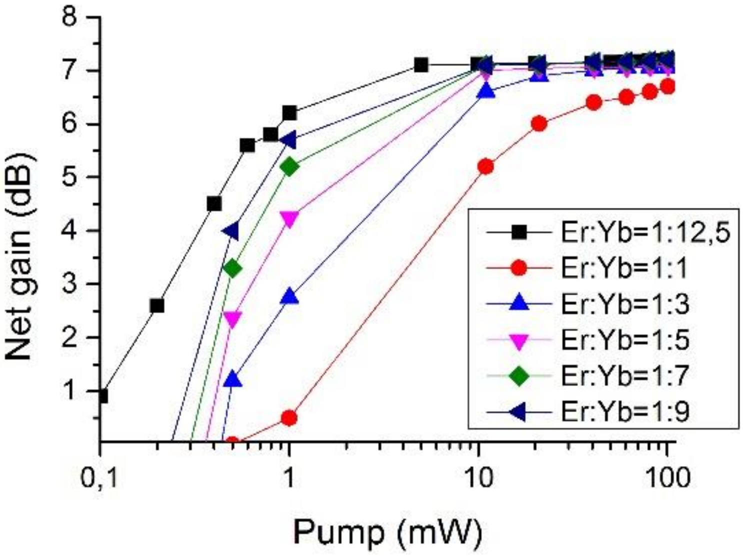

Figure 3.15 Simulated net gain as function of the pumping power in the slot waveguide scheme shown in Figure.3.13. The length of the hybrid waveguide is 2cm.

Estimations of net gain as a function of propagation loss and Erbium concentration have also been simulated and are summarized in Figure.3.16. In order to realize net gain, Erbium concentration should be larger than $1\times10^{20}/cm^3$, the maximum net gain linearly scales when increasing the Erbium concentration or reducing the propagation losses**. Nearly one order of increase of the Erbium concentration from $1\times10^{20}/cm^3$ to $11\times10^{20}/cm^3$ results in 25dB net gain difference**. Moreover, **waveguide losses below 10dB/cm are still compatible to realize net gain**.

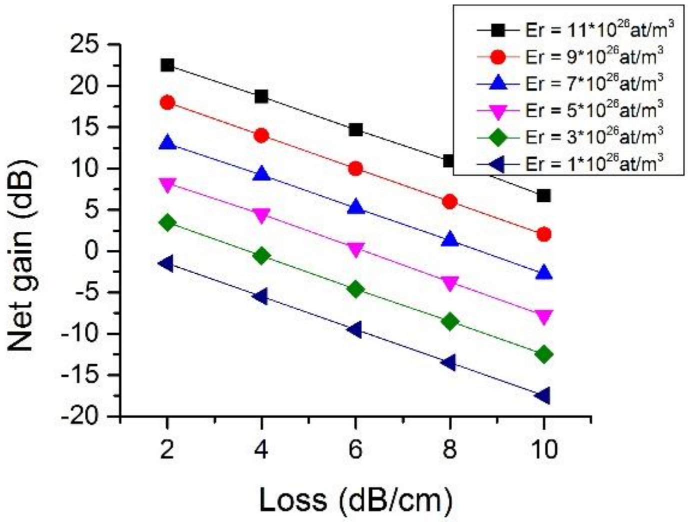

Figure 3.16 Maximum net gain as function of the propagation losses of both signal and pump. Erbium concentration is swept from $1\times10^{20}/\mathrm{cm}^3$ to $11\times10^{26}/\mathrm{m}^3$($Yb^{3+}/Er^{3+}$=12.5:1). The length of the hybrid waveguide is 2cm.

3.4.3 Conclusion

To conclude, all these simulations indicate that reachable net gain in slot waveguides is restricted to the order of ~1dB/mm, which is acceptable for compact integration. Waveguide losses of the order of 2dB/cm and Erbium ion concentration on the order of $1\times10^{21}/\mathrm{cm}^3$ are realistically aggressive values in this purpose. Considering the fabrication results presented in chapter-2 that reported Si and silicon nitride slot waveguides losses around 2-7dB/cm, experimental investigation of integrated net gain can be envisioned. In the later sections, we report our efforts in this direction.

3.5 Er-doped nanocomposite integration with silicon nitride slot waveguides

In this section, we will introduce the integration of the Er^{3+}/Yb^{3+} co-doped nano particles (NPs) covalent-linked with **Poly(methyl methacrylate)** (PMMA) (denoted as **PMMA-NPs: Er^{3+}/Yb^{3+}**), into silicon nitride slot waveguides.

Silicon nitride slot waveguides are preferred considering that: (1) measured linear scattering losses are lower than for silicon slot waveguides when they have very long spiral paths; (2) silicon nitride slot waveguides have larger slots (width and height) envisioned to be more easily filled with nanoparticles; (3) silicon nitride waveguides do not absorb the 980nm laser pump which is used to pump Yb^{3+} co-doped Erbium nanocomposites.

In this section, we first introduce the synthesized core-shell **NPs: Er^{3+}/Yb^{3+}** nanoparticles, which finally were covalent-linked with **Poly(methyl methacrylate)** (PMMA) as Erbium nanocomposite. Polymer waveguides consisted of this new erbium nanocomposite were fabricated and their linear losses, optical gain properties were characterized. The integration of this nanocomposite as the top cladding of the silicon nitride waveguides has been investigated and analyzed regarding to the optical losses and gain properties.

3.5.1 Properties of PMMA-NPs: Er^{3+}/Yb^{3+}

PMMA-NPs: Er^{3+}/Yb^{3+} were synthesized in the State Key Laboratory on Integrated Optoelectronics, College of Electronic Science and Engineering, Jilin University, Changchun, China, in the scheme of a collaboration within a ANR/NSFC project during my PhD studies (projet ANR blanc international 2013-2016: POSISLOT, in collaboration with NSFC/China).

The active Erbium nanoparticles (**NPs: Er^{3+}/Yb^{3+}**), NaYF4/NaLuF4: Yb3+, Er3+ coated with oleic acid (**OA**), were synthesized using a high-temperature thermal decomposition approach. Next, these NaYF4/ NaLuF4: Er, Yb **NPs** were copolymerized with methyl methacrylate (MMA) to synthesize **PMMA-NPs: Er^{3+}/Yb^{3+}**, which is schematically shown in Figure.3.17. In these chemical synthesis process, inorganic NPs are mixed with hydrophobic OA as capping ligands and all reagents in the copolymerization process of NPs and MMA are hydrophobic, which finally suppresses quenching effects due to rare –OH groups. As it is not based on a physical doping technique, this novel material has higher concentration of dopant and its performance is more stable. Two aspects of the research have been done to improve the properties of the polymer based waveguide amplifier.

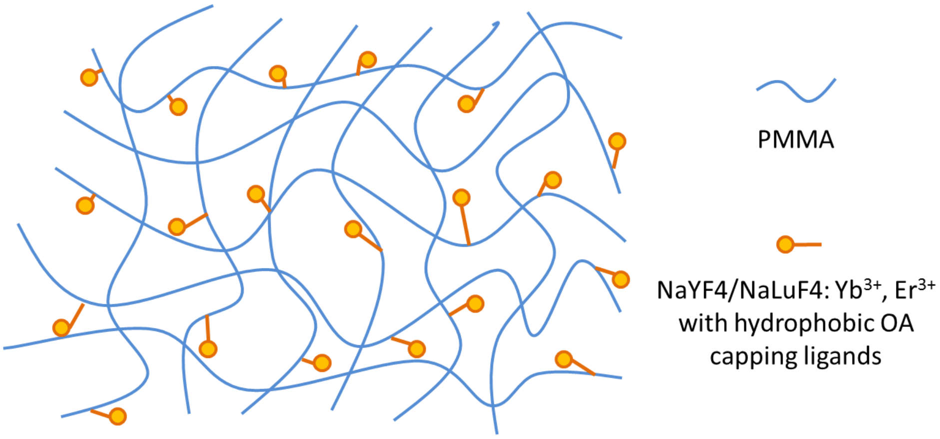

Figure 3.17 Schematic nanocomposite structure PMMA-NPs: Er^{3+}/Yb^{3+}

First, core-shell structures of $NaYF_4/NaLuF_4$:Yb/Er **NPs** were constructed to improve the luminescence properties at λ=1540 nm. Treating the heterogeneous cubic phase (α) $NaYF_4$ NPs as core, the $NaYF_4/NaLuF_4$: Yb/Er core-shell NPs were synthesized via a mild hydrothermal method in a water-ethanol-oleic acid mixture solvent system. Compared with the pure hexagonal phase (β) $NaLuF_4$:Yb/Er **NPs** with similar size [75], the core-shell α-$NaYF_4$/β-$NaLuF_4$:Yb/Er **NPs** exhibit high luminescence intensity at λ=1540 nm band under 980nm-wavelength excitation. As shown in Figure.3.18, the core **NPs** are obtained with average size around 10nm and the total core shell NPs have an average size of 20nm. The root mean square roughness of the nanocomposite film is as small as 0.45nm (characterized by AFM), as shown in Figure.3.18.c&d.

Second, the gain media was synthesized by copolymerizing methylmethacrylate (MMA) monomers with unsaturated organic ligand modified inorganic nanoparticles (NPs) to form nanocomposites. These Er^{3+} and Yb^{3+} codoped **NPs** were well dispersed and stably linked to the organic PMMA matrix via the strong covalent bond. Therefore, both the dispersibility of the **NPs** in polymer matrix and the stability of the nanocomposite were greatly improved, which eased low scattering loss and good stability of the gain media.

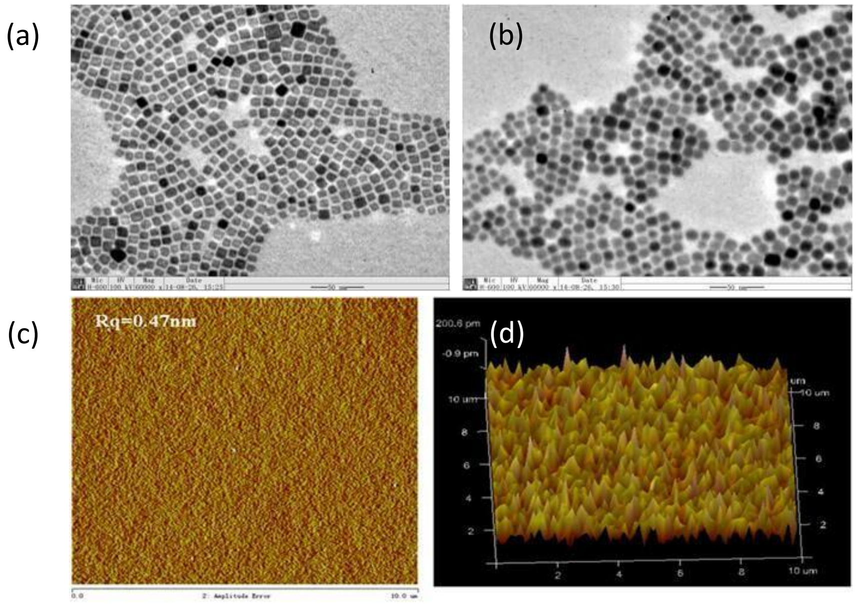

Figure 3.18 (a) Heterogeneous cubic phase (α) $NaYF_4$ NPs with average size10nm; (b) $NaYF_4/NaLuF_4$: Yb/Er core-shell NPs with average size 20nm; (c, d) AFM image of the thin film of **PMMA-NPs: Er^{3+}/Yb^{3+}** with root mean square roughness of 0.47 nm.

3.5.2 Erbium integration with silicon nitride slot waveguides

Infiltrating PMMA-NPs: Er^{3+}/Yb^{3+} into the slots was done by using the spin-coating method. After spin-coating, the device was baked at 100°C for 3hours. The first issue of slot waveguides hybrid integration is the infiltration of tiny slots. As the average NPs size is 20nm and the slot size usually ranges between 100nm and 200nm, there was a large possibility to fully fill the slot considering that nanocomposites are dispersed in PMMA. We characterized cross sections of hybrid silicon nitride slot waveguides with different slot sizes of 120nm, 170nm and 220nm, respectively. Figure.3.19 depicts the related slot waveguide cross sections, showing that NPs composite are well infiltrated into nano-slots. Let notice that the zooms of the SEM figures are limited by the deformation of the PMMA due to over exposure under electron beam.

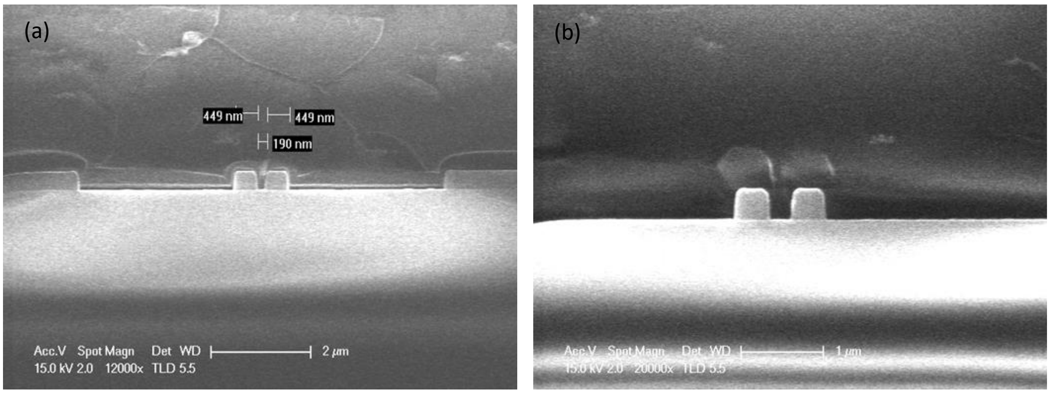

Figure 3.19 SEM characterization of the cross sections of the silicon nitride slot waveguides. (a) Small zoom of the slot waveguide cross-section with slot size around 170nm; (b) Large zoom of the infiltration of a 220nm slot waveguide. The color contrast and polymer infiltration are not stable from one image to the other due to electron beam exposure.

3.5.3 Losses of silicon nitride hybrid slot waveguides and polymer waveguides

As previously indicated, infiltration of nano-slot is possible. Another important investigation has then been to estimate the linear absorption of the prepared **active material (AM)** and the linear losses of the hybrid waveguide obtained after introducing this Erbium AM as the optical cladding of slotted waveguides.

The absorption of the erbium nanocomposite material was measured through the cut-back method for different lengths of straight polymer waveguides by our Chinese partner. The Erbium ion concentration was estimated to around $2.8\times10^{26}\mathrm{m}^{-3}$ and $\mathrm{Yb}^{3+}/\mathrm{Er}^{3+}$ ratio was 10. Erbium NPs doped PMMA waveguides with different lengths from 5mm to 35mm were fabricated [75] and characterized, as shown in Figure.3.20, resulting in waveguide losses α_{wg} around 5.3±0.3dB/cm at the wavelength of 1535nm. The calculated mode overlap factor Γ_{AM} was 84.8% and thus a maximum loss level due to erbium NPs intrinsic absorption was $\alpha_{abs} \approx \frac{\alpha_{wg}}{\Gamma_{AM}} = 6.25$ dB/cm (or 1.44/cm).

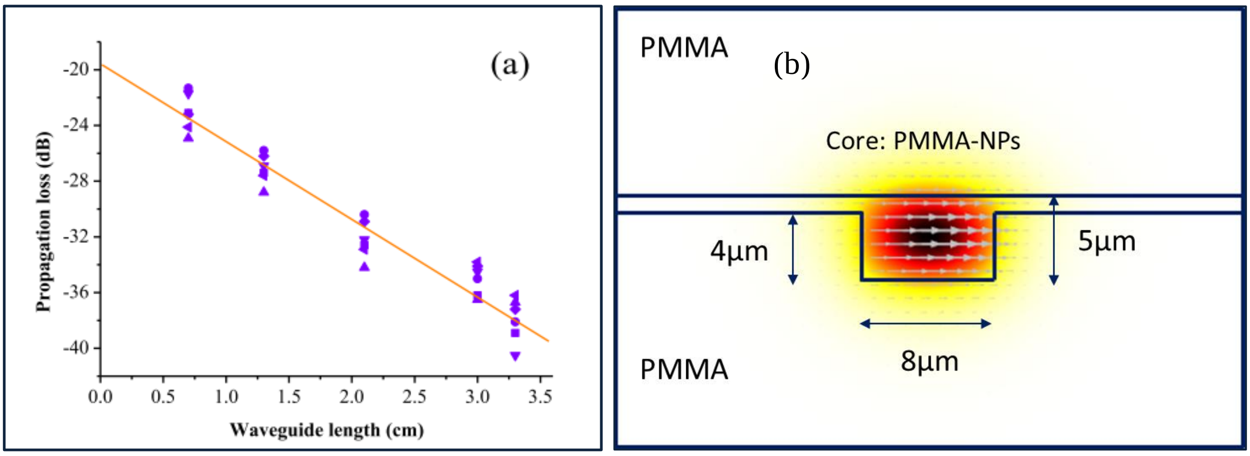

Figure 3.20 (a) Linear propagation losses as a function of waveguide length. The derivate loss level obtained from linear fitting is 5.3±0.3dB/cm at wavelength ~1535nm. (b) Waveguide geometry of the *Er* NPs PMMA waveguides and the electric field E_x confinement of TE mode at wavelength ~1535nm.

As shown in Figure.3.21, transmission losses of hybrid slot waveguides were found in the 7-12dB/cm range both for waveguides with slot width 120nm and 170nm, respectively. The possible integration defects, such as non-uniformities, partial non-infiltration of the slots and so on, require the optimization of the spin coating and baking methods. Experimentally, we have found that these additional defects from the integration of the cladding erbium polymer were always present to some extent in our samples. Transportations between China and France may also have contributed to additional defects. Consequently, we measured very different transmission levels for waveguides with different lengths, as shown in Figure.3.21. The minimum losses for the investigated hybrid silicon nitride slot waveguides were ~7dB/cm (derived from the two slot waveguides with length of 1cm (black line) and 2cm (blue line) in Figure.3.21.b, denoted with green arrows). This ~7dB/cm losses include both the linear losses and absorption losses, and are thus larger than the linear losses of the passive silicon nitride waveguides filled with index liquid cladding and shown in Chapter-2.

More quantitatively, the total losses α_{total} of the hybrid slot waveguides studied in Fig. 3.21 can be expressed as sum of waveguide linear scattering losses α_l, the Erbium doped cladding absorption losses ($\alpha_{abs} * \Gamma_{AM}$), and losses due to additional defects α_{defect}:

$$\alpha_{total} = \alpha_l + \alpha_{abs} * \Gamma_{AM} + \alpha_{defect} \qquad (3\text{-}7)$$

Therefore, a crude estimation of the integration induced defect losses can be made from the total waveguide losses α_{total}, the waveguide linear scattering losses (α_l), and the material absorption ones $\alpha_{abs} * \Gamma_{AM}$ (already known). For instance, by considering maximum total losses of hybrid slot waveguides around 12dB/cm, losses due to defects are estimated to about ~5dB/cm. The related information is summarized in Table.3.4. Therefore, the predicted minimum achievable total losses of hybrid slot waveguides without defects are ~7dB/cm.

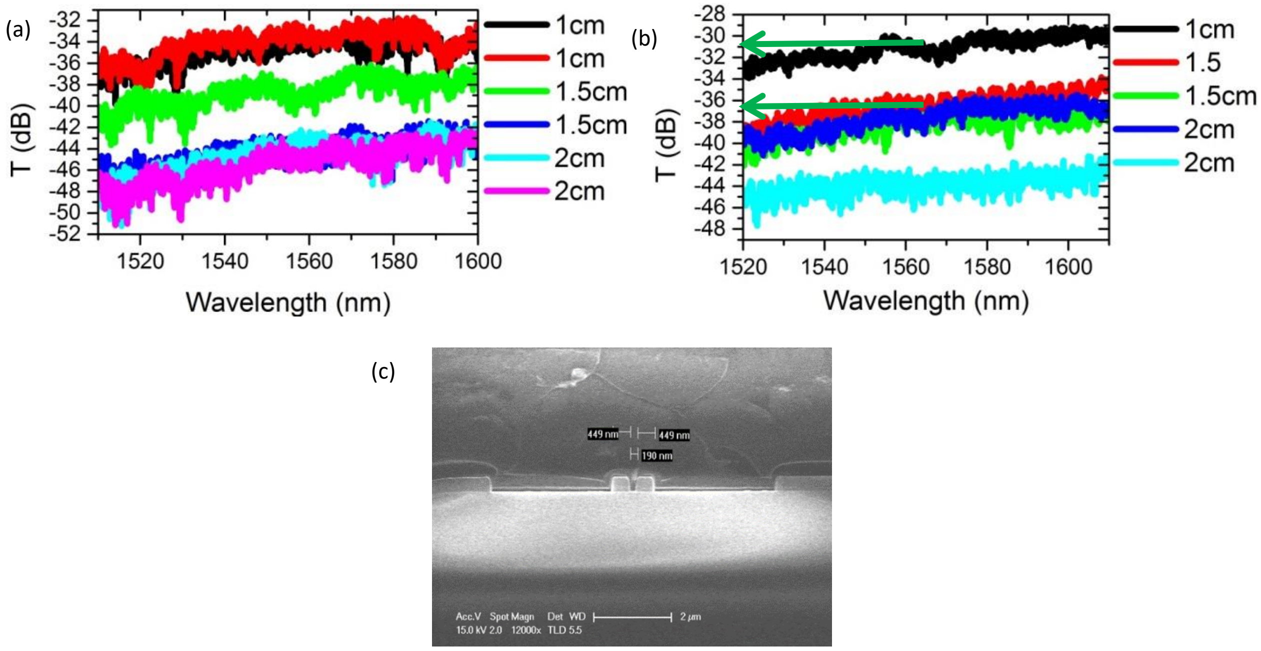

Figure 3.21 Linear transmission spectra of different width silicon nitride slot waveguides. (a) Slot width is 120nm. (b) Slot width is 170nm, of which the cross section is shown in shown in (c).

Table 3.4 Summarized different kinds of losses in PMMA-NPs hybrid silicon nitride slot waveguides.

Hybrid SiN Slot waveguides		Slot 120nm	Slot 170nm
Measured max total losses (dB/cm)	α_{total}	~12	~12
Measured min total losses (dB/cm)	α_{total}		~7
Measured losses without Er AM (dB/cm)	α_{l}	4	4
Absorption of PMMA-NPs: Er3+/Yb3+ dB/cm)	α_{abs}	6.12	6.12
Signal mode overlap factor	Γ_{AM}	40%	43%
Losses due to integration defects (dB/cm)	α_{defect}	5.5	5.4
Predicted minimum total losses (dB/cm)	α_{total}	6.44	6.63

3.5.4 Gain measurement in Erbium polymer waveguides and Erbium slot waveguides

Gain measurements of all the Erbium polymer and Erbium hybrid waveguides have been performed with the setup shown in Figure.3.22. The signal and pump laser sources were connected with polarization rotators and a WDM combiner. The combined signal+pump light beam was guided into free space and filtered by polarization filters. Then, TE or TM polarization was chosen and light was coupled into a polarization maintaining fiber and injected into nanocomposite polymer waveguides or hybrid silicon nitride slot waveguide with the help of a single mode lensed fiber. The output light was collected by objectives and filtered by polarization filters and long pass filters (>1.5µm). Finally, the amplification was analyzed through optical spectrum analyzer (OSA) and power meter.

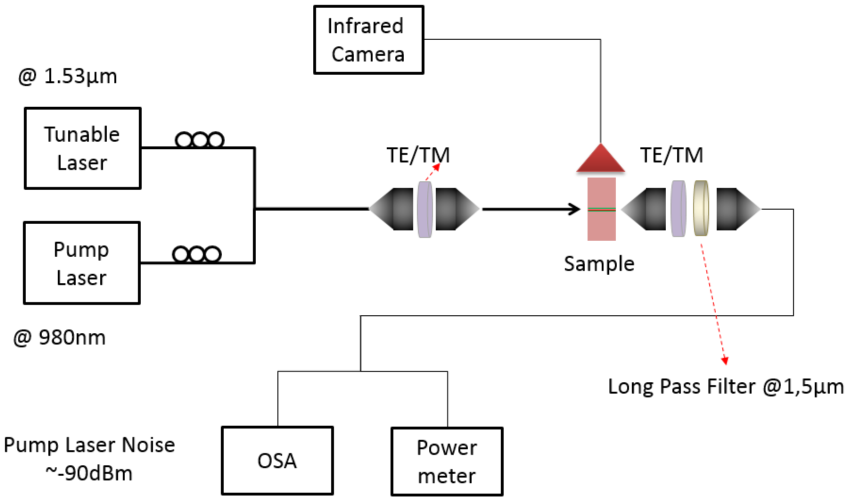

Figure 3.22 Schematic figure of the optical setup that we used to measure the signal gain (1.53µm) by pumping with 980nm laser source.

The laser pump source at λ=980nm could give a maximum power of 170mW (measured at the end of the lensed fiber and before coupling into the chip). In order to make the micro lensed fiber stabilized when suffering high pumping power, we used a long metal holder to fix and guide the optical fiber. The fiber was stretched nearly straight inside of the metal holder and only 5mm of the terminal part of the lensed fiber was out of the holder. By such a method, we found that the fiber could be stabilized during ~2mins. The employed signal source was a tunable laser with a maximum output power of 5mW. The into the chip power coupling loss was estimated to around -4dB on the input facet of the polymer active waveguide.

The internal net gain of the waveguide could be then expressed by the following equation [109]:

$$G(\lambda) = 10\log_{10}\left[\frac{I_p(\lambda)}{I_u(\lambda)}\right] - \alpha_{abs}(\lambda)L - \alpha_s(\lambda)L$$

$I_p(\lambda)$ and $I_u(\lambda)$ being the signal power for a ON and OFF pump, respectively, α_{abs} the waveguide absorption losses due to Erbium ions (measured without any pump power), and α_s the linear scattering losses of the waveguides.

As shown in Figure.3.23, the measured maximum relative gain obtained by this approach at λ=1535nm was in the range of 20-29.2dB for a 1.3cm-long polymer waveguide. Considering the waveguide total propagation losses (absorption+scattering) of 5.3±0.3dB/cm, a maximum net internal gain of 22.3dB was obtained, corresponding to 10-17.2dB/cm net gain in the considered polymer waveguide.

This experiments thus demonstrated the good amplification potentials of the Erbium nanocomposite material made of PMMA and Er^{3+}/Yb^{3+} core shell nanoparticles.

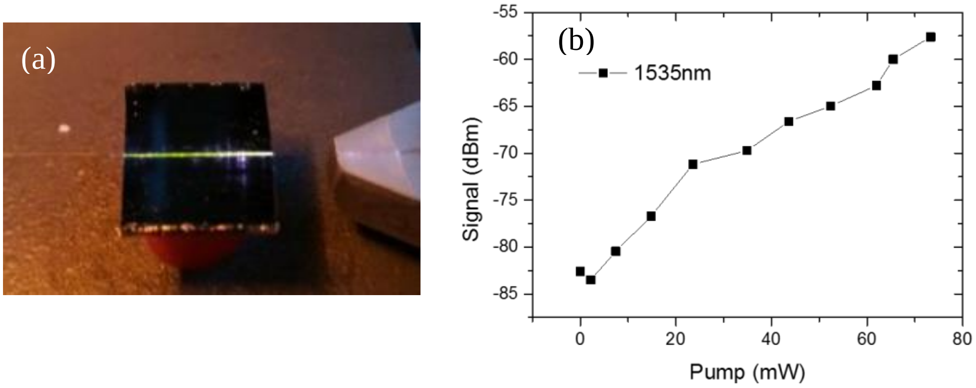

Figure 3.23 Gain measurements of polymer waveguide (a), light injection and (b) signal evolution as function of the pump power.

In the frame of the PhD time, no complete optical gain properties have been properly measured in slot silicon nitride waveguides infiltrated by this promising Erbium doped nanocomposite material, but it is still on progress. After having solved preliminary steps related to the fabrication and optimization of passive silicon nitride waveguides, time was spent with the Chinese partner to understand various issues related to the synthesis of the material. A sample made of SiN slot waveguides was sent to Jilin university that to be spin-coated with the nanocomposite material, so that one main test was achieved in France to characterize the optical gain properties of hybrid Er-SiN slot waveguides. No internal net gain was still measured in the current hybrid slot waveguides, probably due to following reasons: (1) Nano particles were not homogeneously distributed at the bonding interface layer of the nanocomposite and very few nanoparticles were actually embedded inside of the slots or close to the slot waveguides. Therefore, nanoparticles in the top cladding layers may not have played an as important role as in the Erbium polymer rib waveguide in which the Erbium nanoparticles were well dispersed inside relative large micro-scale waveguide cores; (2) As the needed pumping wavelength was 980nm, the pumping power was mainly confined inside the silicon nitride rails rather than in the low index cladding layer. Hence, the pumping efficiency may have been low, leading to only a moderately efficient pumping of nanoparticles. Further steps to improve the fabrication processes to obtain single mode (both for pump and signal) double slot waveguides proposed in section 3.4.2 would be helpful to solve this problem, as well as additional discussions and work with the Chinese partner.

3.5.5 Conclusion

To sum up, a promising Erbium nano material for hybrid integration with hollow core waveguides was characterized during my three-year study in the frame of Chinese-French international program ANR project (POSISLOT). Benefiting from specially synthesized core-shell Yb^{3+}/Er^{3+} nano particles, which were copolymerized with PMMA and processed as Erbium PMMA nanocomposite, related Erbium nanocomposite formed rib waveguide could display an internal net gain of 10-17.2dB/cm. This preliminary results are promising for the future development of integrated hybrid erbium slot optical amplifiers.

3.6 Er_2O_3/Al_2O_3 atomic layer integration with SiN slot waveguides

In this section, we investigate the atomic layer deposition into (silicon nitride) slot waveguides and the relevant gain measurements. The atomic layer deposition was done in the *Department of Micro- and Nanosciences, Aalto University, Espoo, Finland*, in the frame of a collaboration with the group of Professor Zhipei Sun.

In this section, we first introduce the physical properties of the atomic layer technique, such as inter-layer controlling and associated PL lifetime, cross emission and absorption coefficient, and annealing properties. This part of work was done in Finland by Professor Zhipei Sun’s group.

Second, we show results related to our collaboration aiming at the integration of Er_2O_3/Al_2O_3 atomic layers on silicon and silicon nitride chips. Infiltration of the slot waveguides is analyzed, and linear losses of slot waveguides are also compared before and after atomic layer integration.

At last, measurements of the internal gain inside of the silicon nitride waveguides and PL characterization of silicon slot waveguides are presented.

3.6.1 Properties of Er_2O_3/Al_2O_3 atomic layers

The employed atomic layer method was based on a Picosun R-200 advanced ALD tool operating in plasma enhanced mode. The Erbium atomic layer (Er_2O_3) was deposited from the Tris (2,2,6,6-tetra-methyl-3,5- heptanedionato) erbium (known as Er(thd)3 or Er(tmhd)3) and oxygen plasma. Al_2O_3 atomic layer was deposited from a trimethylaluminium source (TMA) and water. The detailed fabrication mechanisms have been depicted in [209].

The fabrication of Er-doped Al_2O_3 layers was done at relatively high temperature (300˚C) to minimize the impurities and the average growth rates were fixed to 0.20 and 0.90 Å/cycle for Er_2O_3 and Al_2O_3, respectively. The growing substrate was silicon. To study the atomic layer PL properties, five different Er_2O_3/Al_2O_3 samples were studied by keeping the same amount of Er_2O_3 layers but changing the number of cycles of the Al_2O_3-layers between every two Er_2O_3 layers to control the inter-ionic distances (i.e. the distance between subsequent Er_2O_3-layers) [210], as illustrated in Figure.3.24.

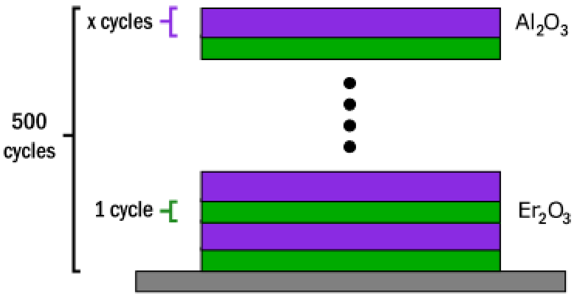

Sample	Number of cycles		Thickness (nm)	% of Er-ions
	Er_2O_3	Al_2O_3		
2	1	2	89.9	7.23
3	1	3	131.6	4.94
5	1	5	242.3	2.68
7	1	7	339.7	1.91
10	1	10	494.4	1.32

Figure 3.24 The tested samples are composed of 500 periods (cycles), as shown on the left. Five different samples were fabricated with different numbers of Al_2O_3 cycles between each two Er_2O_3 layers. The ratios of the number of the Er_2O_3 and Al_2O_3 cycles are shown on the left. The total thickness and Er ion ratios are also summarized. [210]

The photoluminescence was enhanced when there was more Al_2O_3 interlayer cycles. Consequently, the upconversion emission was suppressed according to the results shown in Figure.3.25. Increasing distances between two Er atomic layers also led to longer lifetimes and larger emission and absorption cross sections, as shown in Table.3.5.

In order to deposit high Erbium ion concentrations in slot structures, three Al_2O_3 cycles structures were adopted. A further annealing process at 700°C was adopted to improve PL lifetime up to 5ms and PL intensity became 4 times higher than initially, as shown in Figure.3.26. Erbium ion concentration was estimated to about $5\times10^{21}/cm^3$ and the refractive index at wavelength 1.53µm was estimated to n=1.64 by ellipsometry.

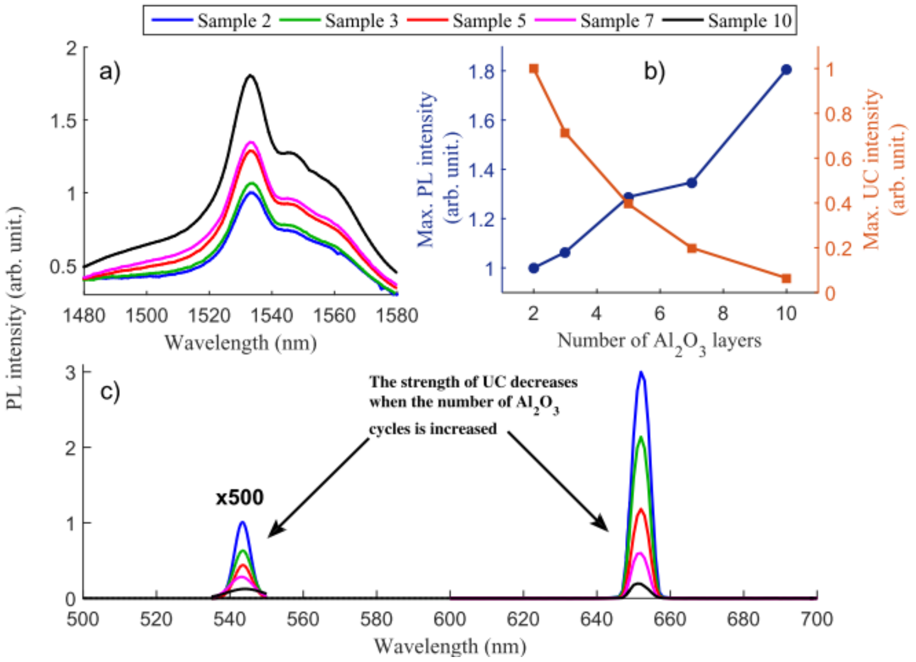

Figure 3.25 (a) PL-spectra of the Samples at the wavelength range 1480-1580 nm;(b) Maximum PL signal as a function of the number of Al_2O_3 layers between each Er_2O_3 layer in the Samples and (c) Up-conversion spectra of the fabricated samples in the 500 - 700 nm wavelength range with λ_{exc}=980nm.[210].

Table 3.5 Emission and absorption coefficients as well as the lifetimes of the studied samples [210].

Sample	Lifetime(ms)	σ_{21} (10^{-20} cm^2)	σ_{12}(10^{-20} cm^2)	λ_{exc}(nm)
2	2.00	1.98	1.96	980
3	2.06	2.07	2.05	980
5	2.18	2.08	2.05	980
7	2.11	2.14	2.12	980
10	2.16	2.20	2.18	980
In this thesis	2.06	0.962	1.015	1480

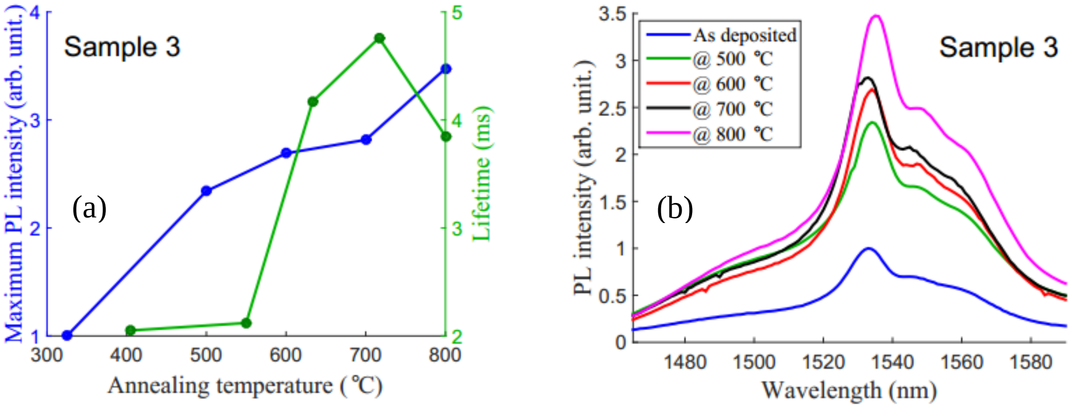

Figure 3.26 (a) PL-spectra of the Samples at the wavelength range 1480-1580 nm;(b) Maximum PL signal as a function of the number of Al_2O_3 layers between each Er_2O_3 layer in the Samples and (c) Up-conversion spectra of the fabricated samples at the wavelength range 500 - 700 nm with λ_{exc} = 980nm.[210].

3.6.2 Al_2O_3:Er Atomic layer integration in SiN photonic slotted structures

Theoretically, slots can be fully filled with the atomic layer deposition technique and lead to a homogeneous growth process on all surfaces of the waveguides, as shown in Figure.3.27.a. In this purpose, the slots should be filled with the two vertical inner walls of the atomic layer. However, slot defects could be observed in practice or obtained when the atomic layer deposition process was not perfectly controlled, which happened to some of the hybrid slot waveguides, as illustrated in Figure.3.27.d. Related SEM characterizations of silicon nitride slot waveguide cross sections are shown in Figure.3.27.c&d. The deposited thickness of the atomic layer was **150-200nm** for the studied silicon nitride slot waveguides.

Under SEM characterization, silicon nitride slots were fully filled when the slot size was below 100nm. When the slot size became larger than 100nm, an air slot was formed between two slot waveguide rails, as illustrated in Figure.3.27.d.

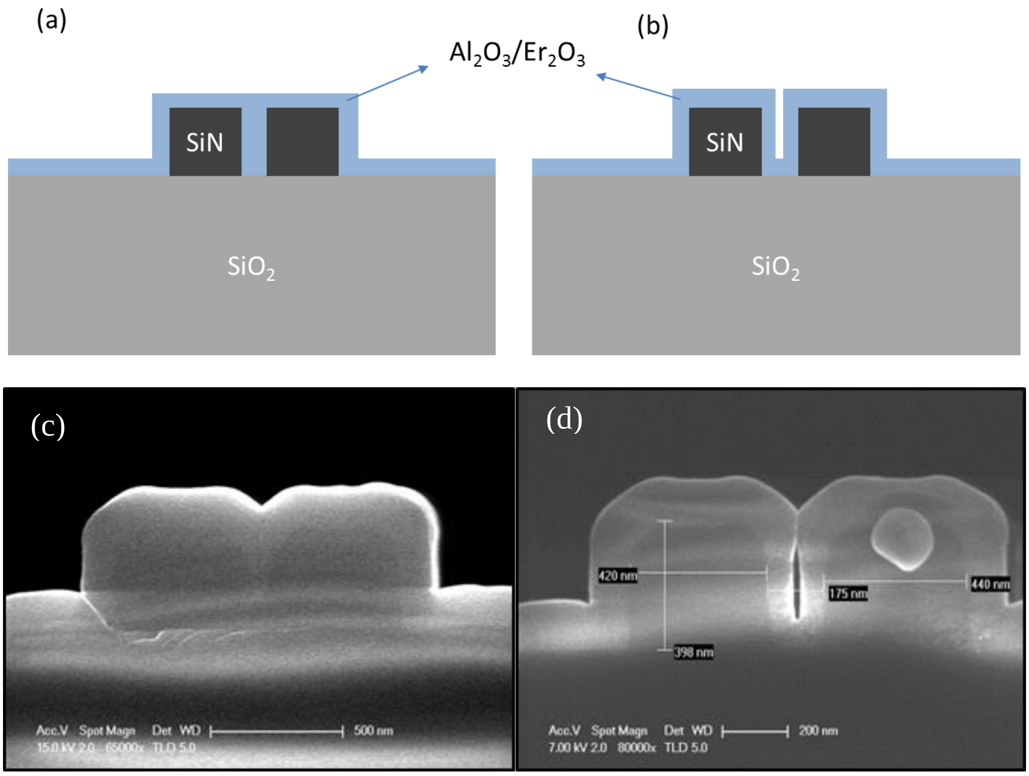

Figure 3.27 Schematic growth of the Erbium doped atomic layer on different width silicon nitride slot waveguides (a) & (b); Atomic layers deposited on slot waveguides with different slot width (c) ~100nm and (d) ~175nm.

3.6.3 Linear losses of Erbium atomic layer hybrid silicon nitride slot waveguides

After atomic layer deposition (ALD), we characterized the waveguide again to measure the optical propagation losses of the hybrid silicon nitride slot waveguides without top cladding liquid.

As shown in Figure.3.28, propagation losses of the different slot width waveguides were around 19dB/cm and 10dB/cm for wavelengths of 1540nm and 1620nm, respectively. As erbium absorption cross-section is reduced when the wavelength is larger than 1620nm, the loss difference between the two wavelengths corresponds to the minimum absorption losses at λ=1540nm due to Erbium. Under this estimate, the maximum total linear scattering and defect losses was ~10dB/cm and the minimum erbium absorption contribution was ~***9dB/cm*** (***2cm^{-1}***), as summarized in Table.3.6. The calculated optical power confinement in atomic layers for the 220nm slot width silicon nitride waveguides was ***30%***, which indicates that the absorption coefficient of the atomic layer bulk material itself is ~30dB/cm (7cm^{-1}).

Table 3.6 Loss contributions in silicon nitride slot waveguides

Slot width (nm)	Total losses @ 1.54µm(α_{total}) (dB/cm)	Linear scattering losses (α_s) (dB/cm) (Max)	Erbium absorption losses (α_{abs}) (dB/cm) (Min)	Confinement factor Γ_{Er}
120	18	8.5	9	25.8%
170	16-21	11	5-10	28%
220	17	6.5	10.5	30%

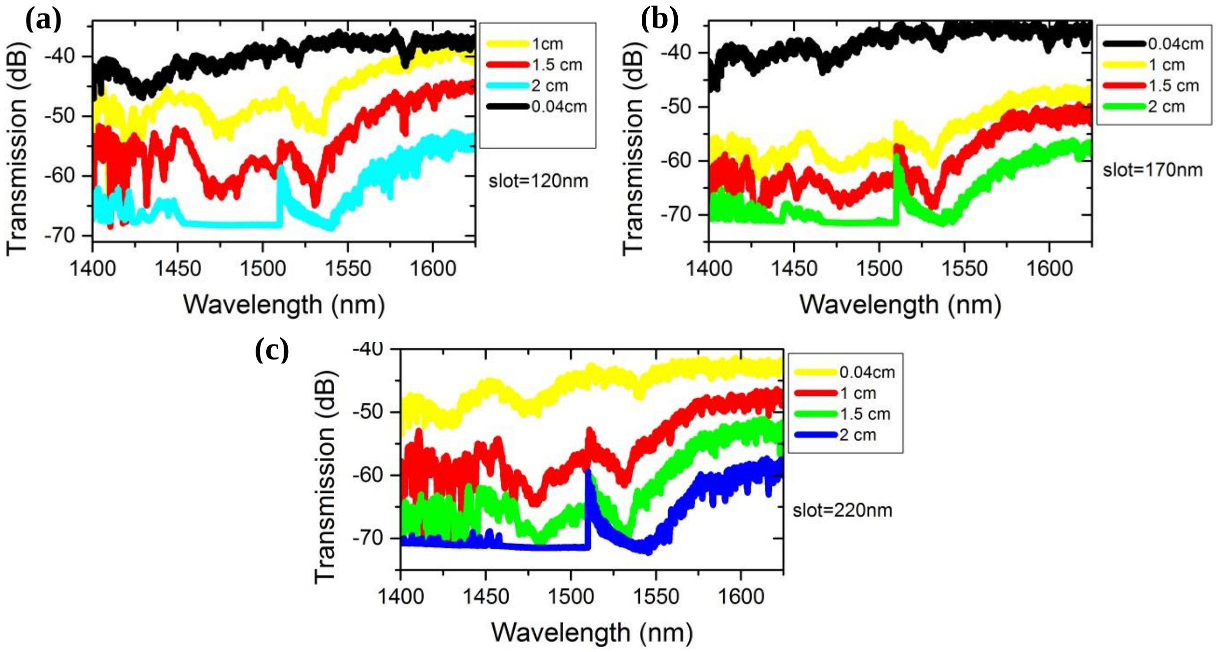

Figure 3.28 Measured transmission spectra of different silicon nitride slot width waveguides: (a) 120nm, (b) 170nm and (b) 220nm.

3.6.4 Gain measurements of Erbium atomic layer hybrid silicon nitride slot waveguides

The provided cross-section coefficients of emission and absorption from our collaborators are shown in Table.3.7. The energy transfer upconversion (ETU) coefficient C_{24} is around $1\times10^{-25}m^3s^{-1}$, which is quite small compared with the Er-doped Al_2O_3 case [109], or with high concentration Erbium silicates [83]. As estimated, the Erbium concentration is $5x10^{27}m^3$, which is one of the highest level achieved in integrated photonic hybrid waveguides according to the state of the art (Table.3.3). Such a high Erbium concentration hybridization with photonic waveguides is expected to result in relative high erbium absorption, as measured with ~10dB/cm at least.

By equation 3-1 and the given spectroscopic parameters in Table.3.7, the estimated modal absorption coefficient of the hybrid waveguides is ***66dB/cm***, which should be the maximum absorption loss level due to Erbium ions by assuming all the ions are active and able to contribute to absorption. In comparison, the maximum Erbium absorption of the hybrid waveguides calculated through linear transmission experiments is 12-17dB/cm (see Figure.3.28), by assuming that linear scattering losses are 4dB/cm (loss value before Erbium integration). The spectroscopic parameters shown in Table.3.7 are thus in good agreement with experimental results obtained for hybrid waveguides integrating the ALD-deposited active material. Hence, the active Erbium ions contribution to absorption is estimated about 18-26% by comparing the experimental absorption losses (12-17dB/cm) and the theoretical ones (66dB/cm).

Table 3.7 spectroscopic parameters values

Spectroscopic parameters		Values
Er-Concentration /m^3	$N_{Er}(/m^3)$	$5x10^{27}$
Pump absorption cross-section	s_{12}@1480nm (m^2)	$0.549\ x10^{-24}$
Pump emission corss-section	s_{21}@1480nm (m^2)	$0.180\ x10^{-24}$
Signal absorption cross-section	s_{12}@1530nm (m^2)	$1.015\ x10^{-24}$
Signal emission corss-section	s_{21}@1530nm (m^2)	$0.962\ x10^{-24}$
Life time of $I_{13/2}$	t_{21}(ms)	5.37
Life time of $I_{11/2}$	t_{32}(μs)	51
Up-conversion coefficient, ETU	$C_{24}(m^3s^{-1})$	$\sim 1\ x10^{-25}$

For the pump wavelength of 1480nm, the measured optical total losses are ~15dB/cm, which are relatively high and raises several issues about the needed optimal waveguide length, pumping power, and finally achievable net optical gain. According to the previous simulations carried out in section 3.4.1, new calculations were performed to investigate potential net gain in hybrid silicon nitride slot waveguides with slot width 220nm according to the spectroscopic parameters given in Table.3.7 and Appendix-A. Figure.3.29 shows the optical net gain as a function of the waveguide scattering losses (α_s), which indicates that the ideal net gain ~20dB is possible in 1cm long waveguides when scattering losses is between 5-10dB/cm according to Table.3.7. As all the spectroscopic parameter were not fully experimentally obtained, the simulated net gains shown here are just rough estimations for reference.

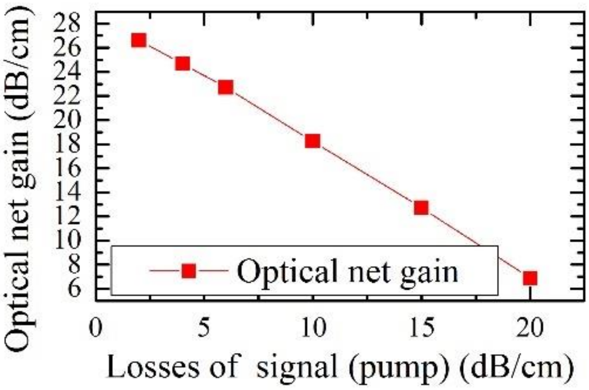

Figure 3.29 Simulated optical gain in 1-centimeter-long hybrid slot waveguides with slot width 220nm according to the spectroscopy parameters in Table.3.8.

To experimentally verify the optical gain of hybrid waveguides, gain measurement of 220nm wide slot silicon nitride waveguides have been performed. The same optical setup as the one shown in Figure.3.22 was used to carry out the measurements, excepted that here we used a 1480nm wavelength pump laser. The 1480nm pump laser source could give a maximum CW power of 1.4W and the fraction of the power that was coupled into the chip was estimated to around ~-8dB on the facet of the waveguide. The normalized electric field confinement in the erbium hybrid silicon nitride waveguides is depicted in Figure.3.30. A schematic *rib waveguide configuration* of this hybrid waveguide is also illustrated.

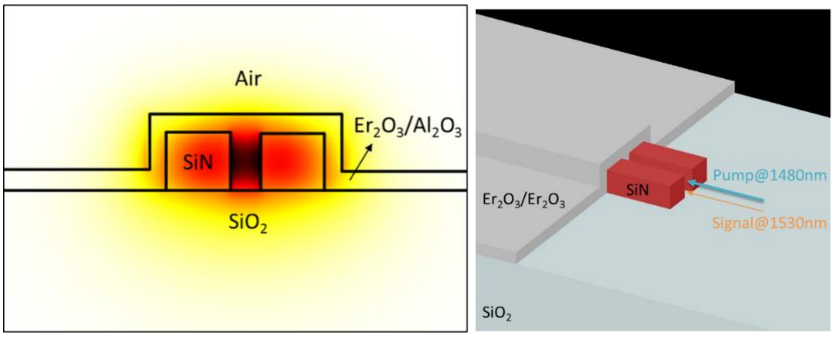

Figure 3.30 The normalized electric field distribution in Er_2O_3/Al_2O_3 atomic layer coated silicon nitride slot waveguides and the schematic waveguide configuration of the atomic layer hybrid silicon slot waveguide.

The experimentally measured relative gain values are depicted in Figure.3.31 and summarized in Table.3.8. A maximum relative gain of 5.32dB was measured in a slot waveguide with a length of 1cm at maximum coupled pumping power of 212mW, as shown in Figure.3.31.a. For short slot waveguides, maximum relative gain 1.59dB was obtained in a 400μm long slot waveguide, which corresponds to 39.8dB/cm relative gain. As summarized in Table.3.9, higher relative gain values per unit length are preferentially found in short waveguides and the gathered results turn out that net gain occurs in 400μm long slot waveguides. The internal net gain is ranging in 1.5-22.8 dB/cm after subtracting scattering and absorption losses from the measured relative gain range 0.74-1.59dB. For strip waveguides with width of 550nm and length 4mm, a relative gain of 2.3dB was also measured with a cladding power confinement factor Γ_{Er} 26.5%. The relative gain is then of 5.75dB/cm.

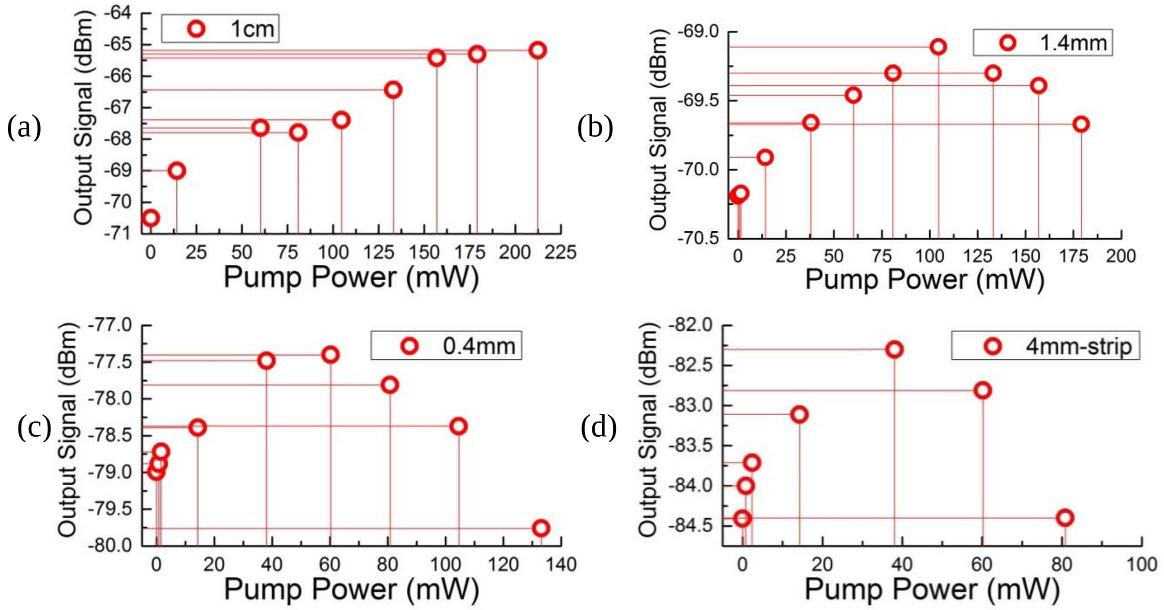

Figure 3.31 Relative gain of three different slot waveguides with 220nm slot width, one strip waveguide with 550nm width; A maximum relative gain 5.32dB, 1.08dB,1.59dB,2.3dB are measured, respectively.

Table 3.8 Comparison of different gain measures in different waveguides

Type of waveguide	Slot			Strip
Length(mm)	10	1.4	0.4	4
With Bends	Yes	no	no	no
Width of slot/strip (nm)	220	220	220	550
Relative Gain (dB)	***1.86-5.32***	***1.08-1.42***	***0.74-1.59***	***2.3***
Relative Gain (dB/cm)	***1.86-5.32***	***7.7-10.1***	***18.5-39.8***	***5.75***
Material Gain g_{Er} (dB/cm)	***6.2-17.7***	***25.7-33.7***	***61-133***	***21.7***
Waveguides losses @1.53μm(dB/cm)	17	<17	<17	Not sure
With or without Net gain (dB/cm)	No	no	Yes (1.5-22.8)	Not sure
Saturation Pump power (mW)	>212	~105	~60	~38

Overall, high internal net gains of the hybrid waveguides larger than 10dB/cm have been mainly measured in *sub-millimeter long* waveguides with Er concentration ~5×10^{21}/cm^3. The needed pumping power coupled into the hybrid waveguide turns out to be moderate about ~50mW, that is comparable with recently published results of Erbium silicate nanowires [194].

The results can be explained by the fact that: (1) Large total propagation losses for pump inhibit the optimal pumping length beyond few hundreds of µm; (2) When waveguide length is shorter than the effective waveguide length, active ions are pumped very efficiently and the buildup of the population inversion is the strongest; (3) The gain properties are more homogenous and stronger in short waveguides due to fewer waveguide defects from hybrid integration; (4) High pumping power enhances the excited states absorption and reduces gain in long structures.

3.7 Conclusion

To conclude, we have investigated hybrid slot waveguides integrated with active erbium doped materials by estimating total propagation losses in involved optical waveguides, and relative gain of active materials and hybrid waveguides. Though, we have not yet successfully measured clear large net gain in our hybrid waveguides, these results are promising for the demonstration of net gain in Si and SiN optical waveguides.

For Yb^{3+} co-doped Erbium NPs nanocomposites integration, we have demonstrated that this active material waveguide could give a large internal net gain of 15.3-22.5dB/cm, which potentially results in hybrid SiN slot waveguides with modal net gain.

For atomic layer deposited Erbium-doped oxide integration, optical gain was highlighted in ultra-short 400µm hybrid slot waveguides, with relative gain in the 0.74-1.59 dB range or net gain of 0.06-0.91dB, corresponding net gain coefficient 1.5-22.8dB/cm.

A further rigorous study is highly required especially trying to remove the layer defects and further minimizing linear waveguide losses. A near field experiment characterizing the signal evolution along the slot waveguide would be also probably a good approach to reveal the large gain coefficient for high concentration erbium materials.

4. Integration of carbon nanotubes in silicon photonics

One of the key challenges and difficulties in silicon photonics is to integrate light sources in/on silicon chips. The option of III-V laser diode locally bonded within complex silicon photonic networks has demonstrated excellent performances in terms of optical power emission and laser tenability but still faces issues: CMOS incompatibility, high cost and requirement of additional steps for bonding with silicon chips. To find new solutions to build light sources directly in silicon photonic networks, active nano-materials have been intensively studied in the last years, with the aim of CMOS compatibility, large scale patterning and low cost. For instance, colloidal CdSe/CdS quantum dots (QDs) have been successfully embedded between two vertical silicon nitride disks [211], and later demonstrated as on chip lasers [102], which represented a significant step for the development of light sources in Si chips. Besides, new monolithic solutions have also been demonstrated by epitaxially growing InAs QDs on top of industrial compatible Si (001) substrates, which finally led to the proof of a disk laser[212]. Therefore, silicon photonic passive resonators directly hybridized with nano-emitting materials are perceived as a promising solution for the realization of low cost and CMOS compatible light sources. Among these new alternative nanomaterials, carbon nanotubes (CNTs) and graphene, have been reported as promising materials for the development of next generation integrated nano devices such as electronic transistors, as well as photonic light emitting, modulating and detecting devices [49][48] in the silicon platform.

Semiconducting single-wall CNTs (s-SWNTs), mostly used for electronic and photonic applications, rolled up from monolayer of graphene, can have different chiralities and various optical band gaps covering the whole telecommunication wavelength window. Hence, s-SWNT emerged as a good candidate to traditional semiconductor-based nano materials to build up on chip light sources and detectors. Furthermore, previous works demonstrated wafer scale deposition of millions of carbon-nanotubes on circuits [213] and shown electrically driven CNT-based light nano-emiters with the capability of modulation at frequencies up to 100 GHz [65], i.e. comparable to or larger than direct III-V-on-silicon laser modulators [214] or silicon modulators [215]. All these features have brought a strong basis to the potentials of CNTs integration in silicon photonics.

However, several important issues still remain to be solved. The first step is to demonstrate strong luminescence from s-SWNT (PL: photoluminescence, or electroluminescence) coupled into integrated waveguides. Although SWNTs coupled into high-*Q* nano cavities [10] and ring resonators [11] have been demonstrated, the measured photon counts are still very low [7], being insufficient for any on-chip communications.

Hence, the study of CNTs integration in photonic devices remains to be explored, primarily by demonstrating strong PL and high coupling enhancement in silicon photonic structures. At the material level, preliminary important steps still represent big challenges, including the ability to obtain high concentrations CNTs in active thin film layers, the control of a proper alignment of CNTs, and the realization of efficient electrical contacts on CNTs-doped layers.

In this chapter, results obtained within the FP7-ICT Cartoon project (2013-2016, coordinator: Laurent Vivien/C2N laboratory), mainly regarding integration in Si photonic structures, will be reported. We will firstly introduce the basic optical properties of the CNTs and will quickly review the state-of-art of CNTs photonic integration methods. In section 4.2, we introduce a method for the preparation of high concentrated CNTs matrices. In section 4-3 and 4-4, we study the integration of high concentration CNTs-doped polymer layer into silicon ring resonators and nanobeam cavities.

In the scheme of FP7-ICT Cartoon project, the experiments have been carried out together with Mrs. Elena Duran (PhD student), from our group in C2N (Orsay). The high concentrated CNTs were prepared by Elena Duran(C2N) and Dr. Arianna Filoramo (CEA, Saclay, senior expert researcher). The devices were fabricated in C2N (Orsay) by Xavier Le Roux, clean room senior engineer.

4.1 Optical properties of CNTs

4.1.1 Optical bands

Carbon nanotubes can be single wall or multiwall and each single wall carbon nanotube is rolled up from a single graphene sheet as a long 1D nano-material. The lengths of CNTs vary from several tens of nanometers to several micrometers. The diameter of single-wall CNTs is of the order of 1 nm and can be expressed by equation 4-1, where $\boldsymbol{C_h}$ is the chiral vector (defined by equation 4-2), (a_1, a_2) representing the two unit vectors of the graphene hexagonal honey comb lattice, as shown in Figure.4.1. The pair number (*n*,*m*) controls the chirality or “twist” of the carbon nanotube, determines its diameter and even its optical properties. For example, Figure.4.1 shows CNTs basic geometry properties. CNTs with $m=n$ are named “armchair” tubes and with $m=0$, they are called “zigzag” tubes.

$$d = \frac{|C_h|}{\pi} = \frac{a}{\pi}\sqrt{n^2 + nm + m^2} \qquad (4\text{-}1)$$

$$\boldsymbol{C_h} = n\boldsymbol{a_1} + m\boldsymbol{a_2} = (n, m) \qquad (4\text{-}2)$$

As the set of (*n*,*m*) parameters entirely describes the single wall CNT (SWNT) physical construction, it directly controls the metallic or semiconducting behavior of the tube. By "Zone-folding approximation" theory based on graphene electronic energy bands and neglecting curvature occurring during wrapping into CNT, SWNTs are metallic when $n\text{-}m = 3k$ (k is an interger) and are semiconducting when $n\text{-}m \neq 3k$ [216].

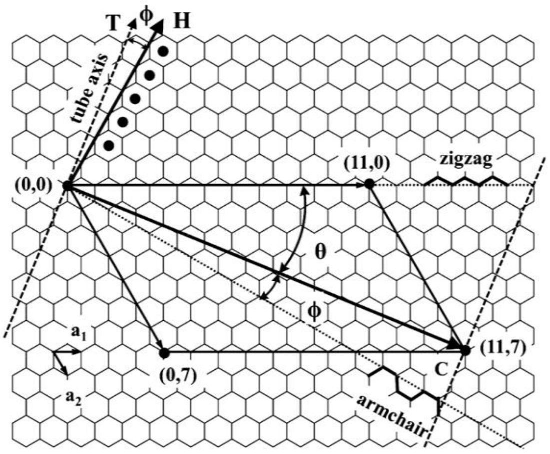

Figure 4.1 (a) Schematic graph of wrapping a graphene sheet into SWCNTs with chirality vector (11,7) [217]. ϕ is the wrapping angle or chiral angle that is relative to the armchair direction. θ is the wrapping angle that is relative to the zigzag direction. Dashed lines are perpendicular to the chiral vector $\boldsymbol{C}$ with same direction as $\boldsymbol{T}$, vector $\boldsymbol{H}$ is perpendicular to the armchair direction. The cross angle of $\boldsymbol{T}$ and $\boldsymbol{H}$ is the chiral angle ϕ.

The band structure of SWNTs is made of a series of one-dimensional subbands and optical transitions only occur between two optical bands (E_{ii}, $i = 1,2,3\ldots$) with same indices. For instance, longitudinal transitions between bandgaps v_1 to c_1 and v_2 to c_2 … denoted as E_{11} and E_{22} transitions are allowed, as shown in Figure.4.2.a. To enter a little more into details, when light polarization is perpendicular to the tube axis, transitions are allowed between two bands with a band index difference equal to 1, but these transitions are usually significantly suppressed due to the large scale anisotropy of CNTs dielectric environments (depolarization effect) [218] [219].

All above physical properties come from the CNTs single particle model which neglects electron hole Coulomb interactions. More detailed models include exciton effects to describe the optical properties of CNTs, which brings the bound states of electron-holes (excitons) energy levels as 1s, 2s, 2p, etc. A more detailed description of the E_{11} and E_{22} transitions is shown in Figure.4.2.c. Excitons in carbon nanotubes play in fact an important role in their optoelectronic properties, [220] [62].

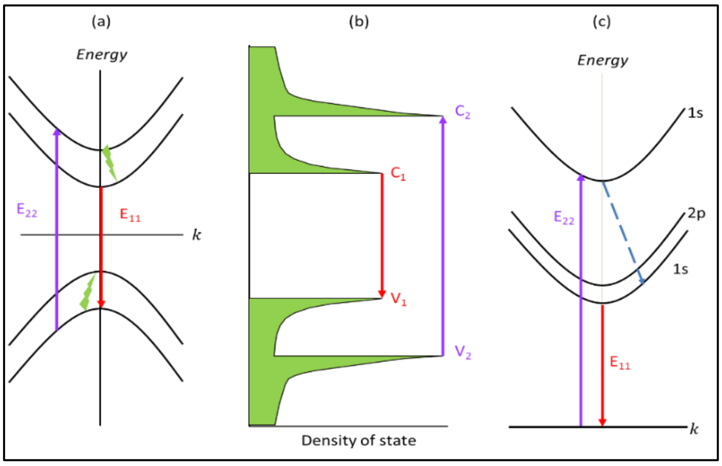

Figure 4.2 Schematic graph of optical transitions (a) (b) and density of states (b) based on single particle model. (c) A simplified display of optical transition between the CNT exciton bands.

4.1.2 Photoluminescence excitation spectroscopy

The transitions related bandgaps E_{11} and E_{22} are inversely proportional to the tube diameters d by d^{-1} and d^{-2} dependencies [218]. A full study of SWNTs light absorption and emission properties can be done by probing these bandgap transitions through photoluminescence excitation spectroscopy (PLE). Exciton relaxation induced PL emission happens when the excitation wavelength reaches absorption resonance and maximum PL intensity can then be detected. Figure.4.3 shows an example of the PLE map of selectively solubilized SWNTs in toluene solution [221]. The 2D map peaks represent the resonantly enhanced PL emission from the E_{11} bandgap transitions when the pumping excitation energy matches the second electronic transitions E_{22}.

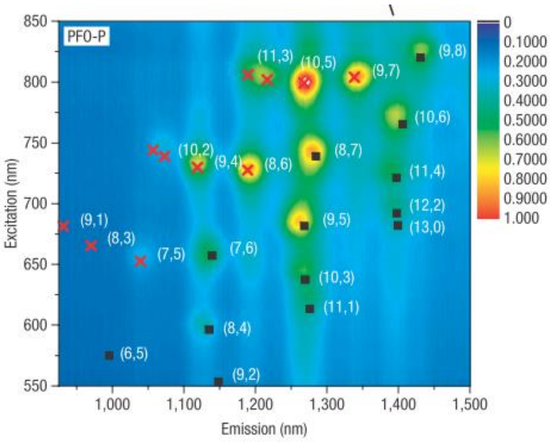

Figure 4.3 Photoluminescence excitation spectroscopy (PLE) map of SWNTs in toluene solution, in which polymer polyfluorene (PFO) were used to selectively solubilize some specific carbon nanotube species. Red cross means $n-m=3q-1$ and black square corresponds to $n-3=3q+1$. [221]

4.1.3 Quantum efficiency

One of the most important parameters of emitting materials is the PL quantum efficiency, defined as the ratio of the number of the emitted photons to the number of the absorbed photons, $\eta = n_{em}/n_{abs}$. To experimentally determine quantum efficiency, equation 4-3 can be used[222], where P and λ are the power and wavelength of the incident laser (*i*) and emission light (*em*) signals. *S* is the excitation spot area, *A* is the fraction of the absorbed incident light beam and S_T is the surface area of the SWNTs area:

$$\eta = \frac{P_{em}\lambda_{em}S}{AP_i\lambda_i S_T} \qquad (4\text{-}3)$$

A quantum efficiency of 7% was measured through single CNT by this method [222]. This measurement method is accurate but still subject to the experimental conditions and several assumptions of the light absorption and reflection. Regardless of the precision of the quantum efficiencies, it can at least be used to compare and improve CNTs emission properties.

Quantum efficiencies of all kinds of SWNTs are different, which is mainly due to their different rates of absorption (E_{22}^S) , emission (E_{11}^S), relaxation between the two states ($C_2 \rightarrow C_1$) that depend on the chiral angle and *p* value (n-m=$3q$+p, p=±1) [223], [224]. Theoretically, E_{22}^S is not tube diameter dependent while E_{11}^S is[223], [224].

Recently, quantum efficiency of SWNTs has been measured up to 20% in molecular F12 wrapped CNT solutions [61]. The polymer wrapped solution-suspended SWNTs has shown a strong dependence on the type of wrapped polymer, for instance, quantum efficiency was 1.6% for PFO-wrapped SWNTs [221], 1.1% for purified DNA-wrapped SWNTs [225], and ~0.1% for surfactant-micellarized nanotubes [226].

4.1.4 Optical gain

Optical gain has been observed in a PFO wrapped SWNTs thin film [66], which was pumped by a ns pulse laser beam focused with narrow strip shape while light was collected from the edge of the strip pump beam or the same edge of the thin film. The first optical gain value was found through the linewidth narrowing of the emission spectra of (8,6) and (8,7) nanotubes, as shown in Figure.4.4. Quantitative calculation by changing the pumping beam length (L_P) and then fitting the PL intensity (I_{ASE}) with L_P according to equation 4-4 indicated the intrinsic optical gain coefficient (g_{int}) of (8,7) nanotube doped thin film is around 190cm^{-1} [66] at the wavelength 1.3μm. Such high optical gain let us foresee that reaching lasing through CNTs integration in photonic nanocavities may be possible. In equation 4-4, I_{spont} is the spontaneous emission intensity and α is the optical loss (cm^{-1}).

$$I_{ASE} \propto \frac{I_{spont}}{g_{int}-\alpha}\left(e^{g_{int}-\alpha}-1\right) \tag{4-4}$$

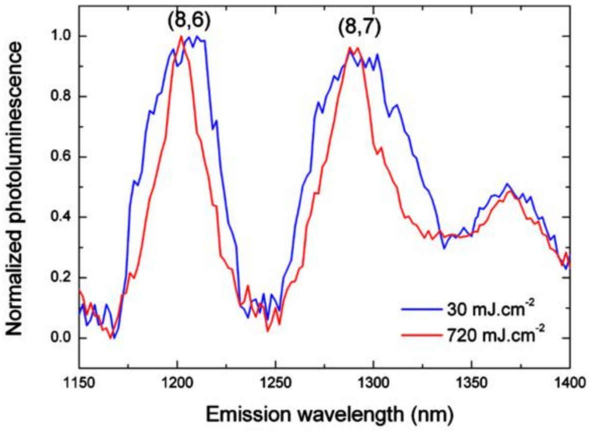

Figure 4.4 High resolution normalized spectra of the amplified spontaneous emission at different pump fluences with an excitation wavelength of 740 nm. A 29% linewidth narrowing (FWHM) from 63 to 45 nm was observed on the photoluminescence of (8,7) nanotube at 1300 nm and linewidth narrowing of 28% from 44 to 32 nm was also observed for the (8,6) nanotube at 1200 nm [66].

4.1.5 Conclusion

In this section, a brief description of the optical properties of s-SWNTs has been given. s-SWNTs have acceptable quantum yield efficiencies, of the order of 1-20% determined through experiments. The intrinsic optical gain in s-SWNTs doped PFO film can reach relative high values, up to 190cm^{-1} at 1.3 μm, which gives encouraging insight that optical gain could be reached in hybrid CNTs-silicon photonic structures for the design and realization of photonic amplifiers and lasers.

4.2 High concentration s-SWNTs-PFO solutions

The motivation of preparing high concentrated s-SWNTs is to explore strong PL coupling with silicon photonic devices and potential stimulated optical gain inside micro resonators and nano cavities. As light emission from single or several nanotubes is too weak and can hardly enable stimulated emission, further increasing the number of light emitters is needed to have a chance to observe high intense stimulated emission. Therefore, a preparation method of highly concentrated s-SWNTs-PFO solution was investigated. Efforts have been made in that direction within the Cartoon project by Mrs. Elena Duran and Dr. Arianna Filoramo and are summarized hereafter in Figure.4.5.

The initial CNTs are produced by the HiPCO process [227], then wrapped by PFO to select and purify certain kinds of carbon nanotubes [221] and finally extracted to lead to high concentrated solutions. At beginning, HiPco CNTs, PFO (Sigma-Aldrich) and toluene were mixed with ratio of 3mg:12mg:20mL. The dispersion of the HiPco CNTs in toluene and PFO wrapping with CNTs was enhanced by sonication (homogeneous+tip). Then, the solution was ultracentrifugated with 150,000*g* for one hour and a supernatant solution was collected, which mainly contains (8,6) and (8,7). This process leads to a high purification level of targeted CNTs, meaning in particular very few metallic nanotubes [116]. Then, we precipitated the low CNT concentration nanotubes wrapped by PFO, recover these precipitated nanotubes and re-dispersed them in fresh solvent to get high concentration CNT-PFO toluene solutions.

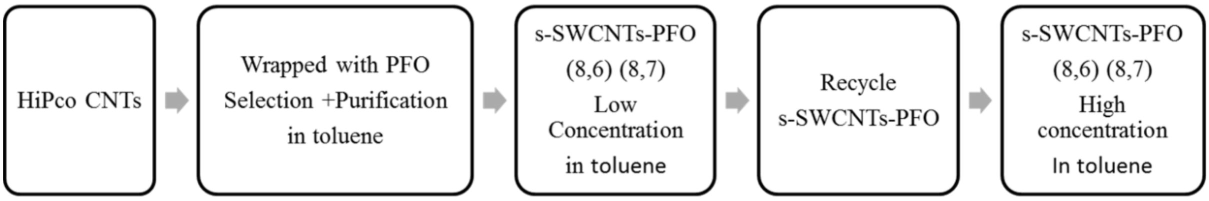

Figure 4.5 Schematic processes used to prepare high concentration carbon nanotubes from HiPco CNTs to high concentration s-SWNTs wrapped by PFO.

As shown in Figure.4.6, the absorption spectra of all the obtained solutions prove that the solution after extraction of semiconducting SWNT has much higher CNT concentration than the initial solution by comparing the absorption spectrum.

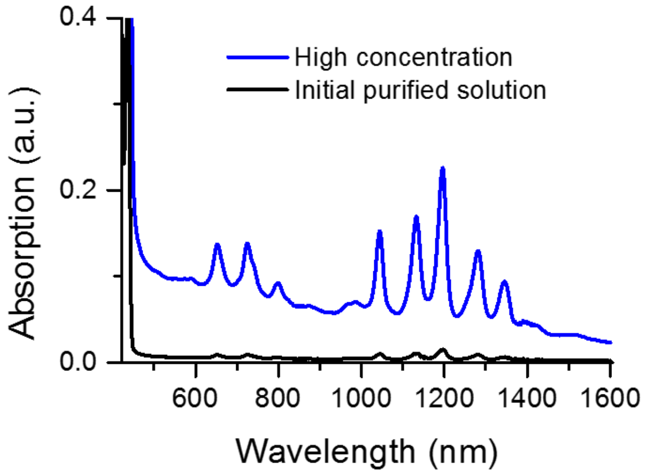

Figure 4.6 Absorbance spectra illustrating the effect of the induced precipitation and re-dispersion with fresh solvent for PFO s-SWNT.

4.3 CNTs integration in ring resonators

To properly integrate CNTs with photonic devices, several methods have been reported. They are mainly classified into two kinds. The first one consists in using chemical vapour deposition (CVD) techniques to grow CNTs directly on top of photonic waveguides, which can be assisted by lateral catalyst particles [118]. Similar waveguide bridge method can be also achieved by using dielectrophoresis to align CNTs between two electrodes [65]. Besides, polymer wrapped SWNTs can be directly spin coated on photonic devices as top cladding layers [117].

In our works, we have adopted a simple drop casting method consisting in dropping several droplets of highly concentrated CNTs solution directly on fabricated silicon chips (~5mm×~20mm) until to achieve a thick layer. Then, the sample was baked at 180°C temperature for 30mins. By this method, the obtained CNT-PFO thin film has a thickness around 2μm. An optical view of such a sample is shown in Figure.4.7. We can find that the CNTs layer is not homogeneous regarding to the optical transparency. The consequence of this matter of fact, especially regarding formation of CNT ribbons, is described hereafter in section 4.3.7.

In the following sections, we study the local interactions between CNTs-PFO layer and silicon ring resonators, i.e. PLE, CNT PL coupling with ring resonator couples, PL resonance evolution as function of pump, PL dependence on excitation polarization, comparison of PL coupling between bus waveguide and ring resonator and the analysis of CNT-PFO emission properties.

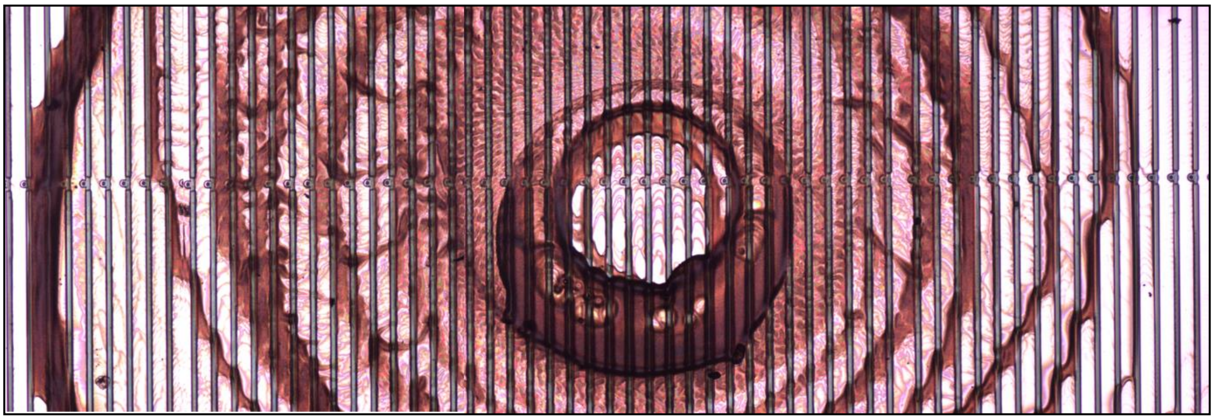

Figure 4.7 Optical view of the fabricated sample after that high concentration CNT solution was baked 30mins at 180°C temperature.

4.3.1 Scheme of CNT local integration and PL excitation and collection

The schematic integration of a s-SWNTs-PFO polymer layer (~2μm) within a silicon ring resonator is depicted in Figure.4.8. Micro-rings in this configuration were partially covered with HSQ resist, excepted in a ~6μm diameter disk located at the bus ring coupler region. The purpose of this approach was to enable a localization of s-SWNTs only at the excitation region fitting with the pump optical beam diameter in order to avoid extra-loss from SWNT which are not excited.

The fabrication started from a 220 nm thick Si film and 2 μm buried silica SOITEC SOI wafer. The designed *gds*-II mask was patterned with ZEP-520A resist and written by e-beam lithography (Nanobeam NB-4 system), and then developed by the inductive coupling plasma reactive ion etching technique. A typically fabricated silicon ring resonator is shown in Figure.4.10, which has ring waveguide width around 350nm and bus waveguide width of 270nm. Later, *HSQ* layer was patterned on top of ring resonators with a thickness of around 800nm, excepted in a 6μm disk region around the coupler, as explained before.

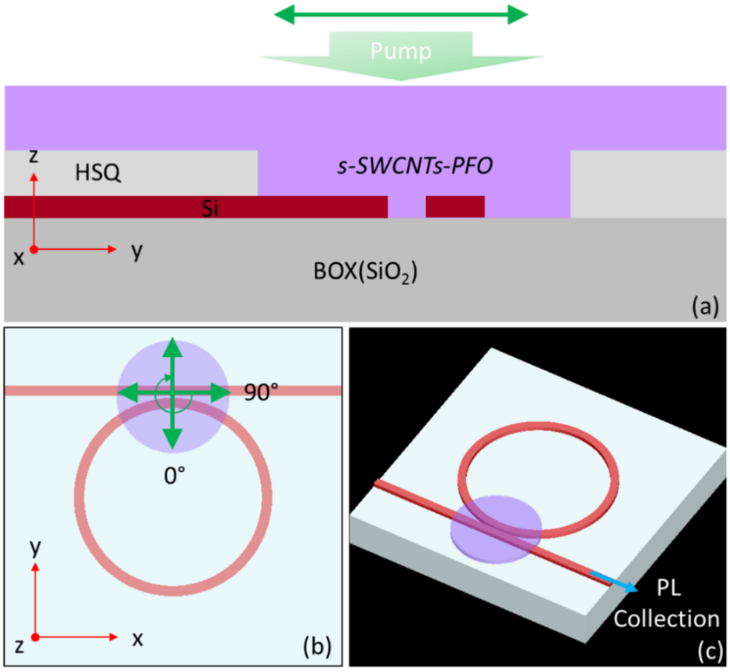

Figure 4.8 Schematic views of the silicon ring resonator with a local integration of a carbon nanotube layer. (a) Cross section view of the different stacking layers: BOX, silicon, HSQ, and s-SWNTs-PFO. (b) Top view of the hybrid CNT ring resonator. The diameter of the CNT layer (violet) "disk" is 6μm. (c) 3D overview of the integrated CNTs ring resonator device.

Figure.4.9 shows the TM mode of the waveguide cross section in the bended ring resonators (*R*=5μm; Figs. 4.9 (a) and (b)), as well as the ring resonator mode excited by a TM dipole source (Fig. 4.9 (c)). The evanescent field becomes very weak on top of HSQ layer, so that CNTs above HSQ bring negligible absorption to the ring photonic mode. **CNTs are thus mainly interacting with the silicon ring resonator in the chosen exposure disk region**, where is later excited with a Ti:Sapphire laser.

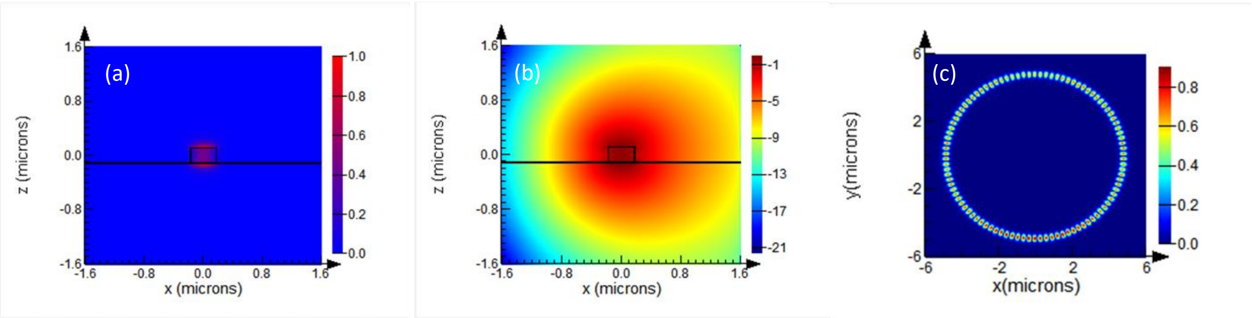

Figure 4.9 Simulated bended waveguide TM modes of the ring resonator: (a) linear scale, (b) log10 scale. (c) Excited ring resonating modes.

Silicon close to the ring resonator with less than 9µm distance was also removed to reduce the scattering light reflection and coupling back into the Si waveguide (see Figure.4.10.a). As shown in Figure.4.10.b, the exposed window is large enough to be well filled by the s-SWNTs-PFO (see Figure.4.10c) and is also compatible with used laser beam diameters for optical pumping (see Figure.4.10.d&e). By simulating pump beam microscopy with Lumerical FDTD software and assuming incident beam is perfectly Gaussian, we estimated the final focused beam through the microscope (50X, NA 0.55) having a FWHM width ~1.5µm (Figure.4.10.c&d) and verified that most of the optical pump energy was well distributed inside the 6µm window.

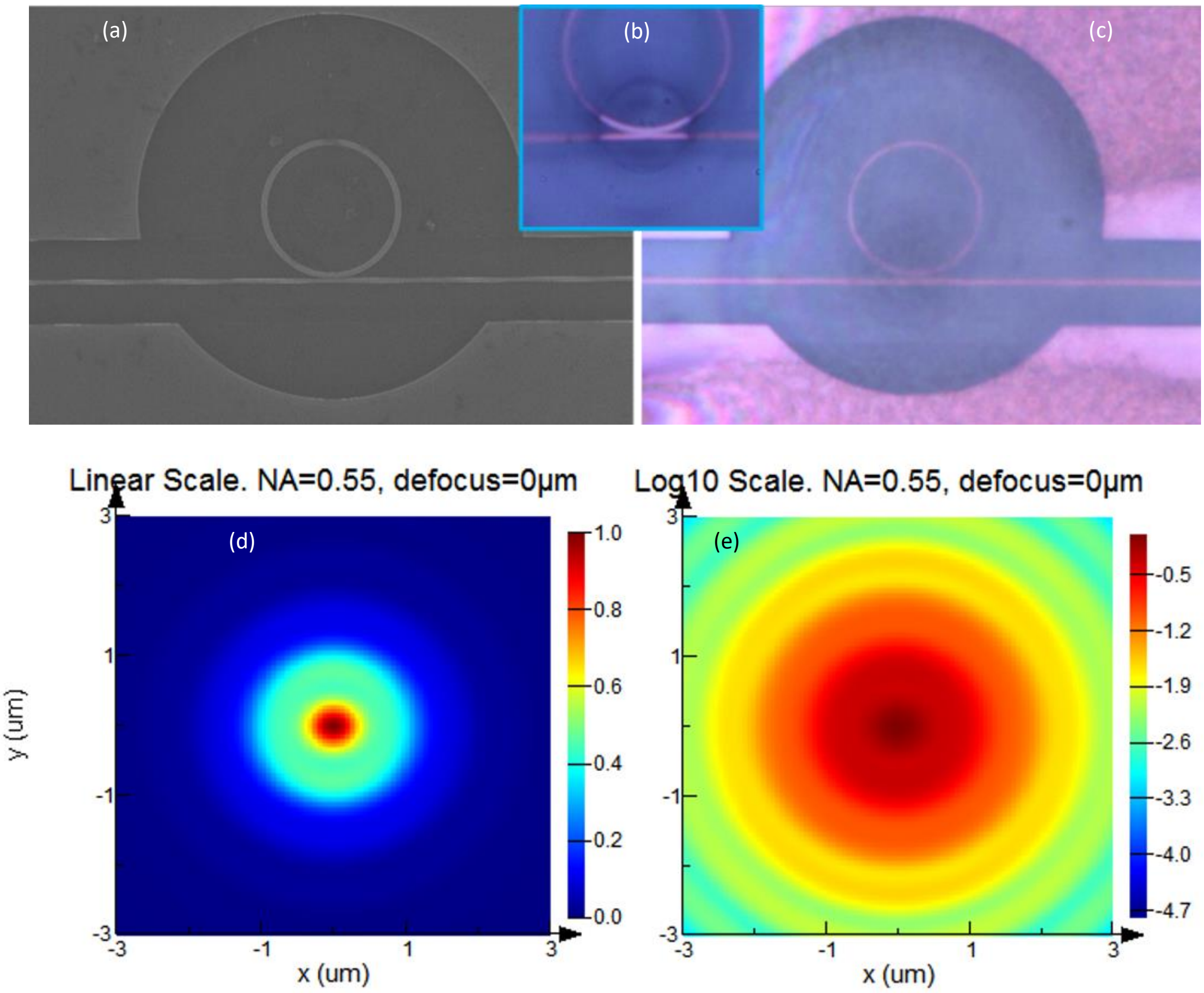

Figure 4.10 Fabricated ring resonator with radius of 5µm. (a) SEM overview, (c) Optical views after CNTs layer was integrated on top SOI ring. Inset (b) is SOI ring with HSQ layer before integrating CNTs. (d) Simulated focused beam size after objective with NA 0.4, and (e) Focused beam profile in log10 scale. The focused beam size is compatible with the integration hole in (b), of which the diameter is around 6µm.

To perform PL experiments, the s-SWNTs layer was excited by a Ti:Sapphire external laser source (λ_{exc}=740nm, CW) that was focused through microscope objective lens with 50X and NA 0.55. **The PL was collected through the bus waveguide edge facet by one polarization maintaining lensed**

fiber. Further, PL was selected through polarization filters, rotators, band pass filters and finally detected by a nitrogen-cooled InGaAs photodetector array, as shown in Figure.4.11. From the silicon resonator to the end of photodetector, the total signal losses were estimated to ~20dB.

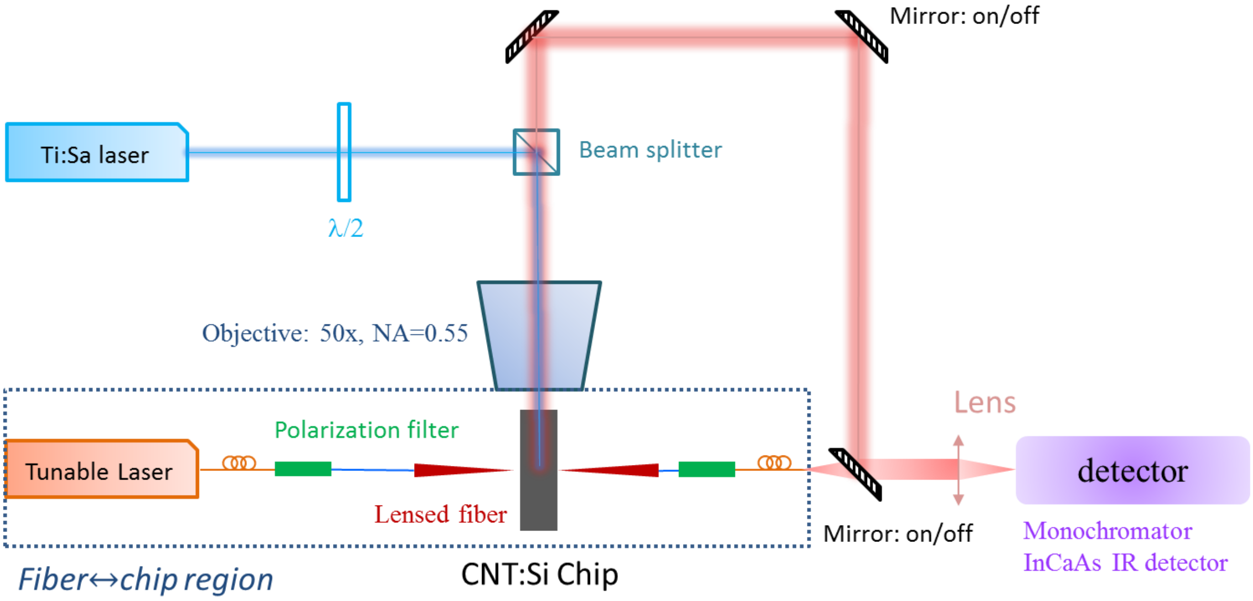

Figure 4.11 Schematic graph of the optical setup that was used to characterize the CNT PL coupling with silicon ring resonators. Fiber to Chip region coupling were adopted to collect PL from the waveguides for section 4.3. The free space PL collection method was used to study the CNT interaction with nanobeam cavities in section 4.4.

4.3.2 Photoluminescence excitation spectroscopy

Photoluminescence excitation spectroscopy (PLE) has been firstly performed by sweeping the excitation wavelength from 700nm to 780nm with a fixed CW power of 1.6mW. The pumping beam was focused around the coupler gap between bus waveguide and ring resonator to both excite the ring resonance and bus waveguide modes. The collected PL was plotted into 2D maps to analyze the most efficient pumping wavelength for the strongest PL emission, as explained in section 4.1.2.

As shown in Figure.4.12, the most efficient pump wavelengths to enhance CNT emission (8,6) and (8,7) were λ=735nm and λ=740nm, respectively. For (8,6) nanotubes, bus waveguide PL coupling was much stronger than for (8,7) ones when pumping wavelength was around 740nm, which is visible in Figure. 4.12.a and Figure.4.12.b. The PL coupling into bus waveguide and ring resonator are discussed just in the following sections.

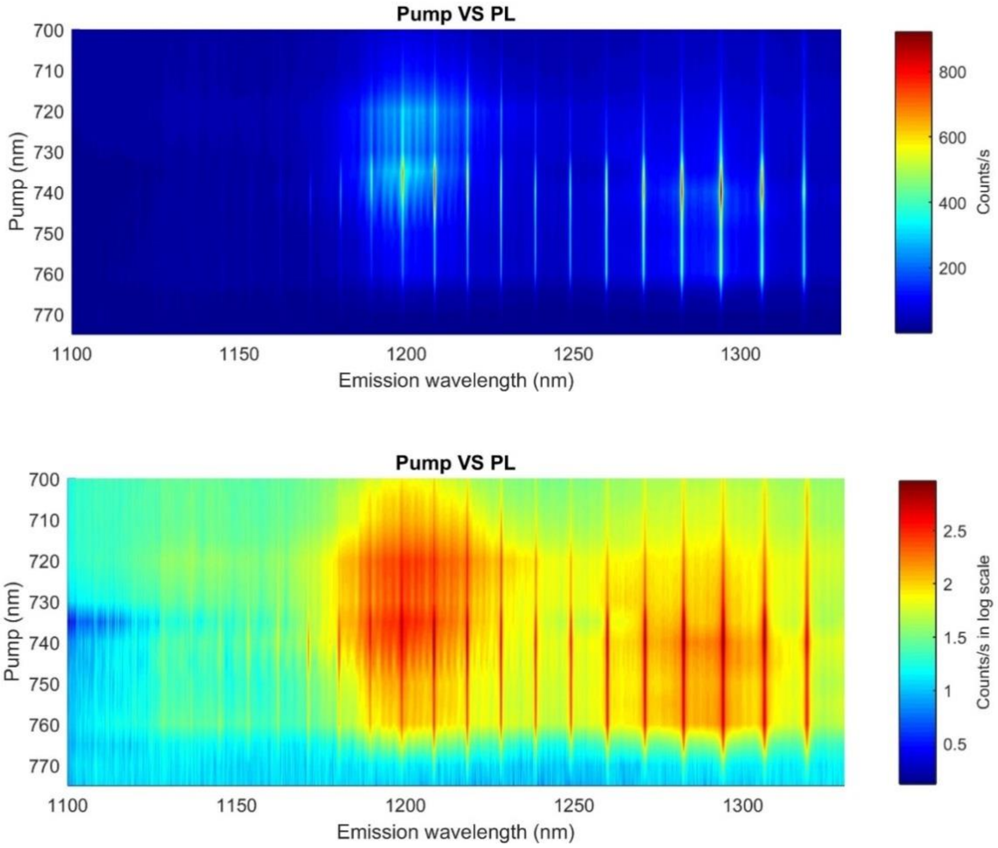

Figure 4.12 Photoluminescence excitation spectroscopy obtained by sweeping the pumping wavelength, which indicates that the most efficient pumping wavelength is 740nm for (8,6) carbon nanotubes.

4.3.3 Enhanced PL coupling by TM polarized resonator modes

In this section, we performed experiments to exploit CNTs PL coupling into the ring resonator TM modes, considering that TM modes are more evanescent than TE ones (see chapter 1 &2). By designing a larger coupler gap than 250nm, the TE mode coupling between bus waveguide and the resonator was indeed minimized. The TM mode resonances measured by a tunable laser covering the 1.26μm-1.35μm wavelength range are shown in Figure.4.13.b. PL coupled into the loaded ring resonator was collected within 10s, as depicted in Fig.4.13.a. From Figure.4.13.a and 4.13.b, it is noticeable that the enhanced PL wavelength resonances match the linear transmission ones, proving that CNT PL coupling with the TM-mode resonance occurred as expected.

As shown in Figure.4.13.a, the total collected CNT PL (I_{CNT}) could be separated into two parts: bus waveguide coupled PL (I_{Bus}) and ring resonator coupled PL (I_{Ring}). The I_{Bus} represents the PL photons having no resonance coupling with the ring resonator while I_{Ring} is the sum of the all PL photons looping inside of the ring resonator and exciting the TM ring modes (see the inset of Figure.4.13.b).

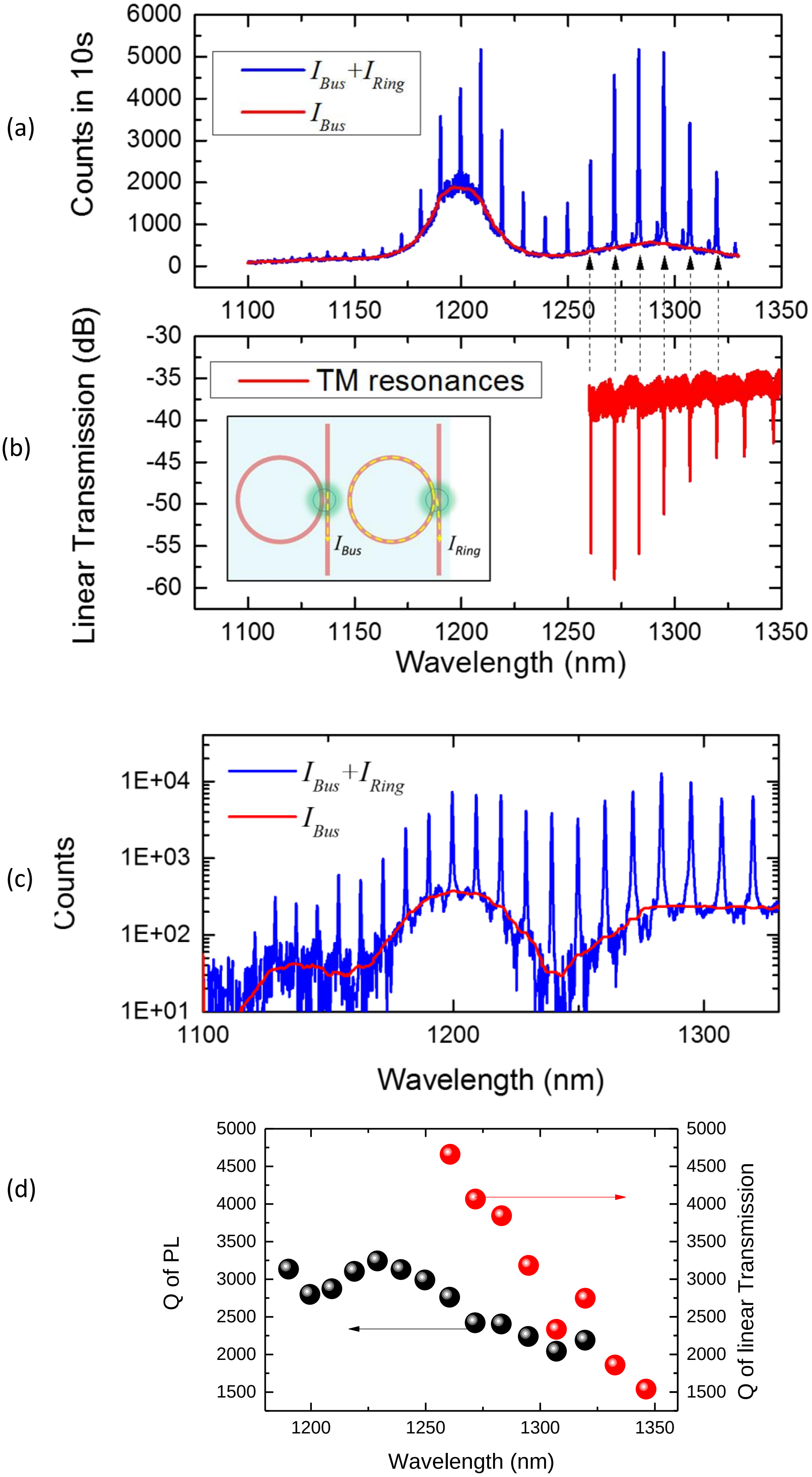

Figure 4.13 (a) PL spectrum collected from the top in 10s (b) TM transmission spectrum of the ring resonator. The inset explains the PL coupling I_{Bus} and I_{Ring}. (c) Maximum enhanced PL spectrum in log10 scale. (d) Extracted Q-factor of the all the ring resonances.

An intense emission (I_{Bus}) at λ=1.2µm from (8,6) CNT was observed (Figure.4.13.a&c), which could be explained by the fact that CNTs layer generally contains more (8,6) CNT than (8,7) CNT. As shown in Figure.4.13.c, the peak resonance intensity (I_{Ring}^{Peak}) is generally one order of magnitude higher than the bus waveguide coupled PL intensity baseline (I_{Bus}). Especially, the ratio I_{Ring}^{Peak}/I_{Bus} is larger than 20 dB at λ=1.24µm.

The extracted *Q*-factors of the ring resonator based on linear transmission spectrum before integration of the CNTs and PL emission spectrum are shown in Figure.4.13.d. *Q*-factors extracted from PL spectrum are smaller than the ones extracted from linear transmission spectrum, which is partially due to the CNT absorption.

To conclude, we were able to locally integrate dense CNTs in silicon ring resonator at the coupler region where the PL coupling enhancement due to the ring resonator can be referred to the light coupling directly into the bus waveguide. By engineering the mode coupling of the ring resonator, we observed two order intensity enhancement of the PL coupled in the ring in comparison with the PL coupled into the bus waveguide. *Q*-factors of the ring resonances become smaller after CNT integration, which is a confirmation of light absorption due to CNTs.

A further excitation laser polarization dependence was found to control the coupling competitions between I_{Ring} and $I_{Bus,}$ making it possible to significantly suppress the CNT PL coupling into the bus waveguide. This point is explained later in sections 4.3.5 and 4.3.6.

4.3.4 Resonance evolution as a function of pump power

In order to study the possible gain in this type of hybrid CNTs silicon ring resonator devices, we swept the CW pumping power and analyzed the output peak photon count and the linewidth evolution of the resonance peaks. As a typical example, Figure.4.14 shows the case of the resonance peak @1283.1nm. The linewidth of the peak remains around 0.52nm and the peak intensity reaches a maximum at pumping power 1.6mW and keeps a near constant level until pumping power 2mW.

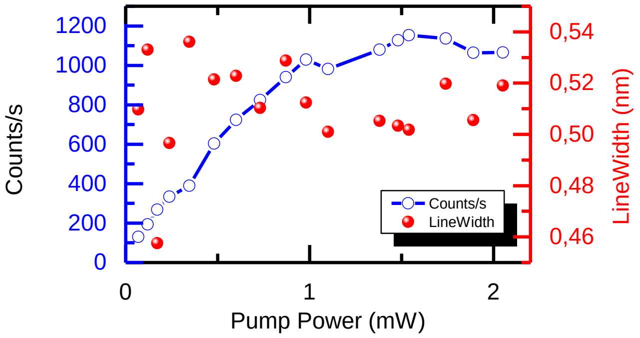

Figure 4.14 Peaks accounts and linewidth of the resonance peak 1283.1nm as function of the excitation power.

Overall, investigations on several peaks led to a similar general trend: the photon account tends to reach saturation after a linear increase while the linewidth of the resonance peaks remains at a nearly constant level. These properties indicate that no net gain was still obtained during these experiments.

4.3.5 Controlling PL coupling with excitation polarization

Starting from these last results of a possible excitation of CNTs and PL collection from integrated waveguides, we conducted further experiments. Among them, we studied the PL coupling dependence on excitation polarization regarding the fact that both absorption and emission photons of CNTs have a strong polarization dependence [228].A preliminary reasonable assumption was made: PL perpendicularly incident to the 0°-plane (see Figure. 4.15) or 90°-plane (see Figure. 4.15) have maximum or minimum coupling efficiencies to the bus waveguide, respectively. The point was mainly to demonstrate that PL emission is not homogeneous over all directions but dependent on the excitation pump polarization.

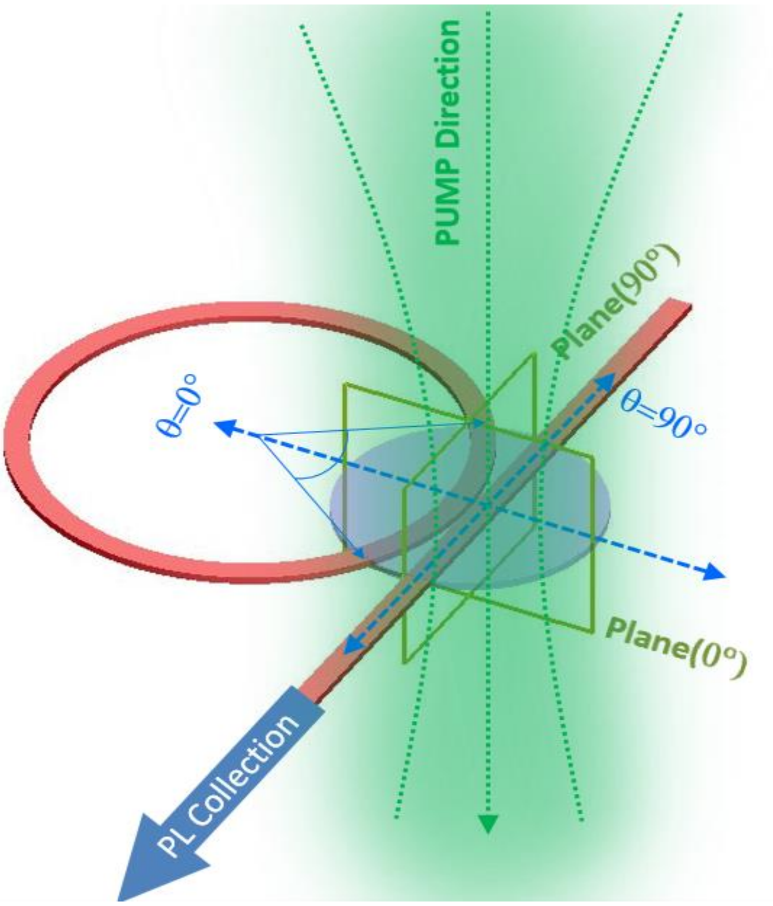

Figure 4.15 Schematic graph of polarization of the pump beam with θ angle regarding to the resonator coupler. The two 0°-plane and 90°- plane represent the nanotube axis plane or projection plane, respectively. Green beam is to shown the pump incidence and its possible polarizations, depicted with blue arrows. The violet disk represents the CNT layer. The PL was collected from the bus waveguide by using lensed fibers.

Experimentally, we performed measurements by tuning the excitation from initial polarization perpendicular to the bus waveguides ($\theta = 0°$) to the polarization parallel to the bus waveguide ($\theta = 90°$). By keeping the same pumping power, we recorded the PL spectrum from the bus waveguide. The related results are shown in Figure.4.16. In order to estimate the coupling competition between the bus waveguide and the ring resonator, we normalized the PL intensity referred to the maximum enhanced peak @ λ =1283.1nm. The total light coupling into the waveguide (I_{Bus}) was integrated along the full window from 1150nm to 1320nm, as shown in Figure.4.16. As illustrated in Figure.4.16, the PL coupling into the bus waveguide is gradually reduced compared with resonating spikes. In Figure.4.17, the quantitative integral of the PL coupled to the bus waveguide shows a rapid decreasing and reaches minimum level of 4.4, which represents ~26% of the initial I_{Bus}. In other words, the assumptions that we made above are verified: **light coupling into the bus waveguide is dependent of the pump light polarization**.

To conclude, we here show PL coupling from s-SWNT-PFO layer into silicon ring coupler with a relatively strong excitation polarization dependence. Then, PL coupling competition between the bus waveguide and the bended waveguide of ring resonators can be quantitatively controlled by pump polarization. This point is discussed in the next section.

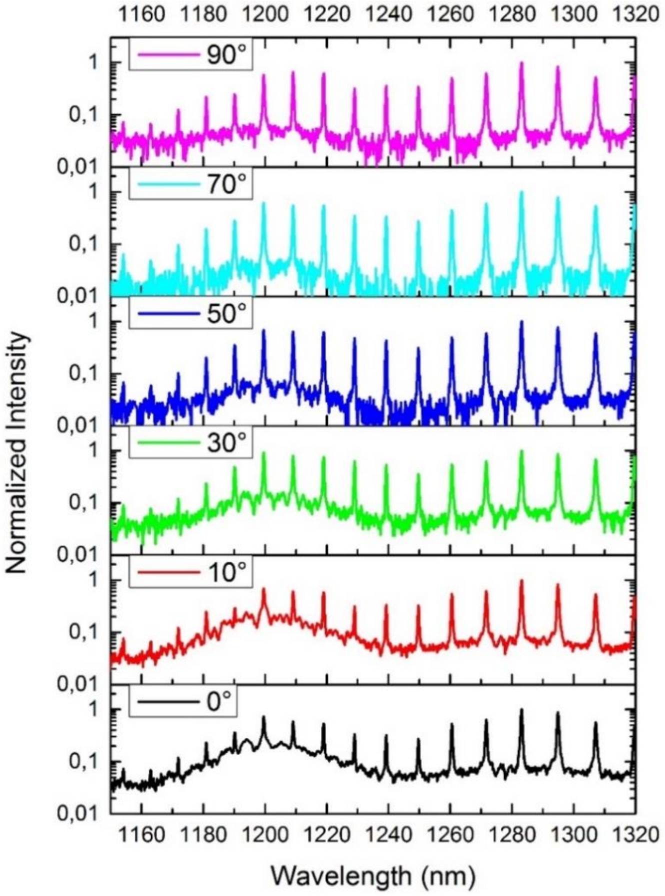

Figure 4.16 Coupled PL spectrum VS the excitation polarization angle θ.

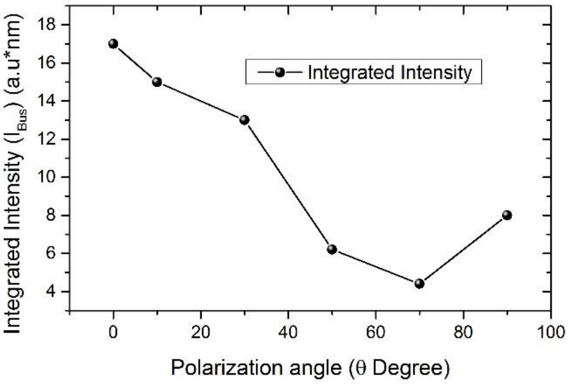

Figure 4.17 Integrated PL coupled into the bus waveguides as function of the excitation angle θ.

4.3.6 PL coupling comparison between bus waveguide and ring resonator

In this section, we compare the CNTs PL coupling into the bus waveguide and into the ring resonator, respectively, by defining one quantitative parameter as mentioned in equations 4-5:

$$\beta^* = \frac{I_{Ring}}{I_{bus}} \qquad (4\text{-}5)$$

The ratio of PL coupling between ring resonator and bus waveguides (β^*) compares the number of photons coupled into the ring resonator and into the bus waveguide over the full wavelength range.

I_{Ring} is the sum of the light intensity of all resonance peaks and I_{bus} is the full intensity coupled into the bus waveguide. Figure.4.18.a shows that the recorded PL spectrum for a 70° excitation polarization angle. As visible, it is made of nearly proper resonance spikes with a negligible background level, which indeed indicates that PL from the bus waveguide is negligible in this case. A calculation confirmed that for the PL coupling in Figure.4.18.a, $\beta*$ could be as high as 0.95 with excitation polarization angle 70° (Figure.4.18.b). Here, it should be noticed that $\beta*$ measurement is highly dependent on the background noise subtraction of the monochromator & IR detector. Hence, each spectrum collection was done with background noise subtraction to properly collect I_{bus}.

In conclusion, we demonstrate excitation polarization dependence of the light coupling into the ring resonator and bus waveguides. PL coupling comparisons show that nearly half photon counts are coming from the ring resonator resonances with specific excitation angle.

Further new design to remove the bus waveguide contribution was performed and is discuss in section 4.3.8.

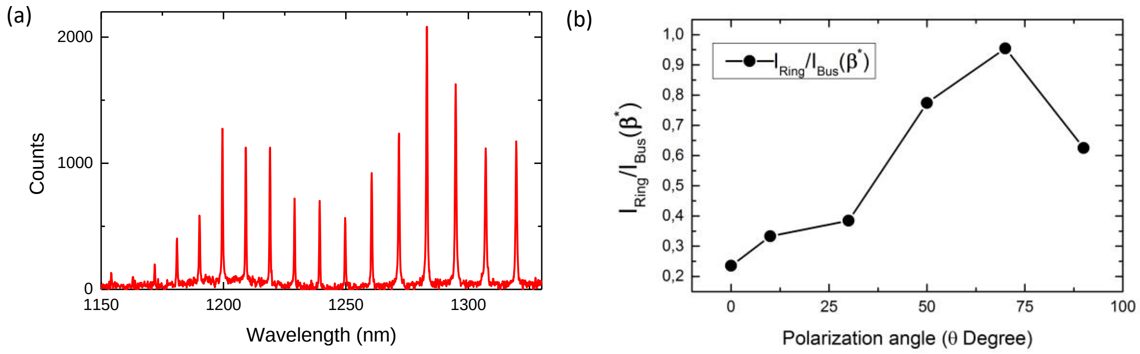

Figure 4.18 PL spectrum collected with excitation angle 70°; (b) PL coupling comparison factor $\beta*$

4.3.7 Influence of the PFO-CNT layer properties

As drop casting method cannot deposit the PFO-CNT layer homogeneously on top of silicon samples and the transparency of the PFO-CNT layer visually varies a lot from one region to another, it raises a question: what is the CNT concentration change over the silicon chip surface? First investigation to reply to this question was performed by using several adjacent TM-mode ring resonators (no TE mode resonance), where the PFO-CNT layer transparency was gradually changed, as shown in Figure.4.19. This group of ring resonators was fabricated and vertically aligned with separation of 50µm, and the coupler gap was changed from 270nm to 330nm. As shown in Figure.4.19.a-f, when transparency visually increases, the collected PL spectra do not differ significantly and all of them display strong PL coupling with 400-1000 Hz photon counts (see Figure.4.20).

We found that collected photon counts are not strongly dependent on the s-SWNT-PFO visual transparency. Instead, photon counts is highly dependent on the pump beam position, which changes the PL coupling efficiency into the bus waveguide We also noticed that the pumping position could influence the relative balance of the excited (8,7) and (8,6) CNTs, which finally may induce different collected PL intensities around the wavelengths of 1.2µm and 1.3µm, as shown in Figure.4.20.

Some assumptions can be made to explain how CNTs are distributed on silicon chip surface and how the distributions change the collected PL intensity. First, when baking the silicon chip after drop casting the s-SWNT-PFO toluene solution, the evaporation of toluene begins from the boundaries of the chip and ends up in the center of the chip. When toluene is evaporating on the borders, we guess that more CNTs are probably transferred to central toluene and less nanotubes and PFO are left on the borders. Further baking of the chip may result in s-SWNTs-PFO localized as ribbons with concentrated s-SWNTs. For instance, Figure.4.7 shows an example of the concentric SWNTs-PFO ribbons with different transparencies and concentrations.

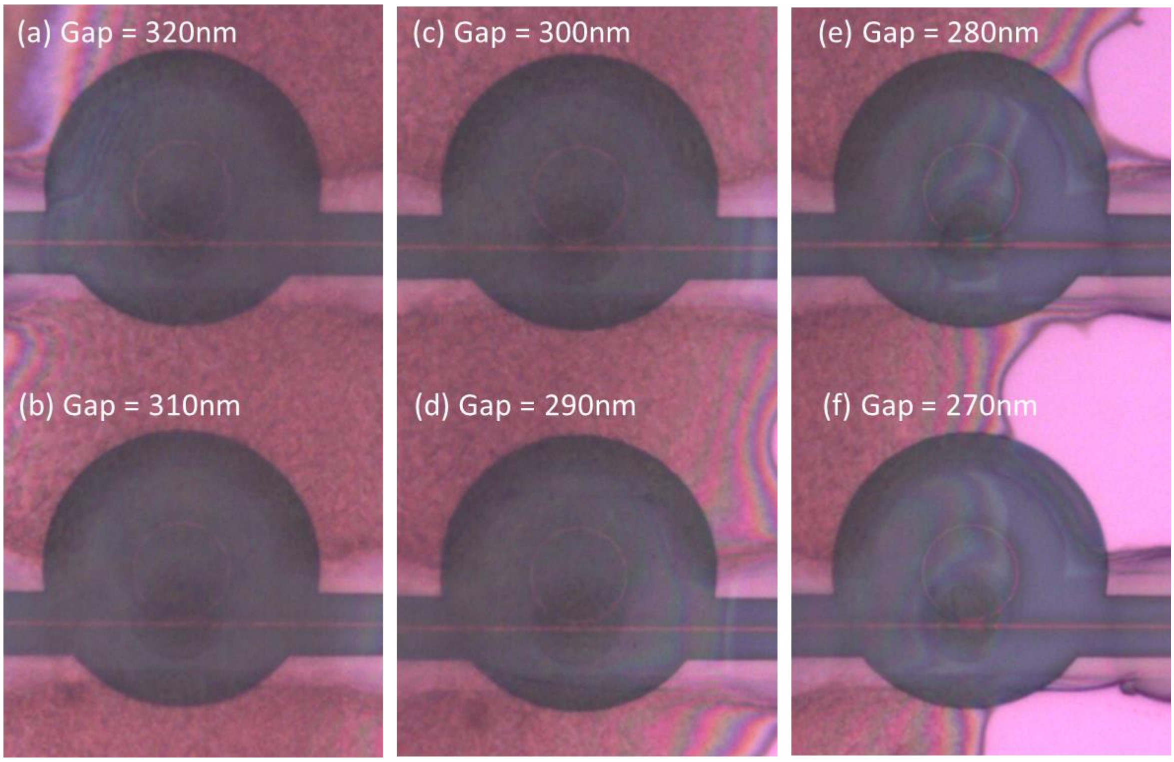

Figure 4.19 Optical views of the TM mode resonating modes with different coupler gaps and different CNT top cladding layers.

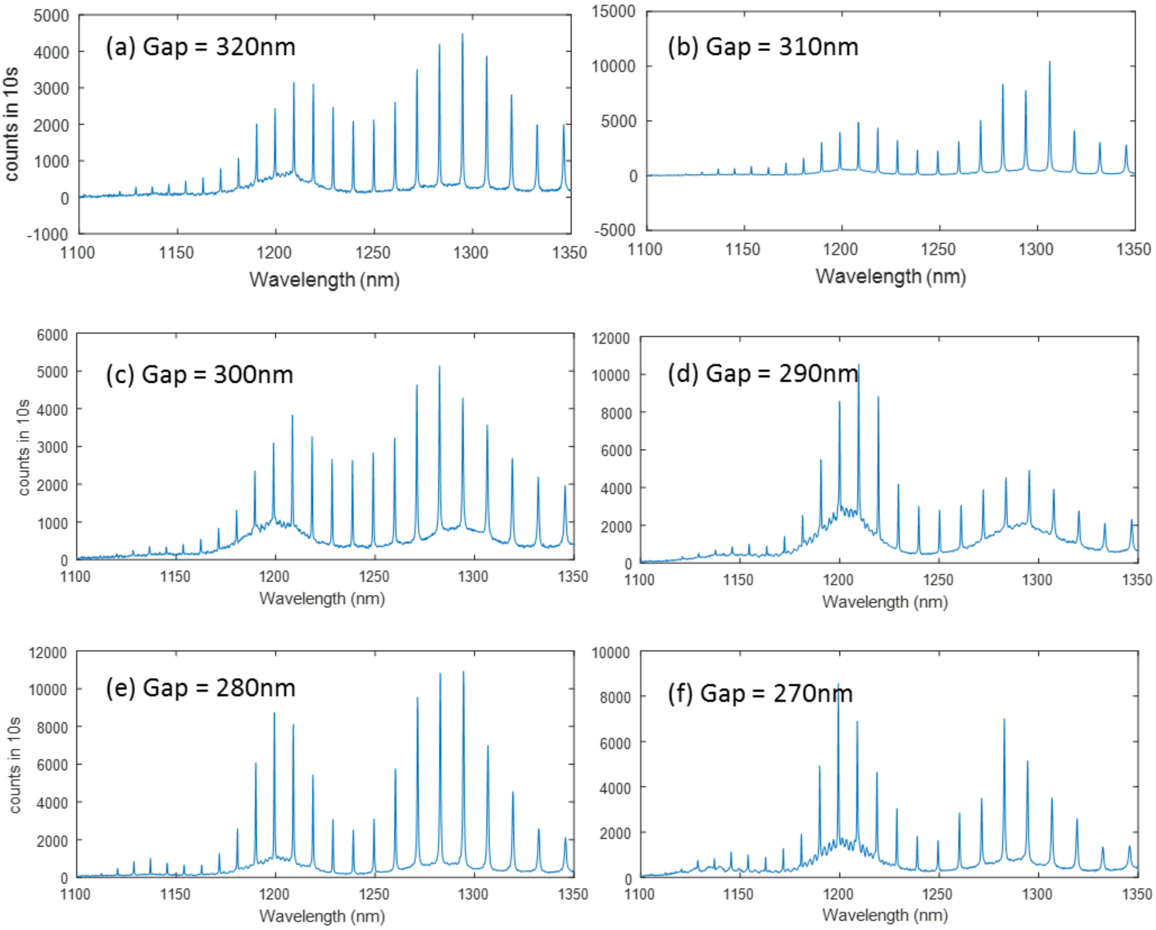

Figure 4.20 Collected photon counts in 10s from the ring resonators shown in Figure.4.17.

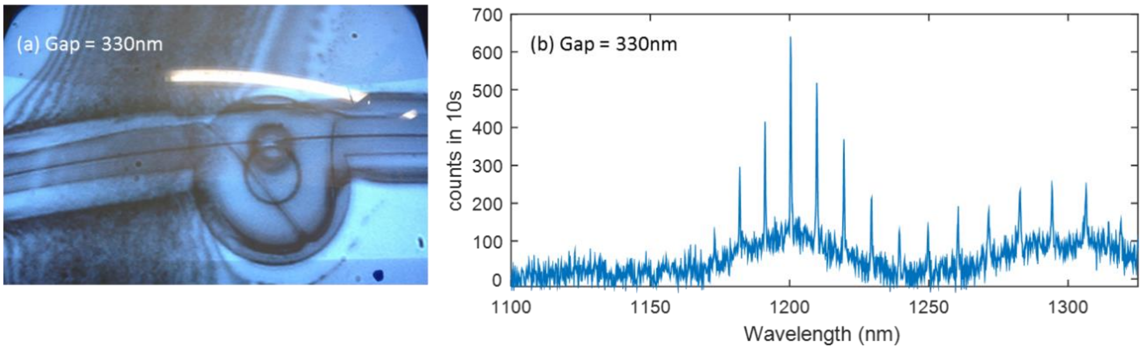

Figure 4.21 (a) Optical view of the ring resonator with PFO-CNT ribbon deviating far from the ring resonator center. (b) Collected photon counts from ring resonator in (a).

Such s-SWNTs-PFO ribbon assumption has been verified by comparing the PL intensity at different locations of the chip cladding s-SWNTs-PFO layer, which revealed that larger PL intensity was collected in low transparent ribbons. Such comparisons have also been done between two TE mode resonating rings shown in Figure.4.22, of which the left ring was without s-SWNTs-PFO ribbon cladding and the right one was covered by a thick s-SWNTs-PFO ribbon. The collected photon counts of such two rings are shown in Figure.4.23. Much intense PL was collected in Figure.4.22.b, i.e. from the ring resonator with the ribbon cladding. On the contrary, the photon accounts from the ring without ribbon cladding were extremely weak.

To conclude, we figure out that baking assisted drop casting method helps dispersed s-SWNTs-PFO in toluene finally assembling into localized high concentration s-SWNTs-PFO ribbon cladding. These ribbons finally contain a large quantity of CNTs and thus can emit intense PL.

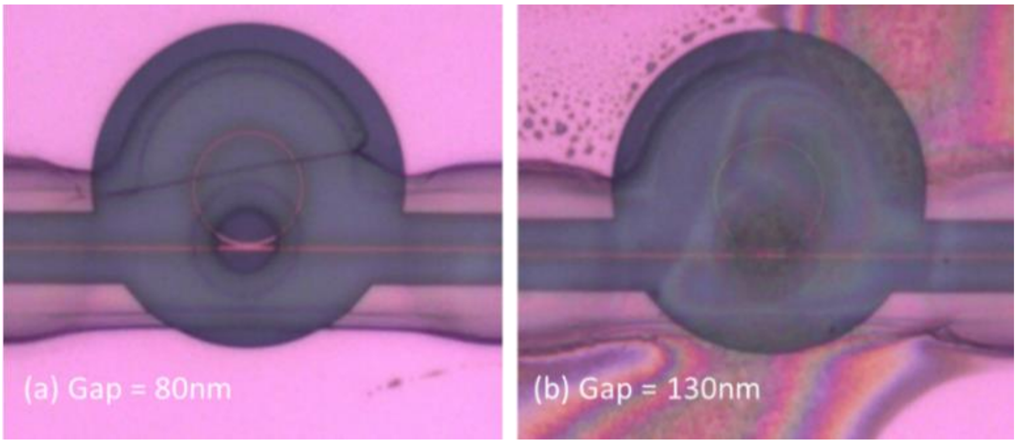

Figure 4.22 Two different silicon ring resonators; (a) is without PFO-CNT ribbon cladding and (b) is with a thick PFO-CNT cladding.

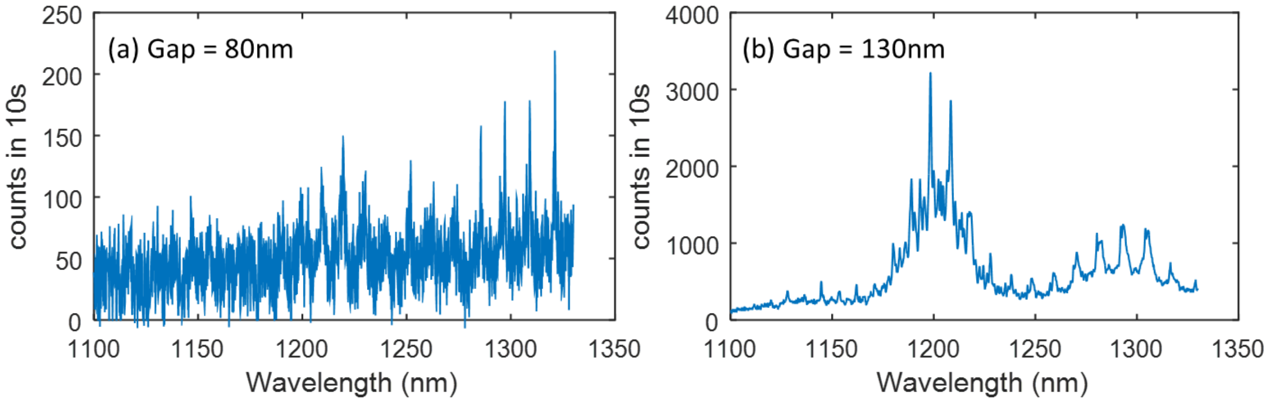

Figure 4.23 Collected photon accounts from the two ring resonators shown in Figure.4.20.

4.3.8 Removing the bus waveguide coupling

As we shown before, the peak photon counts of the resonances were 10~100 times stronger than photon counts from the waveguides. In order to avoid all the photon count from the waveguide, we integrated PFO-CNT cladding on silicon ring resonator only, as shown in Figure. 4.24. The obtained photon counts show signal noise emission ratio around 15dB-22dB, as shown in Figure. 4.25.a&b, in log and linear scales, respectively. Such a high ratio is very useful and meaningful for the potentials of integrated CNTs light emitters.

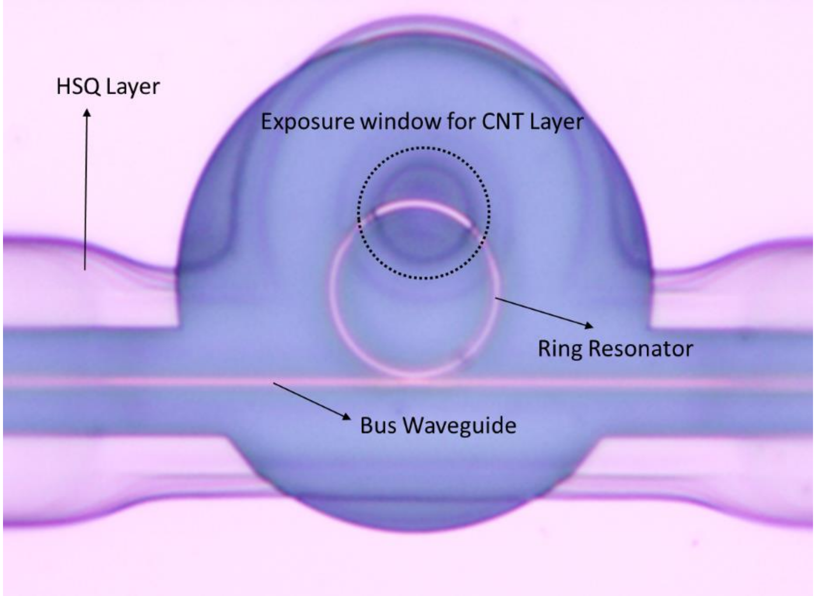

Figure 4.24 Hybrid integration region is designed on silicon ring only in this ring, which is different from the previous hybrid integration region case (open window on top of the coupler region). The PFO-CNT layer was later integrated as cladding.

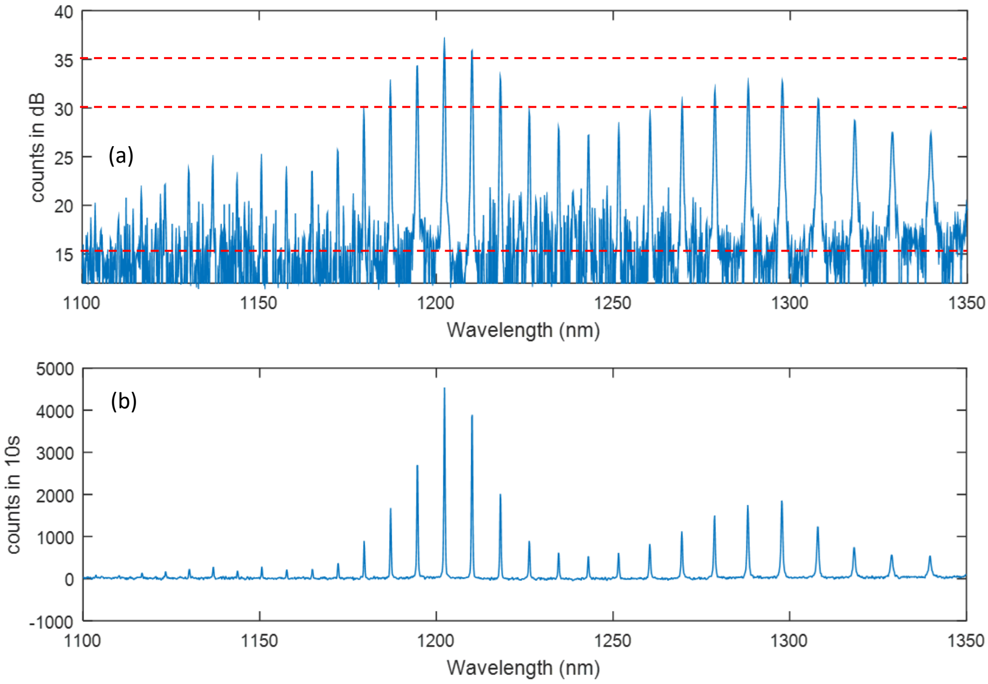

Figure 4.25 Collected photon accounts from the strip ring resonators with PFO-CNT cladding on ring resonator region, of which the exposure region is not on the coupler region but on ring only.

4.3.9 Conclusion

To sum up, we have integrated s-SWNTs-PFO as the cladding layers of tiny silicon ring resonators with 5µm radius. The integration method was crude but proved to be efficient to localize high concentration nanotubes on silicon ring resonators.

At first, we studied CNT PL coupling in silicon resonator coupler region to compare PL coupling efficiencies between bus waveguides and ring resonator. The PL coupling efficiency of the straight bus waveguide turned out to be excitation polarization dependent, which was useful to control the PL competition of the ring resonator and bus waveguide. The resonance PL peaks could be two orders of magnitude higher than the coupled intensity from the bus waveguide. The total coupled photons accounts from resonance spikes took half portion of the full integrated PL accounts. By removing the bus waveguide coupling, we showed that the PL signal directly coupled into the ring resonator intrinsically has 15-22dB signal-noise ratio rejection.

4.4 CNTs Integration in nano cavities

Based on discussion above, new efforts have been performed to study the CNT PL enhancement by the use of silicon nanobeam cavities. State of art works have been reported by bridging CNTs in the center of the 2D photonic crystals [229], 1D silicon nanobeam cavities [118] and SiN nanobeam cavities [65]. However, all these works have been constrained in the aspect that only few nanotubes were integrated in the center of cavities, and attempts to prove lasing effects with CNTs thus failed.

In this section, we propose the integration of PFO-CNT layers on top of hybrid nanobeam cavities, having an air-band mode cavity and dielectric-band mirror spatial distributions on the two sides, as shown in Figure.4.28.

To study the PL coupling from hybrid CNT-PFO nanobeam cavities, we first characterized the PL of hybrid CNT-cavities from our micro-PL setup operating in free space (see Figure.4.26 and Figure.4.11). In order to accurately collect PL, we used a low pass filter before the Ti:Sa laser to filter away long wavelength photons and a long pass filter to reject pump photons. By this way, we collected a huge CNT PL from our high concentration s-SWNTs-PFO ribbon layers, which made it very difficult to resolve the cavity resonance enhancement because the photons coupled into the nanobeam cavity mode were negligible in comparison with photons emitted from the thick PFO-CNTs ribbon (see section 4.3). Therefore, we conducted PL studies at places where the s-SWNTs-PFO layers were homogenous and visually transparent rather than on top of s-SWNTs-PFO ribbons.

4.4.1 CNT integration with air-dielectric nanobeam cavities

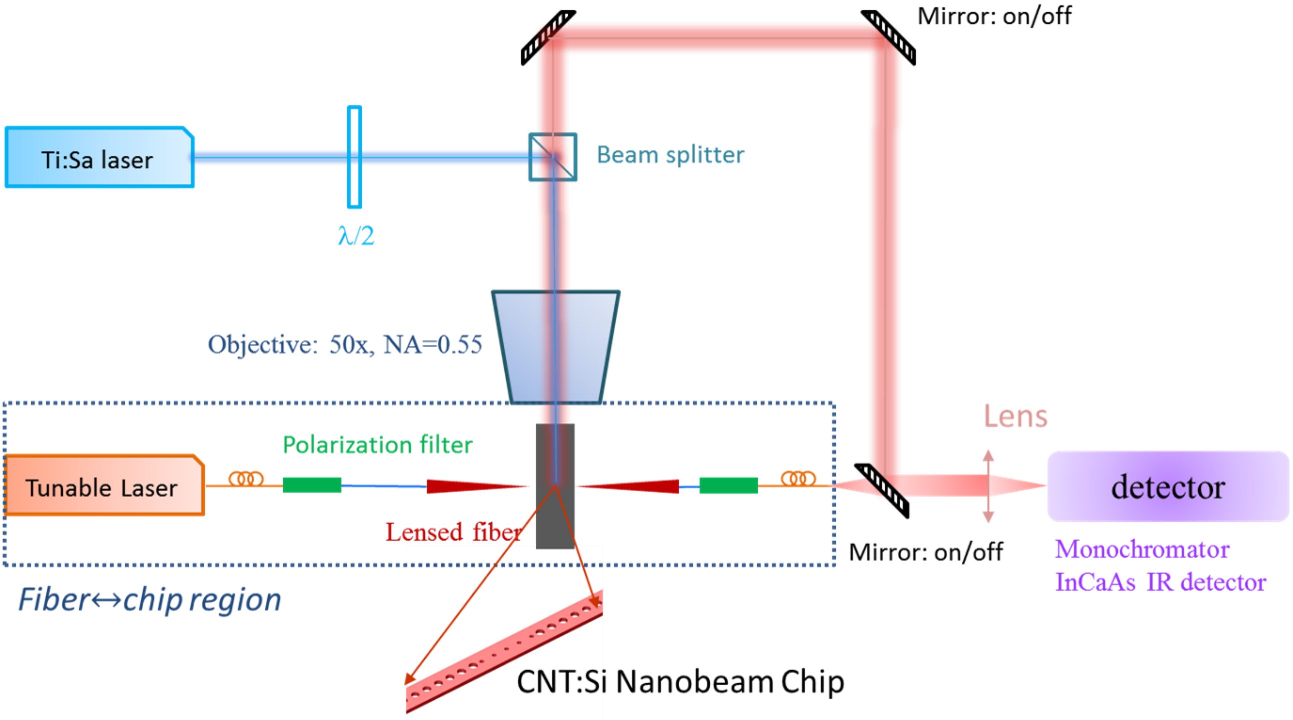

Figure 4.26 Schematic setup used to characterize the PL enhancement from SOI waveguide nanobeam cavities. For the measurements, the PL resonances are resolved from free space.

The excitation beam was focused on the central air-band mode cells, as shown in Figure.4.26 and Figure.4.27 characterized by a large mode confinement factor (Γ_{CNT}^{High}) in the low index s-SWNTs-PFO layers. As CNTs were distributed everywhere, it was necessary to minimize light absorption from CNTs outside the pump excitation regions. In this view, the dielectric mode mirrors, where optical modes are mainly confined inside silicon, brought help. Such kind of nanobeam design ensures large PL coupling efficiency in the central pumping spot and low CNT absorption outside the pump area at the same time.

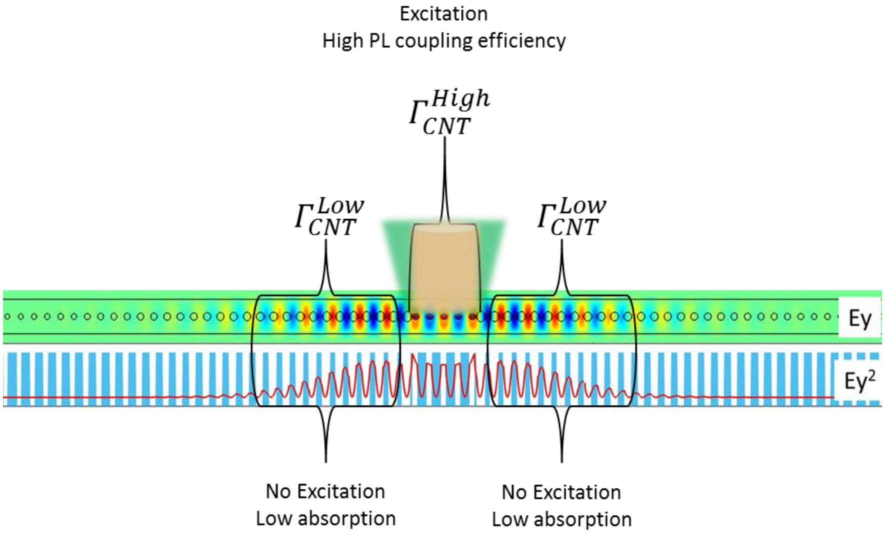

Figure 4.27 Schematic picture to show the pump excitation on nanobeam cavities.

Experimental studies were performed under all above expectations. As the air mode center of the nanobeam cavity was very small, small iteration searches of the right pumping position were required in order to find the resonance peaks. To easily find out the resonance peak, we choose a proper pumping power of 1.6mW. The found resonance is shown in Figure.4.28, corresponding to 200s collection time. In order to estimate the pumping power dependence of this cavity mode enhanced PL peak, we switched pumping power down to 0.2mW and then found a very weak resonance. A further increasing pump power to 1.2mW showed that the resonance peak gradually grew stronger and then reached saturation. The discussed resonance peak intensity here was referred to the CNT(8,7) PL emission peak @ λ=1.28µm. As shown before in section 4.3.4, the ring resonance enhanced CNT PL linearly increased with pump power and then saturated when pump power was over 1.6 mW. On the contrary to the evolution of the PL coupled ring resonances, here, we found that PL resonances from the nanobeam cavities did not linearly increase with pump power before 1.6mW.

The first obtained results are shown in Figure.4.28 and Figure.4.29. However, such nonlinear growth of the resonance peak is weak in comparison with CNT emission (background) but strong enough to evaluate the capabilities of nanobeam cavity for hybrid integration.

To quantitatively show how the resonance intensity varied referred to the CNT PL emission maximum around λ=1.28µm, we analyzed the *Q*-factors of the resonance by fitting the resonance peaks with Lorentzian shapes, as shown in Figure.4.30.b. The base of the Lorentz function was chosen at 0, meaning that the integral of the Lorentzian function contained photons emitted both from background CNTs and from the nanobeam cavity. If the photons from background and cavity would have increased with the same rate ($R_{CNT} = R_{Res}$), the fitted linewidth of the Lorentzian shape should have remained constant. If $R_{CNT} < R_{Res}$, *Q* should increase, otherwise *Q* should decrease. Experimentally, we found a *Q* increase and then a saturated behavior, as displayed in Figure.4.29.b. Accordingly, the resonance linewidth decreased from 0.75nm to 0.6nm, which also meant a *Q* increase. These preliminary results mean that the optical excitation of CNTs, which was coupled within the nanocavity, probably revealed a partial contribution of stimulated emission.

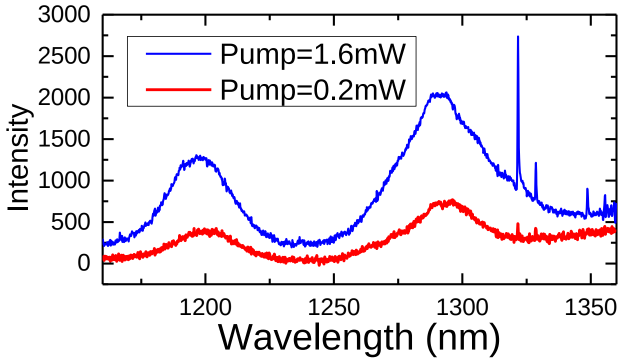

Figure 4.28 PL resonances obtained from two extreme pumping powers and done in two successive measurements.

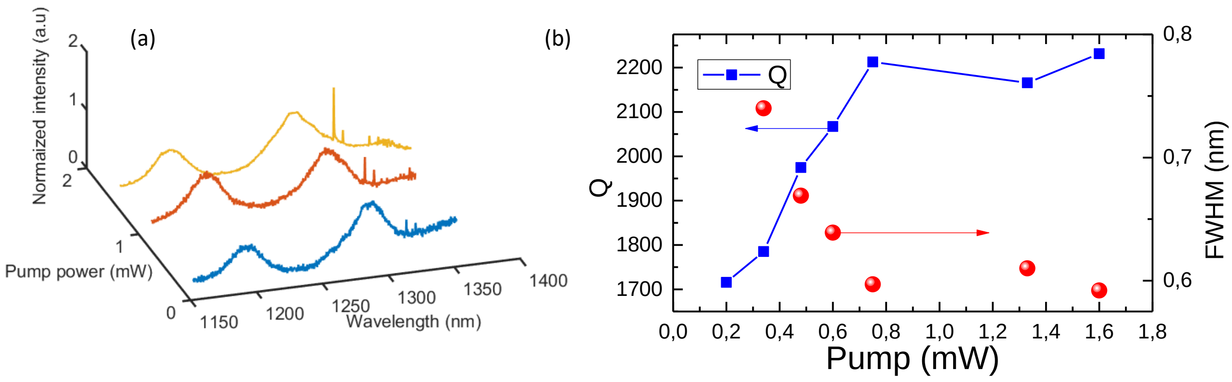

Figure 4.29 PL resonances change as function of the pump power, the *Q* factors and line width of the resonances Vs pumping power.

Different measurements were performed to study the PL resonance evolution by optically pumping different nanobeam positions, as shown in Figure.4.30. We regularly repeated these results in the pumping power range (0mW-2.5mW), i.e. linewidth narrowing of resonances peaks and PL resonance height exceeding the CNT emission, as shown in Figure.4.30.a. The strongest linewidth narrowing was probed, which decreased from 1.03nm to 0.65nm and *Q*-factor became nearly two times larger. The ratios of peak intensity (I_{Res}) to CNT emission (I_{CNT}) are depicted in Figure.4.31and show an increasing trend, which also supports that $R_{CNT} < R_{Res}$. Besides, the resonance wavelengths were found to remain nearly constant, which meant that the studied hybrid nanobeam cavity with CNT-PFO cladding layer could get rid of variations of the pump power and temperature (Figure.4.31.)

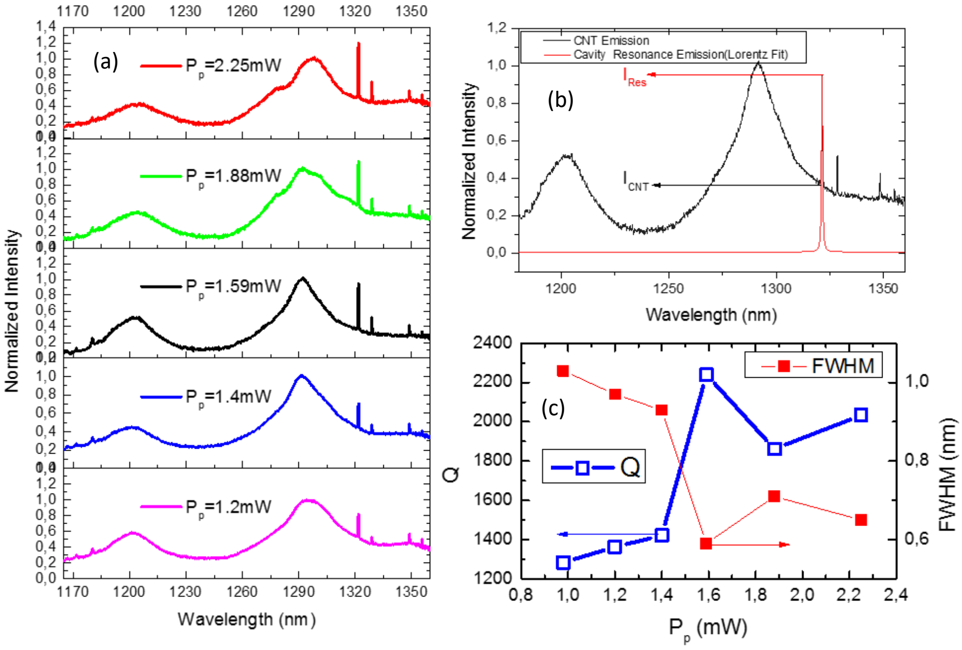

Figure 4.30 PL resonances change as a function of the pump power. The *Q* factors and line width of the resonances Vs pumping power.

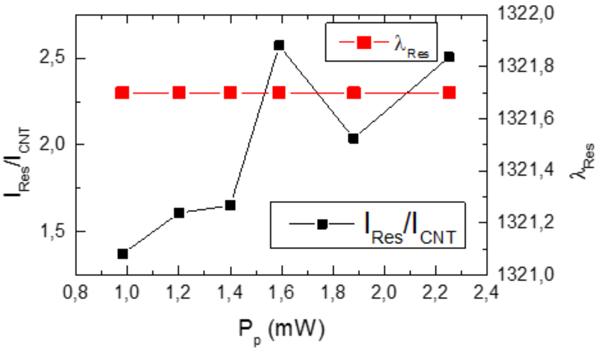

Figure 4.31 The ratios (I_{Res}/I_{CNT}) and resonance wavelength as function of the pumping power.

4.4.2 Conclusion

In this section we explored CNT hybrid integration with nanobeam cavities. Compared with silicon ring resonators, nanobeam cavities investigated here have ultra-small mode volumes, several orders of magnitude lower than micro-ring resonator ones. Hence, Purcell-like factor Q/V is very high and potentially can help in optical gain characteristics.

The obtained results reveal that the PL resonance enhancement due to nano cavities exhibited non-linear growth as a function of the pump power. The resonance of the PL peak intensity grew faster than uncoupled CNT PL emission when increasing the pumping power, which was accompanied by a line width narrowing of the resonance PL peak. These results reveal a possible trend of CNT PL towards stimulated emission and bring the expectation of further demonstration of CNT lasing with *ps*-*fs* pulsed lasers.

4.5 Conclusion

In this chapter, we reported intense PL coupling between high concentration PFO-CNT cladding and silicon micro ring resonators, which intrinsically enabled more than 10^5 photons account/s coupling into the silicon waveguides. Excitation polarization dependence has been proved when the pumping light beam was focused in the directional coupler regions of micro-rings, thus enabling the control of the coupling competition between straight bus waveguides and ring resonator.

We also found preliminary nonlinear increase of the PL intensity in the nanobeam cavity as a function of the pump power and linewidth narrowing of the resonance peak due to the resonance signal intensity (I_{res}) faster growth than the background uncoupled CNT emission.

Further investigations could be realized by pumping hybrid silicon nano cavities or ultra-low loss compact resonators with high concentration CNT cladding layers with pulsed laser beams.

Conclusion and perspectives

This thesis is a contribution to the integration of active materials including Erbium-doped and carbon nanotubes rich layers on silicon for on-chip light emission. Hollow core silicon and silicon nitride photonic waveguides and devices are designed, fabricated, and characterized in the near-1.3µm and near-1.55µm wavelength ranges. A specific focus is on the use of slot waveguides, for which hollow core light confinement properties bring specific advantages when considering the integration of soft materials in silicon photonics including large light-matter overlap factors, reduced two-photon absorption in the telecommunication window, tight confinement of electric fields, ultra-small cavity mode volumes, high optical sensitivities, with the possibility to combine all these points with slow light or localized modes (resonating modes).

The thesis research achievements and contributions can be summarized in three parts: (1) The development of low losses, compact, high *Q*-factor silicon passive photonic structures; (2) The exploration of optical gain properties of hybrid silicon waveguides and resonators through collaborations with material scientists, which focused on the study of Yb^{3+} co-doped Erbium nano particles and high concentration Erbium atomic layer deposited thin films; (3) The integration of high concentration semiconducting single wall CNTs-PFO within silicon ring resonators and hollow core nanobeam cavities and the demonstration of strong photoluminescence (PL) enhancement through cavity/resonator effect, with preliminary encouraging results towards CNT-based integrated optical sources.

More specifically, in the frame of passive waveguide structures development, we designed, fabricated, and characterized, within the silicon-on-insulator and silicon nitride platforms, a range of photonic structures including strip/slot waveguides, micro disks, strip/slot ring resonators, and micro cavities to prepare a set of passive device building blocks needed for hybrid integration on silicon. We devoted our early efforts to optimize slot waveguides with low propagation losses. Several achievements have been made in that direction in simple waveguide and resonator configurations, respectively. Time was spent to understand and manage to control the electron beam lithography equipment tool employed to write nano width (20-60nm), long paths slot waveguides with constant widths while removing stitching errors. Related electron beam doses and step sizes were also studied. As a result, silicon slot waveguides and slot ring add-drop resonators filled with index liquids (refractive index ~1.46) with linear propagation losses 2-7 dB/cm (depending on electron beam lithography exposure area) and *Q*-factors up to 30,000, respectively, have been demonstrated at around λ=1.55µm. Silicon nitride slot waveguides losses were minimized down to ~4dB/cm for compact long spiral structures (2cm long, within ~500µm×500µm). Air mode nanobeam cavities were also investigated, leading to nanobeam cavities with mode volumes V ~$0.03(\lambda/n)^3$ and Q-factors ~70,000 when filled with soft materials. Besides, an air-band mode nanobeam cavity design method enabling a flexible choice of cavity design in air-band resonating mode with dielectric-kind mirror confinement has also been proposed and investigated.

In view of on-chip light amplification, the integration of Erbium-doped materials was studied under two collaborations: one with Prof. Daming Zhang’s team, from the State Key Laboratory on Integrated Optoelectronics, Jilin University, China, and one with Prof.Zhipei Sun’s group, in Department of Micro- and Nanosciences, Aalto University, Finland. Erbium doped layers coming from Jilin were composed of Er^{3+} and Yb^{3+} co-doped core {shell} α-$NaYF_4$ {β-$NaLuF_4$} nanoparticles which were copolymerized with methyl methacrylate (MMA) to synthesize nanocomposite (PMMA-NPs: Er^{3+}/Yb^{3+}). Such special core-shell material is able to reduce surface fluorescence quenching by the shell layer and hence results in strong PL emission. We conducted the experimental characterization that led to the demonstration of an internal net gain up to 10-17dB/cm at λ=1.53μm in Erbium doped polymer rib waveguides fabricated in Jilin. We also tried to integrated this Erbium doped nano materials into our silicon nitride slot waveguide, of which the total transmission losses were~7-12dB/cm, i.e. 2-3 times higher than the initial passive losses. At the present time of this work, internal net gain was not confirmed in such hybrid waveguides and still remains under future investigation. The second Erbium doped material available during this thesis was based on Er_2O_3/Al_2O_3 atomic layers, grown in Aalto University. This collaboration was devoted to integrate high Erbium ion concentration (~$10^{21}/cm^3$) in oxide cladding layers on top of silicon nitride slot waveguides, which were fabricated in our group for the demonstration of on-chip optical net gain. The carried out experiments have conducted to the demonstration of 1.5-22.8dB/cm net gain range for sub millimeter length waveguides.

For light emission on silicon, hybrid integration of light emitting SWCNTs in the cladding layers of ring resonators and nanobeam cavities has been investigated. High concentration PFO wrapped semiconductor CNT toluene solution was used to integrate CNT-PFO polymer on top of silicon. At first, we studied the coupling of SWCNTs photoluminescence (PL) in silicon micro-ring resonators and compared PL coupling efficiencies between the bus waveguide and the ring resonator in several configurations. The PL coupling efficiency of the straight bus waveguide turned out to be excitation polarization dependent, which was proposed as a mean to control the competition between the relative balance between the ring resonator and bus waveguide PL. We showed that the resonance PL peak intensity could be two orders of magnitude higher than the PL intensity coupled into the bus waveguide. Besides, the total coupled photon counts from resonance spikes contributed nearly half of the full integrated PL accounts. By removing the PL collection from the bus waveguide, we showed that the PL signal directly coupled into the ring resonator has intrinsically 15-22dB of signal-noise ratio rejection. Besides, we also reported efforts to investigate potential intensity buildup threshold and linewidth narrowing properties of the hybrid CNT-silicon ring resonators. Additionally, we explored CNT hybrid integration within ultra-small mode volume nanobeam optical cavities, and hence with larger Purcell-like Q/V factors if compared with silicon microring resonators. The obtained results revealed that the PL resonance enhancement due to nanobeam cavity field confinement exhibited a nonlinear growth as a function of the pump power. It was shown that the resonances of the PL intensity grown faster than the base CNT PL emission when increasing the pumping power, which was accompanied by a linewidth narrowing of the resonance PL peak. The main constraints to further demonstrate nonlinear growth of the resonance turned due to the pumping laser power and pulse duration. Measurements under pulse lasing pumping recently achieved led to a threshold behavior in term of PL emission versus pumping power.

To conclude, during this thesis, we explored low loss slot waveguides in silicon and silicon nitride on insulator waveguides, high Q-factor slot resonators and air-band mode nanobeam cavities aiming at serving as hollow core photonic structures for the on-chip integration of active materials, for which we focused our efforts on two families: Erbium doped polymers and oxides and CNTs-PFO polymers. Promising results, i.e. internal net gain of Erbium hybrid slot waveguides, strong CNT PL coupling with silicon ring resonators and CNT PL enhanced emission were provided and discussed. Overall, this work indicates that integrating active light emitting materials within hollow silicon photonic structures may be a promising solution for the realization of light sources/amplifiers in silicon photonics.

Based on obtained results, several perspectives can be anticipated for future works:

First, slot waveguide losses could be further minimized by sidewall roughness chemical polishing. Hollow core slow light photonic crystal waveguides could be developed in order to further enhance the Erbium amplifications by using slow light effects. Wider slot and thicker rail with silicon nitride waveguides could be developed to further ease the infiltration of Erbium doped nano-particles.

Regarding the integration of Erbium doped layers, the present stage of progress has revealed promising optical gain results. Further progress in material preparation and integration within silicon and silicon nitride waveguides and resonators will have to be pursued.

Last, CNTs integration within silicon photonic devices has revealed a strong potential. To go one step farther, CNTs could be aligned locally by using a dielectrophoresis method, which could lead to a better control of light absorption and emission properties in integrated configurations. With aligned CNTs, CNTs PL would have better coupling efficiencies than what CNTs random distributions can provide. Different types of nanobeam cavities could be studied with suited to provide different *Q*-factors, mode volumes and air-band mode confinement factors. These additional studies would likely help to investigate lasing characteristics from CNTs hybrid nanobeam cavities. One immediate important experimental milestone in that direction would be to pump hybrid CNT-silicon resonators with a fs/ps pulsed laser rather than with a CW laser, as down in the present work. Besides, ring resonators or nanobeam cavities, with aligned CNTs and properly fabricated electrodes on two areas of CNT-rich layers, could be also used to study light absorption, modulation, and photodetection based on silicon-CNTs devices.

Appendix

Appendix A--Simulation model of 1480nm pumped regime

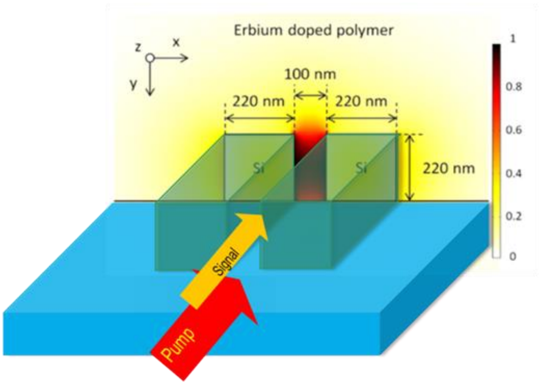

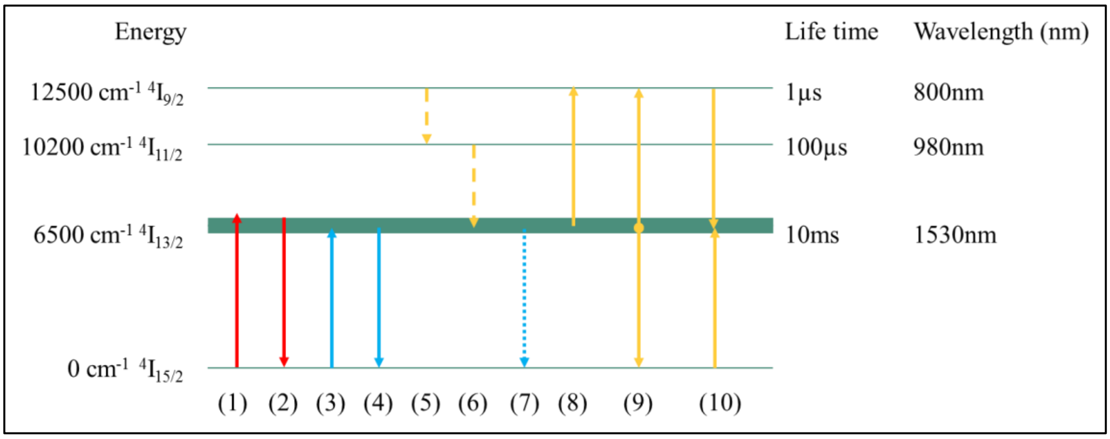

Figure.1 Schematic energy levels of Er3+ ions and transitions that happen during 1480nm wavelength optical pumping.

The simulation model of the erbium hybrid slot waveguide amplification can be divided in the following steps: (1) Calculating the normalized electric field of the signal and pump; (2) Sampling the cross-section of the slot waveguide into finite number of small areas and distinguishing them by materials; (3) Each sampled Erbium area needs one time "amplification simulation" according to its optical intensity $I_{s,p}(x,y)$ and then whole cross-section sampled area properties are integrated to calculate the optical signal and pump changes by one propagation step Δz. The mathematical calculation of the 4-level "amplification simulation" is detailed in the following paragraphs and in the Figures Appendix.

Table.1 Spectroscopic parameters used for simulation model of 1480nm pumped regime

Spectroscopic properties	Names	Value
Signal wavelength	λ_s	1530 nm

Pump wavelength	λ_p	1480 nm
Absorption cross section at 1480 nm	σ_{12p}	7.53×10^{-25} m^2
Emission cross section at 1480 nm	σ_{21p}	0.5×10^{-25} m^2
Absorption cross section at 1550 nm	σ_{12s}	4.1×10^{-25} m^2
Emission cross section at 1550 nm	σ_{21s}	7.53×10^{-25} m^2
ESA cross section	σ_{24p}	0.85×10^{-25} m^2
Spontaneous emission rate of $I_{13/2}$	A_{21}^{R}	111 s^{-1}
Spontaneous emission rate of $I_{11/2}$	A_{32}^{NR}	1×10^{5} s^{-1}
Spontaneous emission rate of $I_{9/2}$	A_{43}^{NR}	1×10^{7} s^{-1}
Up-conversion coefficient	C_{up}	1×10^{-24} m^3/s
Cross-relaxation coefficient	C_{14}	~10^{-22} m^3/s
Erbium ion concentration	N_{Er}	10×10^{26} at/m^3

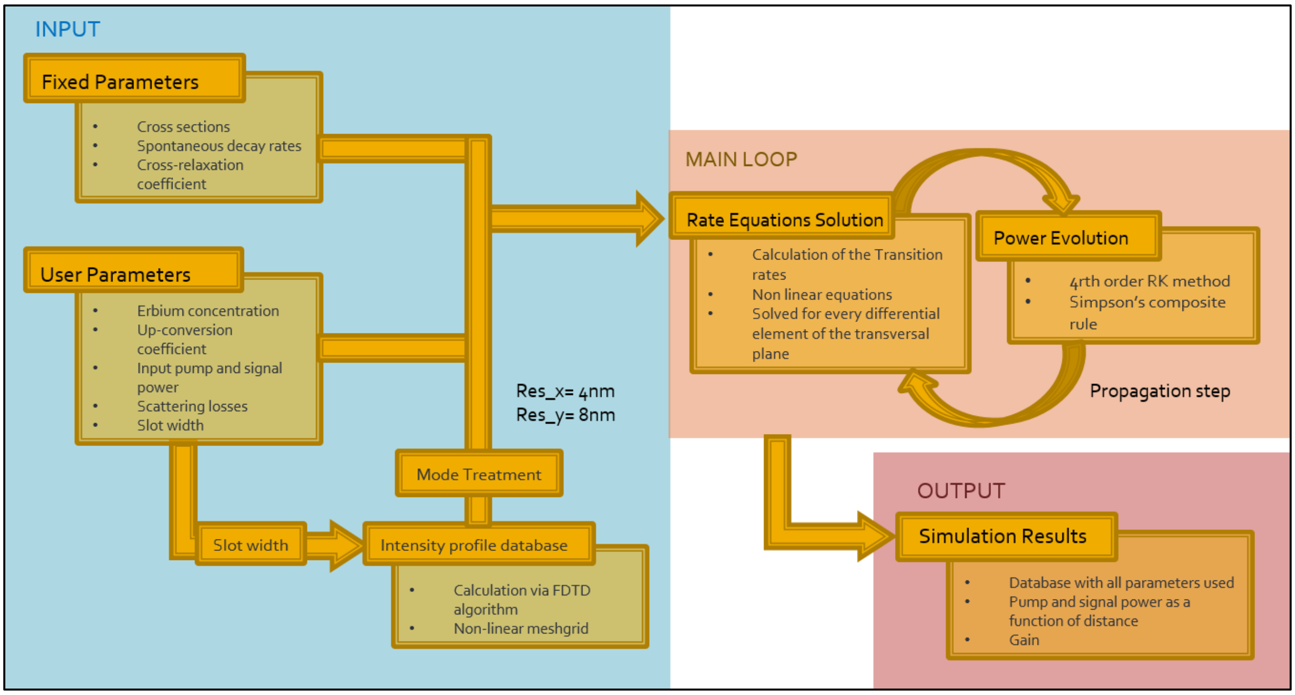

Figure.2. Schematic graph of the numerical steps of the Erbium amplification in slot waveguides.

The simulation of 1480nm pumped regime is mainly based on solving the four-level rate equations (1)-(3) and a conservation equation (4), which is solved in every sampled Erbium area.

$$\frac{\mathrm{d}n_1(x,y,z)}{\mathrm{d}t} = -(W_{12}+R_{12})n_1 + (W_{21}+R_{21}+A_{21}^{R})n_2 + C_{up}n_2^2 - C_{14}n_1n_4 \quad (1)$$

$$\frac{\mathrm{d}n_2}{\mathrm{d}t} = (W_{12}+R_{12})n_1 - (W_{21}+R_{21}+A_{21}^{R}+R_{24}^{ESA})n_2 + A_{32}^{NR}n_3 - 2\left(C_{up}n_2^2 - C_{14}n_1n_4\right) \quad (2)$$

$$\frac{\mathrm{d}n_4}{\mathrm{d}t} = R_{24}^{ESA}n_2 + C_{up}n_2^2 - C_{14}n_1n_4 - A_{43}^{NR}n_4 \quad (3)$$

$$N_{Er} = n_1 + n_2 + n_3 + n_4 \quad (4)$$

where n_i is the population in the energetic level i, N_{Er} is the total Er concentration.

In steady-state regime, all time derivatives are zero ($d/dt = 0$), bringing a nonlinear system of four unknown quantities and four equations. For convenience, the spatial-dependencies of parameters is omitted but is implicit, namely: $n_1 = n_1(x, y, z)$, $n_2 = n_2(x, y, z)$, $n_3 = n_3(x, y, z)$ and $n_4 = n_4(x, y, z)$, which represent the population densities of the four energy levels shown in Figure.3.32.

The description of transitions within the metastable and the pump levels are (analog expressions are used to calculate R coefficients):

$$W_{ijk} = \frac{\lambda_k}{hc}\sigma_{ij}(\lambda_k)I_k(x, y)P_k(z) \tag{5}$$

where σ_{ij} is the cross-section between the energetic levels i and j, I_k and P_k are the normalized intensity (in the transverse plane) and the power (in the propagation direction), respectively; k representing either the pump or the signal beam (namely $k = p$ or s).

At a given z point, the $n_i = n_i(x, y, z)$ Erbium states are known in the full cross-section (active material) and the stimulated emission and absorption probabilities $W_{ijk}(x, y)$ are locally obtained in the full (x, y) plane enabling to update the signal and pumping powers $P_s(z)$ and $P_p(z)$ from z to $z + dz$, respectively, according to the following system of two coupled equations:

$$\frac{\mathrm{d}P_s(z)}{\mathrm{d}z} = -P_s(z)\iint I_s(x, y)[\sigma_{12s}(\lambda_s)n_1(x, y, z) - \sigma_{21s}(\lambda_s)n_2(x, y, z)]\,\mathrm{d}x\mathrm{d}y - P_s(z)\alpha_s \tag{6}$$

$$\begin{aligned}\frac{\mathrm{d}P_p\,(z)}{\mathrm{d}z} = -P_p(z)\iint I_p(x, y)\big[\sigma_{12p}(\lambda_p)n_1(x, y, z) - \sigma_{21p}(\lambda_p)n_2(x, y, z) \\ + \sigma_{24p}(\lambda_p)n_2(x, y, z)\big]\,\mathrm{d}x\mathrm{d}y\ - P_p(z)\alpha_p\end{aligned} \tag{7}$$

where α_S and α_P represents the linear scattering losses of the signal or pump powers. The Excited State Absorption (ESA) could be modeled by using an ESA cross-section by the expression:

$$R_{24}^{ESA} = \frac{\lambda_p}{hc}\sigma_{24p}(\lambda_p)I_p(x, y)P_p(z) \tag{8}$$

As it can be seen from the mathematical expressions, the transversal intensity distribution is considered independent from the power. In this way, a normalization of the mode intensity is made over the effective area and the mode shape is assumed to be constant over the propagation length, the optical power being the quantity fully carrying the information related to the balance between the losses and the effective optical gain. The ESA process for the signal beam is neglected due to the assumed small powers.

The non-linear rate equations are reduced to a 4th order polynomial equation system, which is numerically solved for every differential step. As soon as the population occupancies are known, the integration can proceed in successive steps towards the waveguide output. Composite Simpson's rule is used to consider the discontinuity of the field generated by the slot. To calculate the propagation of the pump, signal and gain, a fourth-order Runge-Kutta routine was implemented. Due to the short propagation distances, amplified spontaneous emission has no important influence on the amplifier gain, so is neglected in the slot waveguide model.

Appendix B--Simulation model of 980nm pumped regime

Compared with appendix A, the difference of the 980nm pumped regime is to solve the 6-level rate equations (1)-(4) and a conservation equation (5)-(6). The used spectroscopic parameters are listed in the table.3.33. With help of the above simulation model, the 980nm pumped regime has been described accordingly.

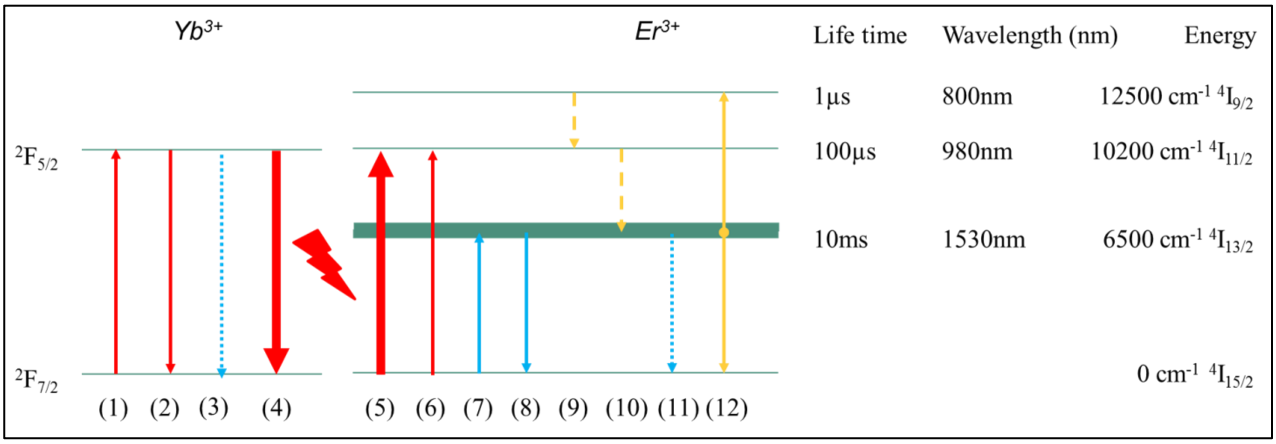

Figure.3 Schematic energy levels of Er3+ ions and transitions that happen during 980nm wavelength optical pumping.

Table.2Spectroscopic parameters used for simulation model of 980nm pumped regime

Spectroscopic properties	Names	Value
Signal wavelength	λ_s	1530 nm
Pump wavelength	λ_p	980 nm
Er Absorption cross section	σ_{12p}	6.14×10^{-25} m^2
Er Absorption cross section	σ_{13p}	1.27×10^{-25} m^2
Er Emission cross section at	σ_{21p}	5.71×10^{-25} m^2
Yb Absorption cross section at	σ_{56}	2.3×10^{-25} m^2
Yb Emission cross section at	σ_{65}	3.6×10^{-25} m^2
Spontaneous emission rate of $I_{13/2}$	A_{21}^{R}	111 s^{-1}
Spontaneous emission rate of $F_{5/2}$	A_{65}^{R}	500 s^{-1}
Nonradiative decay rate of $\mathbf{I}_{11/2}$	A_{32}^{NR}	1×10^{5} s^{-1}
Nonradiative decay rate of $\mathbf{I}_{9/2}$	A_{43}^{NR}	1×10^{7} s^{-1}
Up-conversion coefficient	C_{up}	1×10^{-24} m^3/s
Cross-relaxation coefficient	C_{14}	1×10^{-22} m^3/s
Erbium ion concentration	N_{Er}	1×10^{26} at/m^3
Ytterbium ion concentration	N_{Yb}	10×10^{26} at/m^3
Scattering loss at 980nm	α_p	5dB/cm
Scattering loss at 1550nm	α_s	5dB/cm

$$\frac{dN_1}{dt} = -(W_{13} + W_{12})N_1 + (W_{21} + A_{21}^{R})N_2 + C_{up}N_2^2 - C_{16}N_1N_6 = 0 \tag{1}$$

$$\frac{dN_2}{dt} = (W_{12} - A_{12})N_1 - W_{21}N_2 + A_{32}^{NR}N_3 - 2C_{up}N_2^2 = 0 \tag{2}$$

$$\frac{dN_3}{dt} = W_{13}N_1 - A_{32}^{NR}N_3 + A_{43}^{NR}N_4 + C_{16}N_1N_6 = 0 \tag{3}$$

$$\frac{dN_6}{dt} = -C_{16}N_1N_6 + W_{65}N_6 - A_{65}n_6 + W_{65}n_5 = 0 \tag{4}$$

$$N_{Er} = N_1 + N_2 + N_3 + N_4 \tag{5}$$

$$N_{Yb} = N_5 + N_6 \tag{6}$$

Reference

[1] L. Vivien and L. Pavesi, *Handbook of Silicon Photonics*. 2013.

[2] B. M, B. J-P, C. R, D. E. M. A. N. H, G. T, S. S, I. A, S. L, S. M, S. T, T. H, T. R, V. A. N. R. M, V. H, and W. F, "Towards and Beyond 2015: technology, devices, circuits and systems," 2015.

[3] International Technology Roadmap for Semiconductors (ITRS), "International Technology Roadmap for Semiconductors (ITRS)," *Itrs 2013*, pp. 1–51, 2013.

[4] C. Sun, M. T. Wade, Y. Lee, J. S. Orcutt, L. Alloatti, M. S. Georgas, A. S. Waterman, J. M. Shainline, R. R. Avizienis, S. Lin, B. R. Moss, R. Kumar, F. Pavanello, A. H. Atabaki, H. M. Cook, A. J. Ou, J. C. Leu, Y.-H. Chen, K. Asanović, R. J. Ram, M. A. Popović, and V. M. Stojanović, "Single-chip microprocessor that communicates directly using light," *Nature*, vol. 528, no. 7583, pp. 534–538, 2015.

[5] L. Pavesi and D. J. L. Editors, *Silicon Photonics III*, vol. 122. Berlin, Heidelberg: Springer Berlin Heidelberg, 2016.

[6] P. Dong, L. Chen, and Y. Chen, "High-speed low-voltage single-drive push-pull silicon Mach-Zehnder modulators," *Opt. Express*, vol. 20, no. 6, p. 6163, 2012.

[7] F. Y. Gardes, D. J. Thomson, N. G. Emerson, and G. T. Reed, "40 Gb/s silicon photonics modulator for TE and TM polarisations.," *Opt. Express*, vol. 19, no. 12, pp. 11804–14, 2011.

[8] H. Xu, X. Xiao, X. Li, Y. Hu, Z. Li, T. Chu, Y. Yu, and J. Yu, "High speed silicon Mach-Zehnder modulator based on interleaved PN junctions.," *Opt. Express*, vol. 20, no. 14, pp. 15093–9, 2012.

[9] L. Vivien, A. Polzer, D. Marris-Morini, J. Osmond, J. M. Hartmann, P. Crozat, E. Cassan, C. Kopp, H. Zimmermann, and J. M. Fédéli, "Zero-bias 40Gbit/s germanium waveguide photodetector on silicon," *Opt. Express*, vol. 20, no. 2, p. 1096, 2012.

[10] P. Dong, C. Xie, L. Chen, L. L. Buhl, and Y.-K. Chen, "112-Gb/s monolithic PDM-QPSK modulator in silicon.," *Opt. Express*, vol. 20, no. 26, pp. B624-9, 2012.

[11] L. Chen, C. R. Doerr, L. Buhl, Y. Baeyens, and R. A. Aroca, "Monolithically integrated 40-wavelength demultiplexer and photodetector array on silicon," *IEEE Photonics Technol. Lett.*, vol. 23, no. 13, pp. 869–871, 2011.

[12] L. Chen, C. R. Doerr, P. Dong, and Y. Chen, "Monolithic silicon chip with 10 modulator channels at 25 Gbps and 100-GHz spacing," *2011 37th Eur. Conf. Exhib. Opt. Commun.*, vol. 19, no. 26, pp. 1–3, 2011.

[13] A. Liu, H. Rong, M. Paniccia, O. Cohen, and D. Hak, "Net optical gain in a low loss silicon-on-insulator waveguide by stimulated Raman scattering," *Opt. Express*, vol. 12, no. 18, p. 4261, 2004.

[14] B. Jalali, V. Raghunathan, D. Dimitropoulos, and Ö. Boyraz, "Raman-based silicon photonics," *IEEE J. Sel. Top. Quantum Electron.*, vol. 12, no. 3, pp. 412–421, 2006.

[15] M. A. Foster, A. C. Turner, J. E. Sharping, B. S. Schmidt, M. Lipson, and A. L. Gaeta, "Broad-band optical parametric gain on a silicon photonic chip.," *Nature*, vol. 441, no. 7096, pp. 960–3, Jun. 2006.

[16] H. Rong, S. Xu, Y.-H. Kuo, V. Sih, O. Cohen, O. Raday, and M. Paniccia, "Low-threshold continuous-wave Raman silicon laser," *Nat. Photonics*, vol. 1, no. 4, pp. 232–237, 2007.

[17] L. I. Cary Gunn and Gianlorenzo Masini, "Closing in on Photonics Large-Scale Integration," 2007. [Online]. Available: http://www.photonics.com/Article.aspx?AID=31652.

[18] D. Marris-Morini, C. Baudot, J.-M. Fédéli, G. Rasigade, N. Vulliet, a. Souhaité, M. Ziebell, P. Rivallin, S. Olivier, P. Crozat, X. Le Roux, D. Bouville, S. Menezo, F. Bœuf, and L. Vivien, “Low loss 40 Gbit/s silicon modulator based on interleaved junctions and fabricated on 300 mm SOI wafers,” *Opt. Express*, vol. 21, no. 19, p. 22471, 2013.

[19] S. Grillanda and F. Morichetti, “Light-induced metal-like surface of silicon photonic waveguides.,” *Nat. Commun.*, vol. 6, p. 8182, 2015.

[20] Q. Lin, O. J. Painter, and G. P. Agrawal, “Nonlinear optical phenomena in silicon waveguides: modeling and applications,” *Opt. Express*, vol. 15, no. 25, pp. 16604–16644, 2007.

[21] L. Yin and G. P. Agrawal, “Impact of two-photon absorption on self-phase modulation in silicon waveguides.,” *Opt. Lett.*, vol. 32, no. 14, pp. 2031–2033, 2007.

[22] J. Leuthold, C. Koos, W. Freude, R. Osgood, J. Leuthold, C. Koos, and W. Freude, “Nonlinear silicon photonics,” *Nat. Photonics*, vol. 4, no. 8, pp. 535–544, Jul. 2010.

[23] J. D. E. B. Di Liang, “Recent progress in lasers on silicon,” *Nat. Photonics*, vol. 4, no. July, pp. 511–517, 2010.

[24] G. Roelkens, J. Van Campenhout, J. Brouckaert, D. Van Thourhout, R. Baets, P. R. Romeo, P. Regreny, A. Kazmierczak, C. Seassal, X. Letartre, G. Hollinger, J. M. Fedeli, L. Di Cioccio, and C. Lagahe-Blanchard, “III-V/Si photonics by die-to-wafer bonding,” *Mater. Today*, vol. 10, no. 7–8, pp. 36–43, 2007.

[25] D. Fehly, A. Schlachetzki, A. S. Bakin, A. Guttzeit, and H. H. Wehmann, “Monolithic InGaAsP optoelectronic devices with silicon electronics,” *IEEE J. Quantum Electron.*, vol. 37, no. 10, pp. 1246–1252, 2001.

[26] A. Y. Liu, C. Zhang, J. Norman, A. Snyder, D. Lubyshev, J. M. Fastenau, A. W. K. Liu, A. C. Gossard, and J. E. Bowers, “High performance continuous wave 1.3 μ m quantum dot lasers on silicon,” *Appl. Phys. Lett.*, vol. 104, no. 4, pp. 3–7, 2014.

[27] S. Tanaka, S.-H. Jeong, S. Sekiguchi, T. Kurahashi, Y. Tanaka, and K. Morito, “High-output-power, single-wavelength silicon hybrid laser using precise flip-chip bonding technology,” *Opt. Express*, vol. 20, no. 27, pp. 28057–69, 2012.

[28] B. R. Koch, E. J. Norberg, B. Kim, J. Hutchinson, J.-H. Shin, G. Fish, and A. Fang, “Integrated Silicon Photonic Laser Sources for Telecom and Datacom,” *Opt. Fiber Commun. Conf. Fiber Opt. Eng. Conf. 2013*, p. PDP5C.8, 2013.

[29] T. Shimizu, N. Hatori, M. Okano, and M. Ishizaka, “High density hybridly integrated light source with a laser diode array on a silicon optical waveguide platform,” *Integr. Photonics*, 2012.

[30] M. J. R. Heck, M. L. Davenport, and J. E. Bowers, “Progress in hybrid-silicon photonic integrated circuit technology,” *SPIE Newsroom*, Feb. 2013.

[31] III-V Lab, “III-V/Si Device Integration.” [Online]. Available: http://www.3-5lab.fr/core2.htm.

[32] P. Chaisakul, D. Marris-Morini, J. Frigerio, D. Chrastina, M.-S. Rouifed, S. Cecchi, P. Crozat, G. Isella, and L. Vivien, “Integrated germanium optical interconnects on silicon substrates,” *Nat Phot.*, vol. 8, no. 6, pp. 482–488, 2014.

[33] M. J. R. Heck, J. F. Bauters, M. L. Davenport, D. T. Spencer, and J. E. Bowers, “Ultra-low loss waveguide platform and its integration with silicon photonics,” *Laser Photon. Rev.*, vol. 8, no. 5, pp. 667–686, 2014.

[34] S. P. Singh and N. Singh, “Nonlinear Effects in Optical Fibers: Origin, Management and

Applications," *Prog. Electromagn. Res.*, vol. 73, pp. 249–275, 2007.

[35] M. a Foster, A. C. Turner, M. Lipson, and A. L. Gaeta, "Nonlinear optics in photonic nanowires.," *Opt. Express*, vol. 16, no. 2, pp. 1300–1320, 2008.

[36] I. Agha, M. Davanço, B. Thurston, and K. Srinivasan, "Low-noise chip-based frequency conversion by four-wave-mixing Bragg scattering in SiN_x waveguides," *Opt. Lett.*, vol. 37, no. 14, p. 2997, 2012.

[37] Q. Li, A. a Eftekhar, M. Sodagar, Z. Xia, A. H. Atabaki, and A. Adibi, "Vertical integration of high-Q silicon nitride microresonators into silicon-on-insulator platform.," *Opt. Express*, vol. 21, no. 15, pp. 18236–48, Jul. 2013.

[38] J. F. Bauters, M. J. R. Heck, D. John, D. Dai, M.-C. Tien, J. S. Barton, A. Leinse, R. G. Heideman, D. J. Blumenthal, and J. E. Bowers, "Ultra-low-loss high-aspect-ratio Si3N4 waveguides.," *Opt. Express*, vol. 19, no. 4, pp. 3163–3174, 2011.

[39] A. Gondarenko, J. S. Levy, and M. Lipson, "High confinement micron-scale silicon nitride high Q ring resonator.," *Opt. Express*, vol. 17, no. 14, pp. 11366–11370, 2009.

[40] G. Li, J. Yao, H. Thacker, A. Mekis, X. Zheng, I. Shubin, Y. Luo, J. Lee, K. Raj, J. E. Cunningham, and A. V. Krishnamoorthy, "Ultralow-loss, high-density SOI optical waveguide routing for macrochip interconnects," *Opt. Express*, vol. 20, no. 11, p. 12035, 2012.

[41] A. Biberman, M. J. Shaw, E. Timurdogan, J. B. Wright, and M. R. Watts, "Ultralow-loss silicon ring resonators," *Opt. Lett.*, vol. 37, no. 20, p. 4236, Oct. 2012.

[42] S. K. Selvaraja, G. Murdoch, A. Milenin, C. Delvaux, P. Ong, S. Pathak, D. Vermeulen, G. Sterckx, G. Winroth, P. Verheyen, G. Lepage, W. Bogaerts, R. Baets, J. Van Campenhout, and P. Absil, "Advanced 300-mm Waferscale Patterning for Silicon Photonics Devices with Record Low Loss and Phase Errors," *17th Optoelectron. Commun. Conf.*, p. PDP2-2 p15, 2012.

[43] J. S. Levy, A. Gondarenko, M. a. Foster, A. C. Turner-Foster, A. L. Gaeta, and M. Lipson, "CMOS-compatible multiple-wavelength oscillator for on-chip optical interconnects," *Nat. Photonics*, vol. 4, no. 1, pp. 37–40, Dec. 2009.

[44] F. Ferdous, H. Miao, D. E. Leaird, K. Srinivasan, J. Wang, L. Chen, L. T. Varghese, and A. M. Weiner, "Spectral line-by-line pulse shaping of on-chip microresonator frequency combs," *Nat. Photonics*, vol. 5, no. 12, pp. 770–776, Oct. 2011.

[45] Y. Okawachi, K. Saha, J. S. Levy, Y. H. Wen, M. Lipson, and A. L. Gaeta, "Octave-spanning frequency comb generation in a silicon nitride chip.," *Opt. Lett.*, vol. 36, no. 17, pp. 3398–400, Sep. 2011.

[46] R. Halir, Y. Okawachi, J. S. Levy, M. a. Foster, M. Lipson, and a. L. Gaeta, "Ultrabroadband supercontinuum generation in a CMOS-compatible platform," *Opt. Lett.*, vol. 37, no. 10, p. 1685, 2012.

[47] A. Pospischil, M. Humer, M. M. Furchi, D. Bachmann, R. Guider, T. Fromherz, and T. Mueller, "CMOS-compatible graphene photodetector covering all optical communication bands," *Nat. Photonics*, vol. 7, no. 11, pp. 892–896, 2013.

[48] Q. Bao and K. P. Loh, "Graphene photonics, plasmonics, and broadband optoelectronic devices," *ACS Nano*, vol. 6, no. 5, pp. 3677–3694, 2012.

[49] P. Avouris, M. Freitag, and V. Perebeinos, "Carbon-nanotube photonics and optoelectronics," *Nat. Photonics*, vol. 2, no. 6, pp. 341–350, 2008.

[50] S. Yamashita, "A Tutorial on Nonlinear Photonic Applications of Carbon Nanotube and Graphene,"

Light. Technol. J., vol. 30, no. 4, pp. 427–447, 2012.

[51] M. Liu, X. Yin, E. Ulin-Avila, B. Geng, T. Zentgraf, L. Ju, F. Wang, and X. Zhang, "A graphene-based broadband optical modulator.," *Nature*, vol. 474, no. 7349, pp. 64–67, 2011.

[52] Y. Ding, X. Zhu, S. Xiao, H. Hu, and L. H. Frandsen, "Effective electro - optical modulation with high extinction ratio by a graphene - silicon microring resonator," no. 1.

[53] W. Li, B. Chen, C. Meng, W. Fang, Y. Xiao, X. Li, Z. Hu, and Y. Xu, "Ultrafast All-Optical Graphene Modulator," 2014.

[54] C. T. Phare, Y.-H. D. Lee, J. Cardenas, and M. Lipson, "30 GHz Zeno-based Graphene Electro-optic Modulator," *arXiv:1411.2053 [cond-mat, physics:physics]*, 2014.

[55] Q. Bao, H. Zhang, Y. Wang, Z. Ni, Y. Yan, Z. X. Shen, K. P. Loh, and D. Y. Tang, "Atomic-layer craphene as a saturable absorber for ultrafast pulsed lasers," *Adv. Funct. Mater.*, vol. 19, no. 19, pp. 3077–3083, 2009.

[56] G. Xing, H. Guo, X. Zhang, T. C. Sum, and C. H. A. Huan, "The Physics of ultrafast saturable absorption in graphene," *Opt. Express*, vol. 18, no. 5, pp. 4564–4573, 2010.

[57] X. Hu, M. Zeng, A. Wang, L. Zhu, L. Fu, and J. Wang, "Graphene-assisted nonlinear optical device for four-wave mixing based tunable wavelength conversion of QPSK signal," *Opt. Express*, vol. 23, no. 20, p. 26158, 2015.

[58] T. Gu, N. W. Petrone, J. F. McMillan, A. Van Der Zande, M. Yu, G. Q. Lo, D. L. Kwong, J. Hone, and C. W. Wong, "Regenerative oscillation and four-wave mixing in graphene optoelectronics," *Nat. Photonics*, vol. 6, no. 8, pp. 554–559, 2012.

[59] H. Zhou, T. Gu, J. F. McMillan, N. Petrone, A. Van Der Zande, J. C. Hone, M. Yu, G. Lo, D. L. Kwong, G. Feng, S. Zhou, and C. W. Wong, "Enhanced four-wave mixing in graphene-silicon slow-light photonic crystal waveguides," *Appl. Phys. Lett.*, vol. 105, no. 9, pp. 1–5, 2014.

[60] Y.-M. Lin, A. Valdes-Garcia, S.-J. Han, D. B. Farmer, I. Meric, Y. Sun, Y. Wu, C. Dimitrakopoulos, A. Grill, P. Avouris, and K. A. Jenkins, "Wafer-Scale Graphene Integrated Circuit," *Science (80-.).*, vol. 332, no. 6035, pp. 1294–1297, 2011.

[61] S. Ju, W. P. Kopcha, and F. Papadimitrakopoulos, "Brightly fluorescent single-walled carbon nanotubes via an oxygen-excluding surfactant organization.," *Science*, vol. 323, no. 5919, pp. 1319–1323, Mar. 2009.

[62] Y. Miyauchi, M. Iwamura, S. Mouri, T. Kawazoe, M. Ohtsu, and K. Matsuda, "Brightening of excitons in carbon nanotubes on dimensionality modification," *Nat. Photonics*, vol. 7, no. 9, pp. 715–719, 2013.

[63] S. Wang, Q. Zeng, L. Yang, Z. Zhang, Z. Wang, T. Pei, L. Ding, X. Liang, M. Gao, Y. Li, and L. M. Peng, "High-performance carbon nanotube light-emitting diodes with asymmetric contacts," *Nano Lett.*, vol. 11, no. 1, pp. 23–29, 2011.

[64] M. Kinoshita, M. Steiner, M. Engel, J. P. Small, A. a Green, M. C. Hersam, R. Krupke, E. E. Mendez, and P. Avouris, "The polarized carbon nanotube thin film LED.," *Opt. Express*, vol. 18, no. 25, pp. 25738–45, 2010.

[65] F. Pyatkov, V. Fütterling, S. Khasminskaya, B. S. Flavel, F. Hennrich, M. M. Kappes, R. Krupke, and W. H. P. Pernice, "Cavity-enhanced light emission from electrically driven carbon nanotubes," *Nat. Photonics*, vol. 10, no. 6, pp. 420–427, Apr. 2016.

[66] E. Gauf̀rs, N. Izard, X. Le Roux, D. Marris-Morini, S. Kazaoui, E. Cassan, and L. Vivien, "Optical gain

in carbon nanotubes," *Appl. Phys. Lett.*, vol. 96, pp. 2010–2012, 2010.

[67] S. Nanot, A. W. Cummings, C. L. Pint, A. Ikeuchi, T. Akiho, K. Sueoka, R. H. Hauge, F. Léonard, and J. Kono, "Broadband, polarization-sensitive photodetector based on optically-thick films of macroscopically long, dense, and aligned carbon nanotubes.," *Sci. Rep.*, vol. 3, p. 1335, 2013.

[68] S. Kruss, A. J. Hilmer, J. Zhang, N. F. Reuel, B. Mu, and M. S. Strano, "Carbon nanotubes as optical biomedical sensors," *Adv. Drug Deliv. Rev.*, vol. 65, no. 15, pp. 1933–1950, 2013.

[69] P. W. Ricardo Prada Silvy, Yongqiang Tan, "Single-walled Carbon Nanotubes: Recent Advances, Manufacturing, Characterization and Applications."

[70] "Optical properties of carbon nanotubes." [Online]. Available: https://en.wikipedia.org/wiki/Optical_properties_of_carbon_nanotubes.

[71] J. Clark and G. Lanzani, "Organic photonics for communications," *Nat. Photonics*, vol. 4, no. 7, pp. 438–446, 2010.

[72] X. Zhang, A. Hosseini, X. Lin, H. Subbaraman, and R. T. Chen, "Polymer-based hybrid-integrated photonic devices for silicon on-chip modulation and board-level optical interconnects," *IEEE J. Sel. Top. Quantum Electron.*, vol. 19, pp. 1–15, 2013.

[73] B. Esembeson, M. L. Scimeca, T. Michinobu, F. Diederich, and I. Biaggio, "A High-Optical Quality Supramolecular Assembly for Third-Order Integrated Nonlinear Optics," *Adv. Mater.*, vol. 20, no. 23, pp. 4584–4587, Dec. 2008.

[74] H. Q. Ye, Z. Li, Y. Peng, C. C. Wang, T. Y. Li, Y. X. Zheng, a Sapelkin, G. Adamopoulos, I. Hernández, P. B. Wyatt, and W. P. Gillin, "Organo-erbium systems for optical amplification at telecommunications wavelengths.," *Nat. Mater.*, vol. 13, no. 4, pp. 382–6, 2014.

[75] T. Wang, D. Zhao, M. Zhang, J. Yin, W. Song, Z. Jia, X. Wang, G. Qin, W. Qin, F. Wang, and D. Zhang, "Optical waveguide amplifiers based on NaYF_4: Er^3+, Yb^3+ NPs-PMMA covalent-linking nanocomposites," *Opt. Mater. Express*, vol. 5, no. 3, p. 469, 2015.

[76] L. Alloatti, R. Palmer, S. Diebold, K. P. Pahl, B. Chen, R. Dinu, M. Fournier, J. Fedeli, T. Zwick, W. Freude, C. Koos, and J. Leuthold, "100 GHz silicon–organic hybrid modulator," no. February, pp. 5–8, 2014.

[77] V. Katopodis, P. Groumas, Z. Zhang, R. Dinu, E. Miller, A. Konczykowska, J. Y. Dupuy, A. Beretta, A. Dede, J. H. Choi, P. Harati, F. Jorge, V. Nodjiadjim, M. Riet, G. Cangini, A. Vannucci, N. Keil, H. G. Bach, N. Grote, H. Avramopoulos, and C. Kouloumentas, "Polymer enabled 100 Gbaud connectivity for datacom applications," *Opt. Commun.*, vol. 362, pp. 13–21, 2016.

[78] D. De Felipe, C. Zawadzki, Z. Zhang, A. Maese, M. Wenzel, H. Li, G. Przyrembel, A. Sigmund, M. Möhrle, N. Keil, N. Grote, and M. Schell, "Hybrid InP / Polymer Optical Line Terminals for 40-Channel 100-GHz spectrum-sliced WDM-PON," pp. 1–3, 2013.

[79] B. Esembeson, M. L. Scimeca, T. Michinobu, F. Diederich, and I. Biaggio, "A high-optical quality supramolecular assembly for third-order integrated nonlinear optics," *Adv. Mater.*, vol. 20, no. 23, pp. 4584–4587, 2008.

[80] C. Koos, P. Vorreau, T. Vallaitis, P. Dumon, W. Bogaerts, R. Baets, B. Esembeson, I. Biaggio, T. Michinobu, F. Diederich, W. Freude, and J. Leuthold, "All-optical high-speed signal processing with silicon–organic hybrid slot waveguides," *Nat. Photonics*, vol. 3, no. 4, pp. 216–219, Mar. 2009.

[81] D. Korn, M. Lauermann, S. Koeber, P. Appel, L. Alloatti, R. Palmer, P. Dumon, W. Freude, J. Leuthold, and C. Koos, "Lasing in silicon-organic hybrid waveguides," *Nat. Commun.*, vol. 7, p. 10864, 2016.

[82] T. Vallaitis, S. Bogatscher, L. Alloatti, P. Dumon, R. Baets, M. L. Scimeca, I. Biaggio, F. Diederich, C. Koos, W. Freude, and J. Leuthold, "Optical properties of highly nonlinear silicon-organic hybrid (SOH) waveguide geometries.," *Opt. Express*, vol. 17, no. 20, pp. 17357–68, Sep. 2009.

[83] Lei Wang, Ruimin Guo, Bing Wang, Xingjun Wang, and Zhiping Zhou, "Hybrid Si3N4-Er/Yb Silicate Waveguides for Amplifier Application," *IEEE Photonics Technol. Lett.*, vol. 24, no. 11, pp. 900–902, Jun. 2012.

[84] J. Lemaitre, E. Delcourt, D. Bosc, T. Batte, Q. Gu, and J. Le, "Carbon nanotubes incorporated-hybrid waveguides for photonics applications," 2015.

[85] L. Gervais, N. De Rooij, and E. Delamarche, "Microfluidic chips for point-of-care immunodiagnostics," *Adv. Mater.*, vol. 23, no. 24, 2011.

[86] V. Passaro and M. La Notte, "Photonic structures based on slot waveguides for nanosensors: State of the art and future developments," *Int. J. Res. Rev. Appl. …*, 2012.

[87] V. R. Almeida, Q. Xu, C. a Barrios, and M. Lipson, "Guiding and confining light in void nanostructure.," *Opt. Lett.*, vol. 29, no. 11, pp. 1209–1211, 2004.

[88] D. Korn, R. Palmer, H. Yu, P. C. Schindler, L. Alloatti, M. Baier, R. Schmogrow, W. Bogaerts, S. Selvaraja, G. Lepage, M. Pantouvaki, J. Wouters, P. Verheyen, J. Van Campenhout, P. Absil, R. Baets, R. Dinu, C. Koos, W. Freude, and J. Leuthold, "Silicon-organic hybrid (SOH) IQ modulator for 16QAM at 112 Gbit/s," *2013 Conf. Lasers Electro-Optics Eur. Int. Quantum Electron. Conf. CLEO/Europe-IQEC 2013*, vol. 21, no. 11, pp. 13219–13227, 2013.

[89] T. Baba, "Slow light in photonic crystals," *Nat. Photonics*, vol. 2, no. 8, pp. 465–473, Aug. 2008.

[90] P. Lalanne, C. Sauvan, and J. P. Hugonin, "Photon confinement in photonic crystal nanocavities," *Laser Photonics Rev.*, vol. 2, no. 6, pp. 514–526, 2008.

[91] C. Caer, X. Le Roux, S. Serna, W. Zhang, L. Vivien, and E. Cassan, "Large group-index bandwidth product empty core slow light photonic crystal waveguides for hybrid silicon photonics," *Front. Optoelectron.*, vol. 7, no. 3, pp. 376–384, 2014.

[92] S. Ek, P. Lunnemann, Y. Chen, E. Semenova, K. Yvind, and J. Mork, "Slow-light-enhanced gain in active photonic crystal waveguides.," *Nat. Commun.*, vol. 5, p. 5039, Jan. 2014.

[93] S. Mazoyer, A. Baron, J.-P. Hugonin, P. Lalanne, and A. Melloni, "Slow pulses in disordered photonic-crystal waveguides.," *Appl. Opt.*, vol. 50, no. 31, pp. G113-7, 2011.

[94] J. F. McMillan, M. Yu, D.-L. Kwong, and C. W. Wong, "Observation of four-wave mixing in slow-light silicon photonic crystal waveguides.," *Opt. Express*, vol. 18, no. 15, pp. 15484–97, Jul. 2010.

[95] S. Serna, P. Colman, W. Zhang, X. Le Roux, C. Caer, L. Vivien, and E. Cassan, "Experimental GVD engineering in slow light slot photonic crystal waveguides," *Sci. Rep.*, vol. 6, no. May, p. 26956, 2016.

[96] Y. Takahashi, Y. Inui, M. Chihara, T. Asano, R. Terawaki, and S. Noda, "A micrometre-scale Raman silicon laser with a microwatt threshold.," *Nature*, vol. 498, no. 7455, pp. 470–4, 2013.

[97] C. Caër, X. Le Roux, and E. Cassan, "High-Q silicon-on-insulator slot photonic crystal cavity infiltrated by a liquid," *Appl. Phys. Lett.*, vol. 103, no. 25, pp. 14–18, 2013.

[98] P. Seidler, K. Lister, U. Drechsler, J. Hofrichter, and T. Stöferle, "Slotted photonic crystal nanobeam cavity with an ultrahigh quality factor-to-mode volume ratio," *Opt. Express*, vol. 21, no. 26, p. 32468, Dec. 2013.

[99] D. Yang, S. Kita, F. Liang, C. Wang, H. Tian, Y. Ji, M. Lončar, and Q. Quan, "High sensitivity and high Q-factor nanoslotted parallel quadrabeam photonic crystal cavity for real-time and label-free sensing," *Appl. Phys. Lett.*, vol. 105, no. 6, p. 63118, 2014.

[100] S. Kim, H.-M. Kim, and Y.-H. Lee, "Single nanobeam optical sensor with a high Q-factor and high sensitivity," *Opt. Lett.*, vol. 40, no. 22, p. 5351, Nov. 2015.

[101] D. Yang, H. Tian, and Y. Ji, "High-Q and high-sensitivity width-modulated photonic crystal single nanobeam air-mode cavity for refractive index sensing," *Appl. Opt.*, vol. 54, no. 1, p. 1, 2015.

[102] W. Xie, T. Stöferle, G. Rainò, T. Aubert, Y. Zhu, R. F. Mahrt, E. Brainis, Z. Hens, and D. Van Thourhout, "Integrated Silicon Nitride Microdisk Lasers Based on Quantum Dots," in *Conference on Lasers and Electro-Optics*, 2016, vol. 1, no. c, p. JTh4B.6.

[103] R. Guo, B. Wang, X. Wang, L. Wang, L. Jiang, and Z. Zhou, "Optical amplification in Er/Yb silicate slot waveguide," *Opt. Lett.*, vol. 37, no. 9, p. 1427, 2012.

[104] T.-W. Lu, P.-T. Lin, and P.-T. Lee, "Photonic crystal horizontally slotted nanobeam cavity for silicon-based nanolasers.," *Opt. Lett.*, vol. 37, no. 4, pp. 569–71, 2012.

[105] X. Zhang, A. Hosseini, S. Chakravarty, J. Luo, A. K.-Y. Jen, and R. T. Chen, "Wide optical spectrum range, subvolt, compact modulator based on an electro-optic polymer refilled silicon slot photonic crystal waveguide.," *Opt. Lett.*, vol. 38, no. 22, pp. 4931–4, Nov. 2013.

[106] C. T. Phare, Y.-H. Daniel Lee, J. Cardenas, and M. Lipson, "Graphene electro-optic modulator with 30 GHz bandwidth," *Nat. Photonics*, vol. 9, no. 8, pp. 511–514, 2015.

[107] Z. Zhou, B. Yin, and J. Michel, "On-chip light sources for silicon photonics," *Light Sci. Appl.*, vol. 4, no. 11, p. e358, Nov. 2015.

[108] J. M. Ramírez, F. Ferrarese Lupi, Y. Berencén, a Anopchenko, J. P. Colonna, O. Jambois, J. M. Fedeli, L. Pavesi, N. Prtljaga, P. Rivallin, a Tengattini, D. Navarro-Urrios, and B. Garrido, "Er-doped light emitting slot waveguides monolithically integrated in a silicon photonic chip.," *Nanotechnology*, vol. 24, no. 11, p. 115202, 2013.

[109] S. a Vázquez-Córdova, M. Dijkstra, E. H. Bernhardi, F. Ay, K. Wörhoff, J. L. Herek, S. M. García-Blanco, and M. Pollnau, "Erbium-doped spiral amplifiers with 20 dB of net gain on silicon.," *Opt. Express*, vol. 22, no. 21, pp. 25993–6004, Oct. 2014.

[110] J. D. Bradley, R. Stoffer, L. Agazzi, F. Ay, K. Wörhoff, and M. Pollnau, "Integrated Al2O3:Er3+ ring lasers on silicon with wide wavelength selectivity.," *Opt. Lett.*, vol. 35, no. 1, pp. 73–75, 2010.

[111] G. Singh, Purnawirman, J. D. B. Bradley, N. Li, E. S. Magden, M. Moresco, T. N. Adam, G. Leake, D. Coolbaugh, and M. R. Watts, "Resonant pumped erbium-doped waveguide lasers using distributed Bragg reflector cavities," *Opt. Lett.*, vol. 41, no. 6, p. 1189, Mar. 2016.

[112] Y. C. Yan, a. J. Faber, H. de Waal, P. G. Kik, and a. Polman, "Erbium-doped phosphate glass waveguide on silicon with 4.1 dB/cm gain at 1.535 μm," *Appl. Phys. Lett.*, vol. 71, no. 20, p. 2922, 1997.

[113] H. Isshiki, F. Jing, T. Sato, T. Nakajima, and T. Kimura, "Rare earth silicates as gain media for silicon photonics [Invited]," *Photonics Res.*, vol. 2, no. 3, p. A45, May 2014.

[114] X. Wang, X. Zhuang, S. Yang, Y. Chen, Q. Zhang, X. Zhu, H. Zhou, P. Guo, J. Liang, Y. Huang, A. Pan, and X. Duan, "High Gain Submicrometer Optical Amplifier at Near-Infrared Communication Band," *Phys. Rev. Lett.*, vol. 115, no. 2, p. 27403, 2015.

[115] T. Morishita, K. Yamashita, H. Yanagi, and K. Oe, "1.3 μm Solid-State Plastic Laser in Dye-Doped

Fluorinated-Polyimide Waveguide," *Appl. Phys. Express*, vol. 3, no. 9, p. 92202, Sep. 2010.

[116] E. Gaufrès, N. Izard, L. Vivien, S. Kazaoui, D. Marris-Morini, and E. Cassan, "Enhancement of semiconducting single-wall carbon-nanotube photoluminescence.," *Opt. Lett.*, vol. 34, no. 24, pp. 3845–7, 2009.

[117] A. Noury, X. Le Roux, L. Vivien, and N. Izard, "Enhanced light emission from carbon nanotubes integrated in silicon micro-resonator," *Nanotechnology*, vol. 26, no. 34, p. 345201, 2015.

[118] R. Miura, S. Imamura, R. Ohta, A. Ishii, X. Liu, T. Shimada, S. Iwamoto, Y. Arakawa, and Y. K. Kato, "Ultralow mode-volume photonic crystal nanobeam cavities for high-efficiency coupling to individual carbon nanotube emitters," *Nat. Commun.*, vol. 5, no. May, p. 5580, 2014.

[119] C. D. Chin, V. Linder, and S. K. Sia, "Lab-on-a-chip devices for global health: past studies and future opportunities.," *Lab Chip*, vol. 7, no. 1, pp. 41–57, 2007.

[120] J. Wu and M. Gu, "Microfluidic sensing: state of the art fabrication and detection techniques.," *J. Biomed. Opt.*, vol. 16, no. 8, p. 80901, 2011.

[121] M. La Notte, B. Troia, T. Muciaccia, C. E. Campanella, F. De Leonardis, and V. M. N. Passaro, "Recent advances in gas and chemical detection by Vernier effect-based photonic sensors," *Sensors (Switzerland)*, vol. 14, no. 3, pp. 4831–4855, 2014.

[122] T. Claes, J. G. Molera, K. De Vos, E. Schacht, R. Baets, and P. Bienstman, "Label-free biosensing with a slot-waveguide-based ring resonator in silicon on insulator," *IEEE Photonics J.*, vol. 1, no. 3, pp. 197–204, 2009.

[123] S. Mandal, J. M. Goddard, and D. Erickson, "A multiplexed optofluidic biomolecular sensor for low mass detection.," *Lab Chip*, vol. 9, no. 20, pp. 2924–2932, 2009.

[124] M. La Notte, B. Troia, T. Muciaccia, C. E. Campanella, F. De Leonardis, and V. M. N. Passaro, "Recent advances in gas and chemical detection by Vernier effect-based photonic sensors.," *Sensors (Basel).*, vol. 14, no. 3, pp. 4831–55, Jan. 2014.

[125] R. Boeck, W. Shi, L. Chrostowski, and N. a F. Jaeger, "FSR-eliminated vernier racetrack resonators using grating-assisted couplers," *IEEE Photonics J.*, vol. 5, no. 5, 2013.

[126] M. La Notte and V. M. N. N. Passaro, "Ultra high sensitivity chemical photonic sensing by Mach–Zehnder interferometer enhanced Vernier-effect," *Sensors Actuators B Chem.*, vol. 176, no. 2010, pp. 994–1007, Jan. 2013.

[127] T. Claes, W. Bogaerts, and P. Bienstman, "Experimental characterization of a silicon photonic biosensor consisting of two cascaded ring resonators based on the Vernier-effect and introduction of a curve fitting method for an improved detection limit.," *Opt. Express*, vol. 18, no. 22, pp. 22747–22761, 2010.

[128] K. B. Gylfason, C. F. Carlborg, A. Kaźmierczak, F. Dortu, H. Sohlström, L. Vivien, C. a Barrios, W. van der Wijngaart, and G. Stemme, "On-chip temperature compensation in an integrated slot-waveguide ring resonator refractive index sensor array.," *Opt. Express*, vol. 18, no. 4, pp. 3226–3237, 2010.

[129] X. Fan, I. M. White, H. Zhu, J. D. Suter, and H. Oveys, "Overview of novel integrated optical ring resonator bio/chemical sensors," *Lasers Appl. Sci. Eng.*, p. 64520M–64520M, 2007.

[130] C. Ca, S. F. Serna, W. Zhang, X. Le Roux, and E. Cassan, "Liquid sensor based on high- Q Slot Photonic Crystal Cavity in Silicon-On-Insulator configuration," *Opt. Lett.*, vol. 39, no. 20, pp. 1–3, Oct. 2014.

[131] J. Jágerská, H. Zhang, Z. Diao, N. Le Thomas, and R. Houdré, "Refractive index sensing with an air-slot photonic crystal nanocavity.," *Opt. Lett.*, vol. 35, no. 15, pp. 2523–2525, 2010.

[132] X. Tu, J. Song, T.-Y. Liow, M. K. Park, J. Q. Yiying, J. S. Kee, M. Yu, and G.-Q. Lo, "Thermal independent Silicon-Nitride slot waveguide biosensor with high sensitivity," *Opt. Express*, vol. 20, no. 3, p. 2640, 2012.

[133] X. Wang, J. Flueckiger, S. Schmidt, S. Grist, S. T. Fard, J. Kirk, M. Doerfler, K. C. Cheung, D. M. Ratner, and L. Chrostowski, "A silicon photonic biosensor using phase-shifted Bragg gratings in slot waveguide," *J. Biophotonics*, vol. 6, no. 10, pp. 821–828, 2013.

[134] S. K. Selvaraja, P. De Heyn, G. Winroth, P. Ong, G. Lepage, C. Cailler, A. Rigny, K. Bourdelle, W. Bogaerts@ugent.be, D. VanThourhout, J. Van Campenhout, and P. Absil, "Highly uniform and low-loss passive silicon photonics devices using a 300mm CMOS platform," *Opt. Fiber Commun. Conf.*, no. 1, p. Th2A.33, 2014.

[135] V. R. Almeida, Q. Xu, C. a Barrios, and M. Lipson, "Guiding and confining light in void nanostructure.," *Opt. Lett.*, vol. 29, no. 11, pp. 1209–1211, 2004.

[136] W. Zhang, S. Serna, N. Dubreuil, and E. Cassan, "Nonlinear optimization of slot Si waveguides: TPA minimization with FOM_TPA up to 425," *Opt. Lett.*, vol. 40, no. 7, p. 1212, Mar. 2015.

[137] F. De Leonardis, G. Giannoccaro, B. Troia, V. M. N. Passaro, and A. G. Perri, "Design of optimized SOI slot waveguides for homogeneous optical sensing in near infrared," in *Proceedings of the 4th IEEE International Workshop on Advances in Sensors and Interfaces, IWASI 2011*, 2011, pp. 142–147.

[138] Q. Deng, L. Liu, X. Li, and Z. Zhou, "Strip-slot waveguide mode converter based on symmetric multimode interference," *Opt. Lett.*, vol. 39, no. 19, pp. 5665–5668, 2014.

[139] S. H. Mirsadeghi, E. Schelew, and J. F. Young, "Compact and efficient silicon nanowire to slot waveguide coupler," *13th Int. Conf. Numer. Simul. Optoelectron. Devices, NUSOD 2013*, vol. 1, pp. 31–32, 2013.

[140] Z. Wang, N. Zhu, Y. Tang, L. Wosinski, D. Dai, and S. He, "Ultracompact low-loss coupler between strip and slot waveguides.," *Opt. Lett.*, vol. 34, no. 10, pp. 1498–1500, 2009.

[141] R. Palmer, L. Alloatti, D. Korn, W. Heni, P. C. Schindler, J. Bolten, M. Karl, M. Waldow, T. Wahlbrink, W. Freude, C. Koos, and J. Leuthold, "Low-Loss Silicon Strip-to-Slot Mode Converters," *IEEE Photonics J.*, vol. 5, no. 1, pp. 2200409–2200409, Feb. 2013.

[142] R. Palmer, L. Alloatti, D. Korn, W. Heni, P. C. Schindler, J. Bolten, M. Karl, M. Waldow, T. Wahlbrink, W. Freude, C. Koos, and J. Leuthold, "Low-loss silicon strip-to-slot mode converters," *IEEE Photonics J.*, vol. 5, no. 1, 2013.

[143] K. Shang, S. Pathak, B. Guan, G. Liu, and S. J. B. Yoo, "Low-loss compact multilayer silicon nitride platform for 3D photonic integrated circuits," *Opt. Express*, vol. 23, no. 16, p. 21334, 2015.

[144] D. J. Moss, R. Morandotti, A. L. Gaeta, and M. Lipson, "New CMOS-compatible platforms based on silicon nitride and Hydex for nonlinear optics," *Nat. Photonics*, vol. 7, no. 8, pp. 597–607, Jul. 2013.

[145] K. Kim, "High-Sensitivity Temperature-Independent Silicon Photonic Microfluidic Biosensors," Lehigh University, 2012.

[146] G. Gao, Y. Zhang, H. Zhang, Y. Wang, Q. Huang, and J. Xia, "Air-mode photonic crystal ring resonator on silicon-on-insulator," *Sci. Rep.*, vol. 6, p. 19999, 2016.

[147] M. Soltani, S. Yegnanarayanan, and A. Adibi, "Ultra-high Q planar silicon microdisk resonators for

chip-scale silicon photonics.," *Opt. Express*, vol. 15, no. 8, pp. 4694–4704, 2007.

[148] M. Borselli, T. Johnson, and O. Painter, "Beyond the Rayleigh scattering limit in high-Q silicon microdisks: theory and experiment.," *Opt. Express*, vol. 13, no. 5, pp. 1515–1530, 2005.

[149] L.-W. Luo, G. S. Wiederhecker, J. Cardenas, C. Poitras, and M. Lipson, "High quality factor etchless silicon photonic ring resonators.," *Opt. Express*, vol. 19, no. 7, pp. 6284–9, Mar. 2011.

[150] W. Zhang, S. Serna, X. Le Roux, C. Alonso-Ramos, L. Vivien, and E. Cassan, "Analysis of silicon-on-insulator slot waveguide ring resonators targeting high Q -factors," *Opt. Lett.*, vol. 40, no. 23, pp. 5566–5569, 2015.

[151] Y. Zhang, C. Zeng, D. Li, G. Gao, Z. Huang, J. Yu, and J. Xia, "High-quality-factor photonic crystal ring resonator.," *Opt. Lett.*, vol. 39, no. 5, pp. 1282–5, 2014.

[152] T. W. Lu, W. C. Tsai, T. Y. Wu, and P. T. Lee, "Laser emissions from one-dimensional photonic crystal rings on silicon-dioxide," *Appl. Phys. Lett.*, vol. 102, no. 5, 2013.

[153] J. E. Heebner, a. Schweinsberg, R. W. Boyd, and D. J. Jackson, "Optical transmission characteristics of fiber ring resonators," *IEEE J. Quantum Electron.*, vol. 40, no. 6, pp. 726–730, Jun. 2004.

[154] A. Yariv, "Critical coupling and its control in optical waveguide-ring resonator systems," *IEEE Photonics Technol. Lett.*, vol. 14, no. 4, pp. 483–485, Apr. 2002.

[155] W. Shi, H. Yun, W. Zhang, C. Lin, T. K. Chang, Y. Wang, N. a. F. Jaeger, and L. Chrostowski, "Ultra-compact, high-Q silicon microdisk reflectors," *Opt. Express*, vol. 20, no. 20, p. 21840, 2012.

[156] R. Palmer, S. Koeber, M. Woessner, D. L. Elder, W. Heni, D. Korn, H. Yu, M. Lauermann, W. Bogaerts, L. R. Dalton, W. Freude, J. Leuthold, and C. Koos, "High-Speed Silicon-Organic Hybrid (SOH) Modulators with 230 pm/V Electro-Optic Coefficient Using Advanced Materials," *Opt. Fiber Commun. Conf.*, vol. 1, no. c, p. M3G.4, 2014.

[157] V. M. N. Passaro, M. La Notte, B. Troia, L. Passaquindici, F. De Leonardis, G. Giannoccaro, and P. Bari, "Photonic Structures Based on Slot Waveguides for Nanosensors : State of the Art and Future Developments," vol. 11, no. June, pp. 402–418, 2012.

[158] M. Gould, T. Baehr-Jones, R. Ding, S. Huang, J. Luo, A. K.-Y. Jen, J.-M. Fedeli, M. Fournier, and M. Hochberg, "Silicon-polymer hybrid slot waveguide ring-resonator modulator.," *Opt. Express*, vol. 19, pp. 3952–3961, 2011.

[159] L. Zhang, C. Bao, V. Singh, J. Mu, C. Yang, A. M. Agarwal, L. C. Kimerling, and J. Michel, "Generation of two-cycle pulses and octave-spanning frequency combs in a dispersion-flattened micro-resonator.," *Opt. Lett.*, vol. 38, no. 23, pp. 5122–5, 2013.

[160] C. a Barrios, K. B. Gylfason, B. Sánchez, A. Griol, H. Sohlström, M. Holgado, and R. Casquel, "Slot-waveguide biochemical sensor.," *Opt. Lett.*, vol. 32, no. 21, pp. 3080–3082, 2007.

[161] F. Dell'Olio and V. M. Passaro, "Optical sensing by optimized silicon slot waveguides.," *Opt. Express*, vol. 15, no. 8, pp. 4977–4993, 2007.

[162] Q. Xu, V. R. Almeida, R. R. Panepucci, and M. Lipson, "Experimental demonstration of guiding and confining light in nanometer-size low-refractive-index material.," *Opt. Lett.*, vol. 29, no. 14, pp. 1626–1628, 2004.

[163] T. Baehr-Jones, M. Hochberg, C. Walker, and A. Scherer, "High-Q optical resonators in silicon-on-insulator-based slot waveguides," *Appl. Phys. Lett.*, vol. 86, no. 8, p. 81101, 2005.

[164] S. Xiao, M. H. Khan, H. Shen, and M. Qi, "Compact silicon microring resonators with ultra-low

propagation loss in the C band," *Opt. Express*, vol. 15, no. 22, p. 14467, 2007.

[165] S. Serna, W. Zhang, X. Leroux, D. Gao, D. Zhang, L. Vivien, and E. Cassan, "Potential for large optical gain improvement of erbium-doped slot waveguide amplifiers in silicon photonics," *J. Opt. Soc. Am. B*, vol. 31, no. 9, p. 2021, Aug. 2014.

[166] H. Sun, A. Chen, D. Abeysinghe, A. Szep, and R. S. Kim, "Reduction of scattering loss of silicon slot waveguides by RCA smoothing," *Optics Letters*, vol. 37, no. 1. p. 13, 2012.

[167] A. Spott, T. Baehr-Jones, R. Ding, Y. Liu, R. Bojko, T. O'Malley, A. Pomerene, C. Hill, W. Reinhardt, and M. Hochberg, "Photolithographically fabricated low-loss asymmetric silicon slot waveguides.," *Opt. Express*, vol. 19, no. 11, pp. 10950–8, May 2011.

[168] D. Spencer, J. Bauters, M. Heck, and J. Bowers, "Integrated waveguide coupled Si 3 N 4 resonators in the ultrahigh-Q regime," *Optica*, vol. 1, no. 3, pp. 153–157, 2014.

[169] S. Xiao, M. H. Khan, H. Shen, and M. Qi, "Modeling and measurement of losses in silicon-on-insulator resonators and bends.," *Opt. Express*, vol. 15, no. 17, pp. 10553–10561, 2007.

[170] P. Rabiei, W. H. Steier, C. Zhang, and L. R. Dalton, "Polymer micro-ring filters and modulators," *J. Light. Technol.*, vol. 20, no. 11, pp. 1968–1975, 2002.

[171] F. Xia, L. Sekaric, and Y. A. Vlasov, "Mode conversion losses in silicon-on-insulator photonic wire based racetrack resonators," *Opt. Express*, vol. 14, no. 9, p. 3872, 2006.

[172] C.-W. Tseng, C.-W. Tsai, K.-C. Lin, M.-C. Lee, and Y.-J. Chen, "Study of coupling loss on strongly-coupled, ultra compact microring resonators.," *Opt. Express*, vol. 21, no. 6, pp. 7250–7, 2013.

[173] C. Caer, X. Le Roux, and E. Cassan, "Enhanced localization of light in slow wave slot photonic crystal waveguides.," *Opt. Lett.*, vol. 37, no. 17, pp. 3660–2, Sep. 2012.

[174] C. Caër, X. Le Roux, and E. Cassan, "High-Q silicon-on-insulator slot photonic crystal cavity infiltrated by a liquid," *Appl. Phys. Lett.*, vol. 103, pp. 14–18, 2013.

[175] W. Bogaerts, P. De Heyn, T. Van Vaerenbergh, K. De Vos, S. Kumar Selvaraja, T. Claes, P. Dumon, P. Bienstman, D. Van Thourhout, and R. Baets, "Silicon microring resonators," *Laser Photonics Rev.*, vol. 6, no. 1, pp. 47–73, 2012.

[176] C. A. Barrios, K. B. Gylfason, B. Sánchez, A. Griol, H. Sohlström, M. Holgado, and R. Casquel, "Slot-waveguide biochemical sensor," *Opt. Lett.*, vol. 32, no. 21, p. 3080, Nov. 2007.

[177] W. Zhang, S. Serna, X. Le Roux, L. Vivien, and E. Cassan, "Analysis of slot waveguide ring resonators targeting high Q - factors," no. 1.

[178] "COMSOL Multiphysics® Modeling Software." [Online]. Available: https://www.comsol.com/. [Accessed: 29-Oct-2015].

[179] "Lumerical Solutions, Inc. | Innovative Photonic Design Tools." [Online]. Available: https://www.lumerical.com/. [Accessed: 29-Oct-2015].

[180] Z. M. Meng, Y. H. Hu, C. Wang, X. L. Zhong, W. Ding, and Z. Y. Li, "Design of high-Q silicon-polymer hybrid photonic crystal nanobeam microcavities for low-power and ultrafast all-optical switching," *Photonics Nanostructures - Fundam. Appl.*, vol. 12, pp. 83–92, 2014.

[181] M. Galli, D. Gerace, K. Welna, T. F. Krauss, L. O'Faolain, G. Guizzetti, and L. C. Andreani, "Low-power continuous-wave generation of visible harmonics in silicon photonic crystal nanocavities.," *Opt. Express*, vol. 18, no. 25, pp. 26613–26624, 2010.

[182] J. Zhou, H. Tian, L. Huang, Z. Fu, F. Sun, and Y. Ji, "Parabolic tapered coupled two photonic crystal

nanobeam slot cavities for high-FOM biosensing," *IEEE Photonics Technol. Lett.*, vol. 1135, no. c, pp. 1–1, 2016.

[183] M. Eichenfield, R. Camacho, J. Chan, K. J. Vahala, and O. Painter, "A picogram- and nanometre-scale photonic-crystal optomechanical cavity.," *Nature*, vol. 459, no. 7246, pp. 550–5, May 2009.

[184] K. Hennessy, A. Badolato, M. Winger, D. Gerace, M. Atature, S. Gulde, S. Falt, E. L. Hu, and A. Imamoglu, "Quantum nature of a strongly-coupled single quantum dot-cavity system," *Nature*, vol. 445, no. February, p. 896, 2007.

[185] C. D. Jeffries, L. V Keldysh, and D. W. Snoke, "Cavity Quantum Electrodynamics:Coherence in Context," vol. 298, no. November, pp. 1–6, 2002.

[186] M. Minkov and V. Savona, "Automated optimization of photonic crystal slab cavities.," *Sci. Rep.*, vol. 4, p. 5124, Jan. 2014.

[187] E. Kuramochi, H. Taniyama, T. Tanabe, K. Kawasaki, Y.-G. Roh, and M. Notomi, "Ultrahigh-Q one-dimensional photonic crystal nanocavities with modulated mode-gap barriers on SiO2 claddings and on air claddings.," *Opt. Express*, vol. 18, no. 15, pp. 15859–69, Jul. 2010.

[188] P. Yu, B. Qi, X. Jiang, M. Wang, and J. Yang, "Ultrasmall-V high-Q photonic crystal nanobeam microcavities based on slot and hollow-core waveguides.," *Opt. Lett.*, vol. 36, no. 8, pp. 1314–6, Apr. 2011.

[189] J. D. Ryckman and S. M. Weiss, "Low mode volume slotted photonic crystal single nanobeam cavity," *Appl. Phys. Lett.*, vol. 101, no. 7, p. 71104, Aug. 2012.

[190] T. Hong, C. Hoang, W. Zhang, S. Serna, C. Caer, X. Le Roux, L. Vivien, and E. Cassan, "SOI Slot Photonic Crystal Heterostructure Cavities in the 1 . 3 μm – 1 . 6 μm Range for Hybrid Photonic Integration," vol. 1, no. c, pp. 1–4, 2015.

[191] P. B. Deotare, M. W. McCutcheon, I. W. Frank, M. Khan, and M. Lončar, "High quality factor photonic crystal nanobeam cavities," *Appl. Phys. Lett.*, vol. 94, no. 12, 2009.

[192] Q. Quan, I. B. Burgess, S. K. Y. Tang, D. L. Floyd, and M. Loncar, "High-Q, low index-contrast polymeric photonic crystal nanobeam cavities," *Opt. Express*, vol. 19, no. 22, pp. 22191–22197, Aug. 2011.

[193] Q. Quan, P. B. Deotare, and M. Loncar, "Photonic crystal nanobeam cavity strongly coupled to the feeding waveguide," *Appl. Phys. Lett.*, vol. 96, no. 20, p. 203102, 2010.

[194] X. Wang, X. Zhuang, S. Yang, Y. Chen, Q. Zhang, X. Zhu, H. Zhou, P. Guo, J. Liang, Y. Huang, A. Pan, and X. Duan, "High Gain Submicrometer Optical Amplifier at Near-Infrared Communication Band," *Phys. Rev. Lett.*, vol. 115, no. 2, pp. 1–6, 2015.

[195] L. Yin, D. Shelhammer, G. Zhao, Z. Liu, and C. Z. Ning, "Erbium concentration control and optimization in erbium yttrium chloride silicate single crystal nanowires as a high gain material," *Appl. Phys. Lett.*, vol. 103, no. 12, 2013.

[196] Z. Liu, L. Yin, and C.-Z. Ning, "Extremely Large Signal Enhancement in an Erbium Chloride Silicate Single-Crystal Nanowire," *Cleo 2013*, vol. 2, p. CF1I.6, 2013.

[197] Z. Liu, G. Zhao, L. Yin, and C. Z. Ning, "Demonstration of Net Gain in an Erbium Chloride Silicate Single Nanowire Waveguide," in *CLEO: 2014*, 2014, vol. 2, p. SM4H.4.

[198] F. D. Patel, S. DiCarolis, P. Lum, S. Venkatesh, and J. N. Miller, "A compact high-performance optical waveguide amplifier," *IEEE Photonics Technol. Lett.*, vol. 16, no. 12, pp. 2607–2609, 2004.

[199] L. Yin, H. Ning, S. Turkdogan, Z. Liu, P. L. Nichols, and C. Z. Ning, "Long lifetime, high density single-crystal erbium compound nanowires as a high optical gain material," *Appl. Phys. Lett.*, vol. 100, no. 24, pp. 10–13, 2012.

[200] "Research Projects | EECS at UC Berkeley." [Online]. Available: https://www.eecs.berkeley.edu/Research/Projects/Data/107125.html. [Accessed: 21-May-2016].

[201] J. D. B. Bradley and M. Pollnau, "Erbium-doped integrated waveguide amplifiers and lasers," *Laser Photonics Rev.*, vol. 5, no. 3, pp. 368–403, 2011.

[202] L. Agazzi, K. Wörhoff, and M. Pollnau, "Energy-Transfer-Upconversion Models, Their Applicability and Breakdown in the Presence of Spectroscopically Distinct Ion Classes: A Case Study in Amorphous Al 2 O 3 :Er 3+," *J. Phys. Chem. C*, vol. 117, no. 13, pp. 6759–6776, Apr. 2013.

[203] R. Guo, X. Wang, K. Zang, B. Wang, L. Wang, L. Gao, and Z. Zhou, "Optical amplification in Er/Yb silicate strip loaded waveguide," *Appl. Phys. Lett.*, vol. 99, no. 16, pp. 1–3, 2011.

[204] Y. Tian, T. Wei, F. Chen, X. Jing, J. Zhang, and S. Xu, "Fluorescence characteristics and energy transfer of ytterbium-sensitized erbium-doped fluorophosphate glass for amplifier applications," *J. Quant. Spectrosc. Radiat. Transf.*, vol. 133, pp. 311–318, 2014.

[205] M. Miritello, R. Lo Savio, F. Iacona, G. Franzò, A. Irrera, A. M. Piro, C. Bongiorno, and F. Priolo, "Efficient luminescence and energy transfer in erbium silicate thin films," *Adv. Mater.*, vol. 19, no. 12, pp. 1582–1588, 2007.

[206] R. Ramaswami, K. N. Sivarajan, and G. H. Sasaki, *Optical Networks: A Practical Perspective*. 2010.

[207] N. D. Psaila, R. R. Thomson, H. T. Bookey, A. K. Kar, N. Chiodo, R. Osellame, G. Cerullo, A. Jha, and S. Shen, "Er:Yb-doped oxyfluoride silicate glass waveguide amplifier fabricated using femtosecond laser inscription," *Appl. Phys. Lett.*, vol. 90, no. 13, pp. 90–93, 2007.

[208] K. Suh, M. Lee, J. S. Chang, H. Lee, N. Park, G. Y. Sung, and J. H. Shin, "Cooperative upconversion and optical gain in ion-beam sputter-deposited Er(x)Y(2-x)SiO(5) waveguides.," *Opt. Express*, vol. 18, no. 8, pp. 7724–7731, 2010.

[209] J. Rönn, "Fabrication and characterization of atomic-layer-deposited Er2O3 for optical amplifier devices," Aalto University, 2014.

[210] J. Ronn, L. Karvonen, A. Pyymäki-Perros, N. Peyghambarian, H. Lipsanen, A. Säynätjoki, and Z. Sun, "Enhancement of the photoluminescence in Er-doped Al 2 O 3 fabricated by atomic layer deposition," 2016, vol. 9750, p. 97500P.

[211] W. Xie, Y. Zhu, T. Aubert, Z. Hens, E. Brainis, and D. Van Thourhout, "On-chip hybrid integration of silicon nitride microdisk with colloidal quantum dots," *IEEE Int. Conf. Gr. IV Photonics GFP*, vol. 2015–Octob, pp. 159–160, 2015.

[212] Y. Wan, Q. Li, A. Y. Liu, A. C. Gossard, J. E. Bowers, E. L. Hu, and K. M. Lau, "Optically pumped 13 μm room-temperature InAs quantum-dot micro-disk lasers directly grown on (001) silicon," *Opt. Lett.*, vol. 41, no. 7, p. 1664, 2016.

[213] S. G. Rao, L. Huang, W. Setyawan, and S. Hong, "Nanotube electronics: large-scale assembly of carbon nanotubes.," *Nature*, vol. 425, no. 6953, pp. 36–37, 2003.

[214] A. Abbasi, J. Verbist, X. Yin, F. Lelarge, G. hua Duan, J. Bauwelinck, G. Roelkens, and G. I. Morthier, "Above 40 Gb/s Direct Modulation of a Heterogeneously integrated III-V-on-silicon DFB Laser," in *Latin America Optics and Photonics Conference*, 2016, p. LTu2D.3.

[215] G. T. Reed, G. Mashanovich, F. Y. Gardes, and D. J. Thomson, “Silicon optical modulators,” *Nat. Photonics*, vol. 4, no. 8, pp. 518–526, 2010.

[216] P. G. Collins and P. Avouris, “Nanotubes for electronics.,” *Sci. Am.*, vol. 283, no. 6, pp. 62–69, 2000.

[217] J. W. G. Wilder, L. C. Venema, A. G. Rinzler, R. E. Smalley, and C. Dekker, “Electronic structure of atomically resolved carbon nanotubes,” *Nature*, vol. 391, no. 6662, pp. 59–62, 1998.

[218] A Jorio; G Dresselhaus; M S Dresselhaus, *Carbon Nanotubes*, vol. 111. Berlin, Heidelberg: Springer Berlin Heidelberg, 2008.

[219] H. Ajiki and T. Ando, “Carbon nanotubes: Optical absorption in aharonov-bohm flux,” *Jpn. J. Appl. Phys.*, vol. 34, no. S1, pp. 107–109, 1995.

[220] M. S. Hofmann, J. T. Glückert, J. Noé, C. Bourjau, R. Dehmel, and A. Högele, “Bright, long-lived and coherent excitons in carbon nanotube quantum dots.,” *Nat. Nanotechnol.*, vol. 8, no. 7, pp. 502–5, 2013.

[221] A. Nish, J.-Y. Hwang, J. Doig, and R. J. Nicholas, “Highly selective dispersion of single-walled carbon nanotubes using aromatic polymers.,” *Nat. Nanotechnol.*, vol. 2, no. 10, pp. 640–6, 2007.

[222] J. Lefebvre, D. G. Austing, J. Bond, and P. Finnie, “Photoluminescence imaging of suspended single-walled carbon nanotubes,” *Nano Lett.*, vol. 6, no. 8, pp. 1603–1608, 2006.

[223] Y. Oyama, R. Saito, K. Sato, J. Jiang, G. G. Samsonidze, A. Grüneis, Y. Miyauchi, S. Maruyama, A. Jorio, G. Dresselhaus, and M. S. Dresselhaus, “Photoluminescence intensity of single-wall carbon nanotubes,” *Carbon N. Y.*, vol. 44, no. 5, pp. 873–879, 2006.

[224] S. Reich, C. Thomsen, and J. Robertson, “Exciton resonances quench the photoluminescence of zigzag carbon nanotubes,” *Phys. Rev. Lett.*, vol. 95, no. 7, pp. 1–4, 2005.

[225] J. Crochet, M. Clemens, and T. Hertel, “Quantum yield heterogeneities of aqueous single-wall carbon nanotube suspensions,” *J. Am. Chem. Soc.*, vol. 129, no. 26, pp. 8058–8059, 2007.

[226] M. J. O’Connell, “Band Gap Fluorescence from Individual Single-Walled Carbon Nanotubes,” *Science (80-.).*, vol. 297, no. 5581, pp. 593–596, Jul. 2002.

[227] P. Nikolaev, M. J. Bronikowski, R. K. Bradley, F. Rohmund, D. T. Colbert, K. a Smith, and R. E. Smalley, “Gas-phase catalytic growth of single-walled carbon nanotubes from carbon monoxide,” *Chem. Phys. Lett.*, vol. 313, no. 1–2, pp. 91–97, 1999.

[228] A. Hartschuh, H. N. Pedrosa, L. Novotny, and T. D. Krauss, “Simultaneous fluorescence and Raman scattering from single carbon nanotubes.,” *Science*, vol. 301, no. 5638, pp. 1354–6, 2003.

[229] R. Watahiki, T. Shimada, P. Zhao, S. Chiashi, S. Iwamoto, Y. Arakawa, S. Maruyama, and Y. K. Kato, “Enhancement of carbon nanotube photoluminescence by photonic crystal nanocavities,” *Appl. Phys. Lett.*, vol. 101, no. 14, pp. 2012–2015, 2012.

Journal Publications

1. Thi-Hong Hoang, **Weiwei Zhang**, Samuel F. Serna-Otalvaro, Charles Caer, Xavier Le roux, Laurent Vivien, Eric Cassan*: SOI Slotted Photonic Crystal Cavities Spanning From 1.3 to With Factors Above 800 000*. IEEE Photonics Technology Letters 10/2015; 27(20). DOI:10.1109/LPT.2015.2454335
2. Elena Duran Valdeiglesias, **Weiwei Zhang**, Adrien Noury, Carlos Alonso Ramos, Thi-Hong-Cam Hoang, Samuel Serna, Xavier Le Roux, Eric Cassan, Nicolas Izard, Francesco Sarti, Ughetta Torrini, Francesco Biccari, Anna Vinattieri, Matteo Balestrieri, Al-Saleh Keita, Hongliu Yang, Viktor Bezugly, Gianaurelio Cuniberti, Arianna Filoramo, Massimo Gurioli, Laurent Vivien: *Integration of Carbon Nanotubes in Silicon Strip and Slot Waveguide Micro-Ring Resonators*. IEEE Transactions on Nanotechnology 07/2016; 15(4). DOI:10.1109/TNANO.2016.2556225
3. Samuel Serna, **Weiwei Zhang**, Xavier Leroux, Dingshan Gao, Daming Zhang, Laurent Vivien, Eric Cassan: *Potential for large optical gain improvement of erbium-doped slot waveguide amplifiers in silicon photonics*. Journal of the Optical Society of America B 09/2014; 31(9). DOI:10.1364/JOSAB.31.002021
4. Samuel Serna, Pierre Colman, **Weiwei Zhang**, Xavier Le Roux, Charles Caer, Laurent Vivien, Eric Cassan: *Experimental GVD engineering in slow light slot photonic crystal waveguides*. Scientific Reports 05/2016; 6. DOI:10.1038/srep26956
5. S. Serna-Otalvaro; **W. Zhang**; P. Colman; X. Le roux; J. R. Coudevylle; L. Vivien; E. Cassan, "Experimental investigation of top cladding on properties of silicon slotted photonic crystal waveguides," in *IEEE Journal of Selected Topics in Quantum Electronics* , vol.PP, no.99, pp.1-1.
6. Charles Caër, Samuel F. Serna-Otálvaro, **Weiwei Zhang**, Xavier Le Roux, Eric Cassan: *Liquid sensor based on high-Q slot photonic crystal cavity in silicon-on-insulator configuration*. Optics Letters 10/2014; 39(20). DOI:10.1364/OL.39.005792
7. **Weiwei Zhang**, Samuel Serna, Xavier Le Roux, Laurent Vivien, Eric Cassan: *Highly sensitive refractive index sensing by fast detuning the critical coupling condition of slot waveguide ring resonators*. Optics Letters 01/2016; 41(3). DOI:10.1364/OL.41.000532
8. **Weiwei Zhang**, Samuel Serna, Xavier Le Roux, Carlos Alonso-Ramos, Laurent Vivien, Eric Cassan: *Analysis of silicon-on-insulator slot waveguide ring resonators targeting high Q-factors*. Optics Letters 12/2015; 40(23). DOI:10.1364/OL.40.005566

9. **Weiwei Zhang**, Samuel Serna, Nicolas Dubreuil, Eric Cassan: *Nonlinear optimization of slot Si waveguides: TPA minimization with FOMTPA up to 4.25*. Optics Letters 04/2015; 40(7). DOI:10.1364/OL.40.001212
10. Charles Caer, Xavier Le Roux, Samuel Serna, **Weiwei Zhang**, Laurent Vivien, Eric Cassan: *Large group-index bandwidth product empty core slow light photonic crystal waveguides for hybrid silicon photonics*. Frontiers of Optoelectronics 09/2014; 7(3). DOI:10.1007/s12200-013-0384-0
11. Mazeas, Florent, Michele Traetta, Marco Bentivegna, Florian Kaiser, Djeylan Aktas, **Weiwei Zhang**, Carlos Alonso Ramos et al. "Engineered silicon ring resonator for wavelength multiplexed photon-pair generation." *arXiv preprint arXiv:1609.00521* (2016) (Optics Express, accepted).
12. Federico La China, Francesca Intonti, Niccolò Caselli, Francesco Lotti, Francesco Sarti, Anna Vinattieri, Adrien Noury, Xavier Le Roux, **Weiwei Zhang**, Eric Cassan, Carlos Alonso Ramos, Elena Durán Valdeiglesias, Nicolas Izard, Laurent Vivien, Massimo Gurioli: *Near-Field Fano-Imaging of TE and TM Modes in Silicon Microrings*. ACS Photonics 11/2015; 2(12). DOI:10.1021/acsphotonics.5b00327
13. Junfei Xia, Samuel Serna, **Weiwei Zhang**, Laurent Vivien, and Éric Cassan, "Hybrid silicon slotted photonic crystal waveguides: how does third order nonlinear performance scale with slow light?," Photon. Res. **4**, 257-261 (2016)
14. Meiling Zhang, **Weiwei Zhang**, Fei Wang, Dan Zhao, Chunyang Qu, Xibin Wang, Yunji Yi, Eric Cassan, Daming Zhang. High-gain polymer optical waveguide amplifiers based on core-shell NaYF4/NaLuF4: Yb3+, Er3+ NPs-PMMA covalent-linking nanocomposites, Scientific report, **Accepted.**

List of Figures

List of Table

Résumé en français du manuscrit de thèse

Titre :

Integration hybride sur silicium de materiaux dopes erbium ou riches en nanotubes de carbone semiconducteurs pour l'emission et l'amplification de la lumiere sur puce

Ce travail de thèse est une contribution à la thématique de l'intégration de matériaux actifs en photonique silicium pour la réalisation de fonctions actives. L'accent a été mis sur des matériaux préparés en film minces pouvant être déposés sur substrats silicium pour la réalisation de sources de lumière intégrées.

La version complète du manuscrit rédigé en anglais décrit le travail de 3 ans et demi réalisé à l'Institut d'Electronique Fondamentale UMR 8622, (et au C2N, UMR 9001 à partir du 01/06/2016), depuis mon stage de Master M2 (mars à septembre 2013) sous la direction d'Éric Cassan.

Mon équipe d'accueil a été le groupe Minaphot, dirigé par Delphine Morini, comprenant 3 chercheurs / enseignants chercheur, un ingénieur et un technicien salle blanche, et une douzaine de doctorants/postdoctorants.

Les structures photoniques intégrées présentées dans ce manuscrit ont été fabriquées au sein de la Centrale de Technologie Universitaire de l'IEF/C2N-Orsay, grâce à l'expertise et sous la supervision de Xavier Le Roux.

Le travail mené a conduit à une structuration des résultats en trois parties principales :

1. Structures photoniques passives à cœur creux pour l'intégration hybride sur puce.
2. Structures actives silicium/Erbium pour l'amplification optique sur puce.
3. Structures actives pompées optiquement à base de nanotubes de carbone intégrés en photonique sur silicium.

Chacune de ces étapes a conduit à des résultats que nous présentons ci-après.

1. Structures photoniques passives à cœur creux pour l'intégration hybride sur puce.

L'objectif de la thèse n'a pas été de développer spécifiquement des structures passives en photonique silicium mais d'intégrer des matériaux actifs pour la réalisation de sources de lumières intégrées. Néanmoins, le développement de structures passives est apparu comme une étape préliminaire indispensable. L'accent a été mis sur la conception, la fabrication, et la réalisation de guides d'ondes et de résonateurs optiques à faibles pertes. L'approche classique en photonique silicium dans le fenêtre télécom (λ~1.55µm) repose sur l'utilisation de guides strip fabriqués à partir de substrats silicium sur isolant, SOI (**Fig. 1**) :

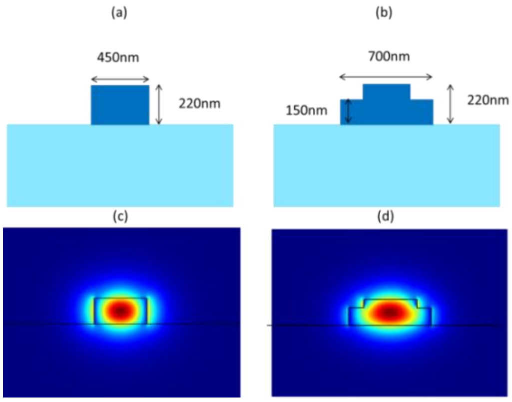

Fig. 1 : Vues schématiques en coupe de guides silicium sur isolant présentant des dimensions typiques, ainsi que les distributions de champ électromagnétique correspondantes à λ=1.55µm.

Le choix qui été fait dans le présent travail repose en revanche sur l'utilisation de guides à cœur creux ('slot waveguides') en raison de l'excellent recouvrement qu'ils permettent entre leur mode optique fondamental quasi-TE et les matériaux de couverture utilisés (**Fig. 2**) :

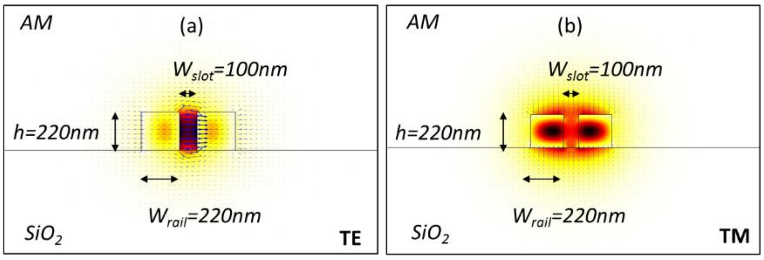

Fig. 2 : Résultats de simulation de guides à fente ('slot') sur silicium sur isolant, présentant des dimensions typiques, ainsi que les distributions de champ électromagnétique correspondantes à λ=1.55µm.

Un travail important d'optimisation des injecteurs de lumière dans ce type de guides optiques a été conduit en vue de leur utilisation dans des circuits photoniques SOI. Ce travail a porté à la fois sur les étapes de conception/simulation et sur celles liées à l'optimisation des étapes de fabrication en salle blanche. Deux types principaux d'injecteurs ont ainsi été optimisés : injecteurs par couplage en bout et injecteurs par couplage évanescent (ou latéral). Ces deux types de géométries sont décrits en **Figs. 3 et 4**.

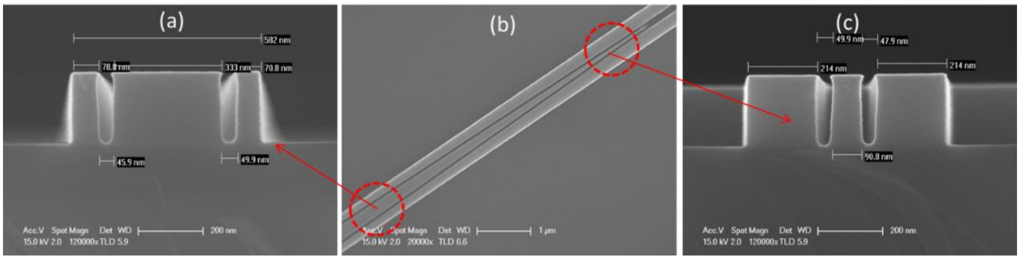

Fig. 3 : Structures silicium fabriquées pour l'injection de lumière par couplage en bout

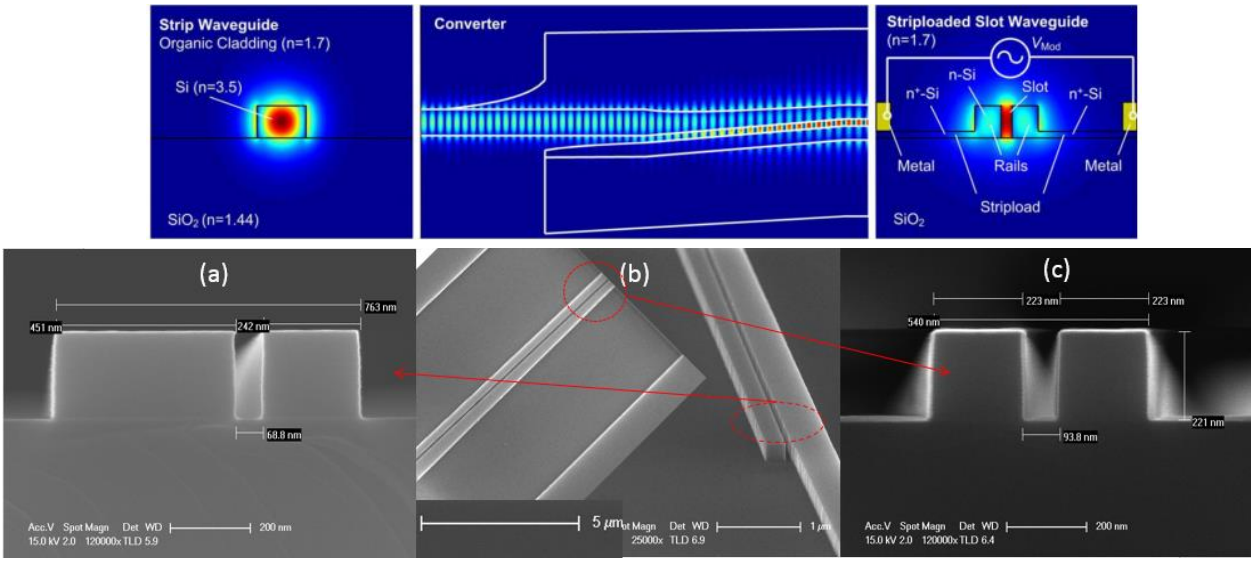

Fig. 4 : Haut : principe du couplage évanescent de la lumière dans un guides slot SOI. Bas : Structures silicium fabriquées pour l'injection de lumière par couplage évanescent (latéral).

Ces travaux préliminaires ont permis d'obtenir des pertes de couplage guide-strip/guides-slot typiquement inférieures à 0.3dB dans les différentes configurations étudiées et donc de lever un point d'étape important pour l'utilisation des guides silicium slot. Différentes étapes ultérieures, comme la correction des erreurs de raccord de champ de la lithographie électronique, ont également été menées avec succès. La méthodologie d'optimisation des procédés technologiques de salle blanche a été appliquée de manière complémentaire à des guides et résonateurs fabriqués à partir de substrat silicium nitrure sur silicium, définissant ainsi une seconde famille de guides SiN/SiO_2 complémentaires à ceux Si/SiO_2.

L'ensemble a permis la fabrication de guides et de résonateurs variés satisfaisant les objectifs d'intégration hybride de la thèse.

A titre d'exemples, les **Figs. 5-7** montrent un ensemble de réalisations typiques de cette thèse, pour lesquels des guides slot Si/SiO_2 et SiN/SiO_2 et des résonateurs en anneaux basés sur ces guides ont conduit à :

- Des pertes de propagation typiquement comprises entre 1dB/cm et 7dB/cm.
- Des résonateurs à facteur de qualité de quelques dizaines de milliers pour des structures couvertes par des liquides d'indice.

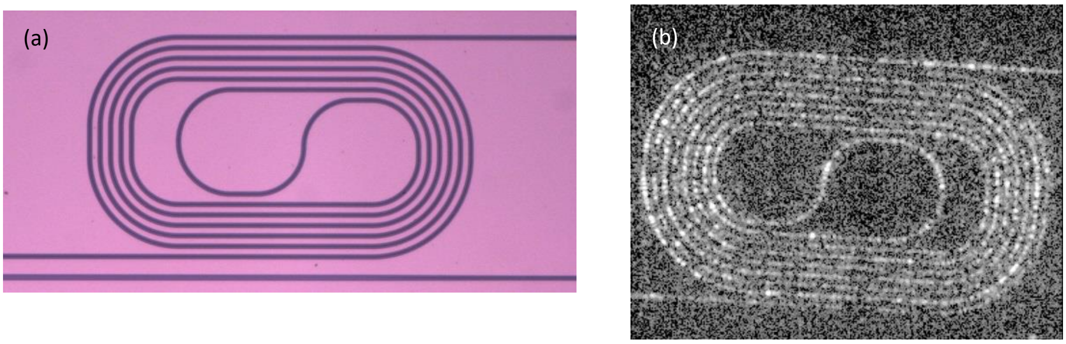

Fig. 5 : Guides SiN en spirale permettant de caractériser les pertes de propagation sur des distances déroulées de plusieurs millimètres.

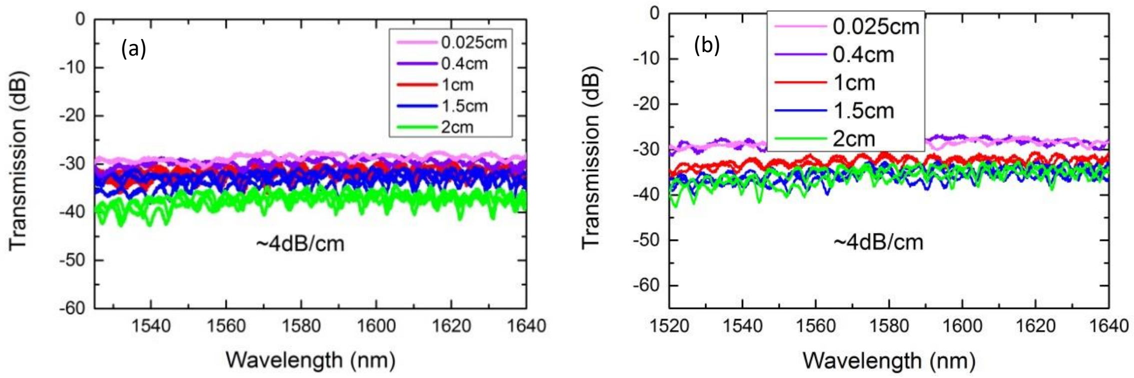

Fig. 6 : Mesures de transmission optique des structures présentées en Fig. 5.

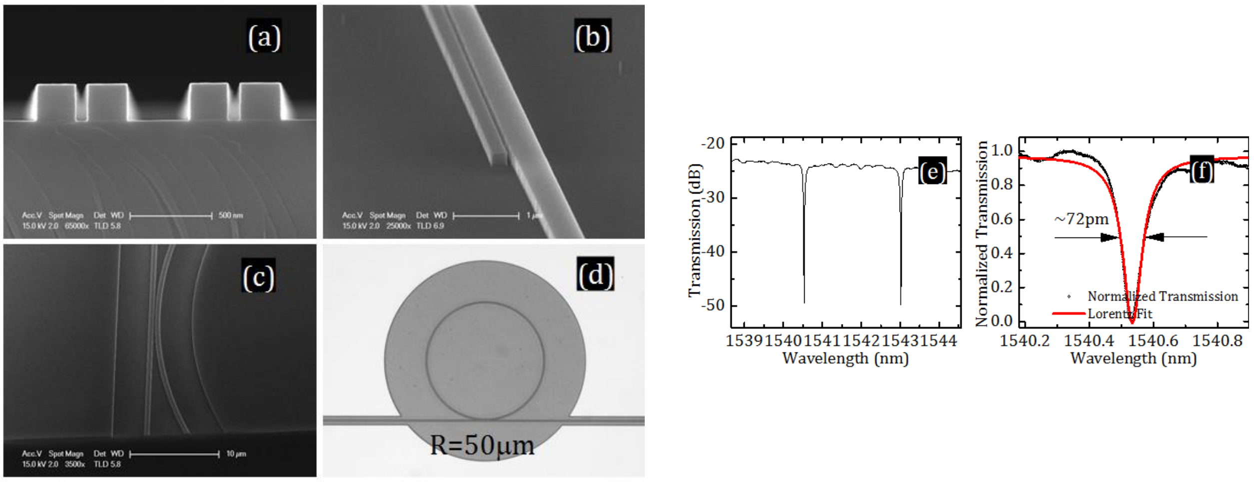

Fig. 7 : Résonateurs en anneaux SOI : vues de détail prises au microscope électronique à balayage et résultats de caractérisations optiques effectuées sur ces échantillons.

2. Structures actives silicium/Erbium pour l'amplification optique sur puce.

Dans un deuxième temps, les travaux poursuivis ont visé à l'intégration de matériaux actifs dopés à l'Erbium dans les guides à fentes présentés en première partie en vue de la démonstration de gain optique sur puce dans la fenêtre télécom (λ~1.55µm).

Le schéma d'intégration correspondant est présenté en **Fig. 8**.

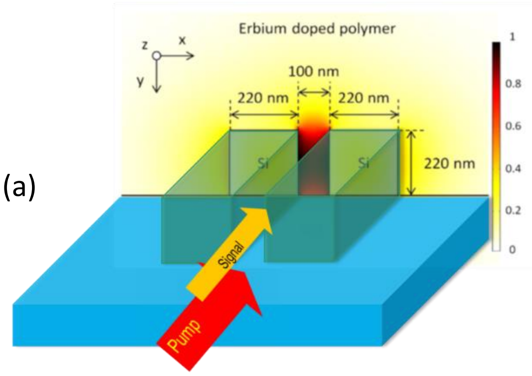

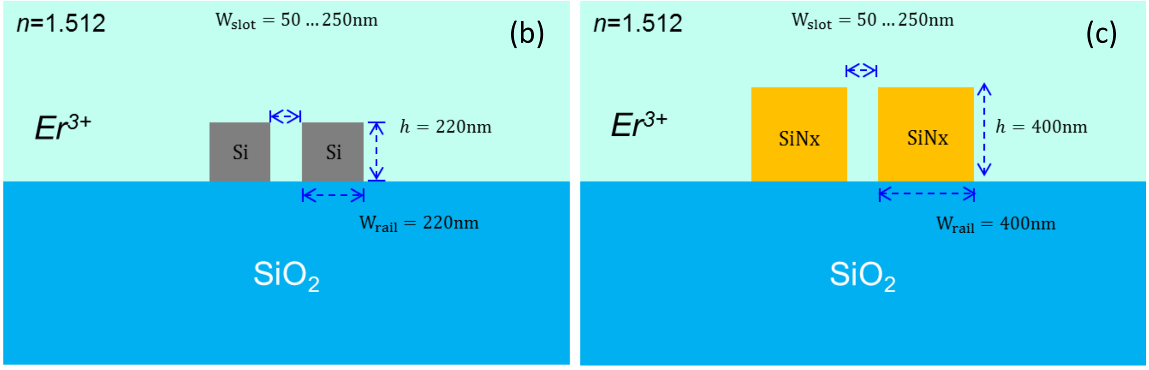

Fig. 8 : Vues de principe des configurations étudiées en vue de la réalisation d'amplificateurs à guides dopés Erbium en photonique sur silicium : familles de guides Si/SiO_2 et SiN/SiO_2.

Plus précisément, nous avons travaillé dans le cadre de deux collaborations avec deux équipes étrangères :

- Le groupe du SKLIO de l'Université de Jilin en Chine développant des films minces dopés aux ions Er^{3+} et co-dopés aux ions Yb^{3+} sous la forme de nanoparticules cœur/coquille α-$NaYF_4$ {β-$NaLuF_4$} copolymérisées avec du methyl methacrylate (MMA) pour donner une synthèse de nanocomposites (PMMA-NPs: Er^{3+}/Yb^{3+}).
- Le groupe du département de Micro- and Nanosciences del'université Aalto (Finlande), produisant par croissance ALD (Atomic Layer Deposition) des films minces dopés Erbium d'oxyde Al_2O_3 jusqu'à des concentrations de 10^{21} cm^{-3}.

La première de ces deux collaborations nous a amené à la démonstration de gain optique sur puce à partir d'une géométrie de guide en arête inversée fabriqué en polymère actif. Un gain interne de l'ordre de 25dB sur puce a été obtenu par cette approche pour une puissance de pompe optique de l'ordre de 70 à 80mW (voir **Fig. 9**) :

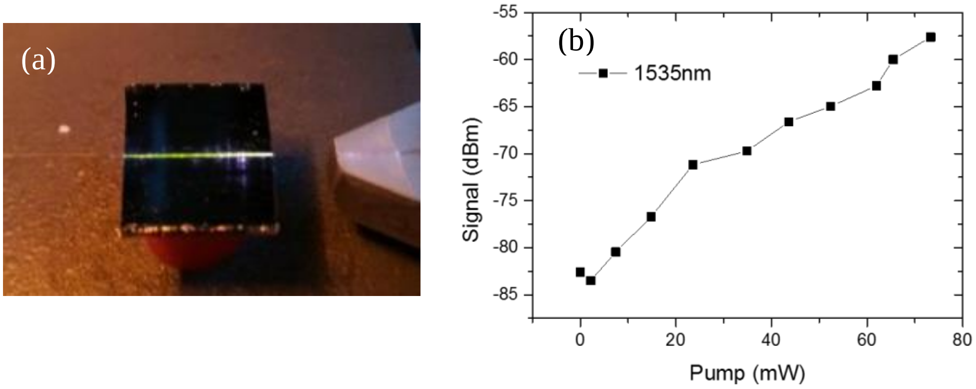

Fig. 9 : Mesure de gain optique dans un guide polymère dopé aux nanoparticules Erbium-Yttertium/PPMA synthétisées au sein de l'université de Jilin (collaboration dans le cadre du projet ANR/NSFC POSISLOT) ; pompage à λ=980nm.

La second collaboration s'est focalisée, quant à elle, sur l'intégration d'oxyde Al_2O_3 dans des guides à fentes SiN fabriqués à Orsay. Les problématiques d'intégration des matériaux ont été étudiées dans un premier temps (voir **Fig. 10**) :

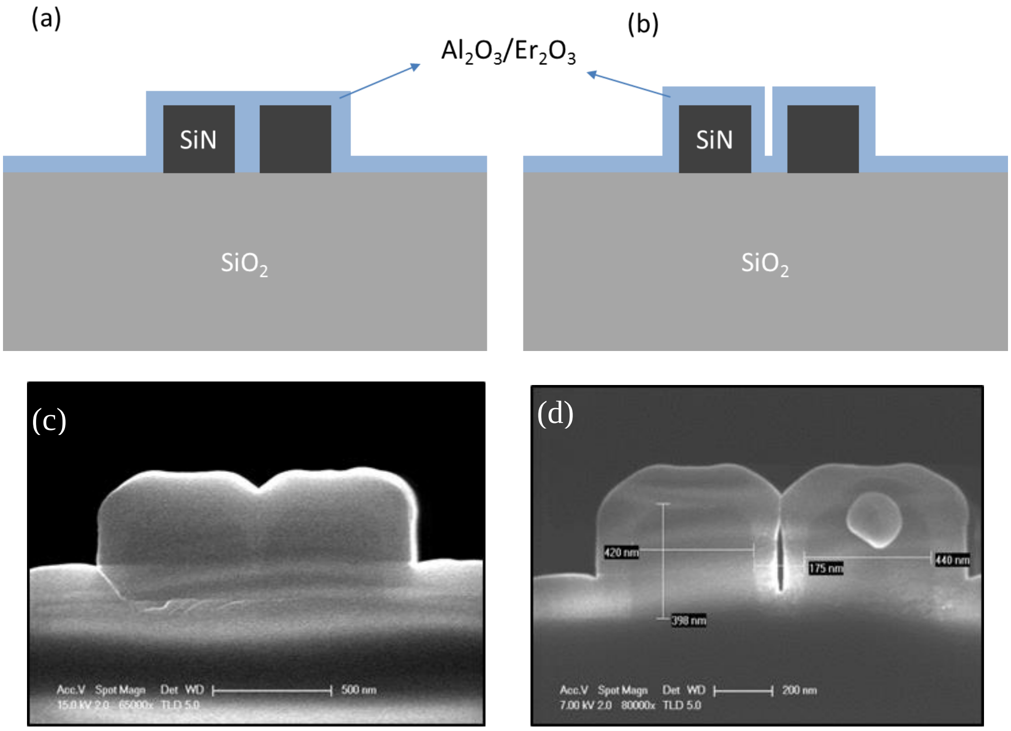

Fig. 10 : Intégration de couches minces d'oxyde Al_2O_3 dans des guides à fentes SiN en vue de la réalisation d'amplificateurs intégrés sur puce par pompage optique à λ=1480nm.

Des modélisations numériques ont été menées de manière complémentaire de manière à anticiper les niveaux possibles de gain dans les guides actifs fabriqués et caractérisés. A partir des profils en coupe des champs (voir **Fig. 11**), un algorithme de calcul des intensités de champs de pompe et de signal a été implémenté dépendant de manière réaliste des paramètres spectroscopiques du milieu amplificateur, des niveaux du signal et la pompe en entrée, et de la section du guide à fente.

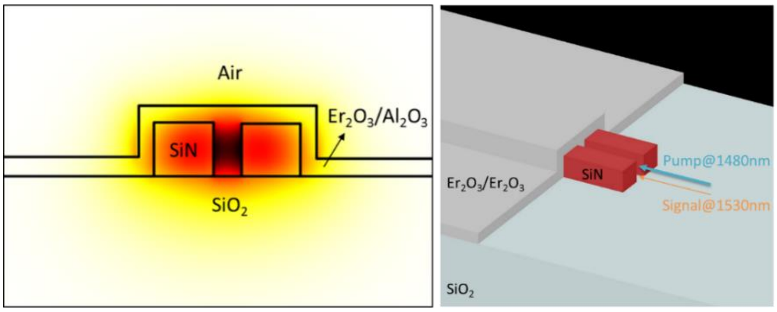

Fig. 11 : Vue en coupe du guide et du profil du champ considéré pour la modélisation de l'amplification de la lumière dans un guide à fente SiN rempli par un oxyde Al_2O_3 dopé à l'Erbium.

Ces modélisations ont ainsi permis d'anticiper le niveau de gain optique net dans la configuration étudiée en **Fig. 11** pour un signal de pompe de l'ordre de 100mW :

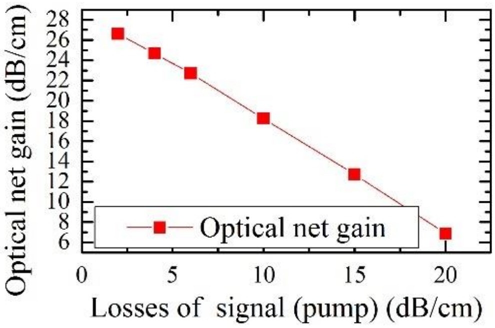

Fig. 12 : Gain net prédit par les simulations numériques dans la configuration de la figure 11.

Dans le temps imparti de la thèse, le résultat le plus marquant a été obtenu pour un guide de longueur 400µm, pour lequel un gain relatif de 1.5dB a été obtenu pour une puissance de pompe de l'ordre de 50mW à λ=1480nm :

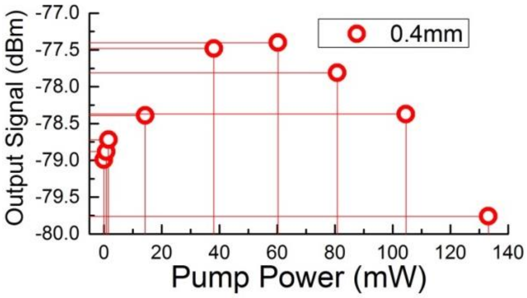

Fig. 13 : Evolution du niveau de signal (λ=1550nm) en sortie du guide SiN slot de la **Fig. 10** en fonction de la puissance de pompe (λ=1480nm).

3. Structures actives pompées optiquement à base de nanotubes de carbone intégrés en photonique sur silicium.

De manière complémentaire, nous avons exploré une seconde voie destinée à la démonstration de structures émittrices/amplificatrices sur puce, exploitant l'utilisation de nanotubes de carbone semi-conducteurs. Notre équipe du C2N, en forte collaboration avec le CEA-Saclay (Dr. Arianna Filoramo), a développé une méthode de préparation de solutions riches en nanotubes de carbone semi-conducteurs (séparation par centrifugation). Cette solution a pu être déposée sous la forme de goutes (drop-cast) sur des substrats, et une technique spécifique de préparation des échantillons a permis de localiser, par évaporation du solvant (toluène), de fortes concentrations de nanotubes de carbone semiconducteurs. Au final, les couches minces (plus ou moins homogènes) qui en ont résulté ont constitué un milieu actif qui a pu être intégré de manière planaire sur des échantillons de silicium pour le développement de fonctions optiques intégrées par intégration hybride.

Les études menées dans ce manuscrit ont été orientées vers le développement de sources optiques intégrées. Nous avons cherché, notamment :

- à démontrer qu'un pompage vertical des structures photoniques pouvait donner lieu à une extraction de photoluminescence (PL) en sortie guidée par la tranche, dans des guides à fentes,
- qu'un renforcement significatif de la PL était obtenue par effet de recyclage des photons dans des résonateurs diélectriques à base de guides à fente.

Globalement, ces études peuvent être vues comme une contribution vers la démonstration de l'utilisation possible de milieux riches en nanotubes de carbone semi-conducteurs pour l'émission de lumière sur puce, et si possible la démonstration de l'effet laser en configuration intégrée.

La principale configuration expérimentale qui a été exploitée est décrite en **Fig. 14**.

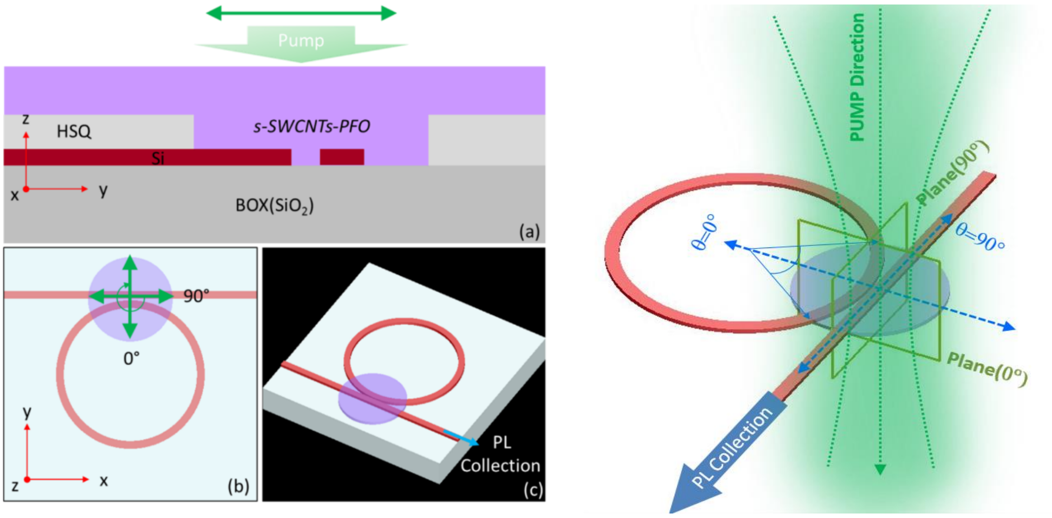

Fig. 14 : Configuration expérimentale utilisée pour l'étude expérimentale des propriétés de photoluminescence de nanotubes de carbone semi-conducteurs et couplage de la lumière dans des guides d'ondes optiques.

Cette configuration repose sur le dépôt de résine HSQ en couverture des structures, en vue de leur protection, puis dépôt localisé dans des cuvettes ouvertes à cet effet de polymère PFO dopé aux nanotube de carbone (dépôt planaire mais interaction localisée du fait des ouvertures).

Cette approche a permis de démontrer un renforcement spectaculaire de la PL émise par les nanotubes de carbone semi-conducteurs présents dans la zone de couplage des résonateurs optiques en anneau exploités et le couplage de cette émission vers des guides optiques.

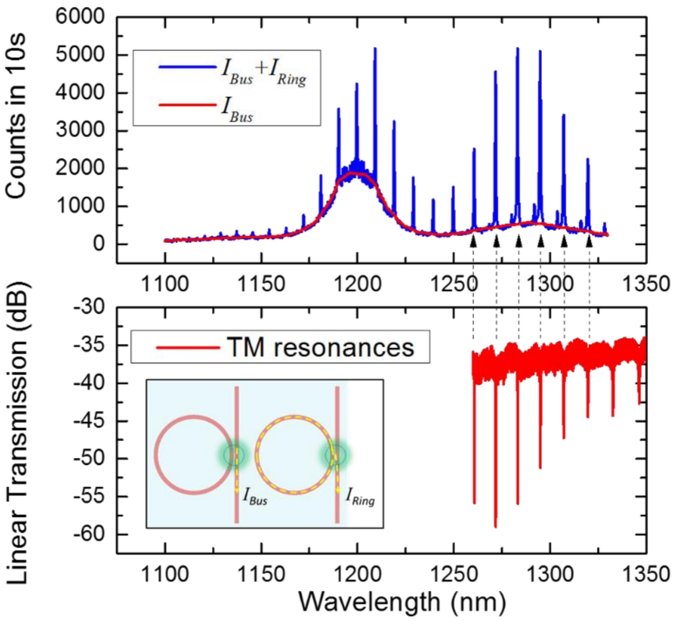

Fig. 15 : Résultats expérimentaux de luminescence : collection de la PL renforcée par le recyclage des photons dans une configuration de résonateur en anneau.

Pour conclure, l'ensemble des travaux présentés dans cette thèse apporte une contribution au développement d'une photonique hybride sur silicium exploitant les propriétés de la plateforme de guidage optique sur SOI et celles de matériaux actifs (polymères dopés à l'Erbium ou aux nanotubes de carbone). L'accent a été mis sur un ensemble d'études dédiées à l'émission (partie 3) et à l'amplification (partie 2) de la lumière sur puce dans des structures de guides et de résonateurs optiques passifs optimisés (partie 1).

Titre : Integration hybride sur silicium de materiaux dopes erbium ou riches en nanotubes de carbone semiconducteurs pour l'emission et l'amplification de la lumiere sur puce

Mots clés : Silicium, integration hybride, nanotubes, erbium, l'amplification de la lumiere, l'emission de la lumiere

Résumé : Ce travail de thèse est une contribution à la thématique de l'intégration de matériaux actifs en photonique silicium pour la réalisation de fonctions actives. L'accent a été mis sur des matériaux préparés en couches minces pouvant être dépose sur substrats silicium pour la réalisation de sources de lumière intégrées.

L'approche classique en photonique silicium dans le fenêtre télécom (1.55µm) repose sur l'utilisation de guides strip fabriqués à partir de substrats silicium sur isolant, SOI). Le choix qui été fait dans ce travail repose en revanche sur l'utilisation de guides à cœur creux ('slot waveguides') en raison de l'excellent recouvrement qu'ils permettent entre leur mode optique fondamental quasi-TE et les matériaux de couverture utilizes. Les contributions de cette thèse ont porté à la fois sur les étapes de conception/simulation et sur celles liées à l'optimisation des étapes de fabrication en salle blanche.

Des guides slot Si/SiO_2 et SiN/SiO_2 et des résonateurs en anneaux basés sur ces guides ont conduit à :

- des pertes de propagation typiquement comprises entre 1dB/cm et 7dB/cm.
- des résonateurs à facteur de qualité de quelques dizaines de milliers pour des structures couvertes par des liquides d'indice.

Dans un deuxième temps, les travaux poursuivis ont visé à l'intégration de matériaux actifs dopés à l'Erbium dans les guides à fentes présentés en première partie en vue de la démonstration de gain optique sur puce dans la fenêtre télécom (1.55µm). Une première collaboration nous a amené à la démonstration de gain optique sur puce à partir d'une géométrie de guide en arête inversée fabriqué en polymère actif. Un gain interne de l'ordre de 25dB sur puce a été obtenu par cette approche pour une puissance de pompe optique de l'ordre de 70 à 80mW. Une seconde collaboration s'est focalisée, quant à elle, sur l'intégration d'oxyde Al_2O_3 dans des guides à fentes SiN fabriqués à Orsay. Les problématiques d'intégration des matériaux ont été étudiées dans un premier temps. Le résultat le plus marquant a été obtenu pour un guide de longueur 400µm, pour lequel un gain relatif de 1.5dB a été obtenu pour une puissance de pompe de l'ordre de 50mW à longueur d'onde 1480nm.

De manière complémentaire, nous avons exploré une seconde voie destinée à la démonstration de structures émittrices/amplificatrices sur puce, exploitant l'utilisation de nanotubes de carbone semiconducteurs. Notre équipe du C2N, en forte collaboration avec le CEA-Saclay, a développé une méthode de préparation de solutions riches en nanotubes de carbone semiconducteurs (séparation par centrifugation). Au final, les couches minces qui en ont résulté ont constitué un milieu actif qui a pu être intégré de manière planaire sur des échantillons de silicium pour le développement de fonctions optiques intégrées par intégration hybride.

Par cette approche, nous avons démontré :
- qu'un pompage vertical des structures photoniques pouvait donner lieu à une extraction de photoluminescence (PL) en sortie guidée par la tranche, dans des guides à fentes,
- qu'un renforcement significatif de la PL était obtenu par effet de recyclage des photons dans des résonateurs diélectriques à base de guides à fente.

Pour conclure, l'ensemble des travaux présentés dans cette thèse apporte une contribution au développement d'une photonique hybride sur silicium exploitant les propriétés de la plateforme de guidage optique sur SOI et celles de matériaux actifs (polymères dopés à l'Erbium ou aux nanotubes de carbone).

Title: Hybrid integration of Er-doped materials and CNTs on silicon for light emission and amplification

Keywords: Erbium doped materials, CNT, silicon photonics, light amplification, light emission

Abstract: This thesis is a contribution to the hybrid integration of active materials including Erbium-doped and carbon nanotubes rich layers on silicon for on-chip light emission. Hollow core silicon and silicon nitride photonic waveguides and devices are designed, fabricated, and characterized at both 1.3µm and 1.55µm wavelength ranges. A specific focus is made on using slot waveguides, for which hollow core light confinement properties bring specific advantages for the integration of soft materials in silicon photonics. The key properties include large light-matter overlap factors, reduced two-photon absorption in the telecommunication window, tight confinement of electric fields, ultra-small cavity mode volumes, and high sensitivity resonators.

In a first step, we designed, fabricated, and characterized within the silicon-on-insulator and silicon nitride platforms a range of photonic structures including strip/slot waveguides, micro disks, strip/slot ring resonators, and micro cavities aiming at preparing a set of passive device building blocks needed for hybrid integration on Si. Silicon slot waveguides and slot ring add-drop resonators filled with index liquids with linear propagation losses 2-7 dB/cm and Q-factors up to 30,000, have been demonstrated around λ=1.55µm. Propagation loss of silicon nitride slot waveguides were minimized down to ~4dB/cm for compact spiral structures (2cm long, within ~500µm×500µm area). Air-band mode nanobeam cavities were also investigated, leading to nano cavities with mode volumes $V \sim 0.03(\lambda/n)^3$ and Q-factors ~70,000 when filled with soft materials.

In a second step, hybrid integration of Erbium doped materials and semiconducting single-wall carbon nanotubes (SWCNTs) was investigated for light emission under optical pumping.

Integration of Erbium-doped materials was studied within the framework of two collaborations: Prof. Daming Zhang's team, in State Key Laboratory on Integrated Optoelectronics, Jilin University, China, and Prof. Zhipei Sun, in Department of Micro- and Nanosciences, Aalto University, Finland. Erbium doped layers coming from Jilin were composed of Er^{3+} and Yb^{3+} co-doped core {shell} α-$NaYF_4$ {β-$NaLuF_4$} nanoparticles which were copolymerized with methyl methacrylate (MMA) to synthesize nanocomposite (PMMA-NPs: Er^{3+}/Yb^{3+}). We conducted the experimental characterization that led to the demonstration of an internal net gain up to 10-17dB/cm at λ=1.53µm in Erbium doped polymer rib waveguides fabricated in Jilin. The second Erbium doped material available during this thesis was based on Er_2O_3/Al_2O_3 atomic layers, grown in Aalto University. This collaboration was devoted to integrate high Erbium ion concentration ($\sim 10^{21}/cm^3$) in oxide cladding layers on top of silicon nitride slot waveguides, which were fabricated in our group for the demonstration of on-chip optical net gain. The carried out experiments have conducted to the demonstration of 1.5-22.8dB/cm gain for sub millimeter length waveguides.

In another direction, hybrid integration of SWCNTs emitting at wavelengths around 1.3 µm on ring resonators and nanobeam cavities has been investigated. First, we studied the coupling of SWCNTs photoluminescence (PL) in silicon micro-ring resonators and compared it with the PL intensity coupled into the bus waveguide. It has been shown that the pump beam polarization controls the light coupling into the straight bus waveguide. We demonstrated an enhancement of the PL intensity of 20dB at resonance. We also explored CNT hybrid integration with ultra-small mode volume nanobeam optical cavities, and hence with larger Purcell-like Q/V factors in comparison with the one obtained in micro-ring resonators. The results revealed that the PL resonance enhancement due to nanobeam cavity field confinement exhibited a nonlinear growth as a function of the pump power. It was also shown that the resonance of the PL peak intensity grows faster with the pump power than the PL background, which is accompanied by a line width narrowing of the resonance PL peak. This result is the first step to achieve an integrated laser based on carbon nanotubes.

To conclude, during this thesis, we designed, fabricated, optimized and characterized low loss silicon and silicon nitride slot waveguides and air mode nanobeam cavities for hybrid integration. Two materials were studied: Erbium doped polymers and oxides and CNTs-PFO polymers. Promising results, i.e. internal net gain of Erbium hybrid slot waveguides, strong CNT PL coupling with silicon ring resonators and CNT PL enhanced emission were obtained and results were discussed. This work demonstrates that the integration of light emitting materials in hollow silicon photonic structures is a promising solution to obtain light sources/amplifiers in silicon photonics.